EASTMAN KODAK COMPANY
APPARATUS AND OPTICAL DIVISION

FINAL REPORT

PHASE IV

LUNAR PHOTO STUDY

Contract NAS 9-7625

30 November 1967 - 30 November 1968

Prepared by

EASTMAN KODAK COMPANY
Kodak Apparatus Division
Rochester, New York 14650

For

NASA MANNED SPACECRAFT CENTER
Mapping Sciences Laboratory
Houston, Texas 77058

Prepared by: J. B. Hustler
J. B. Hustler

T. J. Lauroesch
T. J. Lauroesch

Approved by: George T. Keene
G. T. Keene

L. R. Martin
L. R. Martin

14 March 1969

Kodak

FOREWORD

This final report for Contract NAS 9-7625 covers the study period from 30 November 1967 to 30 November 1968. Contract NAS 9-7625 is Phase IV of work done by Eastman Kodak Company for NASA related to the same basic subject, viz., photography of the moon.

Phase I work was done under Contract NAS 9-3826 in the period 1 December 1964 to 1 October 1965. The contract authorized a study to investigate the materials and techniques for making realistic lunar models, to examine the interpretation of photographs of simple geometric shapes and typical lunar surface features with lunar photometric characteristics and to prepare motion pictures simulating the landing approach of a Lunar Module.

Contract NAS 9-3826 was extended for the period 1 November 1965 to 1 November 1966 to carry out Phase II work. Kodak investigated the preparation of contour maps from lunar photographs by the photoclinometric method and compared this method to the stereo mapping technique. A method was proposed for mapping by the comparison of relative luminosities obtained from stereo photographs. Methods were studied for enhancing lunar photographs by superimposition and high contrast printing. Techniques were studied for rating the quality of lunar photographic systems by edge trace analysis and by use of a file of comparison photographs. Additional motion pictures were prepared simulating a Lunar Module landing using a larger model.

Phase III work under Contract NAS 9-3826 covered the period from 1 June 1967 to 30 July 1967 during which time additional motion picture simulations were prepared for new lighting conditions and trajectories.

Contract NAS 9-7625 was monitored by Mr. James L. Dragg of the Mapping Sciences Laboratory. The work has covered three areas related to lunar photography - motion picture simulations of Lunar Module landings, lunar photometry and mapping, and rating and improving lunar photographs.

Work done under the current contract was based substantially on the experience gained in the earlier contracts. In this report many references are made to the final reports[1][2] for the work done under Phases I and II. In cases where broad reference is made to the previous work, the exact location is not cited for the description of the earlier effort. In cases where very specific information is drawn from the earlier reports (e.g., data, conclusions, formulas), the origin of the item is called out.

Five computer programs were written for the current work. Each of these programs has been delivered to the Technical Monitor in three parts: (1) a description of the program, including the setup of the data deck; (2) the source deck in Fortran IV language, and (3) a listing of the program in Fortran IV. This information has been omitted from this report except for brief descriptions of the use and content of the programs. The five programs are: EGADS, FILT, LODAP, LUNA II and MAP.

A change has been made from earlier reports in the symbols used to describe the photometric function $\phi(g, \alpha)$. The letters g and α are widely used in publications to represent the phase angle and auxiliary angle respectively describing the geometry of illumination and viewing of the lunar surface. Readers referring to the final reports of Phases I and II and bimonthly reports of Phase IV may be confused by the use of the other symbols (α, τ) to describe the photometric function.

---

(1) All references are listed in the BIBLIOGRAPHY

SUMMARY

A realistic 10' X 10' lunar model was made at a scale of about 1:50 to represent a portion of a potential landing site in Sinus Medii. Construction was based on a contour map of the area furnished by NASA. The visual appearance of the moon was achieved by dusting with cupric oxide and lighting with a source simulating the sun.

Motion pictures of this model were made to simulate a portion of the view from a LM window during one of the final minutes of a landing. The motion picture sequences showed two basic approaches to landing - a straight-in approach along a 14° incline to a primary site and a dogleg maneuver to a secondary site. A motion picture was made for each trajectory for sun elevations of 5° and 12°; when projected at 24 frames/sec, these motion pictures show events in real time. Still photographs were made at seven selected positions along the trajectory during the filming of the motion pictures for the straight-in approach.

A demonstration and an error analysis made for the photoclinometric mapping technique for 30° sun elevation were compared with results obtained at 15° sun elevation on an earlier contract under which the method was developed. It was shown on a laboratory model that photographic mapping at 30° sun elevation can be done with accuracy comparable to that at 15° sun elevation. Accuracy depends on correctly placing densities on the film characteristic curve for photographic photometry, forcing a trade-off between using small phase angles with low scene contrast and large phase angles with lower sensitivity to slope changes. It was concluded that the optimum sun elevation for a photographic mapping mission depends on the average slope of the terrain being mapped and the accuracy desired. In general rugged terrain should be mapped at higher sun elevations.

Tests were made on the ϕ_1/ϕ_2 method of lunar mapping suggested on a previous contract. From the ratio of the relative luminosity in two views of a stereo pair a unique slope can be obtained. The ϕ_1/ϕ_2 method offers best accuracy for mapping gradual slopes when stereo photographs are available but there is insufficient surface detail to permit conventional stereo mapping.

The photometric function was measured with improved confidence for a small range of slopes on a single photograph from Lunar Orbiter. Techniques were developed to obtain data from spherical craters.

It was shown that predictions of the smallest details recognizable in lunar photographs are best made by combining methods for predicting limiting resolving power for a lens-film system with knowledge from a previous contract relating the threshold of resolving power to the threshold of recognition for lunar subjects.

Performance evaluation was done by edge gradient analysis on laboratory and Lunar Orbiter photographs. Crater shadows make satisfactory test objects when the crater is about 10 times the diameter of the smallest recognizable crater. A film-process combination must be treated as a nonlinear system when it exhibits photographic adjacency effects. Therefore, the MTF of the photo optical system can be derived from knowledge of its components, but component transfer functions can not be determined by analysis of the overall MTF curve.

Measurement of Lunar Orbiter photographs confirmed the results obtained using laboratory photographs on a previous contract in which the threshold of recognition of lunar subjects was related to the threshold of resolving power.

Identification of rocks and craters is improved with multiple views of a lunar surface, but rapid presentation of such photographs offers little advantage. Enhancement of photographs was demonstrated by grain integration and ring smear masking techniques. Detail rendition is improved in a system limited primarily by film grain rather than by lens quality.

TABLE OF CONTENTS

TABLE OF CONTENTS (Continued)

TABLE OF CONTENTS (Continued)

LIST OF ILLUSTRATIONS

LIST OF ILLUSTRATIONS (Continued)

LIST OF ILLUSTRATIONS (Continued)

LIST OF ILLUSTRATIONS (Continued)

LIST OF TABLES

I. MOTION PICTURE SIMULATIONS OF THE VIEW FROM A LM WINDOW DURING LUNAR LANDING

A. Introduction

The object of this work was to make a series of motion pictures showing a portion of the view from the LM window as seen by an Apollo astronaut for about the last minute of approach to the lunar landing site. Variations in the motion pictures in the series have been made to show changes in the visibility of features on the lunar landscape resulting from different sun elevations and different LM trajectories. These motion pictures are for use by NASA personnel performing studies on the effects of changes in lighting conditions.

The lunar photometric function is an important characteristic of the moon's surface which has a major influence on the visibility of subjects. The lunar surface gives a high degree of backscattering. Hence, the amount of light reflected by a lunar subject depends on the relative positions of the sun and the observer, as measured from the moon's surface.

Planning an Apollo landing on the moon requires taking into account the ability of the astronaut to observe potential hazards. Theoretical studies can describe the relative visibility of subjects in terms requiring interpretation for prediction of the subjective value. However, a realistic simulation provides a visual experience supplementing the calculations and interpretation, at least for a specific set of conditions.

B. Description of Making the Lunar Model

Previous work has developed techniques of making realistic lunar models. In the present work these techniques have been applied to the construction of a scale model of a specific area of the moon.

NASA furnished a contour map made by photometric reduction from video analog tapes of a small portion of Framelet 400 of Telephoto Frame 122 from Lunar Orbiter II. The contour map covers a square area about 750 feet on a side in Sinus Medii, a potential landing site for Apollo astronauts.

A 500 feet square portion of the contour map served as a guide in the construction of a square model 10 feet on the side at a scale of about 1:50. A photograph was taken of the contour map for the area to be represented in the model. This photograph was reproduced as four transparencies, each representing a quadrant. The model was made in square quadrants 5 feet on a side. For each quadrant, a box was built with removable sides. Each box was painted white for use as a projection screen for one of the transparencies. While the contour map was projected onto the floor of the box, the contour lines were painted in black. Allowances were made in projection for the presence of the box sides. Wire brads were driven perpendicularly into the floor of the box along the contour lines and allowed to protrude in an amount proportional to the contour height. The brads were spaced closely in locations of marked change in direction of the contour. Figure 1A shows one of the quadrants at this stage, with contour lines and wire brads; Figure 1B shows the four quadrants together.

Each quadrant was finished before assembly of the complete model. Plaster of Paris was poured into the quadrant box to a depth within about one-half inch of the tops of the wire brads and allowed to dry. The remaining depth was filled with Marblex self-hardening clay.

Marblex clay was chosen for a number of reasons. It was desirable to have a model made of a material not easily damaged in handling or by falling objects, particularly with the prospect of repeated dusting and dust removal. Preliminary tests showed that the dried Marblex clay was compatible with the cupric oxide dust to be used to simulate lunar

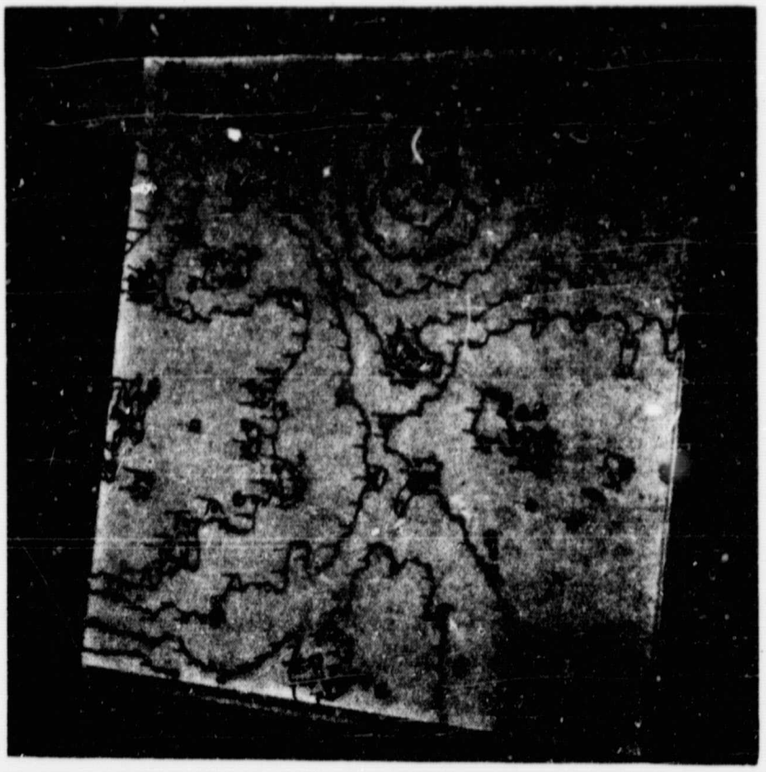

A One quadrant before addition of clay showing contours with nails set to correspond to the elevations

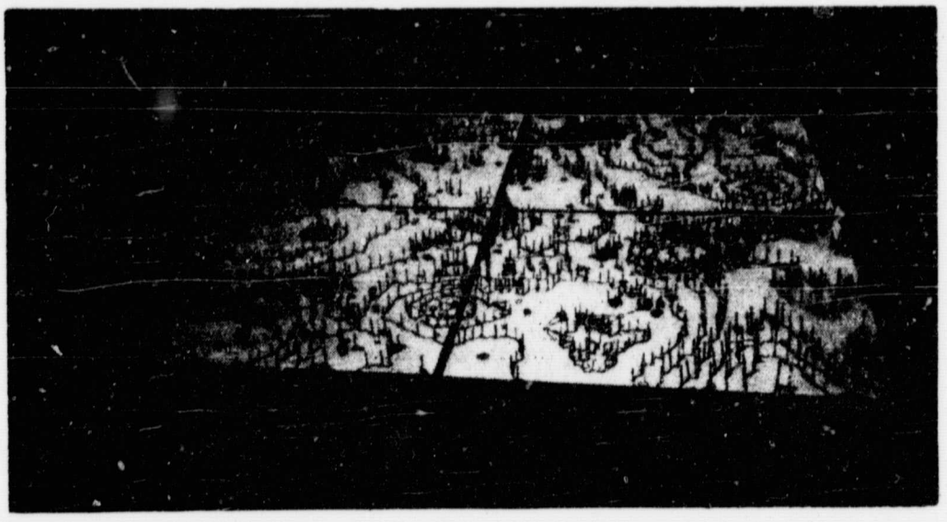

B Four quadrants before addition of clay

FIGURE 1. TWO STAGES IN MAKING MODEL FROM CONTOUR MAP

photometric characteristics. Ordinary modeling clay does not have either of these desirable properties. An advantage of the Marblex clay over plaster of Paris was that the hardening could be retarded several days to permit careful shaping. The material remained readily workable when covered with moist cloths and plastic to limit evaporation. Preliminary tests showed that during drying the Marblex clay developed only hairline cracks which were easily and permanently repaired. Experience on the final model indicated that the resistance to cracking may depend on the batch of material. About one-half of the model was made with a batch which dried relatively slowly; this portion of the model has been free of cracks. The other half of the model has consistently required repair of cracks after standing more than a few days. Unfortunately, the cause of the problem cannot be identified beyond question. The base layer of the first half of the model was made with thick plaster of Paris which was allowed to dry about 3 days before applying the Marblex clay which subsequently dried relatively slowly. The second half of the model was made with a base layer of thin plaster of Paris which was allowed about 3 weeks drying time before finishing with Marblex clay which dried rather rapidly. The cracking of the completed model could have been related to the preparations prior to application of the Marblex clay.

Craters smaller than the minimum detail on the contour map were added in random locations as follows: 170 craters with 2-feet diameters, 120 with 3-feet diameters and 80 with 4-feet diameters. The number of craters added to the model was based on two guides. On the contour map, 50 craters were counted in the diameter range from 5 to 10 feet within the area of the map being used. This area represents about 1/100 of a square mile on the moon, within which, from previous work, one expected to find about 500 such craters. The same data lead one to expect about 2 times as many 2 1/2 feet craters (representing the range 1-5 feet) as 7 1/2 feet craters (representing the range 5-10 feet). However, while the ratio of craters of each size was felt to be correct,

the absolute number of craters was less than anticipated. Therefore, the ratio of numbers of craters of two different sizes was preserved but the detail was extended on the basis of the crater count on the map.

Repairs to the model have been made using vinyl spackle which was sanded to match the surface after drying. Painting the model with epoxy paint provided some reduction in hairline cracks. A coating of epoxy paint on a model made with common modeling clay would be a good candidate for investigation in future model construction.

Each quadrant of the model was completed in the same manner. After removal of the sides of the boxes and joining of the bases, the intervening spaces were filled in and shaped using Marblex clay. Figure 2 shows a comparison of profiles prepared from measurements of the finished model with those prepared from the contour map furnished by NASA.

Figure 3 shows the portion of the contour map from which the model was prepared. Figure 3 is a transparent overlay for Figure 4 which is a high quality, vertical photograph of the completed and dusted model. In Figure 5 the quality of the photographic reproduction has been degraded from Figure 4 to simulate that in Figure 6, the portion of the Lunar Orbiter photograph from which the contour map was prepared by NASA.

Figure 5 was prepared from the negative of Figure 4 by defocusing in the enlargement stage and adding a granular pattern to simulate the phosphor noise of the Lunar Orbiter Ground Reconstruction Electronics.

The general resemblance of Figures 5 and 6 suggests faithful interpretation of the lunar scene by the contour map and in turn, careful execution of the model after the contour map.

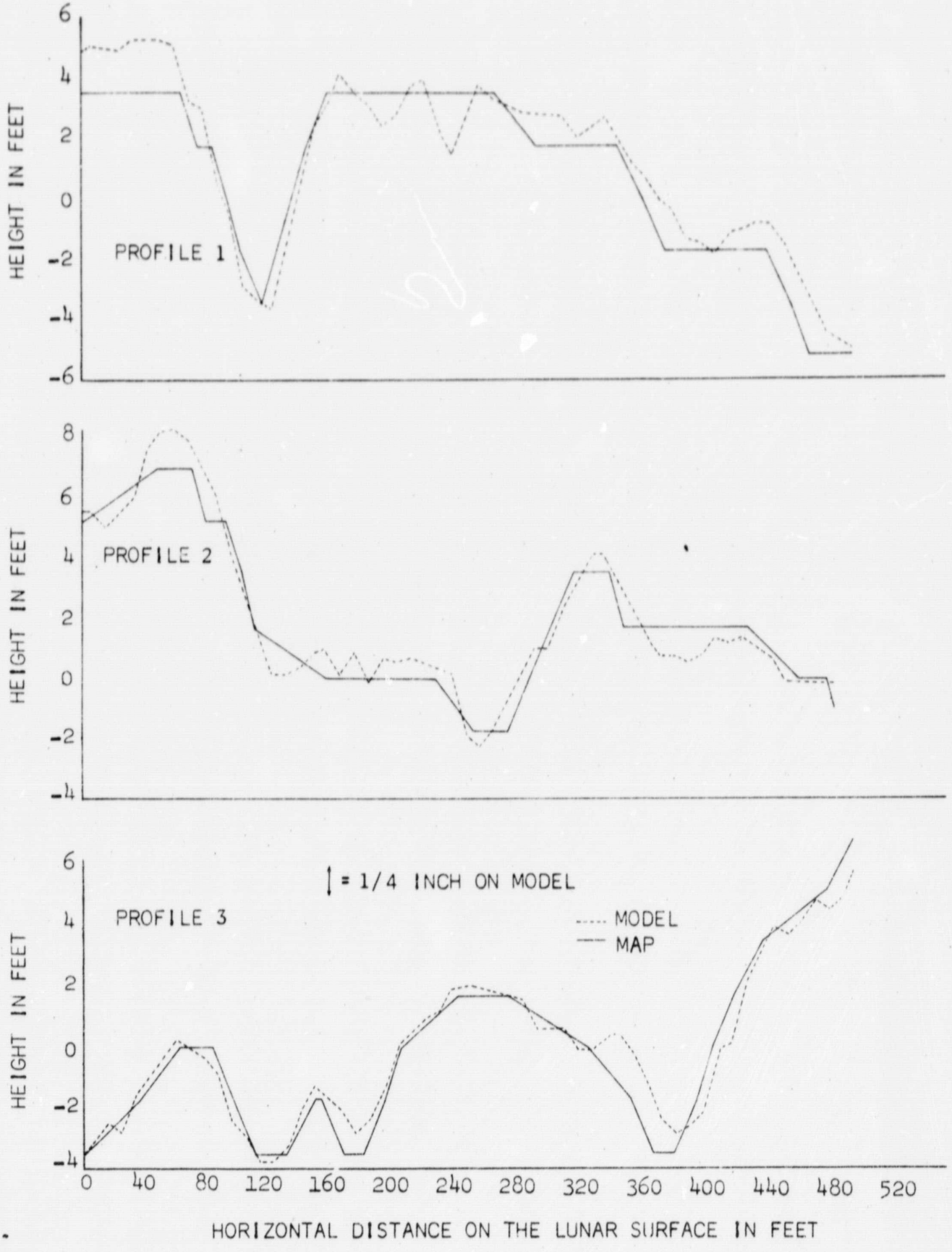

FIGURE 2. PROFILES OF COMPLETED MODEL

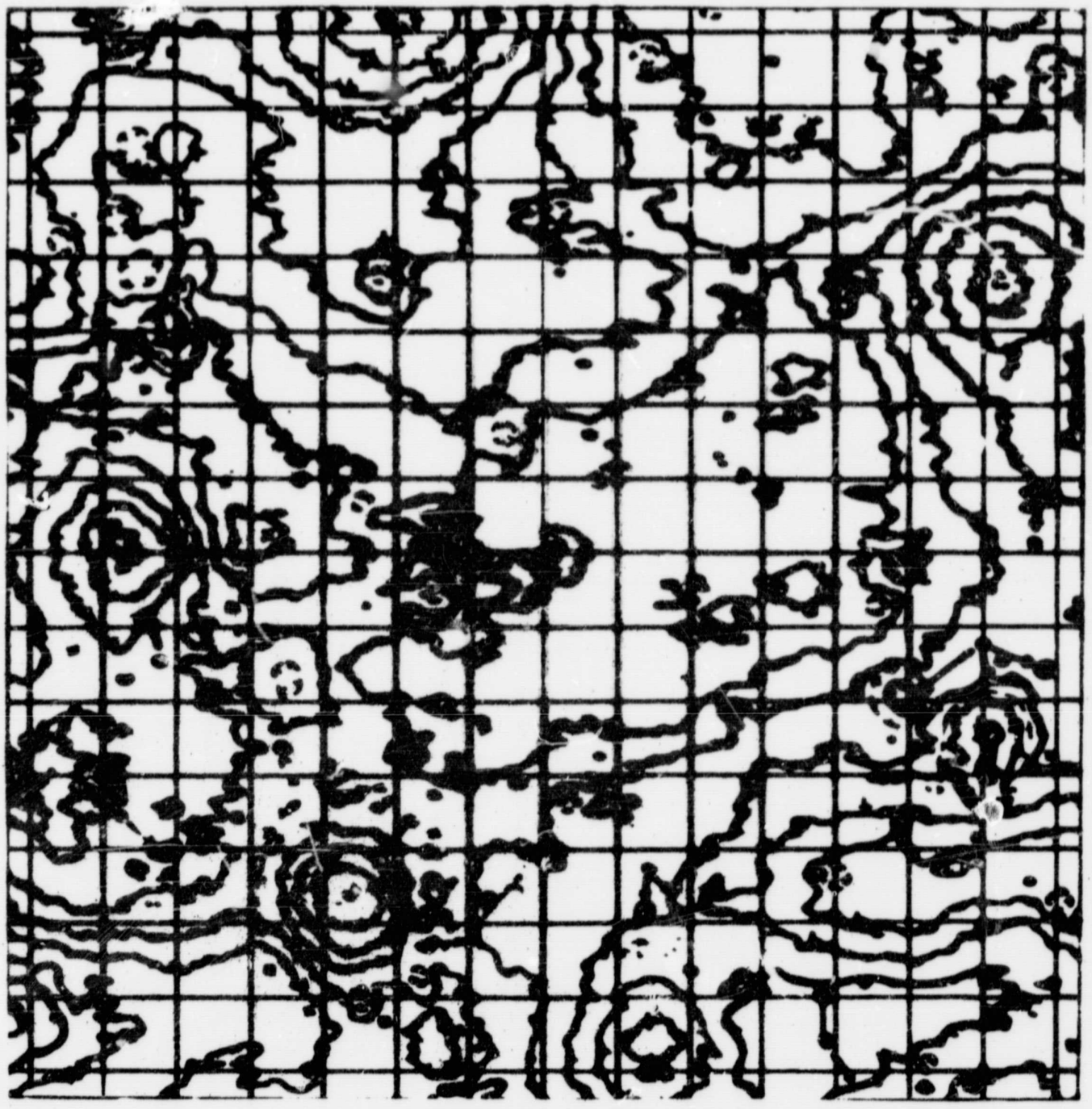

FIGURE 3. NASA CONTOUR MAP OF SINUS MEDII
SHOWING AREA ABOUT 500 FEET SQUARE
CONTOUR INTERVAL = 0.53 METER/UNIT

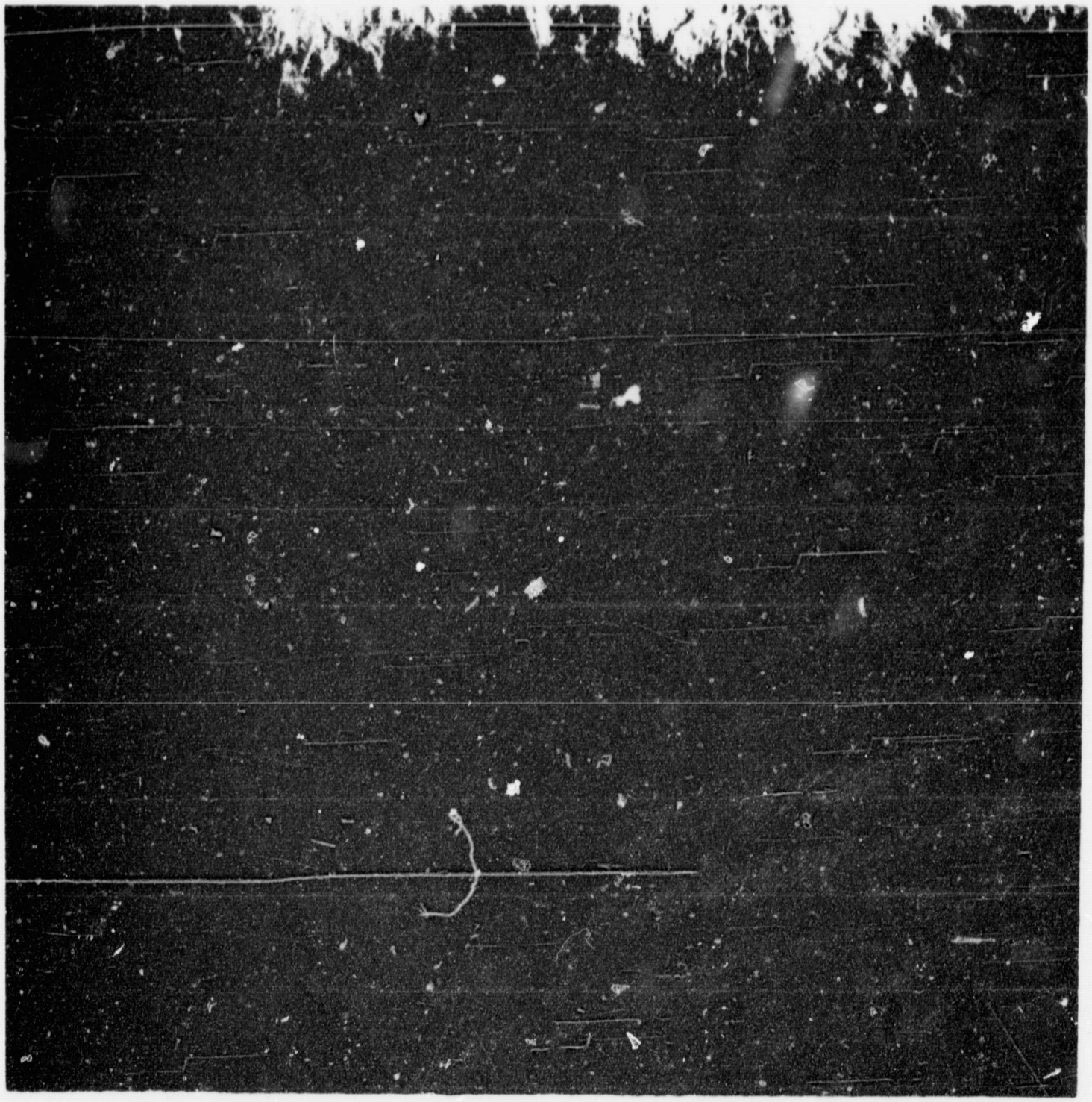

APPROXIMATE RESOLUTION 7 INCHES AT LUNAR SCALE

FIGURE 4. HIGH RESOLUTION PHOTOGRAPH OF MODEL

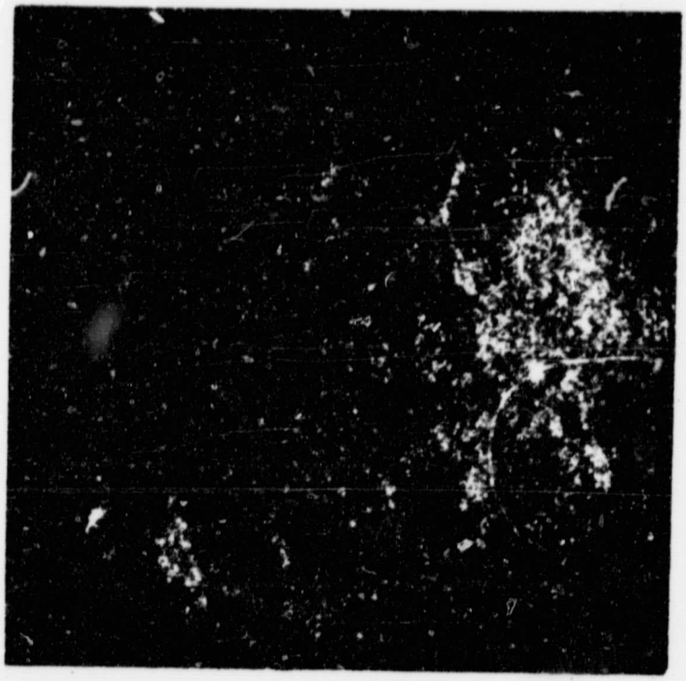

FIGURE 5. PHOTOGRAPH OF MODEL DEGRADED TO LUNAR ORBITER QUALITY APPROXIMATE RESOLUTION 1 METER AT LUNAR SCALE

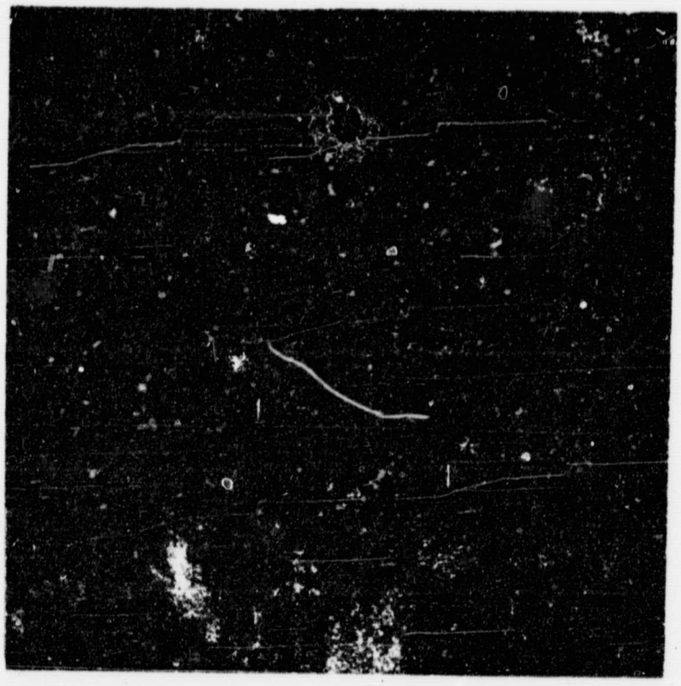

FIGURE 6. LUNAR ORBITER PHOTOGRAPH IN SINUS MEDII

Prior to each occasion of photography, the model was freshly dusted with cupric oxide. Figure 7 shows the preparations for dusting the model using the procedure previously developed.

C. Description of Making the Motion Pictures

The motion picture simulations were made by time-lapse photographic technique using a 16mm roll film camera with single frame capability (Eastman Kodak Cine - Kodak Special). The camera was actuated for individual exposures by the Kodak Electric Release Control for Cine-Kodak Special.

The camera was mounted on a fixture fastened to a dolly which rode down a ramp. Figure 8 shows this equipment with the ramp along the side of the model. Figure 9 shows the camera and fixture in detail. The fixture was constructed to allow the camera to ride in outrigger fashion so that the ramp remained out of the field of view. The ramp provided a constant slope of about 14°. Small changes from this basic path were added by the motions of the fixture which had 3 degrees of freedom in both translation and rotation. The camera fixture moved along a path parallel to the ramp surface by a lead screw. Periodically, it was necessary to restart the lead screw; the dolly was moved down the ramp to position the camera correctly to retain continuity of action.

The model was illuminated by a source simulating the angular size and position of the sun. Figure 10 shows a schematic diagram of the projector used for this purpose, a Kodak Master Model 1000-watt Projector with f/2.3 lens of 5" focal length. A condenser lens retainer acted as a field stop (with the slide gate of the projector removed) to give a full field angle of illumination of 25 degrees. At a distance of 30 feet to the center of the model the apparent angular subtense of the source was about 0.4°, nearly the angular size of the sun viewed from the moon. The sun was positioned 5° to the left of the initial straight

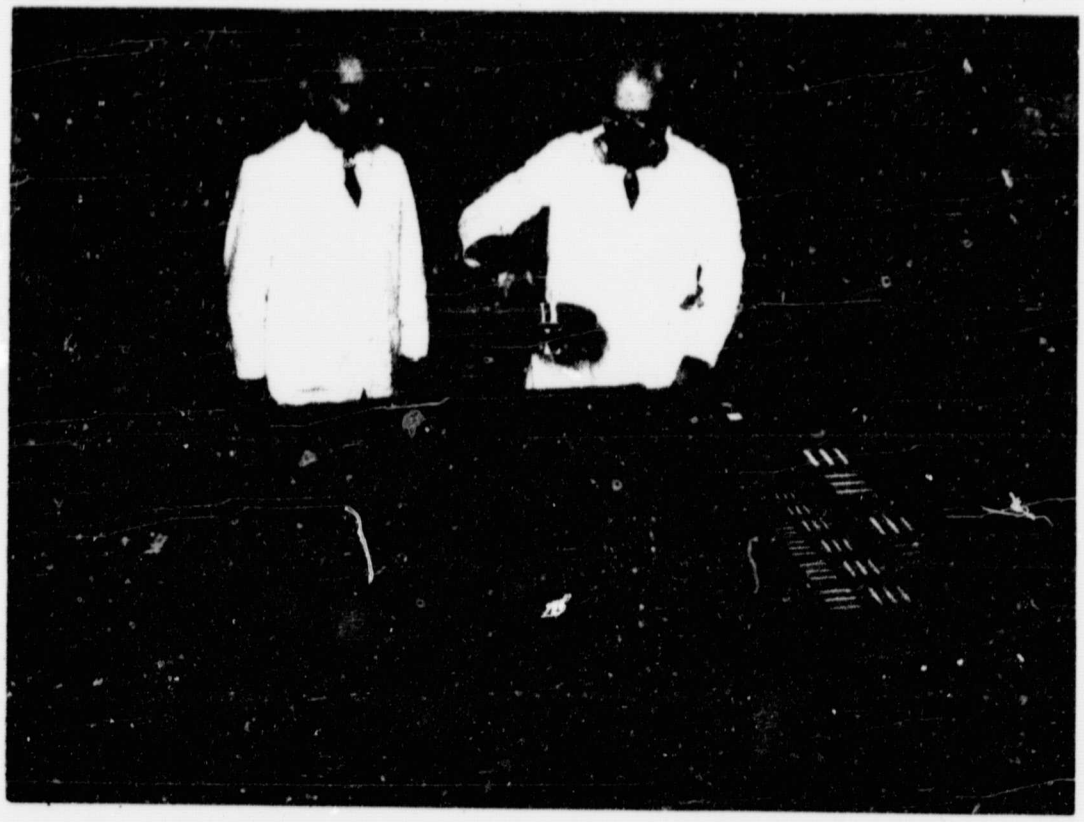

FIGURE 7. PREPARING TO DUST THE MODEL

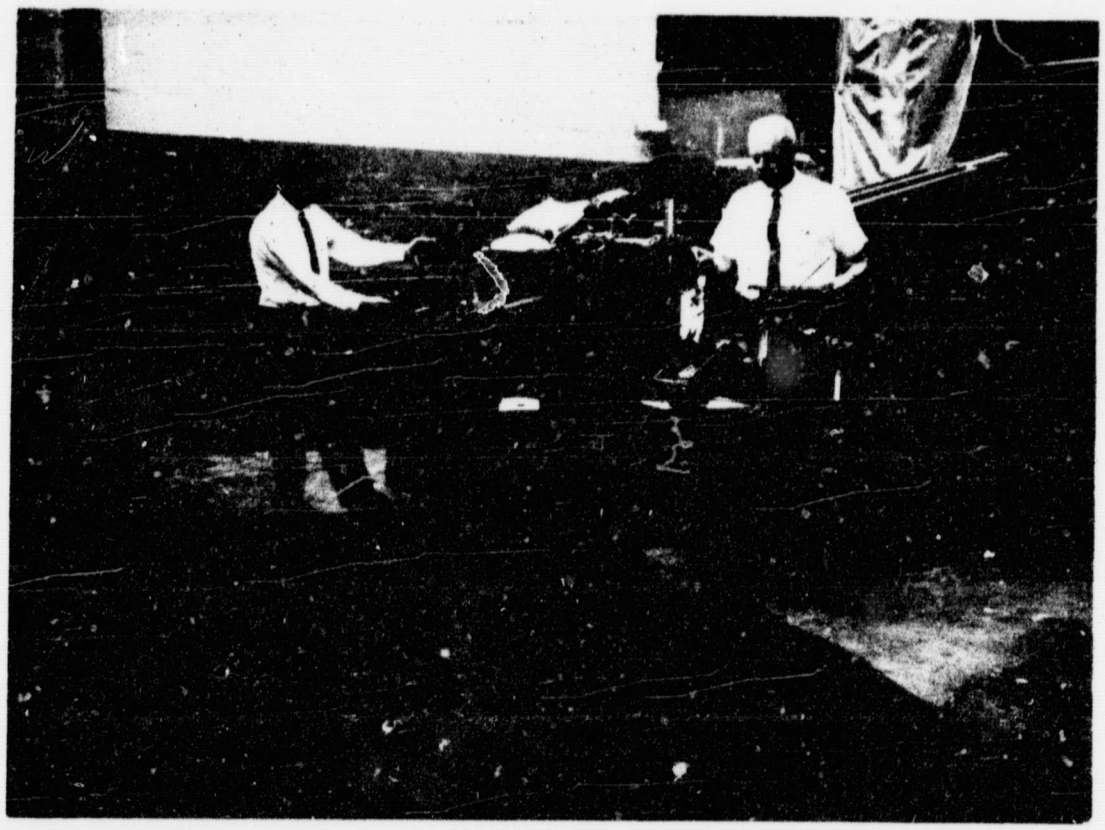

FIGURE 8. PHOTOGRAPH OF RAMP ALONGSIDE MODEL

FIGURE 9. PHOTOGRAPH OF CAMERA AND FIXTURE IN DETAIL

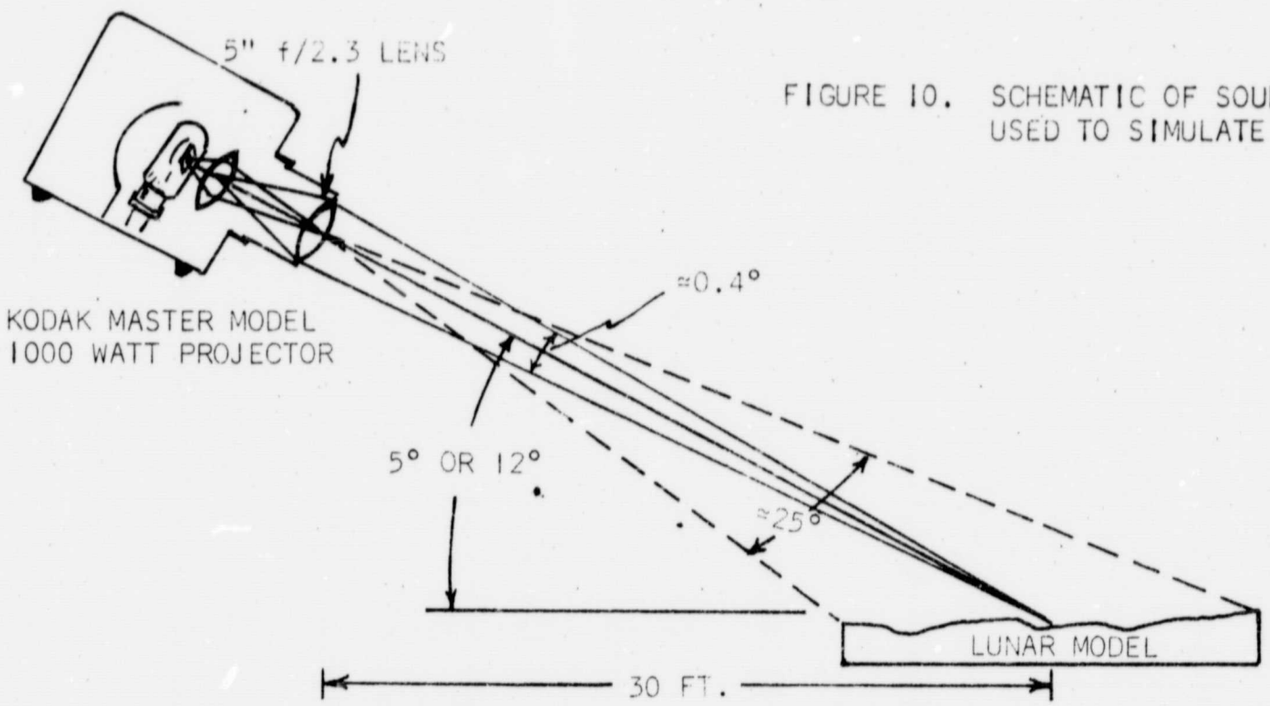

FIGURE 10. SCHEMATIC OF SOURCE USED TO SIMULATE SUN

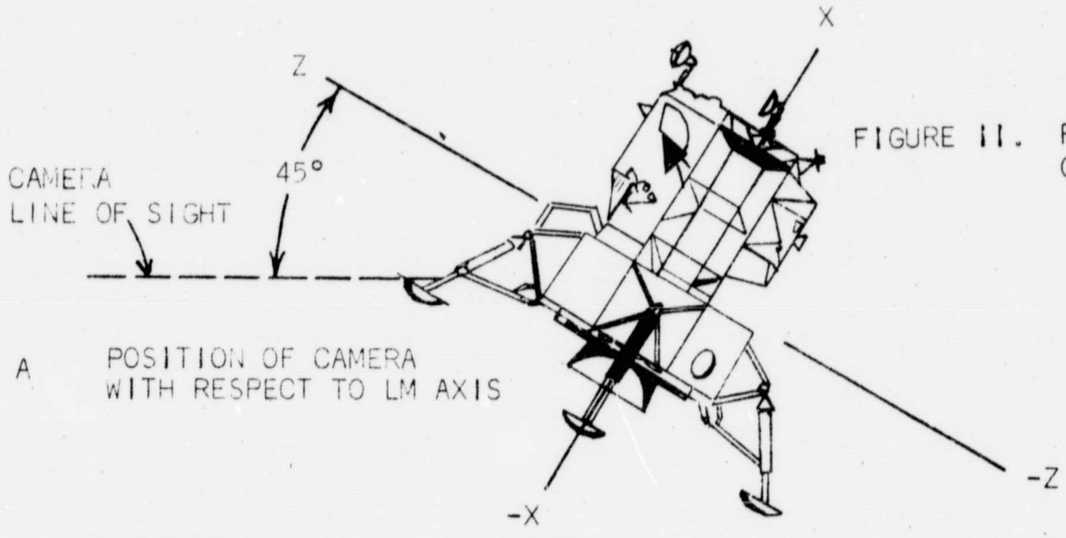

A POSITION OF CAMERA WITH RESPECT TO LM AXIS

FIGURE 11. POSITION AND FIELD OF VIEW OF CAMERA

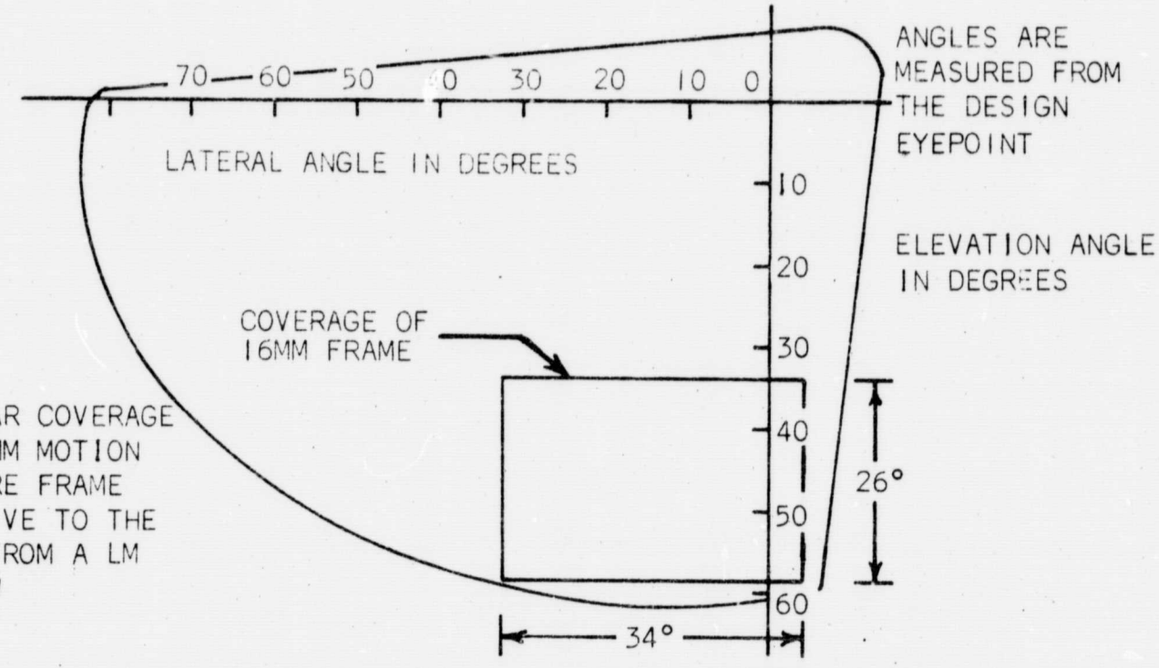

B ANGULAR COVERAGE OF 16MM MOTION PICTURE FRAME RELATIVE TO THE VIEW FROM A LM WINDOW

trajectory line described in a subsequent paragraph, i.e., on the model side of the ramp.

The camera was assumed to be firmly mounted to the LM. Figure 11A shows the geometric relationship of the camera to the LM. Figure 11B shows the field of view of the camera with respect to the astronaut's view of the LM window from the nominal eye-point.

Two basic trajectories were used in the preparation of the motion pictures, one giving a straight line approach (as seen in a plan view) to the primary landing site and the other using a dogleg maneuver to shift from the primary landing site to a secondary landing site. Two views of the trajectories are shown in Figure 12.

Four motion pictures were made with the straight-in approach. Motion pictures #1A and #2A were made under identical conditions except for position of the light source; the sun elevation was 5° for motion picture #1A and 12° for motion picture #2A. For these two motion pictures a scale of 1:50 was used, the same as the scale used to construct the model. Distance and attitude descriptors for the LM in this trajectory are shown in Figure 13 starting at 621 seconds elapsed time from ignition.

Motion picture #1 is the same as motion picture #2 except for sun elevation, 5° in motion picture #1 and 12° in motion picture #2. The scale is 1:150 in these two motion pictures. Distance and attitude descriptors for the LM in this trajectory are also shown in Figure 13. The scale of 1:150 permits filling the frame of the camera with model for a longer interval of time. Dimensions of features shown in Figure 12 must be multiplied by 3 to be applicable to motion pictures 1 and 2.

Figures 14 and 15 show the attitude and distance descriptors for the LM in the dogleg maneuver in motion pictures #3 and #4 which were

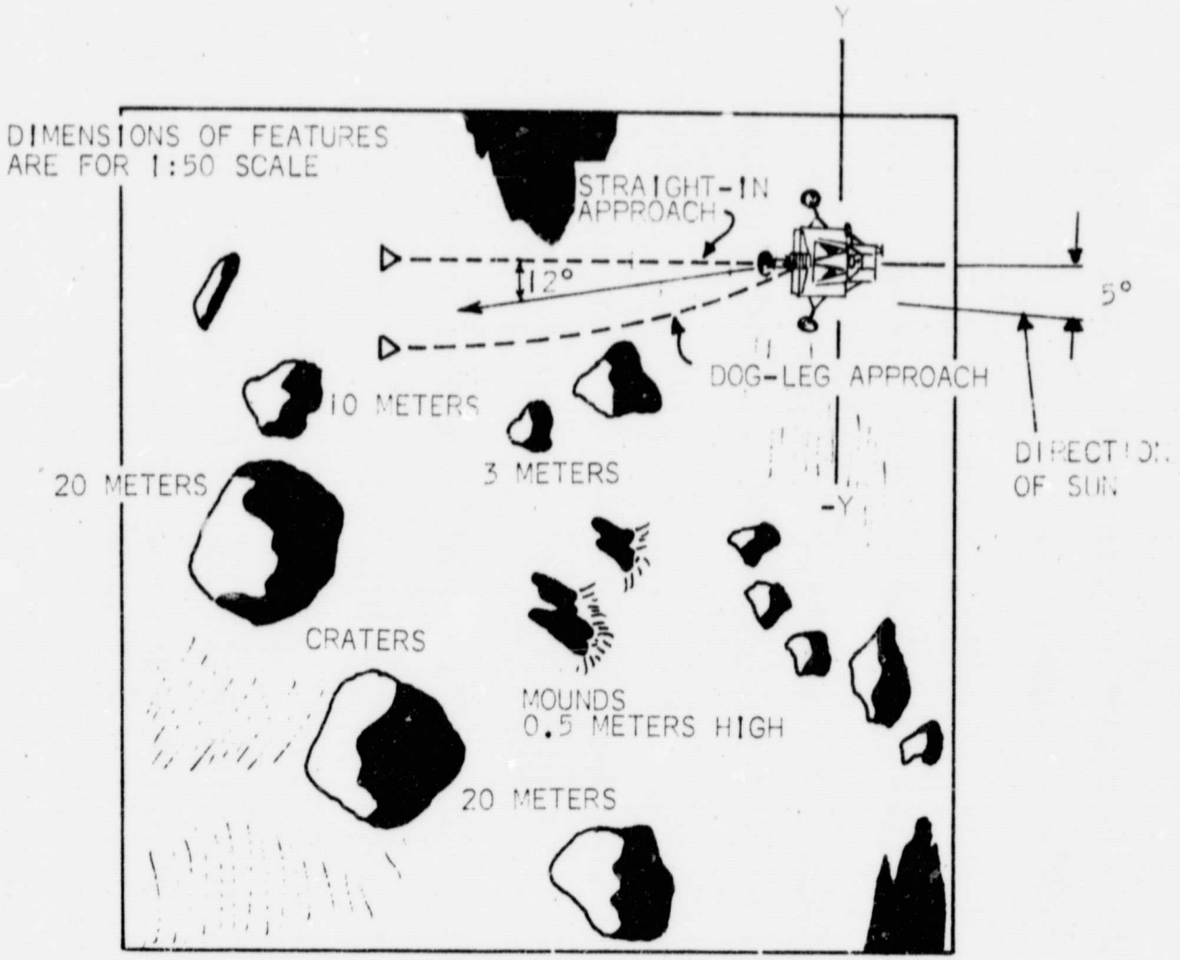

A. PLAN VIEW

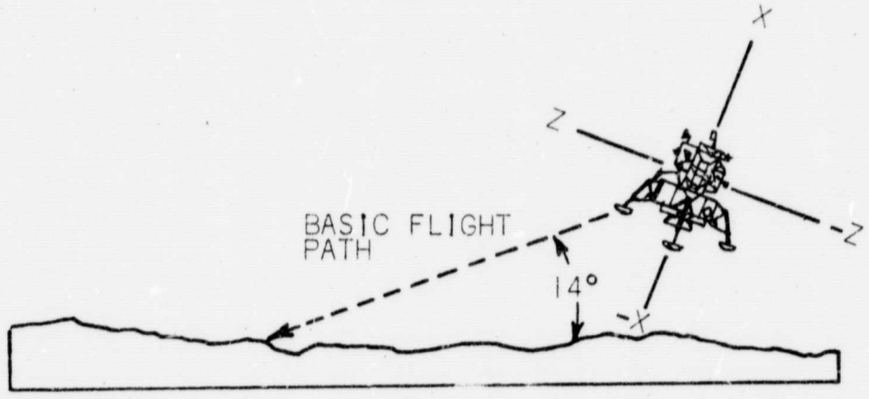

B. SIDE VIEW

FIGURE 12. STRAIGHT-IN AND DOG-LEG TRAJECTORIES

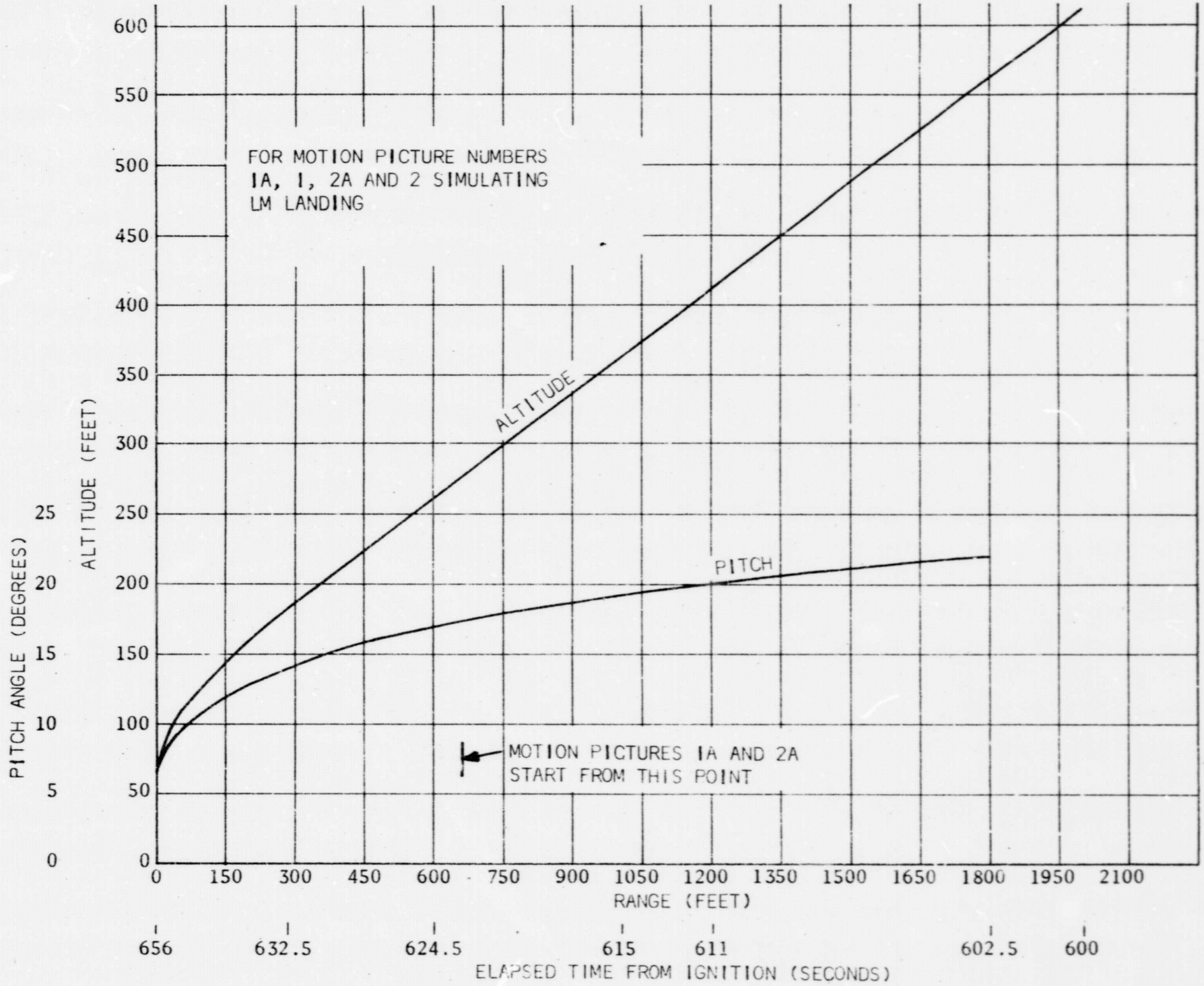

FIGURE 13. TRAJECTORY DATA FOR STRAIGHT-IN FLIGHT PATHS

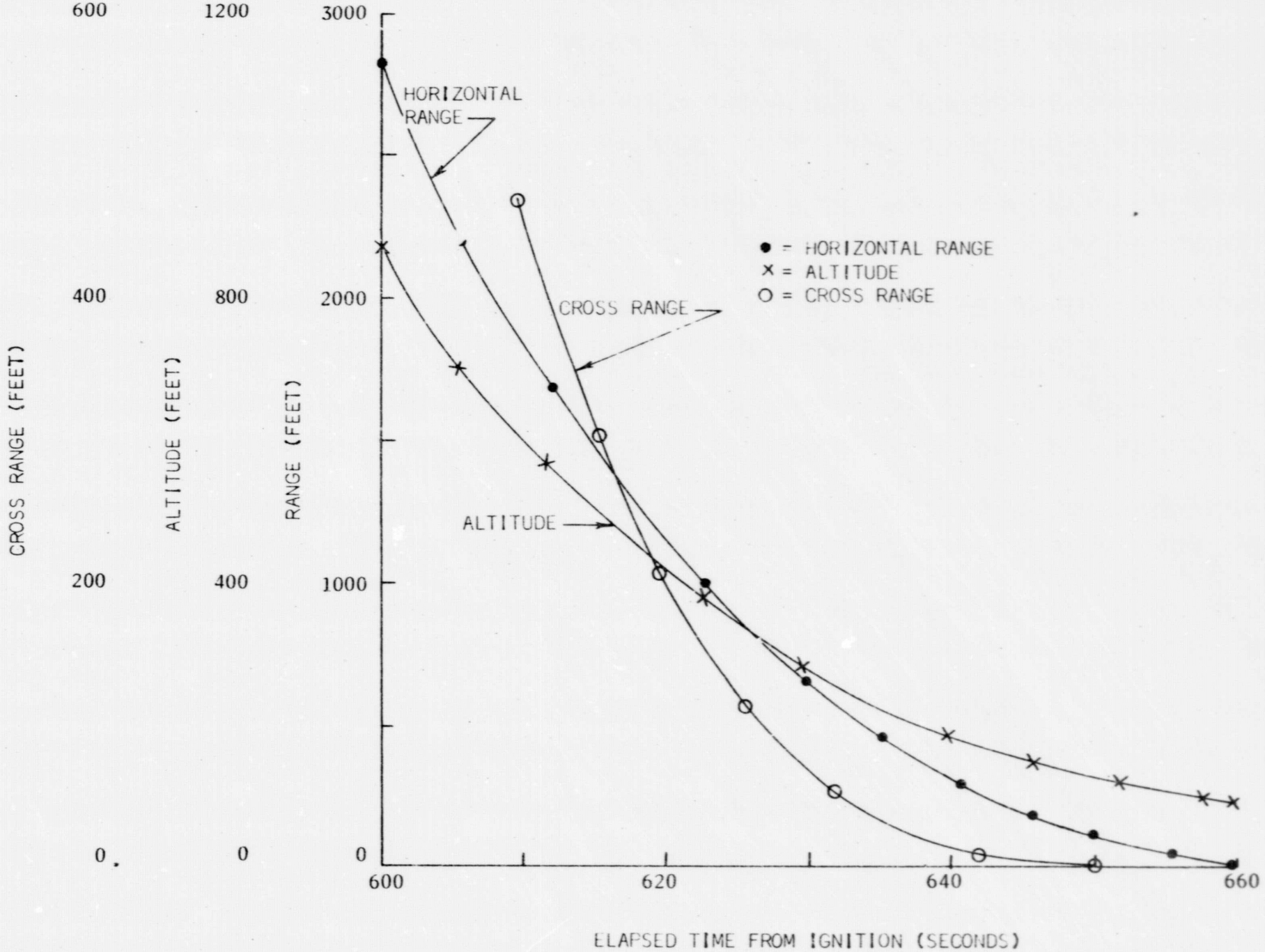

FIGURE 14. DISTANCE DESCRIPTORS FOR DOGLEG MANEUVER IN MOTION PICTURE SIMULATING LUNAR LANDING

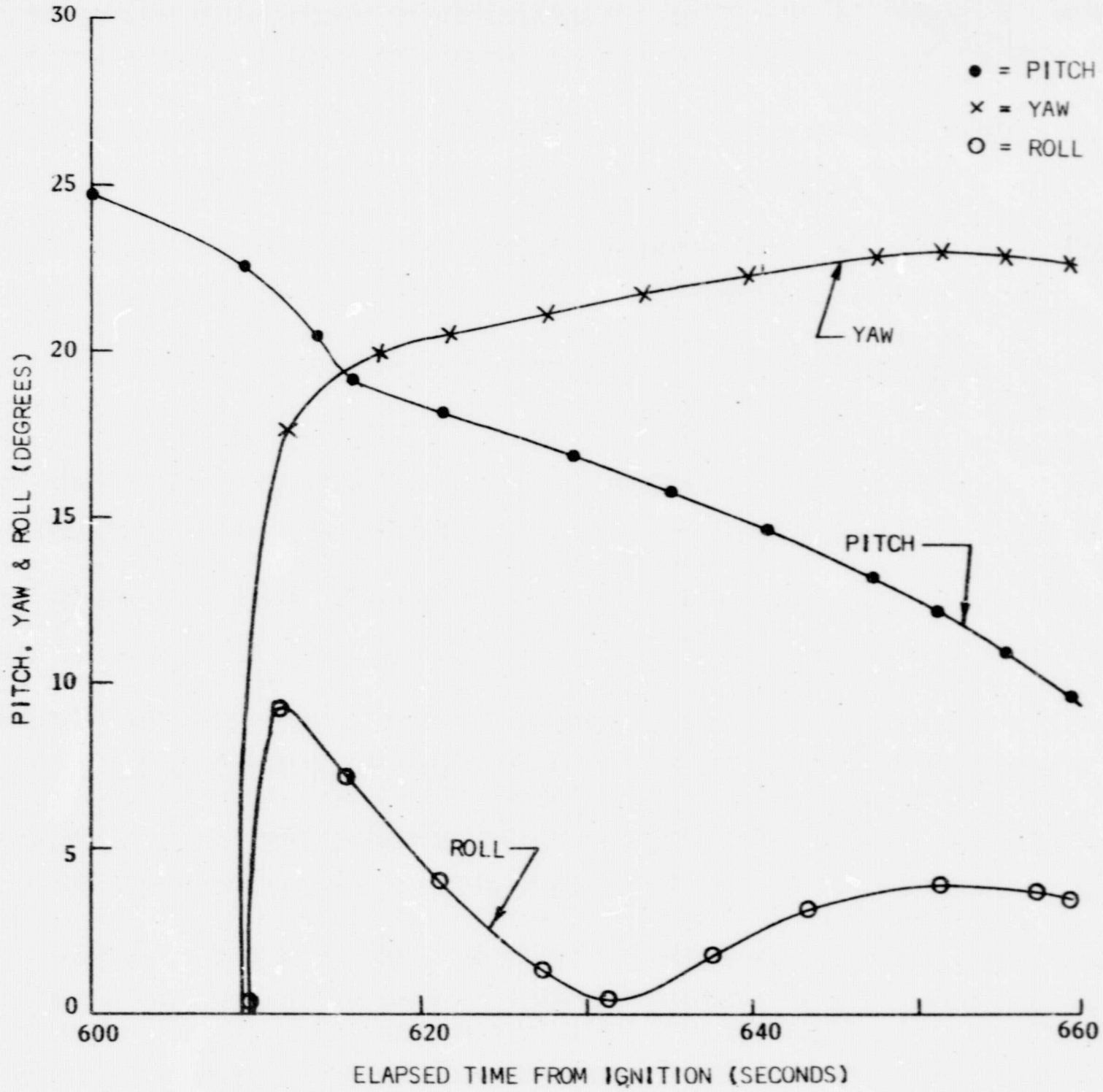

FIGURE 15. ATTITUDE DESCRIPTORS FOR DOGLEG MANEUVER IN MOTION PICTURES SIMULATING LUNAR LANDING

made at a scale of 1:250. In motion picture #3 the sun elevation is 5° while in motion picture #4 it is 12°. A multiplier of 5 must be used to make dimensions in Figure 12 applicable to these two motion pictures.

In each of the motion pictures, except #1, the landing sites were marked with a small, open triangle at the request of NASA. The equilateral triangle was 1 inch on a side, corresponding to 4.16, 12.5 and 20.8 feet on the moon at the three scales of 1:50, 1:150 and 1:250.

In early frames of each motion picture, the image of the model was not large enough to fill the frame of the camera. The apparent lunar horizon caused by this limitation in the model is about 16° below the position where the real lunar horizon would occur. During the filming of the motion pictures, a shadow was cast on the foreground in front of the model by a panel placed in front of the light source. Black felt plush was used to provide a background behind the model. This procedure placed both the foreground and background at the minimum density on the negative. When making motion picture #1A, one of the boxes supporting the ramp was not covered with plush during the exposure of several frames. Although the presence of these images is a cosmetic defect in this motion picture and distracts the attention of the viewer, this defect does not affect the quality of the useful area of the picture. The defect did not warrant remaking the motion picture.

In the last few seconds of each simulation, the camera was put through motions to represent a pitch-up maneuver by the LM and the initiation of the vertical descent. The shadow of the camera and its support appear in the last few frames of each motion picture; the camera film plane was about 4 inches from the model surface during the last exposure.

The motion pictures were filmed on Kodak Double X Negative Film, Type 7222, and printed on Kodak Fine Grain Duplicating Positive

Film, Type 7366. Since the average illuminance on the model was very low and the model had about 7% reflectance, camera exposure times were 4 or 5 seconds depending on lighting conditions. The films were given standard processing.

The lens in the camera was an f/2.8 Kodak Cine Ektar of 15mm focal length. During the photography, the aperture of the lens was adjusted slightly to compensate for the reduction in illuminance at the far side of the model compared to that at the near side. The lens was set at f/16 at the start of the motion picture and adjusted to f/14 by the end of the motion picture, a change of about 1/2 stop.

A magnetic sound track may be added if desired as the motion pictures were made for projection at 24 frames per second to simulate real time. During projection, the viewer can eliminate distortion of perspective by sitting at a distance from the screen that is 2 1/2 times the height of the projected image.

The sketch of the model that was given in Figure 12 shows the vicinity of the landing sites and gives the sizes of certain features. The sizes of craters are given for the scale of 1:50 used in motion pictures 1A and 2A. For motion pictures 1 and 2 with scale of 1:150 and 3 and 4 with scale of 1:250, the sizes in Figure 12 must be multiplied by factors of 3 and 5, respectively.

D. Description of Preparation of Still Photographs

In connection with motion pictures 1A, 1, 2A and 2, still photographs were made of the model at 7 selected points along the trajectory. These photographs were reproduced as enlarged prints. One purpose of these prints was to make them available as visual cues to evaluate the potential of such aids for previewing.

The still photographs were made with the same procedure and equipment used in making the motion pictures except that Kodak Plus X Negative, Type 7231 was used. This film was given standard processing. Enlargements of 25X were made on Kodak Polycontrast Enlarging Paper, Type F. The prints were dry-mounted on 8 1/2 x 11 card stock for delivery.

Table I lists the conditions for the still photographs, one of which is shown in Figure 16. For proper perspective, the viewer should hold this figure at a distance from his eyes corresponding to two and one-half times the height of the picture, i.e., 19 inches.

The steps used in making the still photographs yield tone reproduction characteristics that cause the prints to have very nearly the appearance of the model seen by an observer looking at it under the lighting conditions for the corresponding motion picture.

TABLE I

CONDITIONS FOR STILL PHOTOGRAPHS TAKEN CONCURRENTLY
WITH MOTION PICTURES OF LM LANDING

Straight-in Approach - 5° and 12° Sun Elevation

Motion Picture#	Photo Number	Elapsed Time From Ignition	Pitch Angle (degrees)	Altitude (ft)	Horizontal Range (ft)
1A & 2A	1	621	17.0	280	660
	2	627	15.0	220	420
	3	633	13.5	175	260
	4	639	11.5	135	150
	5	645	9.5	100	80
	6	653	7	72	10
	7	661	0	54	0
1 & 2	1	600	22.6	600	2000
	2	612	20.0	410	1200
	3	622	17.0	280	650
	4	632	14.0	190	300
	5	642	11.8	140	140
	6	654	9.0	90	35
	7	658	3.0	70	0

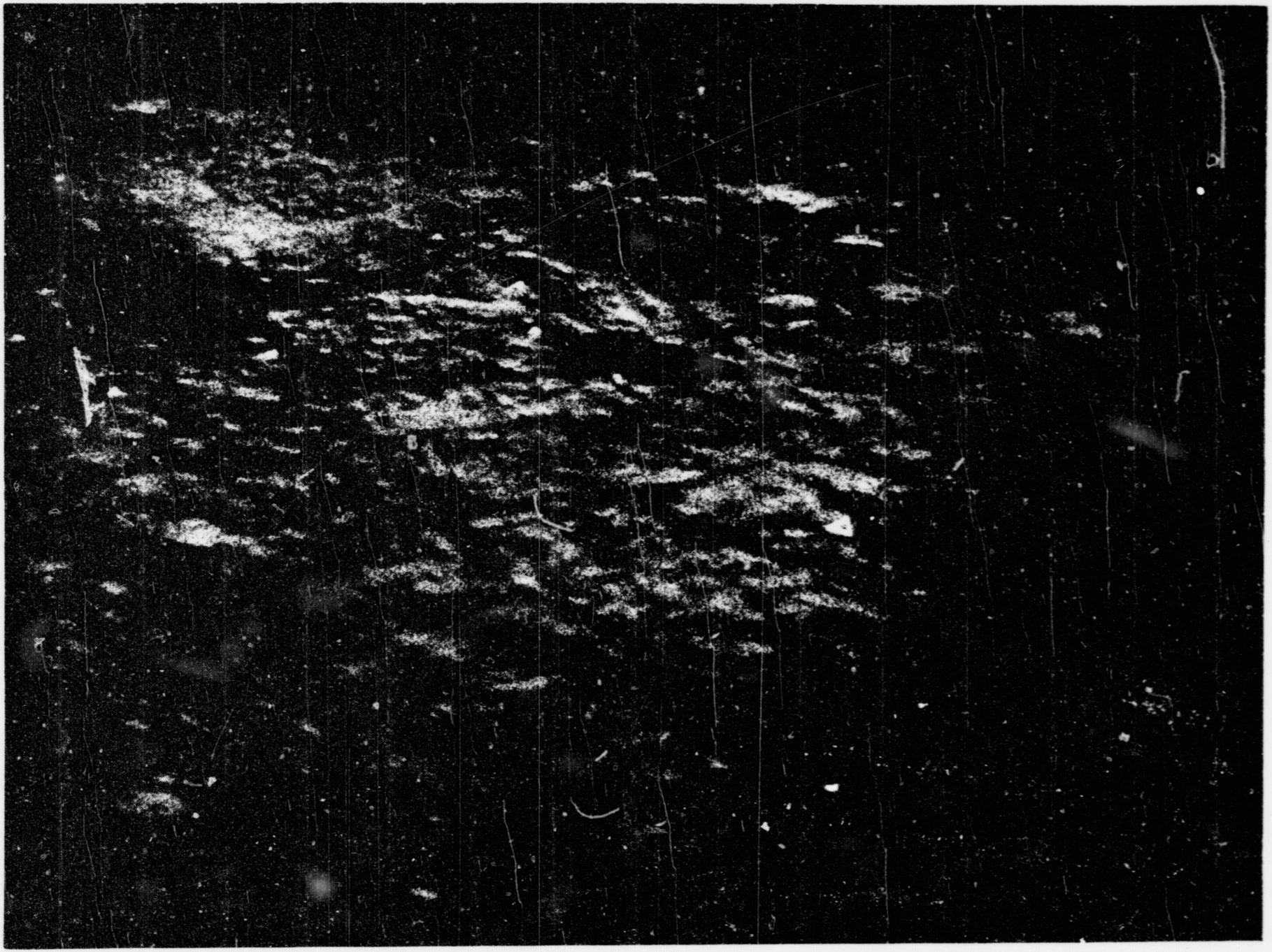

FIGURE 16. STILL PHOTOGRAPH FOR MOTION PICTURE 2A (1:50) 12° SUN ELEVATION; 260 FEET HORIZONTAL RANGE TO TOUCHDOWN POINT

II. LUNAR PHOTOMETRY AND MAPPING

A. Introduction

Earth-based telescopic measurements have shown the moon's surface to produce a high amount of backscattering. The luminance of the lunar surface for all conditions of illumination and viewing can be expressed in terms of the luminance for vertical illumination and viewing and a factor of proportionality, ϕ, using the lunar photometric function.

The photometric function for any area on the lunar surface is represented in terms of phase angle g, between the directions of incidence and emittance (viewing), and angle α, which is the component of the angle of emittance projected into the phase plane. The angle α is negative when it overlaps the phase angle. Figure 17 illustrates these geometric relationships.

The graphical representation of the value of the photometric function in terms of the two variables α and g is shown in Figures 18 and 19 for lunar maria.[3]

Knowledge of the photometric function can be combined with information about parameters of the photographic system (f-number N, exposure time t, and lens transmittance T), the normal surface albedo (reflectance) ρ and the illuminance I to make a prediction of the exposure E on the film plane in a photographic system. Equation 1 describes the relationship between these variables.

$$E = \frac{10.76\ I\ \rho\ \phi\ Tt}{4N^2} \qquad \text{Equation 1}$$

Exposure E is given in meter-candle-seconds if exposure time t is given in seconds and I is given in foot-candles; ϕ, N, T and ρ are dimensionless. The conversion factor 10.76 gives the number of square feet in a square meter.

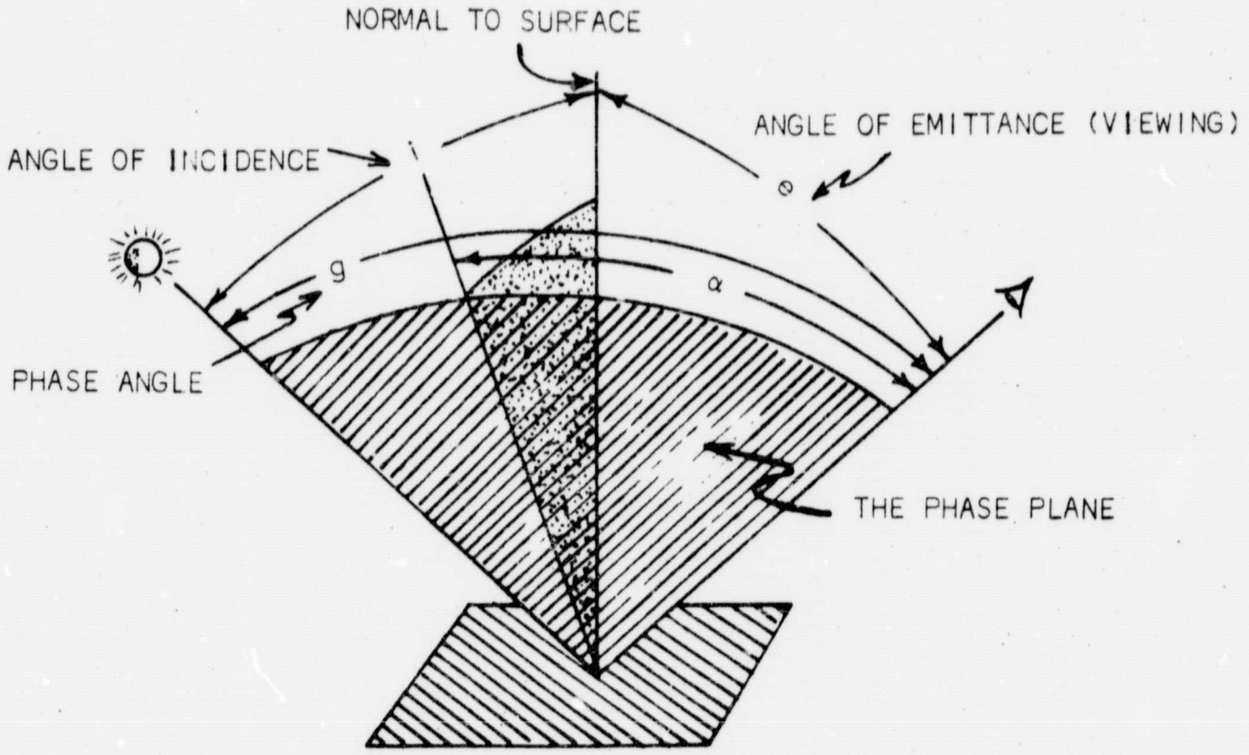

FIGURE 17. GEOMETRIC RELATIONSHIPS BETWEEN α AND g

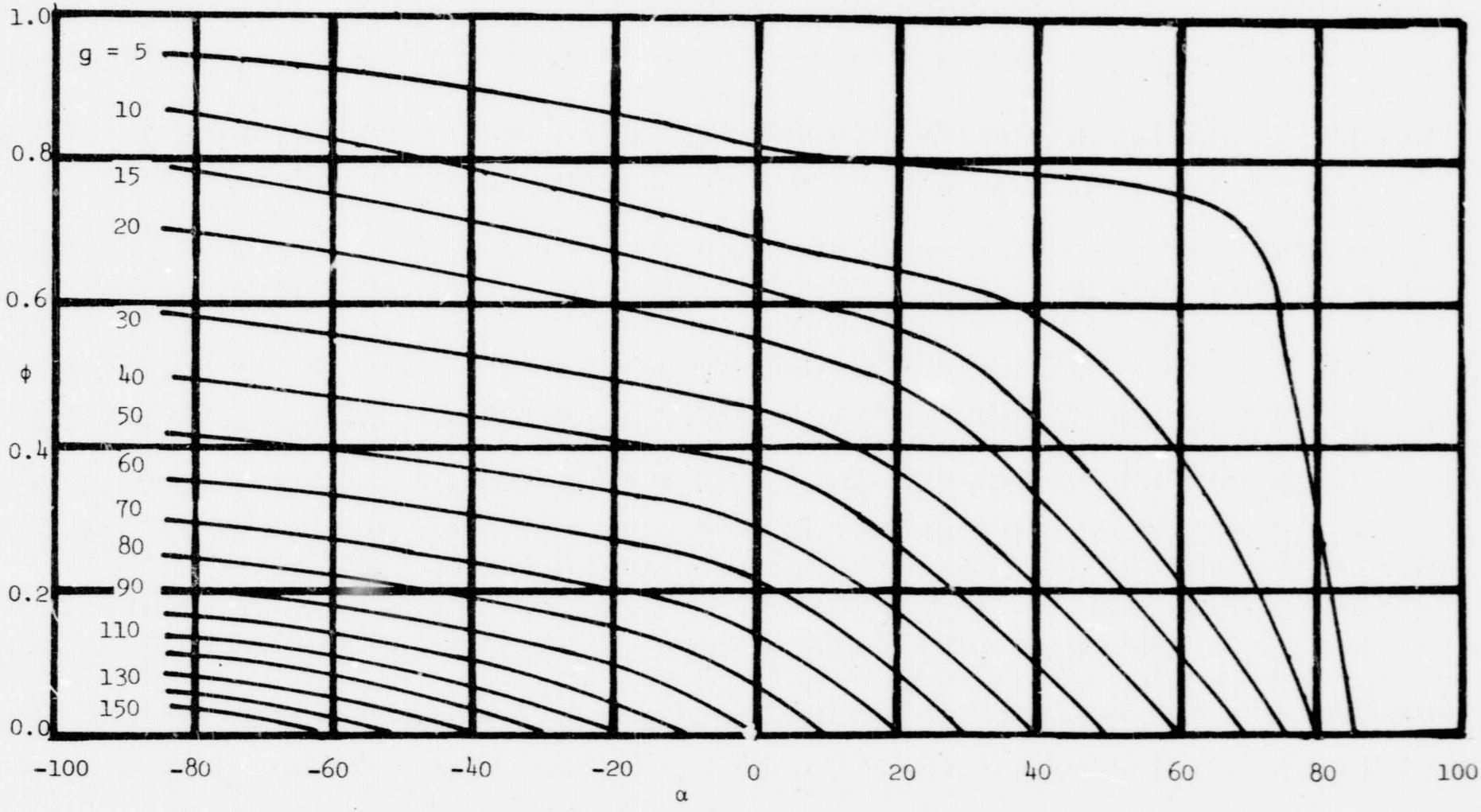

FIGURE 18. PHOTOMETRIC FUNCTION OF LUNAR MARIA BASED ON DATA FROM FEDORETZ, 1952

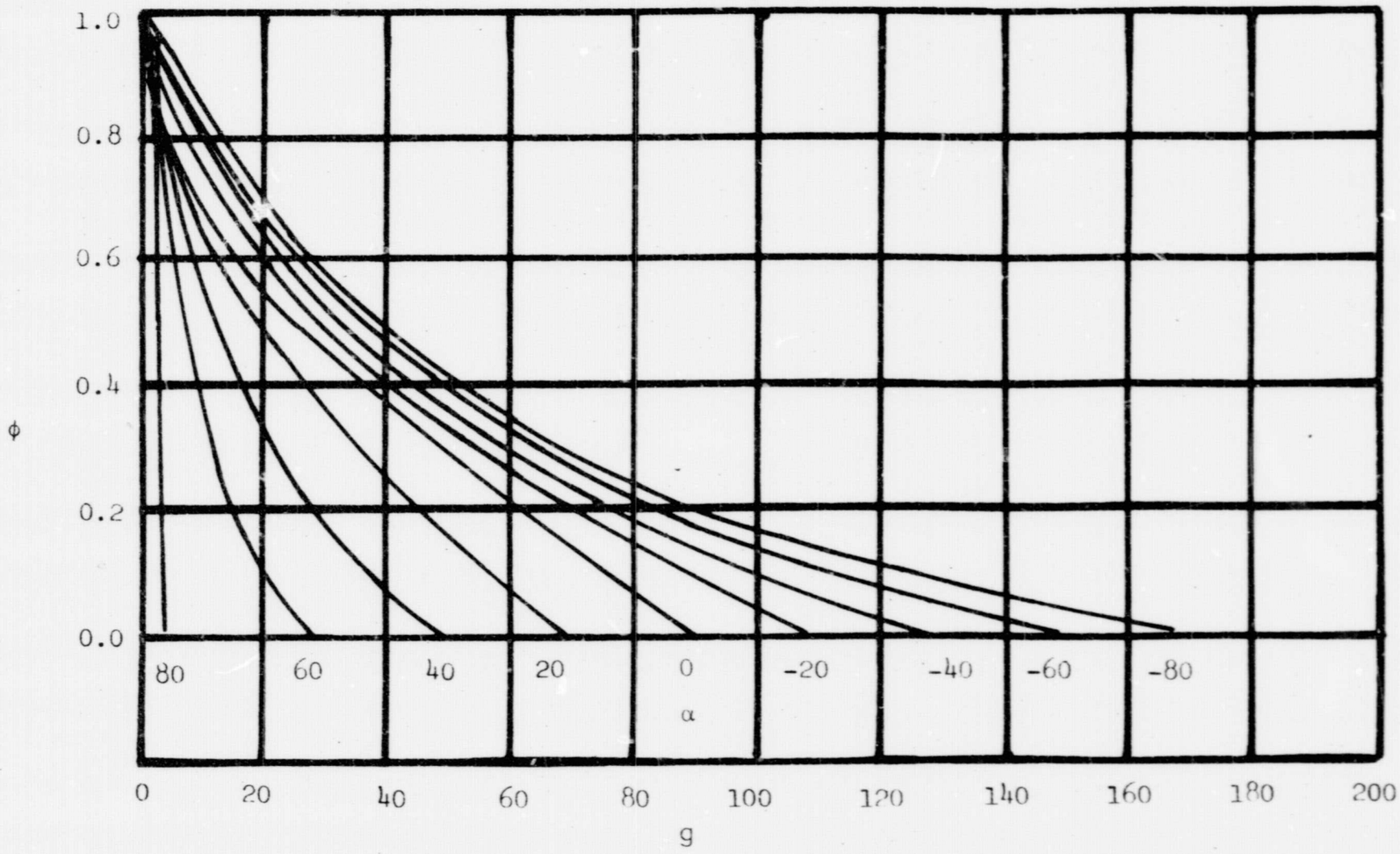

FIGURE 19. PHOTOMETRIC FUNCTION OF LUNAR MARIA BASED ON DATA FROM FEDORETZ, 1952

Equation 1 is basic to all of the work reported in this section. Efforts were made to improve knowledge of the photometric function by solving the relation for ϕ with initial knowledge of all the other values including g and α. Work on mapping was carried out by solving the relationship first for ϕ and then for α.

Dependence of the photometric function on α and g indicates that tilt of the normal to the area under observation in a plane normal to the phase plane does not enter into the computation for observed luminance.

B. Photoclinometric Mapping

1. Summary

The work of Phase II, Contract NAS 9-3826[4] has been extended in a study of photoclinometric mapping from a single photograph. New profiles prepared from photographs of Model KLM 6-65 with a sun elevation of 30° are compared to profiles for a 15° sun elevation, and an error analysis made on the technique for the 30° condition.

Mapping of a lunar model at 30° sun elevation can be done at least as well as at 15° sun elevation.

2. Background

The lunar photometric function expresses the variation in lunar luminance with the geometry of illumination and viewing. The photometric function at a point is described by two variables, g and α. For vertical photography with very small angular coverage, the phase angle g is the complement of the solar altitude and α is the component of the lunar surface slope in the phase plane.

The measurement of luminance values from a vertical photograph of the lunar surface together with knowledge of the photometric function and other calibration data provides a photometric method for generating lunar surface profiles. To determine these luminance values at points near the optical axis, the photograph is scanned with a microdensitometer in lines parallel to the phase plane at the nadir point. The phase angle is the complement of the solar altitude at the nadir point, therefore the luminance differences occurring in the scene photographed are a function of the single variable α, the ground slope in the phase plane. On the basis of a single scan, no information is available about the surface slope in any direction other than the phase plane. But the slope in the direction perpendicular to the phase plane can be deduced or inferred from a number of adjacent scans. The profiles obtained by adjacent scans can be assembled on the basis of the scanning geometry relating the end points of the separate scans. Contours are constructed by connecting points showing common values of elevation in the phase plane. This procedure was used in Phase II work.

The slope is found by use of three relationships. The first relationship is the characteristic curve of the photographic film which relates optical density to exposure. The second relationship relates exposure to the various optical parameters of the camera and illumination conditions of the scene. This relationship is given by Equation 1:

$$E = \frac{10.76\ I\ \rho\ \phi\ Tt}{4N^2}$$

where: E = exposure (meter candle seconds)
I = scene illumination (ft. candles)
ρ = albedo
ϕ = relative luminosity factor (function of g and α)
T = lens transmittance
t = exposure time (seconds)
N = lens f-number

The third relationship is the empirical representation of the photometric function in terms of g and α.

Assuming a constant albedo within the picture area of a single vertical photograph, all the variables in Equation 1 are constant, except ϕ which only changes as α varies. For a short scan over an area of constant slope, g and α are constant. The density changes obtained from the microdensitometer traces of the photograph may therefore be related to changes in surface slope. The slope, tan α can be related to the height difference, Δh, and separation, Δx, between two points by the following relationship:

$$\Delta h = \Delta x \tan \alpha \qquad \text{Equation 2}$$

A profile may be generated using the expression:

$$h_{x_n} = \sum_{i=0}^{n} \tan \alpha_i \, \Delta x_i \qquad \text{Equation 3}$$

where h_{x_n} = height at point x_n relative to the height at point x_0, the starting point.

3. Previous Work

Much of the work done in the Phase II Lunar Photo Study under Contract NAS 9-3826 involved application of the photometric mapping technique to the photography of laboratory subjects.

Initially, simple geometric shapes, cones and spherical concavities were photographed. The subjects were dusted with cupric oxide which has reflectance properties similar to the lunar surface, as shown in Figure 20. Figure 20 is comparable to Figure 18, the lunar photometric function.

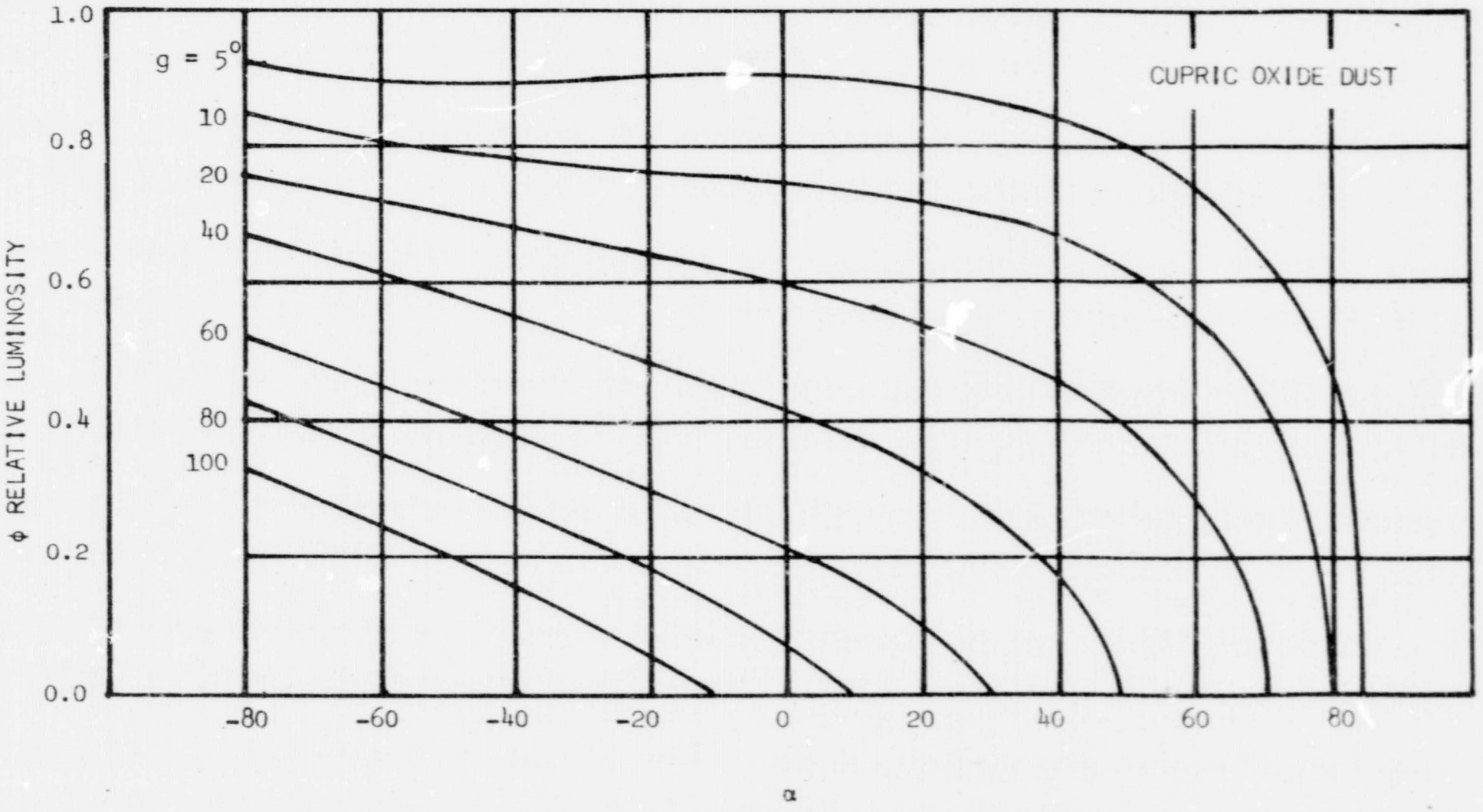

FIGURE 20. RELATIVE LUMINOSITY ϕ FOR CUPRIC OXIDE DUST VERSUS ANGLE α FOR SEVERAL PHASE ANGLES g

The last part of the Phase II work included mapping the portion of the Lunar Model KLM 6-65 (scale of 1:48)[5] that is outlined in Figure 21. The model was illuminated by a source simulating the sun at an elevation of 15°. SO-243 film was used with an optical system capable of producing a system resolution of 130 lines/mm, high contrast, at a scale of 1:30,000 (model scale 1:48 and photographic scale 1:625).

A contour map of the area outlined in Figure 21 was made from the height profiles determined from 22 microdensitometer scans. This map compared favorably to one determined from stereo photographs of the model and to a map made from measurements on the model itself.

Quantitative evaluation of the photometric mapping technique was obtained by comparing height measurements made on the model to those results obtained from the photograph. This comparison showed that photometric mapping could determine lunar heights with a standard deviation of ±2.6 inches where excursions in heights were as much as 20 inches.

4. Present Work

The purpose of the current work is to investigate the mapping capability of the photometric technique at a sun elevation of 30° by comparing the results to those obtained at 15° sun elevation.

Vertical photographs were taken of both Model KLM 6-65 and a flat plane surface, dusted with cupric oxide, on SO-243 film at a scale of 1:30,000 and a sun elevation of 30° using a system having a limiting resolving power of 130 lines/mm, high contrast. The film was processed in D-19/D-76 to a gamma of 1.2. The plane surface is used to correct for the light fall-off which occurs across the width of the model because of changing distance from the light source.

A Davidson autocollimator with divisions to 1 second of arc was used to establish a perpendicular to the base of the model and to set the camera optical axis coincidence with this perpendicular. A surveyor's transit was used to establish the sun elevation of 30 degrees ±10 minutes.

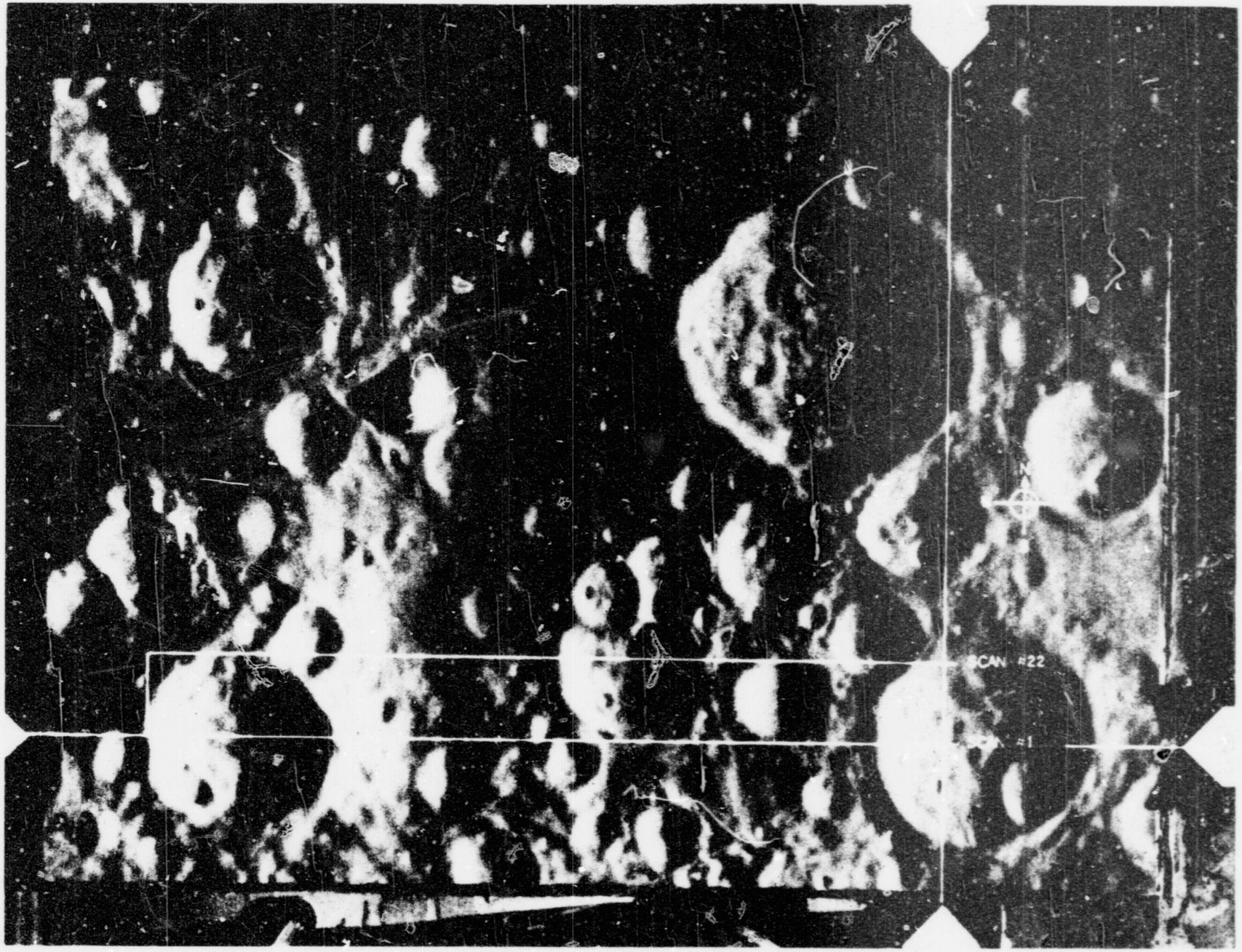

FIGURE 2i. PHOTOGRAPH OF MODEL KLM 6-65 SHOWING THE 8 x 80 FOOT AREA MAPPED BY PHOTOCLINOMETRY

Photographs of the model and the plane surface were scanned in the phase plane with a microdensitometer using a spot of 2-microns diameter. Twenty-two scans were made at separations of 4 microns within the area shown in Figure 21. In each scan 271 samples were taken at separations of 3 microns. The data from each scan were stored on punch cards for computer analysis.

A photographic step tablet processed with the photographs was also traced to provide exposure calibration. A modified least squares curve fit was made relating film exposure E to microdensitometer output voltage V:

$$E = -0.6497 + 3.630V - 3.840V^2 + 2.179V^3 \qquad \text{Equation 4}$$

A ϕ versus α equation for the photometric function of cupric oxide dust at a phase angle of 60° (sun elevation of 30°) was generated using the same modified least square technique, where α is the slope angle in the phase plane.

$$\alpha = 26.263 + 0.781\ \phi - 616.803\ \phi^2 + 416.895\ \phi^3 \qquad \text{Equation 5}$$

An equation was obtained for zero α to account for light fall off on the model as a result of the inverse-square law. To get this equation, the mean microdensitometer voltage was computed for each of the twenty-two scans made on the image of the plane surface. Through this mean, a first degree equation was obtained for each scan which adjusted each point to this mean. An average equation was derived based on the individual equations of the twenty-two scans. This average equation is:

$$V = 1.237 + 5.8 \times 10^{-4}\ x \qquad \text{Equation 6}$$

where V = microdensitometer voltage

x = feet on the moon in the phase plane from the start of the scan

The microdensitometer data from the photograph of the model and Equations 4 through 6 were used as inputs for the computer program LUNA II. This program, written for the Phase II work, computes lunar surface profiles from the microdensitometer data.

In LUNA II, an array of voltages is computed using Equation 6 corresponding to the points across the model at which microdensitometer readings will be made. This voltage array is converted to an exposure array using the exposure-voltage equation. A new array is created by dividing the value of ϕ corresponding to zero α by each member of the exposure array. This ϕ/E ratio is used to correct the microdensitometer voltages obtained from the trace of the model photograph for the apparent slope which results from the effect of the light fall-off. The ratio is given the symbol A:

$$A = \frac{\phi}{E} \qquad \text{Equation 7}$$

The value of A at each point is adjusted to zero slope, therefore any variation in E can be attributed to a change in ϕ, i.e., $EA = \phi$ and one does not have to go through the lengthy calculation solving Equation 1. This artifice can only be used when an area of known slope (preferably zero) is available in the photograph.

The microdensitometer voltages for a single scan are read into the program, converted to exposure and then changed to a ϕ value by multiplying the exposure value by the A value corresponding to the position of the data point in the scan. This ϕ value is converted to a value of α using Equation 5.

A surface profile is generated by reiterative use of Equation 2:

$$\Delta h = \Delta x \tan \alpha$$

where Δx is the distance between data points. The heights in a scan are cumulative relative to the height of the first data point.

The resulting profiles are adjusted to the model profiles by taking the first and last point in each profile and setting each equal to the known model heights.

5. Results of Present Work

Five scans were selected for comparison with model heights at intervals of 0.4 foot. The data points in each of the 5 adjusted profiles were subtracted from the corresponding model measurements and an average and standard deviation were calculated for height differences:

average deviation = -0.35 inch
standard deviation = ±2.32 inches

Four of these profiles are shown in Figure 22. Only four are shown for convenience, at a scale large enough to show the differences.

6. Error Analysis

An error analysis for this photometric mapping technique was performed in the Phase II work. This analysis consisted of computing the variance of the uncertainty for each of the factors, converting these variances to log exposure variances and combining the variances as random errors by computing the root sum of squares (RSS) to represent the total log exposure error. This log exposure error was converted to an uncertainty in α.

Because this experiment is a duplicate of that done in Phase II, the errors in the individual items are the same. Therefore the RSS error is the same. The individual variances and their RSS are tabulated in Table II.

The uncertainty in α resulting from the log exposure error is different because Phase II work was done at a phase angle of 75° and

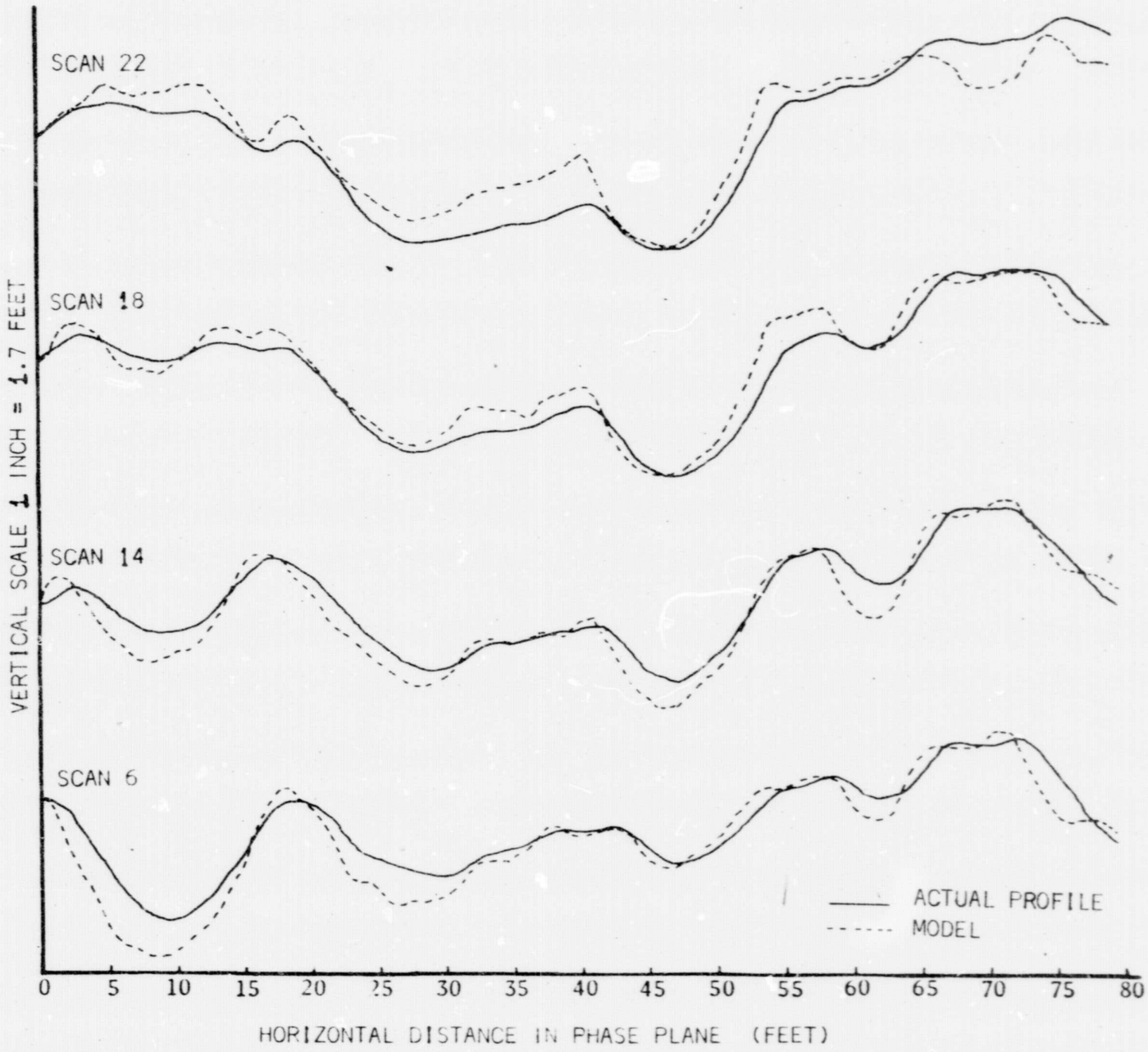

FIGURE 22 PROFILES OBTAINED BY PHOTOCLINOMETRY AT 30° SUN ELEVATION

TABLE II

ERROR ANALYSIS FOR
PHOTOCLINOMETRIC MAPPING IN LABORATORY

Factor	Variance in log E
Illumination	8.1×10^{-5}
Albedo	1.9×10^{-4}
Lens Transmittance	4.0×10^{-5}
Shutter Time	1.0×10^{-5}
f/Number	4.0×10^{-5}
Processing	4.0×10^{-4}
Photometric Function	4.9×10^{-5}
Microdensitometry	4.0×10^{-5}
Root Sum Square	± 0.03

the current work at 60°. Therefore a new uncertainty in α was calculated from the following relationship:[6]

$$\Delta\alpha = [\text{antilog } (\Delta \log \phi)-1] \; (\phi_{\alpha=0}) \; (\Delta\alpha/\Delta\phi) \qquad \text{Equation 8}$$

For small changes in log E (±0.030 from Table II) the resulting changes in log ϕ will be approximately the same. Therefore, from Equation 8 the uncertainty in α becomes:

$$\Delta\alpha = [\text{antilog } (\Delta \log \phi)-1] \; (\phi_{\alpha=0}) \; (\Delta\alpha/\Delta\phi)$$
$$= (1.10-1) \; (0.226) \; (211) = \pm 4.7°$$

The uncertainty in α is therefore ±4.7°.

The results of the Phase II work are compared with the current experimental results below:

	Phase II	Current
average deviation in height	0.0 inch	-0.35 inch
standard deviation in height	±2.56 inches	±2.32 inches
α uncertainty	±1.9 degrees	±4.7 degrees

Examination of the above results indicates an apparent discrepancy, viz., mapping at 30° sun elevation yields a slight deviation from a zero mean (the negative value for average deviation in height means the map is generally higher than the model) but results in a smaller standard deviation in height. This smaller deviation in height was unexpected because the larger α uncertainty should produce a greater uncertainty in height.

In an attempt to rationalize this discrepancy, a review was made of the height-adjusting technique used in the Phase II work. The adjusting technique differed considerably from that in the current analysis.

For the Phase II mapping, line drawings of 22 unadjusted profiles were assembled on an illuminator and adjusted by comparison with a vertical photograph. Once the profiles were adjusted, a line was arbitrarily drawn under the assembled profile. This line was considered zero elevation. Profiles were then generated in the Y direction (perpendicular to the phase plane). The profiles in the phase plane were next adjusted by taking the first and last point determined from the Y direction profiles and linearly adjusting each scan to these points. For comparison with the same zero elevation as the model, each data point in each scan was subtracted from the corresponding measured height of the model and an error curve generated for each scan. This error curve was used to adjust each scan to the model. The adjusted heights were again subtracted from the corresponding model heights to compute the average and standard deviations in height. It is felt that this last adjustment would not be possible in practice because the data required from the area being mapped would not be available (if the data were available there would be no reason to make the map).

To compare the results at the two different phase angles under the same conditions, the unadjusted heights from the Phase II work were adjusted using only the first and last data points in each scan. In practice, these data points could be obtained from stereo analysis of the lunar area. An average and standard deviation of the height differences were calculated for these adjusted scans. The results compared with the current work at 30° sun elevation are:

	Phase II Run 15°	Phase IV Run 30°
average deviation	-3.02 inches	-0.35 inch
standard deviation	±3.31 inches	±2.32 inches

Neither measurement has zero mean; the negative average deviation means that the map is generally higher than the model. The results from the 30° map show better agreement with the model than those of the map made at 15°.

In mapping at 15° sun elevation, some data points occurred in shadow areas where no data were available to compute heights. When this occurred the computer was instructed to use the sun elevation as the slope angle to compile heights. This technique may cause significant error in height determination for areas in shadow. To investigate this possibility, all the heights that were derived from areas in shadow were removed from the data and another comparison was made against the model. No marked change occurred when the data were rerun without these points, but this result is not too surprising since only eleven points in all five scans were in shadow.

The accuracy of photographic photometry varies as a function of the point on the characteristic curve at which measurements are made. Microdensitometers used in making density measurements have an inaccuracy associated with them. This inaccuracy may be thought of as causing a "band" of measurements surrounding a mean value. It is estimated that the standard deviation of the width of this band is ±0.03 density units for the microdensitometer used in these experiments and is probably representative of these instruments. If the densities being measured are on the toe of the characteristic curve, the uncertainty in exposure caused by this error is much greater than for densities on the straight line portion of the curve. For SO-243 film processed to a gamma of 1.2, the uncertainties in exposures differ by a factor of two between areas exposed on the toe and those exposed on the straight line.

This exposure uncertainty may account for the differences between the results of the 15° and 30° mapping experiments. Many crater walls in the 15° photographs were on the toe portion of the curve, while all of the areas in the 30° photographs were contained on the straight line portion of the characteristic curve.

7. Conclusions

Mapping of a lunar model at 30° sun elevation can be done at least as well as at 15° sun elevation.

Uncertainty in α for a given uncertainty in ϕ increases as phase angle decreases; therefore, one would expect mapping accuracy to decrease as phase angle decreases. But as phase angle decreases the scene contrast decreases, and the scene can be recorded on the straightest, most accurate part of the characteristic curve of the film. The effect of combining these two opposing errors would have to be evaluated before deciding on the best exposing conditions for a mapping mission.

C. ϕ_1/ϕ_2 Method of Mapping

1. Summary

The ϕ_1/ϕ_2 mapping technique was applied to mapping a portion of Lunar Model KLM 6-65 dusted with cupric oxide. Only fair correlation was achieved between map profiles and profiles made from measurements on the model.

An error analysis indicated that by increasing the size of the scanning aperture from 10μ to 50μ and making 5 replicate scans of the same area, the error in determining exposure could be reduced to allow measuring slopes to within ±5° around a nominal value of zero using the photometric function of cupric oxide. This same uncertainty in exposure results in a slope measuring capability of ±3° when using the lunar photometric function.

The ϕ_1/ϕ_2 mapping technique is useful when mapping flat areas that do not show small details and are quite difficult to map using normal stereo techniques because of the low contrast of the scene.

2. Introduction

Photometric lunar mapping is done by determining the value of the relative luminosity factor ϕ through photographic photometry. Knowing the phase angle at which the photograph was taken, one can

obtain the slope of the lunar surface (in the phase plane) from the photometric function. From the slope value and the distance between data points, lunar height contours can be determined.

Solving for the relative luminosity factor requires the solution of Equation 1:

$$\phi = \frac{4\ N^2 E}{10.76\ T\ t\ I\ \rho}$$

Uncertainty in any one of the six variables in this equation causes an uncertainty in ϕ.

The ϕ_1/ϕ_2 mapping method[7] provides a way of eliminating most of the variables. Two photographs are taken of the same area at different phase angles. A value is determined for the ratio of the ϕ value from one photograph to the ϕ value from the same area in the second photograph. From the equation for ϕ it can be seen that many of the variables cancel, leaving T, t, and E which are the lens transmittance, exposure time and exposure. For areas near the optical axis or in the same place in the field, the ratio of T_1/T_2 is unity. Also, with good exposure control the ratio of t_1/t_2 is unity. The remaining ratio, E_1/E_2, is a unique function of lunar slope over a reasonable range of slopes, and one can compute the lunar slope from the ratio E_1/E_2. The only uncertainties in this procedure are the uncertainties in exposure determination.

3. Laboratory Test of the ϕ_1/ϕ_2 Method of Mapping

A portion of Lunar Model KLM 6-65, outlined in Figure 23, was used to investigate this mapping technique. This model was dusted with cupric oxide and illuminated by a simulated sun at an elevation of 30°. Two photographs were taken of the model at a scale of 1:25,000 (1:48 model scale, 1:52 photo scale) and phase angles of 45° and 75°. Extreme care was used in establishing the sun elevation and stereo angles. It is

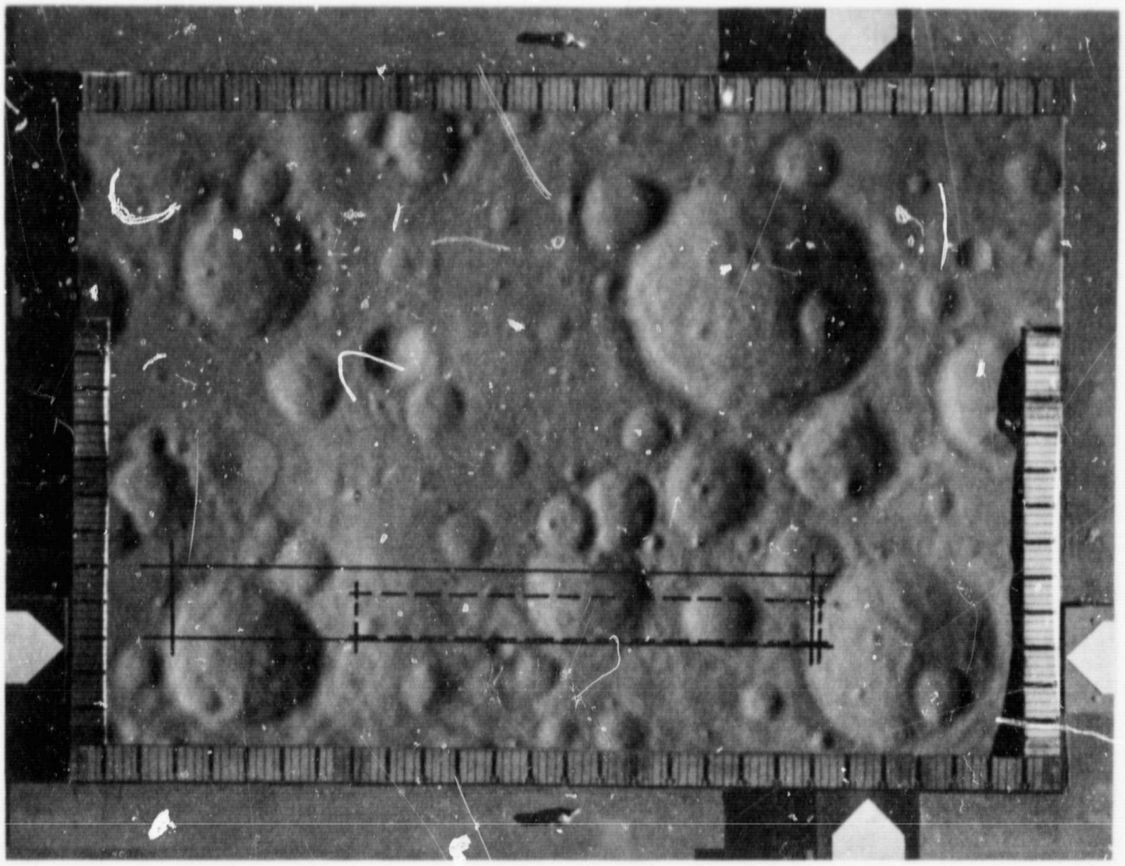

The Solid Lines Show the Area Initially Scanned for ϕ_1/ϕ_2 Mapping. The Dotted Lines Bound the Area Without the Large Crater that was Used for a Special, Separate Analysis of the Data

The Scales on Each Side of Model KLM 6-65 Are Used to Locate Points on the Images for the ϕ_1/ϕ_2 Method of Mapping

FIGURE 23. ϕ_1/ϕ_2 MAPPING ON LUNAR MODEL KLM 6-65

estimated that these angles are within ±5 minutes of arc of the nominal values. The Type SO-243 film was processed in a one-to-one mixture of D-19/D-76 to produce a gamma of 1.2.

A plane surface dusted with cupric oxide dust was also photographed using the same conditions as for the model. This plane surface was used to determine the amount of light fall-off across the width of the model because of the inverse-square law.

Figure 24 shows the relationship between slopes and the ϕ_1/ϕ_2 ratio for a sun elevation of 30° at a stereo angle of ± 15° from the vertical. These data are based on lunar photometric function data[8]. Figure 24 also shows this relationship based on the photometric function of cupric oxide dust.

The photographs and calibration step-tablets were traced with a microdensitometer in the phase plane using a 2μ diameter spot with samples taken every 3μ. A total of 22 scans each separated by 4μ was made within the area outlined by the solid lines shown in Figure 23.

It is necessary to obtain exact registration of corresponding data points in the photo pairs to do accurate mapping using the ϕ_1/ϕ_2 method. Exact registration was obtained from the model photographs by use of the coordinate grid system on the edges of the model.

The scale of the photograph constantly changes across the width of the model because of the oblique angle under which the photography was done. For a constant sampling increment this changing scale separates the data points by different amounts on the model surface. Separation of the data points must be known quite accurately because this information and the slope between data points are used to compute elevations.

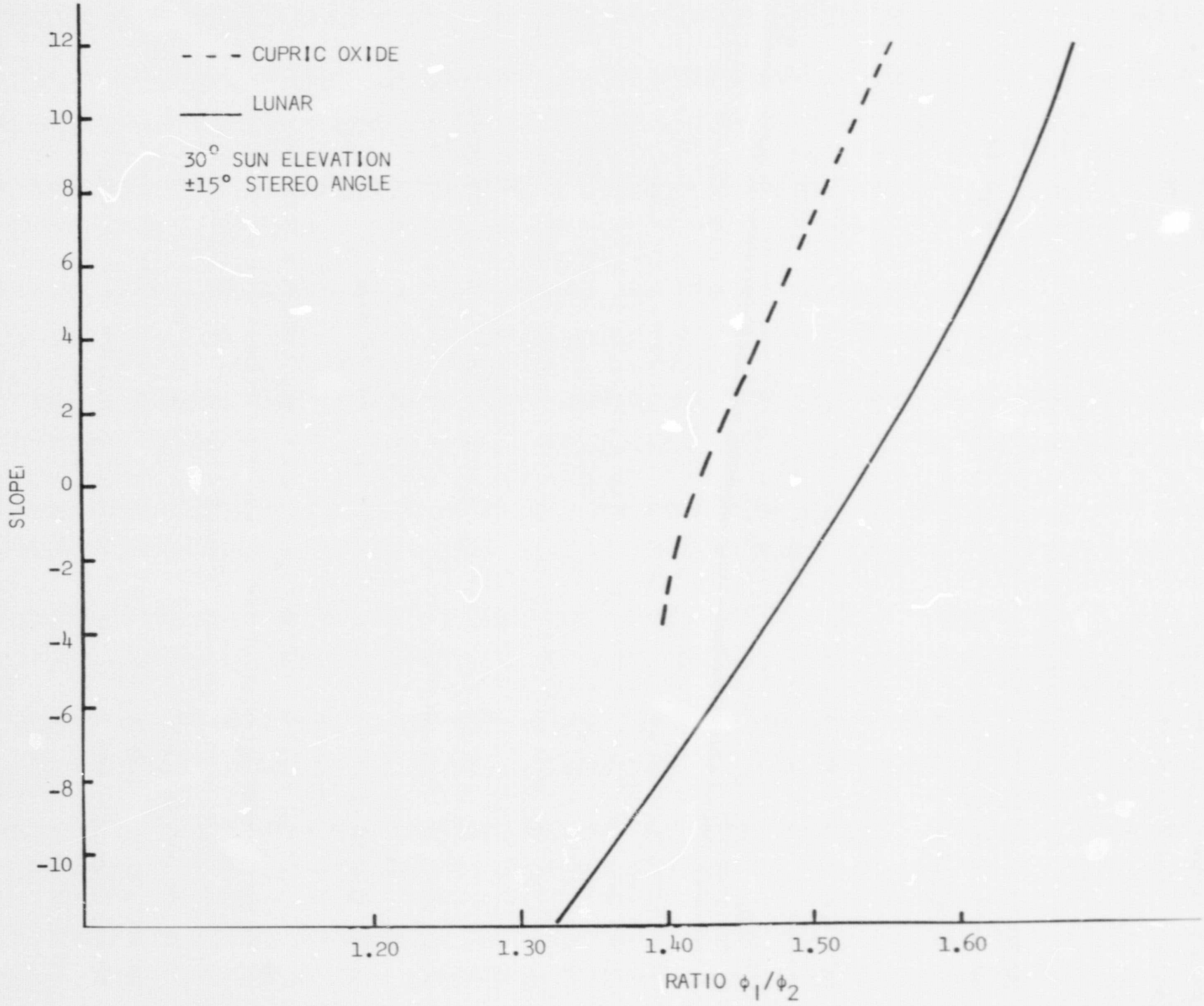

FIGURE 24. SLOPE VERSUS ϕ_1/ϕ_2 RATIO FOR LUNAR AND CUPRIC OXIDE PHOTOMETRIC FUNCTIONS

This change in scale can be corrected in one of two ways. The photos can be rectified using standard photogrammetic techniques or the scale change differences for each location on the model can be computed from the following relationship:[9]

$$\Delta S = \frac{-\sin\theta}{H}\Delta Y \qquad \text{Equation 9}$$

where ΔY = distance of the point in question from the isocenter

θ = stereo angle

H = altitude

ΔS = scale change

The isocenter is a point on the principal line a distance $D = F \tan(\theta/2)$ from the intersection of the optical axis and the film plane in a direction toward the lower edge of the photograph. F is the focal length of the lens. The principal line is a line in the film plane containing the points where the nadir and the optical axis intersect the film plane. By applying the scale change equation the exact data point spacing may be found for any pair of points on the model.

It was planned to use the scale change equation in this work but the calculated scale change across the model was so small we decided to use a constant scale. It is also difficult to establish a technique for locating the intersection of the optical axis and image plane when using such a small (approximately 2mm x 2mm) image. This intersection point must be determined quite accurately if the scale change is to be properly compensated.

If the ϕ_1/ϕ_2 method of mapping is to be used in mapping the lunar surface, the scale change will have to be compensated. The optical center is usually located by the use of four fiducial marks properly set around the edge of the picture format.

The digitized microdensitometer voltages were converted to exposures using the following relationship:

$$E = -23.04 + 51.78V - 36.88V^2 + 9.65V^3 \qquad \text{Equation 10}$$

The ratio of E_1/E_2 was computed for each pair of data points. The value of this ratio was converted to lunar slope from the following relationship curve-fitted by least mean square technique:

$$\text{Slope} = -145.8 + 101.6\ R \qquad \text{Equation 11}$$

where R = value of the E_1/E_2 ratio

Elevation changes relative to the first elevation point were computed from the slope S and the distance ΔX between two data points using the trigonometric relationship of:

$$\Delta H = \Delta X \tan S \qquad \text{Equation 12}$$

A comparison of the profiles generated from the elevation data and the profiles made from model measurements showed no correlation at all. To get some understanding of the reason the map profiles did not agree with the model, an abbreviated error analysis was performed.

The major uncertainty in this mapping technique is the determination of exposure. Part of this uncertainty arises from errors in the microdensitometer. This microdensitometry uncertainty can be thought of as the measurement of a band of densities rather than just a single value. The microdensitometer uncertainty is constant over the range of densities in which we work. This band of densities causes a wide range in exposure error depending on the placement of the average density on the characteristic curve. The greatest error occurs if the band of densities falls on either the toe or the shoulder of the characteristic curve.

If the exposure is adjusted so that regions of slope zero are exposed at a density of about 1.0 where maximum resolution occurs, slopes steeper than about -12° (leaning away from the sun) are exposed in the toe region of the characteristic curve for the photography at 75° phase angle. The placement on the toe results in a large exposure uncertainty. The average slope is about 15° for the wall of the large crater occurring at the left end of the mapping area shown in Figure 23. Examination of the data points from the 75° phase angle photographs indicates exposure values of about twice the magnitude expected in this region. Therefore, the exposure ratio is quite different from the correct value.

Table III lists the values of E_1/E_2 ratio for various slopes. These data are based on the photometric function of cupric oxide for a sun elevation of 30° and stereo angles of ±15°. It can be seen that as the slope becomes steeper than -6° the value of the ratio becomes ambiguous.

Under these conditions slopes steeper than -6° cannot be accurately mapped with the ϕ_1/ϕ_2 method. The large elevation excursion caused by a single pair of data points affects the remaining elevation data points because of the cumulative manner in which the profiles are generated.

The validity was also questioned of using a single exposure value for each data point used to compute the exposure ratio. This mapping technique is very sensitive to errors in exposure determination. To test the validity of using a single exposure determination, a short Monte Carlo simulation was performed. In this work a frequency distribution was created by computing the slopes resulting from exposure values randomly selected within a certain range of exposures. The exposure range was selected based on the uncertainty in measuring the absolute density by the microdensitometer. These density uncertainties were converted to exposure uncertainties through the characteristic curve of the film.

TABLE III

VALUES OF ϕ_1/ϕ_2 RATIO (CUPRIC OXIDE) FOR VARIOUS SLOPES

AT 30° SUN ELEVATION AND ± 15° STEREO ANGLE

	g = 45°		g = 75°		
Slope	α	ϕ	α	ϕ	Ratio ϕ_{45}/ϕ_{75}
-12°	3°	0.331	-27°	0.238	1.391
-10	5	0.323	-25	0.231	1.397
-8	7	0.313	-23	0.224	1.397
-6	9	0.304	-21	0.218	1.396
-4	11	0.294	-19	0.210	1.398
-2	13	0.284	-17	0.202	1.406
0	15	0.273	-15	0.192	1.421
2	17	0.263	-13	0.[illegible]	1.443
4	19	0.253	-11	0.172	1.470
6	21	0.242	-9	0.162	1.499
8	23	0.230	-7	0.151	1.522
10	25	0.216	-5	0.141	1.537
12	27	0.200	-3	0.130	1.543

Approximately 100 different exposure values were used in forming the frequency distribution of slope. The 2-sigma limits of the frequency distribution indicate that slopes as steep as ±12° could be calculated for a nominal α value of zero.

The Monte Carlo simulation was rerun using 10 exposure values randomly chosen and combined to form an average exposure value. The width at the 2-sigma level of the slope frequency distribution created from the average exposure values was reduced by about a factor of four.

While 100 iterations are not sufficient for an accurate Monte Carlo simulation, it is large enough to indicate trends, and at this time a larger simulation is not warranted.

Based on the error analysis, it was decided to map a relatively smooth area on the model. The area chosen is outlined with broken lines in Figure 23. Also, each scan was rescanned five times and an average taken. Five scans rather than ten were chosen to reduce the amount of data collected and because the Monte Carlo simulation did not show a significant reduction in slope uncertainty by going from five to ten determinations.

The two photographs were rescanned under the above conditions using the same microdensitometer set-up.

Analysis of the data obtained from the retracing indicated that no significant smoothing had been obtained from averaging the five scans. The precision of retracing the same area with the microdensitometer was so great that the fluctuations caused by the film grain matched one another in all five scans. When the five were combined, no smoothing occurred and no improvement in mapping was obtained.

It was decided to use a larger scanning aperture in the microdensitometer in order to smooth the data. Only a single scan was made of each area, but the resulting analog traces were very smooth. The new data were used to generate profiles using the same techniques as before. The resulting profiles showed better agreement with the model profiles, but the correlation was still not good. Two of the scans are compared to the model profiles in Figure 25.

A review of the mapping technique was made in an attempt to get some insight into ways to improve the mapping accuracy. This exposure uncertainty arises primarily from two sources. The first is the uncertainty associated with the microdensitometer, and the second is the uncertainty caused by the film grain noise.

The microdensitometer standard deviation in measuring density at a nominal level of 1.0 is estimated to be ±0.03 density units. The density standard deviation caused by the film grain when using a 10μ scanning aperture is ±0.02 density units.

The value for two standard deviations of this combination, representing a confidence level of 95%, equals ±0.072. The density uncertainty was converted to a voltage uncertainty using Figure 26. Figure 26 was obtained by tracing with the microdensitometer the step tablet used for calibration and plotting microdensitometer voltages against the densities of the step tablet. The voltage uncertainty is ±0.3 volts around a mean of 7.6 volts.

Slope S is a function of the ratio R of exposures from two photographs. Using the relationship between exposure and voltage, and substituting X for the voltage from the 45° phase angle photography and Y for the 75° phase angle voltages, we have the relationship:

$$\text{Ratio } R = \frac{E_{45}}{E_{75}} = \frac{28.8 - 7.16\,X + 0.635X^2 - 0.02X^3}{28.8 - 7.16\,Y + 0.635Y^2 - 0.2Y^3} \qquad \text{Equation 13}$$

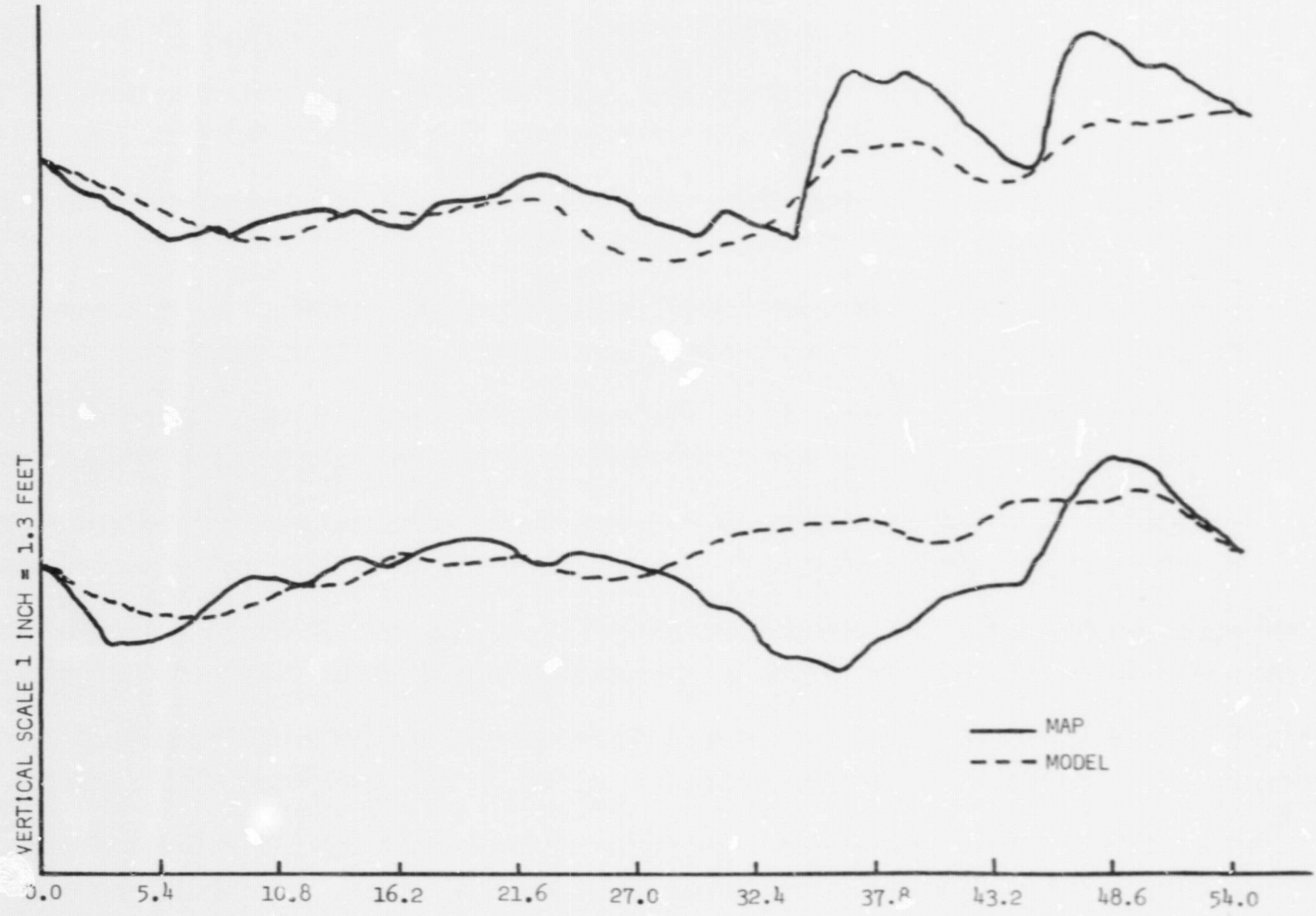

FIGURE 25. PROFILES OBTAINED BY ϕ_1/ϕ_2 MAPPING AT 30° SUN ELEVATION

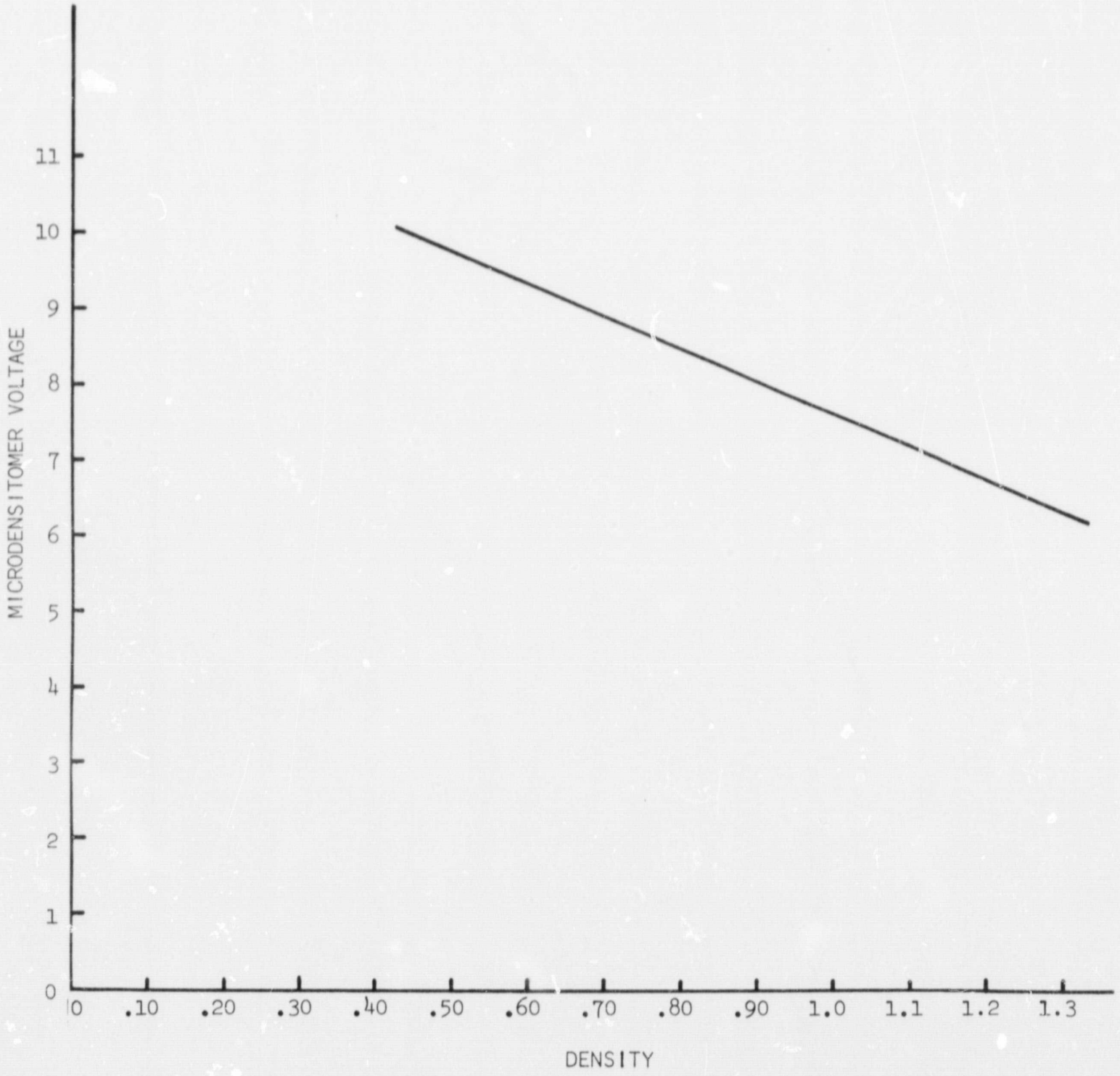

FIGURE 26. RELATIONSHIP BETWEEN DENSITY AND MICRODENSITOMETER OUTPUT VOLTAGE

The partial derivative of the ratio with respect to the 45° phase angle voltage (X) equals:

$$\frac{\partial R}{\partial X} = \frac{(28.8 - 7.16Y + 0.635Y^2 - 0.02Y^3)\ (-7.16 + 1.27X - 0.06X^2)}{(28.8 - 7.16Y + 0.635Y^2 - 0.02Y^3)^2} \qquad \text{Equation 14}$$

This derivative was evaluated at voltages corresponding to zero α.

$$\frac{\partial R}{\partial X} = -0.655$$

Substituting the value of ±0.3 for the voltage uncertainty (∂X) the uncertainty in exposure ratio becomes:

$$\partial R = -0.655\ (0.3)$$
$$\partial R = \pm 0.196$$

Slope S is related to the exposure ratio R by Equation 11:

$$\text{Slope } S = -145.8 + 101.6\ R$$

$$\frac{dS}{dR} = 101.6$$

The slope uncertainty due to the ratio uncertainty is:

$$dS = 101.6\ dR = 101.6\ (0.196)$$
$$dS = \pm 19.9°$$

This slope uncertainty of almost ±20° accounts for the poor agreement between the map and model profiles. This uncertainty was only based on the exposure uncertainty of the 45° phase angle photograph assuming no uncertainty in determining exposure from the 75° photograph.

This assumption is not true, of course. However, the exposure uncertainty from the 75° photograph would be slightly less than the 45° because the average density would be slightly lower and therefore the granularity would be reduced.

Because this mapping technique is sensitive to uncertainty in exposure determination, a large microdensitometer scanning aperture must be used to reduce the effect of grain noise. For example the standard deviation of the density variation caused by grain using a 50μ diameter spot is ±0.0095 at a nominal value of 1.0. The large microdensitometer aperture also integrates the small detail in the photograph reducing the effective resolution of the mapping technique. The use of multiple scans of the same area using a large aperture will reduce microdensitometry uncertainties. The Monte Carlo simulation performed earlier indicated that at least five scans over the same path would be required.

It is estimated that the use of a 50μ scanning aperture and five multiple scans would reduce the exposure uncertainty sufficiently to allow slopes to be determined with an accuracy of ±5° around a nominal value of zero. The slope accuracy of ±5° is an estimate based on the error analysis and was not demonstrated in this study.

4. Conclusions

The ϕ_1/ϕ_2 mapping may be used on areas that are generally flat with slopes no steeper than -6° and in which small detail is absent or of little interest. A large microdensitometer scanning aperture must be used (at least 50μ on SO-243 film) and at least 5 scans of the same area should be made. Under these conditions a slope uncertainty of ±5 degrees around a nominal value of zero should be obtained.

The accuracy will be better for the lunar photometric function than for the cupric oxide photometric function assuming both are known equally well. The gradient of the curve shown in Figure 24 for the lunar photometric function is less than for the cupric oxide curve. This lower gradient causes a smaller error in lunar slope for a given uncertainty in ratio. The ±5° uncertainty estimated for the cupric oxide would be reduced to about ±3° uncertainty for lunar mapping. Also the range of mappable slopes is increased because the curve for lunar slopes does not exhibit the ambiguities beyond -6° as does the cupric oxide data. Slopes steeper than -12° will result in exposure values falling on the toe of the characteristic curve and larger exposure uncertainties will occur.

If one is interested in mapping a very flat area on the lunar surface with the highest degree of slope certainty and with no interest in small detail, the ϕ_1/ϕ_2 mapping technique is the one to use. This conclusion is based on the comparison of slope uncertainties generated for the ϕ_1/ϕ_2 method and those generated from the usual photoclinometric techniques. If the lunar photometric function is known to the same degree of accuracy as the cupric oxide photometric function, the lunar slope uncertainty estimated for the ϕ_1/ϕ_2 technique is ±3° while that for the single photograph photoclinometric technique is ±5° based on the log exposure uncertainty computed in Phase II work for a lunar mission with accurate knowledge of the lunar photometric function. The log exposure uncertainty was converted to an alpha uncertainty using the lunar photometric function at a g of 60°.

The ϕ_1/ϕ_2 technique requires stereo photographs which normally can also be used to produce maps using standard stereo techniques. However, absence of small details may make stereo mapping difficult.

D. Improvement of Photometric Function

1. Summary

Data were obtained for the photometric function with improved confidence for one specific lunar area photographed by Lunar Orbiter III. This information fills a gap between older earth-based information and recent Surveyor information; these measurements represent 2 extreme capabilities in scale, an important parameter in photometric measurements.

Special techniques were used to examine craters and obtain the photometric function over a wider range of viewing geometry than can normally be covered in a single view of a relatively flat area.

An error analysis was performed to demonstrate the improved confidence in the new data.

2. Introduction

The original earth-based measurements of the lunar photometric function were made using integrated light from the whole moon. Measurements from earth are limited to a resolution of about 1/2 mile, a factor of about 1000 poorer than the resolution of Lunar Orbiter pictures.

Lunar Orbiter photographs offer a unique opportunity to refine the measurements of photometric function, to produce values with increased confidence for a wide variety of topographic features and to examine the effects of photographic scale on the measurement of this function.

In this study, values for the photometric function were obtained from measurements on high resolution photographs taken by Lunar Orbiter III of a potential landing site.

In this procedure Equation 1 (page 26) was solved for values of ϕ. The GRE films from LOP photographs taken with the 24-inch lens were traced on a microdensitometer. The output voltage of the microdensitometer was related to exposure on the spacecraft film by use of calibration information. The exposure values were converted to lunar surface luminance values using data for lens transmittance, f-number shutter speed, and the solar constant. Using slope data from stereo analysis of the photographs and applying an average albedo value calculated from photography of the same area using the 80mm lens, the surface luminance values were converted to relative luminosities. Since the photographs were taken at a known phase angle, the relative luminosities could be related to the values of the two variables g and α. The photometric function thus obtained was compared to a generally accepted lunar photometric function for the same slopes and sun angles.

Since the range of slopes was relatively limited in the landing sites for which stereo elevations were available, additional values of the relative luminosities were obtained for a wider range of slopes by fitting a spherical geometric model to a suitable crater.

3. Error Analysis of NASA Elevation Data

NASA furnished thirteen contour maps listed in Table IV. These maps were prepared by the Army Map Service (AMS) from Lunar Orbiter II photographs taken with the 80mm lens. NASA also furnished the partial reassemblies listed in Table V. These reassemblies contained point elevation values computed photogrammetrically by NASA from Lunar Orbiter III photographs taken with the 24-inch lens.

An error analysis was performed on the contour maps (from the 80mm lens) and the elevation data (from the 24-inch lens) provided by NASA to assess the confidence in the slopes used in the calculation of photometric function.

TABLE IV

NASA CONTOUR MAPS FROM 80MM LOP II PHOTOGRAPHS

Map Number	Area	LAC	Relative Errors in Meters (90% Probability) Horizontal	Vertical
ORB - II - 2 a (25)	Mare Tranquillitatis	61	66	112
ORB - II - 6 a (25)		60	88	262
b			"	"
c			"	"
d			"	"
ORB - II - 11 a (25)		76	62	142
b			"	"
c			"	"
d			"	"
ORB - II - 13 a	Oceanus Procellarum	57	85	194
b			"	"
c			"	"
d			"	"

Map Scale 1:25,000

Contour interval:25 meters

Mercator Projection

TABLE V

NASA REASSEMBLIES

OF 24-INCH LOP III PHOTOGRAPHS

FOR WHICH ELEVATION DATA WERE FURNISHED

Spacecraft Frame Number	Reassembly Section	KI Number *	Framelet Numbers
187 HR	2 of 3	3067	343 - 373
187 HR	3 of 3	3067	375 - 406
188 HR	2 of 3	3066	471 - 503
188 HR	3 of 3	3066	504 - 536

* Kodak Identification Number

The contour maps listed in Table IV indicate that for the best case the relative error in elevation (vertical) for any point is 112 meters at a 90 percent confidence level. This value was interpreted to indicate that an elevation measured from the map will be within ±112 meters of the true elevation with 90 percent confidence. The spot elevations on the reassembled pictures listed in Table V have errors relative to each other of 25 to 35 meters. In a tabulation of data from these reassemblies, NASA denotes the relative error term as sigma. This specification of accuracy was interpreted to mean that elevations determined from the reassemblies are correct to within ±25 to ±35 meters with approximately 68 percent confidence.

The error data supplied by NASA leads to an estimate of the error in the slopes that are determined from the maps. The general equation for slope is:

$$S = (h_2 - h_1)/d \qquad \text{Equation 15}$$

where: S = Slope
h_2 = elevation of point 2
h_1 = elevation of point 1
d = horizontal distance from point 1 to point 2

When h_1, h_2 and d are taken as true elevations and distance, the slope determined from the map is given by

$$\hat{S} = (\hat{h}_2 - \hat{h}_1)/d \qquad \text{Equation 16}$$

where: $\hat{S}$ = slope estimate
$\hat{h}_2$ = estimate of elevation of point 2
$\hat{h}_1$ = estimate of elevation of point 1

The distribution of $\hat{S}$ is normal with a mean $(h_2 - h_1)/d$ and a variance given by:

$$\sigma_S^2 = 2(1 - \rho)\sigma^2 / d^2 \qquad \text{Equation 17}$$

where: σ_S^2 = variance of distribution $\hat{S}$

ρ = correlation coefficient between elevations $\hat{h}_1$ and $\hat{h}_2$

σ = variance of distribution of $\hat{h}$

Note the inclusion of the correlation coefficient, ρ. The correlation coefficient is a measure of the correlation between the elevations $\hat{h}_1$ and $\hat{h}_2$. It expresses the fact that if one point has a positive error of a given magnitude, the other point will probably also have a positive error of nearly the same magnitude. Therefore an equation can be written to define the 90 percent confidence interval for the measurement of slope determined from the maps. Thus, for a slope, $\hat{S}$, measured from the maps, the confidence is 90 percent that it is within the following limits:

$$\text{Con}\left(\hat{S} - 1.64\sqrt{2(1 - \rho)}\sigma/d \leq \frac{h_2 - h_1}{d} \leq \hat{S} + 1.64\sqrt{2(1 - \rho)}\sigma/d\right) = 0.90 \qquad \text{Equation 18}$$

The above relation is a first order estimate of the accuracy of slopes determined from the maps. Table VI gives estimates of slope error made using this equation for slopes calculated from elevation data on the maps and reassemblies listed in Tables IV and V.

TABLE VI

ESTIMATES OF ERRORS IN SLOPES CALCULATED FROM ELEVATIONS GIVEN IN CONTOUR MAPS AND REASSEMBLIES

Equation used to estimate error:

$$\text{Con}\left(\hat{S} - 1.64\sqrt{2(1-\rho)}\,\sigma/d \leq \frac{h_2 - h_1}{d} \leq \hat{S} + 1.64\sqrt{2(1-\rho)}\,\sigma/d\right) = 0.90$$

Example	Conditions ρ	v*	σ	$h_2 - h_1$	d	$\hat{S}$	Calculated Slope	Estimated Error
1	0	112m		25m	286m	0.0875	5°	±28°
2	0.5	112		25	286	0.0875	5°	±20°
3	0.8	112		25	286	0.0875	5°	±14°
4	0	112		25	475	0.0526	3°	±18°
5	0.5	112		25	475	0.0526	3°	±13°
6	0.8	112		25	475	0.0526	3°	± 8°
7	0		30m	7	562	0.0124	0.67°	± 6°
8	0.5		30	7	562	0.0124	0.67°	± 4°
9	0.8		30	7	562	0.0124	0.67°	± 2°

* $v = 1.64\,\sigma$

Examples 1 to 6 are taken from contour maps made from LOP pictures taken with the 80mm lens.

Examples 7 to 9 are taken from reassembled pictures made using the LOP 24-inch lens. Spot elevations at many points in the pictures were supplied by NASA.

4. Sensitometric Calibration

Two methods were available for sensitometric analysis relating GRE film density to exposure on the spacecraft film: the preexposed edge print data and the tone reproduction characteristics of the Lunar Orbiter system.

Since the input signal to the GRE from the spacecraft was recorded on tape, the comparison between the edge print data and scene information could be made in two ways - by analysis of the densities on the GRE films or by comparison of signal strengths on the tape.

The goal of this investigation was to make a comparison of the results obtained from the tapes (on a sample basis only because data reduction from the tapes requires considerable analysis) with the results obtained by measurement of photographic densities, as a test of the effects of flare in the GRE. This investigation could not be carried out because of an unresolved incompatibility between the tape and computer equipment.

A comparison was made of the reliability of calibration by use of the tone reproduction characteristic and the edge print densities.

A procedure was developed for determining the tone reproduction characteristics for a particular reconstructed record from Lunar Orbiter. The procedure was developed in order to verify whether densities in the Orbiter edge data could be used to obtain accurate exposure information from a lunar scene. A calibration applies to only a particular film record and must be calculated for each film record being analyzed. Exposure calibration data for the Ground Reconstruction Electronics (GRE) will vary from machine to machine and from one film record to another for any one machine.

This analysis shows the edge data can be used to obtain exposure information accurate to within ±0.06 log exposure units. This accuracy is approximately equal to the uncertainty in the exposure given the edge print on the actual vehicle film.

Table VII is a summary of the calibration data required. The GRE calibration data and test signals were measured before and after each recording of lunar data. These signals include a bar function, a stairstep function, a 400 kc tone, a multiburst function, and an unmodulated d.c. signal.

Figure 27 contains the tone reproduction diagram. The curves are numbered clockwise from I to IV starting in the lower right quadrant. The photo subsystem readout calibration was obtained from the applicable Quality Control test report.[10] The data collection procedure is specified in a QC Procedure Document.[11] The sensitometric curve is a nominal curve for BIMAT-processed SO-243. Edge data exposure calibration data is documented in a letter of certification.[12]

Quadrant I relates density on the GRE record film to kinescope grid voltage. This voltage is equal to the difference between the bias voltage and gain voltage set during calibration procedures and measured at test points A1TP5 and A1TP4 in the video signal processor of the GRE.[13] Density values are obtained by reading the image of the stairstep function with a densitometer. The stairstep function generator, which is linear with respect to time, divides the grid voltage into 9 equal steps (10 levels) of equal amplitude increments. The first step corresponds to the bias level and the tenth to the gain level.

Quadrant II is a transfer curve representing the communications link and that part of the ground system prior to the GRE. It

TABLE VII

CALIBRATION DATA REQUIRED FOR L.O.P.

TONE REPRODUCTION

GRE

1. Bias voltage required for a density of 0.50.
2. Gain voltage required for a density of 2.00.
3. A recorded image of the stairstep function.

P.S. Readout Section

1. Voltage calibration of spacecraft film density versus video output.

Spacecraft Film

1. Sensitometric curve for BIMAT-processed SO-243 film.

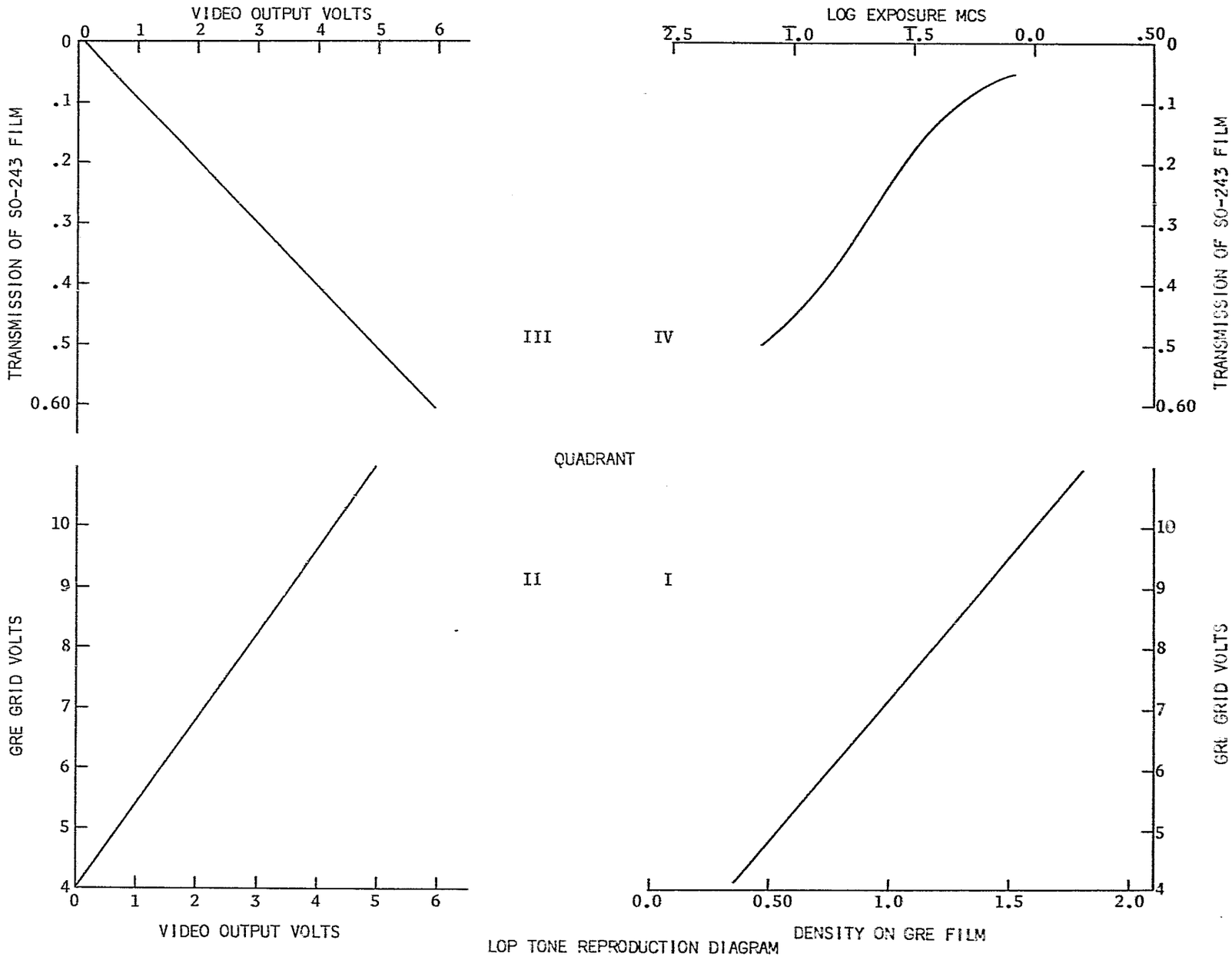

LOP TONE REPRODUCTION DIAGRAM

FIGURE 27. LOP TONE REPRODUCTION DIAGRAM

is assumed that these elements of the system produce zero attenuation of the spacecraft signal. While this assumption is not strictly true, optimization procedures for video readout from the spacecraft specify that the video signal out of the spacecraft be adjusted to 5.0 volts to match a 5-volt video input to the GRE used in set-up.

Quadrant III relates output voltage from the spacecraft video amplifier to spacecraft film transmission. The curve is a plot of data obtained in subassembly test phases of the readout assembly construction. The data used are from the same readout section that was flown in Lunar Orbiter III.

The sensitometric curve in Quadrant IV shows transmission vs log exposure for BIMAT-processed SO-243 film. It is an average curve taken from a series processed by BIMAT soaked in imbibant PS 485K-1 with a pickup of 6.62 grams/sq. ft. The plot covers only the straight line portion of the curve from a density of approximately 0.3 to 1.3 which corresponds to the density range readout by the Orbiter system.

After obtaining the tone reproduction diagram, the system was tested using step tablet densities in the edge data read from the GRE record film and the log exposure values reported in reference 12. The results for three values of video signal voltage are shown in Table VIII. Although the 5.5-volt video signal input provides the smallest error, the 5.0-volt input is typical of readouts. Within a density range from 0.5 to 1.7 on the GRE record film, the system can predict exposure to within approximately 0.06 log exposure units, approximately equal to the uncertainty in exposure given the original spacecraft flight film. Exposure predictions for densities above 1.7 show a rapidly increasing error because these GRE densities represent densities on the toe of the spacecraft film where a small density difference represents a large difference in exposure. For mapping purposes, significant lunar image information is at GRE densities below 1.7.

TABLE VIII

COMPARISONS BETWEEN SPACECRAFT FILM EXPOSURES PREDICTED BY TONE REPRODUCTION AND VALUES KNOWN FROM REFERENCE 12

A. 5.0-volt video signal input to the GRE

GRE Film Density	Log E Obtained From Edge Data	Log E Obtained From Tone Reproduction	Δ Log E
.51	$\bar{1}$.83 ±.05	$\bar{1}$.90	+.07 ±.05
.64	$\bar{1}$.66 ±.05	$\bar{1}$.73	+.07 ±.05
.86	$\bar{1}$.46 ±.05	$\bar{1}$.51	+.05 ±.05
1.20	$\bar{1}$.25 ±.05	$\bar{1}$.29	+.04 ±.05
1.72	$\bar{1}$.05 ±.05	$\bar{2}$.94	-.11 ±.05

B. 4.5-volt video signal input to the GRE

GRE Film Density	Log E Obtained From Edge Data	Log E Obtained From Tone Reproduction	Δ Log E
.51	$\bar{1}$.83 ±.05	$\bar{1}$.97	+.14 ±.05
.64	$\bar{1}$.66 ±.05	$\bar{1}$.76	+.10 ±.05
.86	$\bar{1}$.46 ±.05	$\bar{1}$.56	+.10 ±.05
1.20	$\bar{1}$.25 ±.05	$\bar{1}$.34	+.09 ±.05
1.72	$\bar{1}$.05 ±.05	$\bar{1}$.05	0.00 ±.05

C. 5.5-volt video signal input to the GRE

GRE Film Density	Log E Obtained From Edge Data	Log E Obtained From Tone Reproduction	Δ Log E
.51	$\bar{1}$.83 ±.05	$\bar{1}$.89	+.06 ±.05
.64	$\bar{1}$.66 ±.05	$\bar{1}$.69	+.03 ±.05
.86	$\bar{1}$.46 ±.05	$\bar{1}$.47	+.01 ±.05
1.20	$\bar{1}$.25 ±.05	$\bar{1}$.23	-.02 ±.05
1.72	$\bar{1}$.05 ±.05	---	

The major reason for developing the tone reproduction system was to verify the use of edge data in predicting lunar exposure. It was felt that the phosphor blooming encountered in nearly all GRE kinescope tubes would sufficiently falsify the edge data densities to produce erroneous exposure determinations. The GRE test signals would be relatively less affected since they are a constant pattern and are not influenced as much by adjacent areas as are the edge data.

Figure 28 compares exposure predictions by the tone reproduction method with those predicted by the edge data; the dashed line represents a 1:1 correlation between the two methods. A log exposure difference of approximately 0.06 is found over most of the exposure range. Since the edge data method is more easily applied in computer programs, this method of exposure prediction was used.

5. LOP Photo Geometry

The areas for which films and tapes were obtained are listed in Table IX. The areas chosen for use in improvement of the photometric function were restricted to areas for which contour maps were available.

The relationship between camera, sun, and surface configuration for photography of Frame 187, LOP III, is illustrated in Figures 29 and 30. The location of the camera axis intercept (ℓ = 44.4°W, B = 2.3°S in conventional selenographic longitude and latitude) is some 40 miles north of the crater Flamsteed in Oceanus Procellarum. It is a flat surface covered with numerous fresh craters, many having a ray pattern, and exhibiting local clustering. It is unfortunate that this character occurs in over 60 percent of these pictures; however, the slopes appear to be free of large boulders (> 1 meter), fresh craters greater in diameter than 10 meters, and extreme variations in albedo. Elevation data indicate very little change in topography, i.e., a difference in elevation of less than 15 meters over a distance of five kilometers. Hence, the general slope in the region is less than 1.5°.

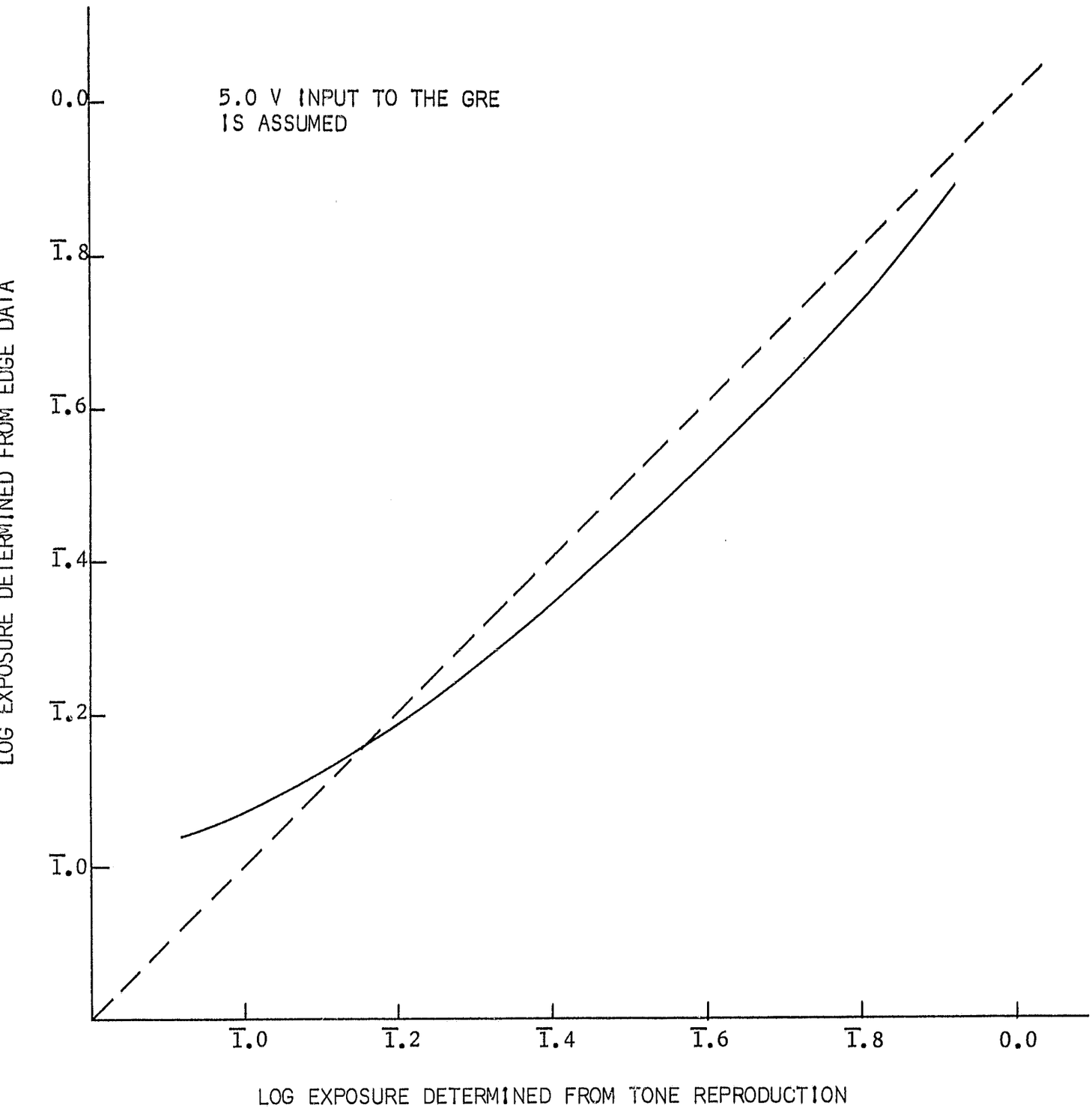

FIGURE 28. COMPARISON OF EXPOSURE DETERMINATIONS USING EDGE DATA AND TONE REPRODUCTION

TABLE IX

FILMS AND TAPES OBTAINED FROM NASA FOR IMPROVEMENT OF THE PHOTOMETRIC FUNCTION

GRE FILMS

Frame Number	Site Number	KI* Number	24-Inch Lens Framelet Number	80mm Lens Framelet Number
187	IIIP12A	3067	358, 359, 360 361, 362, 375, 376, 377	Complete Frame
188	IIIP12A	3066	478, 479, 480 481, 488, 489 490, 491, 504 505, 506, 507	Complete Frame

TAPES**

Frame Number	Site Number	KI* Number	24-Inch Lens Framelet Number
187	IIIP12A	3067	359, 360 361, 362

*Kodak Identification Number

**The tapes were not used as planned because of an unresolved incompatibility between the tape and computer equipment.

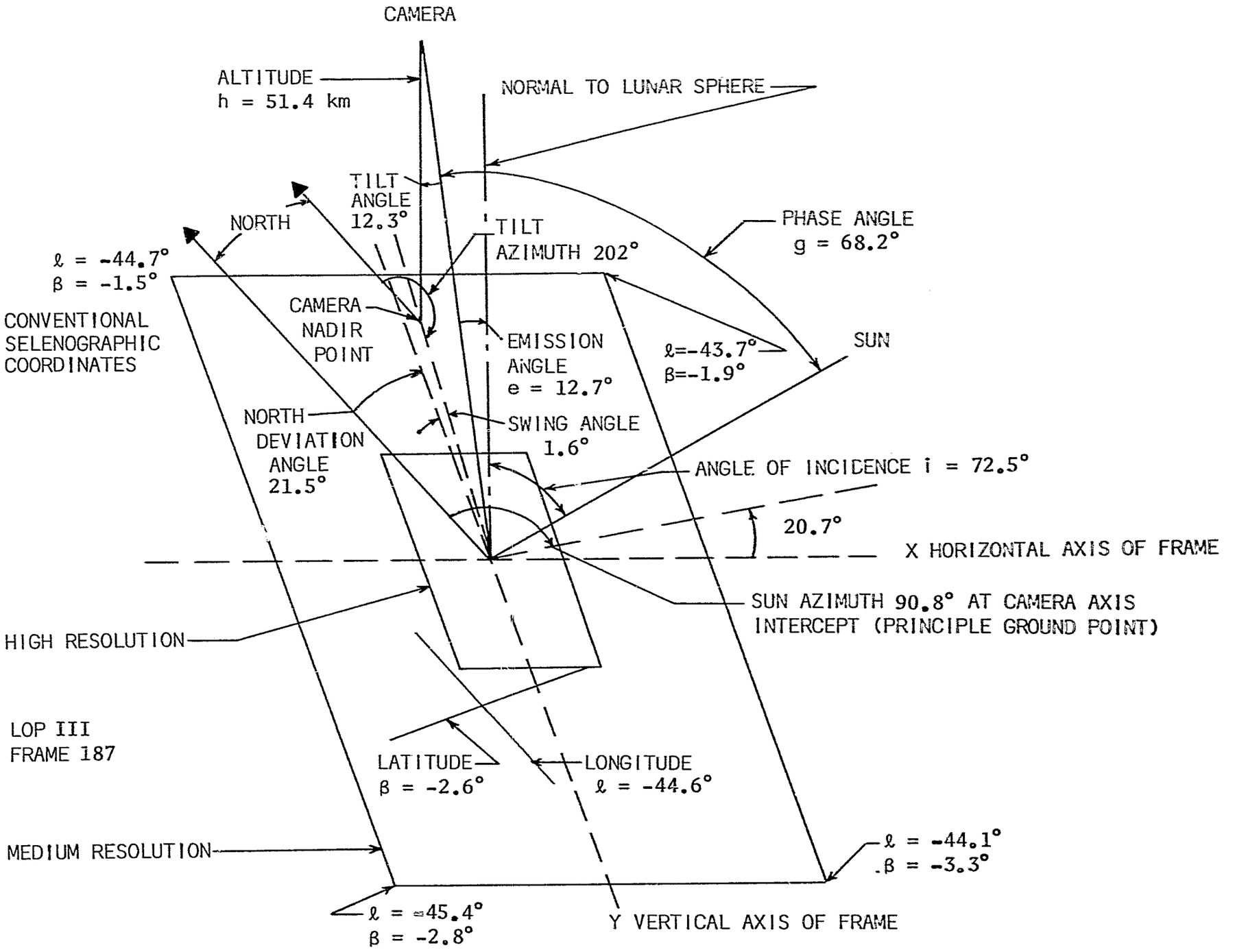

FIGURE 29. GEOMETRY FOR FRAME 187, LOP III

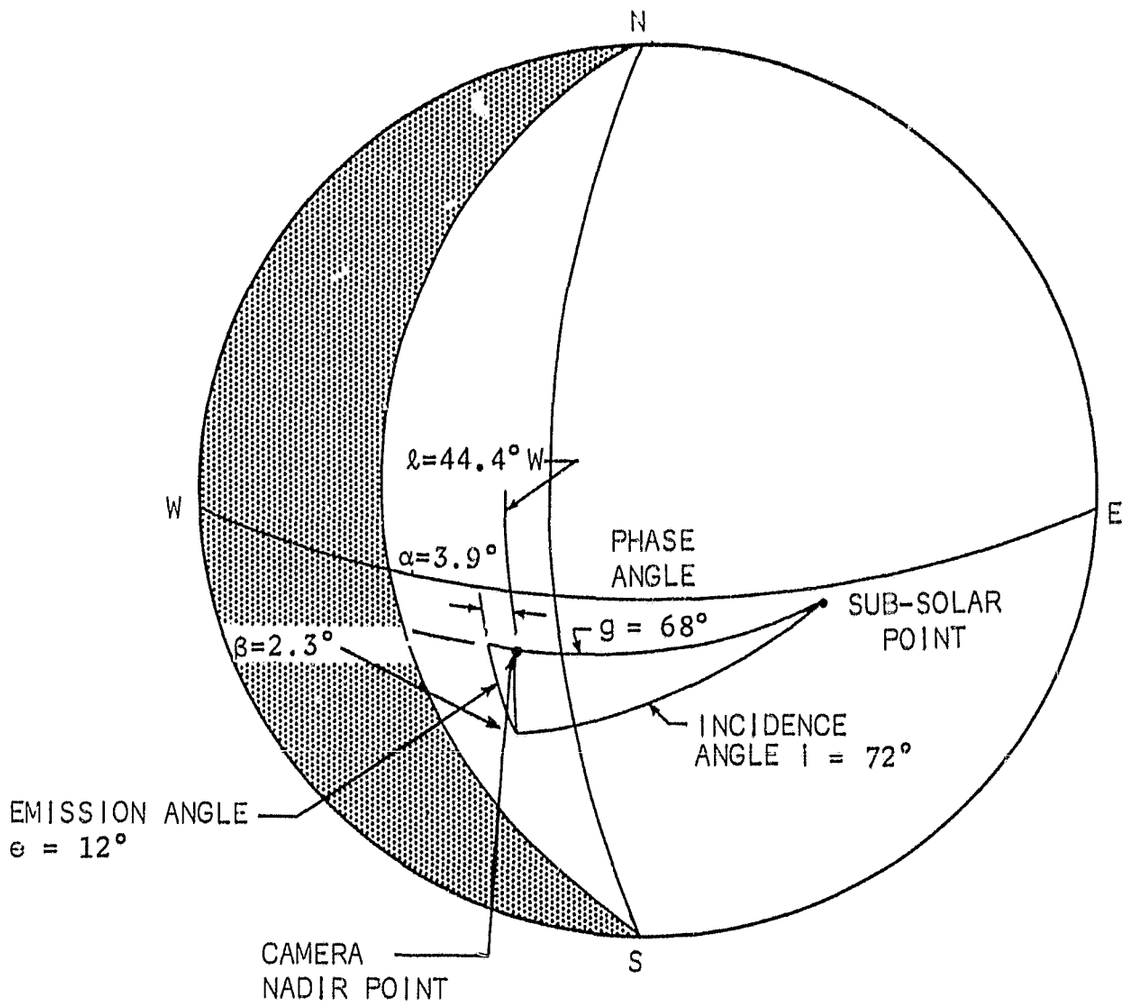

FIGURE 30. LOCATION ON MOON FOR FRAME 187, LOP III

In the high resolution (24-inch camera) scan areas selected, a range of only 0.45° in surface longitude is possible. The corresponding surface-spacecraft geometry allows a range in phase data of only 3.9°. The total high resolution area involved in the analysis is less than 12 square kilometers.

To obtain an approximate check on the photographic sensitometry involved in the preparation of the GRE films, Langley Research Center forwarded latent images of exposures on the sensitometer maintained at the Center. The film used was taken from the same stock as the film used in the GRE. Prior to processing, exposures were made on a sensitometer which is routinely kept in calibration. Precautions were taken against the influence of latent image keeping changes in the film by making the interval between exposure and processing comparable for both samples.

6. Choice of Areas of Photographs for Analysis

High contrast renditions revealed a non-uniform density gradient across the width of each framelet, but the repetition over many framelets allowed its removal by averaging. Vertical streaking extending the entire length of both high and low resolution frames was apparent in the central region covering 50 percent of the total picture In addition some dropoff in intensity resembling vignetting was esent. Less than 20 percent of the frame format in both the 35mm and 24-inch reproductions was free from density non-uniformity.

The slopes scanned by microdensitometer on the high resolution film were selected subject to the following requirements.

1. Non-uniform areas (vertical streaking, vignetting, etc.) were avoided.

2. Regions of high crater density and hence diverse surface orientation, and elevations separated by other types of rough ground (rocks, crevices) were excluded.
3. Slopes of wide range and large separations on either side of the nadir point in the phase plane were chosen.
4. Fresh craters, especially those "collared" with a bright ray system, and other high albedo areas were kept to a minimum.
5. The elevation points used from those supplied by NASA did not occur on the rims or slopes of craters that were small in comparison with the length of scan.

Sixteen slopes averaging 500 meters in length and satisfying the above criteria were selected. Four of these were scanned in a feasibility analysis.

Many of the same limitations applied to the medium resolution photographs. However, as the purpose of using these frames was to provide a check on the uniformity of surface albedo and to correlate with albedo data from Surveyor, these scans were not restricted to areas of computed elevation or to specially shaped sampling region. Avoiding craters greater than 5 meters in diameter, nine rectangular regions were selected, each approximately 200 meters on a side. One area was measured on Frames 187 and 188. GRE films from Frame 190 containing the Surveyor site were not available, but a reassembly print of this frame was examined and found to have a visual appearance comparable to the areas scanned in Frames 187 and 188.

7. Procedure for Microdensitometer Scanning

We discarded our original intention to use a microdensitometer aperture capable of registering television scan line noise to enable filtering, primarily because of the large volume of data. To

provide this capability would have required over 10,000 data points per slope. On the other hand, the aperture chosen could not greatly exceed either the resolvable surface roughness or the accuracy of locating the elevation points (±0.1mm). Consequently, a circular aperture of 100-microns diameter was used at a sampling rate of 10 samples per millimeter. This size was also convenient for reading the step tablets in the edge data necessary to determine exposure values, and, hence, also was used with the medium resolution frames.

The edge print of each framelet was measured in the step tablet and the linearity pattern. The latter was scanned to measure any non-uniform processing gradient.

Because the processed film was in a 35mm roll with each framelet displayed end to end, and the phase plane was inclined 21.5° to the long axis of a framelet, scanning in a phase direction even between the closest elevation points would cause the scan to leave the film strip. Consequently, to avoid tedious matrix calibration between framelets, scanning was done out of the phase plane.

Scanning out of the phase plane in this study can be justified from the dimensions involved. In a typical example in this study, the film was scanned between elevation points separated by about 600 meters in a direction nearly parallel to the long dimension of the framelet. This direction was inclined about 20° to the phase plane of the starting point of the scan. For a scan near the nadir point, the phase plane for the end point of the scan would have been about 1/4° from being parallel to the phase plane at the starting point. (This angle is found by dividing the product of the 600 meter separation and the sine of 20° by the spacecraft altitude of 51 kilometers.) However, the points used in the study were some distance from the nadir point and the deviation between phase planes was smaller because of the increased slant range. The maximum deviation was 9' for phase planes of

points used in this study. In observations from the earth, points near the two poles of the moon are about 1/2° apart but are considered to have parallel phase planes. Thus, within an acceptable error of less than 1/4°, the end points of a scan and all intermediate points can be considered to have parallel phase planes. An observation in one plane is then the equivalent of an observation in any other.

A series of observations along the direction of scan is the equivalent of a single observation, except for the advantageous collection of more data available for averaging and use with an average phase plane. And a series of observations over a tilted plane can be regarded as equivalent to a single observation for a single value of α, except for the advantageous collection of more data.

The situation is comparable to making observations from the earth: observations taken from points on a common luminous longitude require changing the line of sight in a direction nearly perpendicular to the phase plane at the first point, but the phase plane at the new point is parallel to the phase plane of the initial point within a fraction of a degree.

The measured elevation points did not occur at equal distances from an edge of a framelet. Lacking the capability to follow the direct route between points, a direct trace was approximated by a series of short traces along the film separated by 100 microns across the film.

To get values of the albedo from 80mm photographs, a small square was scanned on LOP Frames 187 and 188 in raster fashion (26 scans, 26 samples per scan).

8. Measurement of Albedo Value from 80mm Photographs

Frame 190 from the medium resolution camera contained the site of Surveyor I, 22 km northeast of the nearest scan area, and provided information about the albedo, subject to the degree of similarity between the areas in Frames 187, 188 and 190.

Examination of the 80mm frames revealed that the Surveyor I site (ℓ = 43.35°W ± 0.1°, β = 2.58°S ± 0.16°) was similar to the terrain in Frames 187HR and 188HR. A recent analysis[14] of Surveyor I data provided luminance factors and found that the lunar photometric properties for homogeneous areas greater than 6 centimeters in diameter were independent of scale. If the same small area is evaluated in the overlapping portions of two adjacent 80mm frames, the photographic consistency can be assessed by the relation:

$$\frac{\phi_1}{\phi_2}\,\frac{\rho_1}{\rho_2} = \frac{E_1}{E_2} \qquad \text{Equation 19}$$

ρ_1 = albedo of the area as shown in frame 1

ρ_2 = albedo of the area as shown in frame 2

E_1 = exposure for the area in frame 1

E_2 = exposure for the area in frame 2

ϕ_1 = relative luminosity of the area in frame 1

ϕ_2 = relative luminosity of the area in frame 2

A local normal albedo was calculated using Surveyor I findings (ρ = 7.2%, luminance = 110 ft-lamberts at g = 69°, α = -3°) by measuring densities from an area 3.4mm x 2.7mm on frames 187 and 188 exposed by Orbiter III using the 80mm lens. The microdensitometer voltages corresponding to 882 data points for each framelet were converted

to exposures by means of a third degree equation fitted to the edge print calibration step tablet. An average exposure was determined for each area and the ratio E_1/E_2 was found by Equation 19.

$$E_1/E_2 = 0.814 = \frac{\rho_1 \phi_1}{\rho_2 \phi_2}$$

The exposure times of the two photographs are the same and the transmission of the lens is essentially the same for the two positions of the field of view. The value is reasonably consistent with the value of ϕ_1/ϕ_2 (0.75 ±0.10) predicted from the geometry and from photometric function, and indicates a faithful reproduction of intensities to ±3.3%. Corresponding Orbiter exposure for the Surveyor site is E_3 = 0.303 mcs. Using this value and the photometric curve for the appropriate phase angle and alpha angle gives a slightly higher normal albedo with considerable uncertainty -

$$\rho = 8.0\% \pm 15\%$$

Calculations were also made using the Surveyor I albedo value of 7.2% (±10%). The relative intensity, ϕ, is then found from equation 1:

$$\phi = \frac{0.0328}{\rho} E \text{ (24-inch lens)}$$

0.0328 is a constant encompassing exposure time, lens transmission, solar constant, lens f/number, etc.

9. Reference Photometric Analysis

In order to compare new information about the photometric function with previous information, two established standards of comparison were used, viz. the JPL fit to Fedoretz data and the Hapke theoretical function.

The JPL fit[15] to Fedoretz data is generally accepted as a representative interpretation of this original data which has widespread scatter.

The theoretical function developed by Hapke[16] is widely known, was developed with regard to the structure of the lunar surface, and fits successfully the appropriate observational data.

10. Measurement of Flat Areas

Six areas in which slope was known from NASA stereo elevations were analyzed by conversion of scan voltages to exposures and then to relative intensities employing the edge print data from each framelet.

As outlined in the description of the procedure for microdensitometry, the data for the line between elevation points (generally separated by a small amount in the direction across the 35mm framelet) were obtained by scanning in a step-wise fashion. About 15 to 30 scans, each containing about 30 points per scan, were made using an aperture of 100 microns diameter and sampling at 100 micron intervals.

To avoid including sharp features, only data falling within 5% of the average voltage for each horizontal scan (one complete scan between elevation points ≈ 20 horizontal scans) were registered. An average ϕ and the rms scatter were then tabulated from approximately 400 sample points per area. The rms deviation, calculated before filtering, seldom was greater than 5%.

Values of α and τ are obtained from elevation points by the relations[17]:

$$\tan \alpha = \frac{\lambda_1 \operatorname{Cos}\phi \operatorname{Sin}\tau + \mu_1 \operatorname{Sin}\phi \operatorname{Sin}\tau + \nu_1 \operatorname{Cos}\tau}{\lambda_3 \operatorname{Cos}\phi \operatorname{Sin}\tau + \mu_3 \operatorname{Sin}\phi \operatorname{Sin}\tau + \nu_3 \operatorname{Cos}\tau} \quad \text{Equation 20}$$

τ = true surface slope

α = slope projected into the phase plane

ϕ = azimuth of scan plane

λ_i, μ_i, ν_i = direction cosines[18] in the local coordinate system of sun and camera

The phase angle for this α is calculated using;

$$\text{Cos } g = \text{Cos } \gamma_s \text{ Cos } \gamma_c - \text{Sin } \gamma_s \text{ Sin } \gamma_c \text{ Cos } \phi_c \qquad \text{Equation 21}$$

where γ_s = zenith angle of sun

γ_c = zenith angle of camera

ϕ_c = azimuth of camera from incidence plane

11. Measurement of Craters

A need for a larger variation in slope was apparent from the small range in elevation heights in the data supplied by NASA. Elevation points supplied by NASA limited the range of measurement to very small slopes (<2°) of minimal 500-meter length. The narrowness of data point spread with which to correlate the photometric function, led to analyzing a conveniently located crater whose shape could be approximated by a spherical model. Fortunately an apparently spherical crater of 600 meters diameter was located in the midst of the computed elevation sites on Frame 188. This crater (located at ℓ = 44.285°W, β = 2.343°S) is fresh enough to present minimal rounded edges and a range in slope up to 20°. It has a comparatively smooth interior at one meter resolution with almost no evidence of slumping or erosion by adjacent craters. The crater was scanned by the microdensitometer at an angle of 21.5° from the incidence plane.

Figure 31 illustrates scan geometry for a spherical crater.

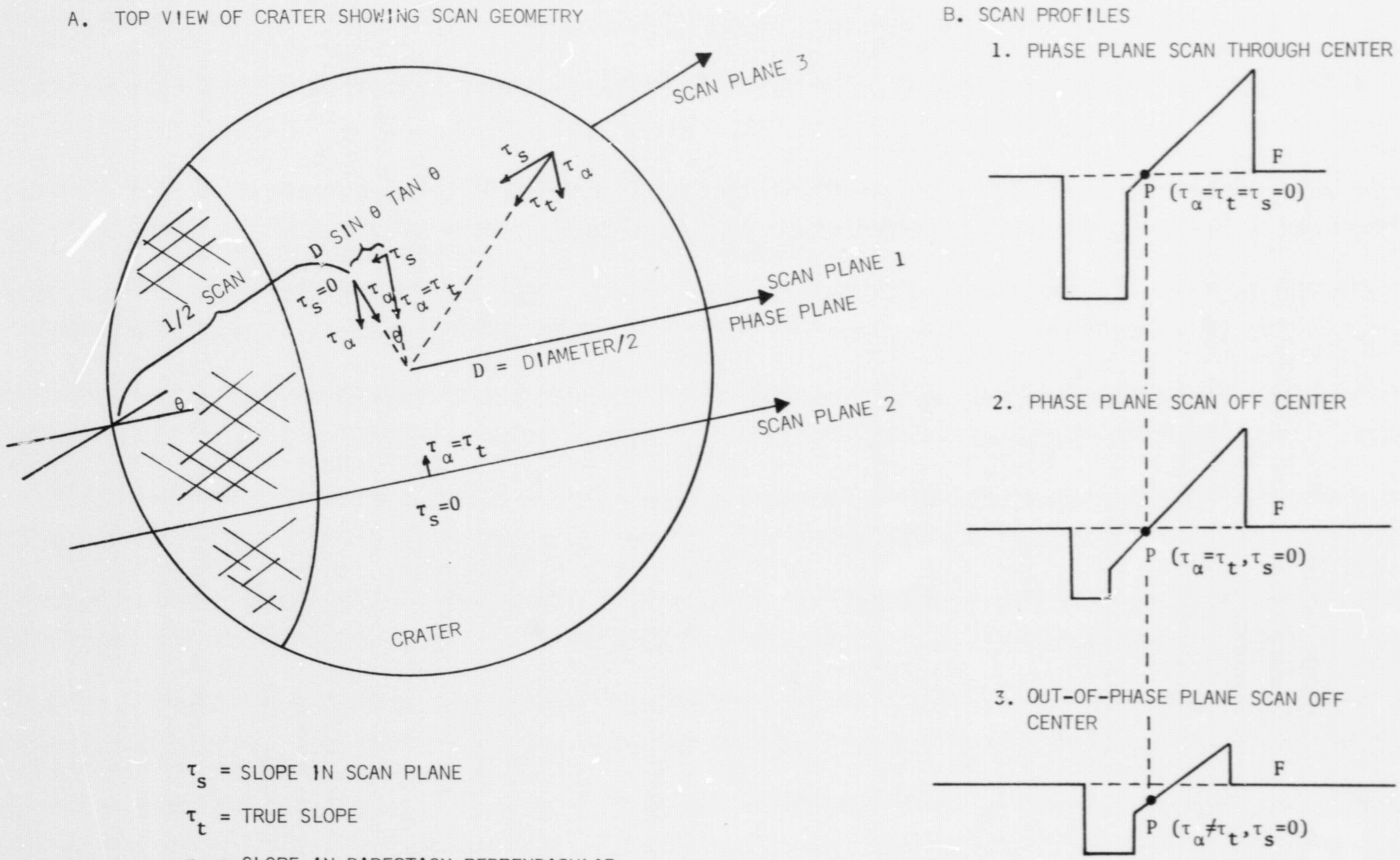

τ_s = SLOPE IN SCAN PLANE

τ_t = TRUE SLOPE

τ_α = SLOPE IN DIRECTION PERPENDICULAR TO PHASE PLANE

FIGURE 31. SLOPE-SCAN GEOMETRY OF SPHERICAL CRATER MODELS

Within the crater the values of α are obtained for each point by Equation 20 where:

$$\tau = \text{local normal} = \tan^{-1} \sqrt{\frac{x^2 + y^2}{a^2 - x^2 - y^2}} \qquad \text{Equation 22}$$

x,y = coordinates in surface plane (origin at center of the crater)

a = spherical radius

Comparison of results from these measurements with theoretical and observational models was possible in the region from $65° < g < 70°$, $0° < \tau < 20°$.

For the apparently spherical crater, it was necessary to calculate α and τ (slope) for each of the 493 data points in each scan. The intensity profile allowed the elimination of the effects of rounded rim, shadow, and penumbra from the data. Consequently, all useful information was limited to negative luminance longitudes by the local sun-crater configuration (solar elevation = 20°). The point at which $\alpha = \alpha_{max}$ (shown as point P in Figure 31) corresponds to the α of a flat ($\tau = 0°$) area of the same phase orientation (shown as level F) since the surface normal would then be tipped along a luminance longitude. Since no scan was made along a diameter or in the phase plane, the point at which $\tau = 0°$ in the scan plane characterizes a slope perpendicular to this plane and is proportional to the cosine of the angle between scan and phase plane. For example, a maximum slope of 22° could be achieved in this model ($\tau = 19°$ in scan plane) corresponding to $\alpha = -15°$, and a minimum slope of 10° ($\tau = 0°$ in scan plane) occurs for $\alpha = \pm 1.5°$ ($\alpha_{max} = +2.7°$).

A second scan of this crater (crater 1) was made between a different set of elevation points. Scans were also made on two nearby, smaller craters (crater 2 and 3). Figure 32 shows the area of the LOP picture containing craters 1, 2 and 3.

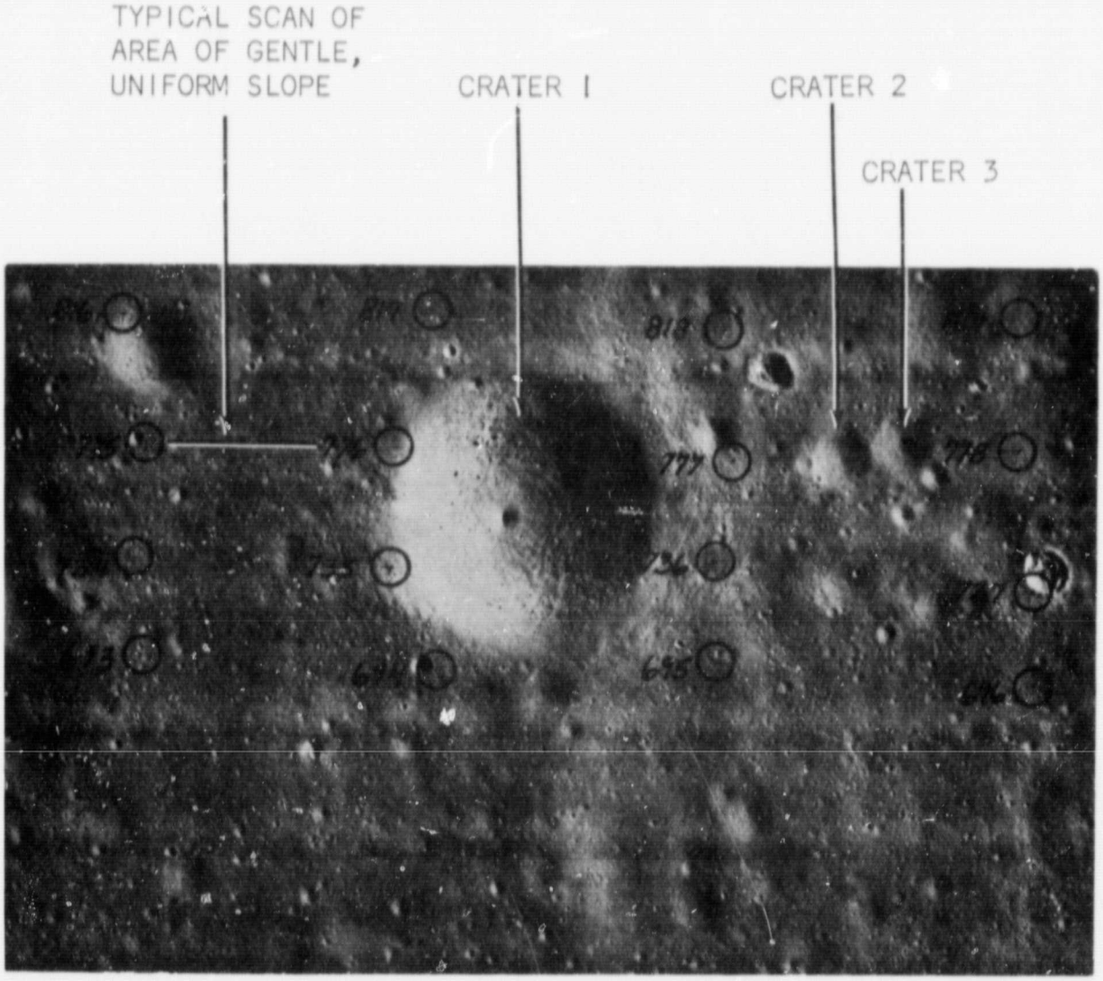

FIGURE 32. PORTION OF LUNAR ORBITER III FRAME 188 THAT WAS USED IN PHOTOMETRIC FUNCTION WORK. NUMBERS AND CIRCLES ARE ELEVATION DATA POINTS SUPPLIED BY NASA

12. Error Analysis of Flat Area Measurements

Errors in the photometric properties of the areas between known elevation points are caused by inaccuracies in the computed slope, the noise caused by small terrain irregularities, the calibration of microdensitometer voltage with spacecraft exposures, and the estimates of the normal albedo.

An estimate of the error in slopes based upon uncertainties in the elevation determinations was developed above. Assuming no correlation between the estimated heights provided by NASA for each site, columns 7 and 8 of Table X relate the slopes and predicted slope error. This uncertainty is then reflected in the error $\Delta\alpha$ in luminance longitude, column 9. Errors in the computation of α and phase angle, g, are assumed negligible in view of the accuracy of the specified surface X-Y coordinate system, also provided by NASA, and the data presented in the post-mission photo supporting data.

The uncertainty in ϕ (relative intensity) is a result of the exposure fluctuation (terrain noise, film phosphor noise, etc.), calibration errors, and albedo discrepancy. Table X suggests an rms scatter of 5% or $\Delta\phi = 0.005$ for flat areas. Calibration errors include the sum of the sensitometry error in determining exposures for the edge print data (5%), curve fitting discrepancies (3%), and microdensitometry variability (7%). These give a total calibration uncertainty of 9% when combined as random errors.

Because of the relation of ϕ to ρ expressed by Equation 1, the higher albedo value derived from the 80mm camera sampling areas tends to reduce ϕ by 15% in comparison with measurements of ϕ from Surveyor I. However, extrapolation from Surveyor data by use of a known curve of the photometric function (Fedoretz or Hapke) is subject to the inaccuracy of these curves. It is felt that the Surveyor value for ρ (7.2% $\pm$0.7, 1-sigma) falls within the estimated error of calculated albedo, $\rho = 8.0\%$.

TABLE X

PHOTOMETRIC FUNCTION FROM LUNAR ORBITER III PHOTOGRAPHS
From areas of small, uniform slope

Frame	Framelet	Average Relative Luminance $\bar{\phi}$	RMS	g	α	τ (scan plane)	Error in Slope Δτ	Error in Luminance Longitude Δα
187	351	0.089	0.004	66.9°	+5.0°	0.1°	±8.2°	5.1°
187	359	0.097	0.007	67.1°	4.6°	0.1°	9.2°	6.4°
187	362	0.098	0.007	65.7°	5.7°	0.4°	7.4°	5.1°
188	503	0.091	0.006	69.0°	2.3°	0.0°	8.3°	5.7°
188	479	0.115	0.015	69.5°	2.1°	0.3°	8.8°	6.1°
188	479	0.088	0.0007	67.7°	3.1°	1.2°	9.5°	6.6°

The Surveyor value may be used subject to the degree of similarity between LOP Frames 190 and 188. These areas are believed to have identical photometric properties based on our subjective evaluation.

In summary, assuming the mutual independence of these errors, the total error in ϕ is estimated at ±14.3%.

13. Error Analysis of Spherical Crater Model

In addition to possible errors in slope, albedo, and microdensitometry, the usefulness of the spherical model is dependent upon the accuracy of measurement of the diameter and length of shadows in the phase plane, the degree to which craters resemble a section of a sphere, and the assumption that the photometric properties of craters are the same as those for flat areas.

The uncertainty in α is subject to the accuracy of the determination of crater slope which in turn is dependent upon geometrical measurement and applicability of the spherical model. Figure 33 shows the effect of estimating D/d to be 7.5 in measuring the diameter and shadow length of the crater for the first spherical model (Crater 1), believed to have a diameter/depth ratio (D/d) of 8. The corresponding error in α, proportional to the cosine of the angle between the direction of slope and the phase plane, is largest just inside the rounded crater rim where $\Delta\alpha = 3.5°$.

Figure 34 compares idealized and actual intensity profiles revealing evidence of edge rounding in Crater 1 and indicates the position of maximum α.

One is tempted to use intensity profiles of craters to determine D/d with knowledge of the photometric function, especially in the case of shallow craters. The effect of changing D/d will affect the

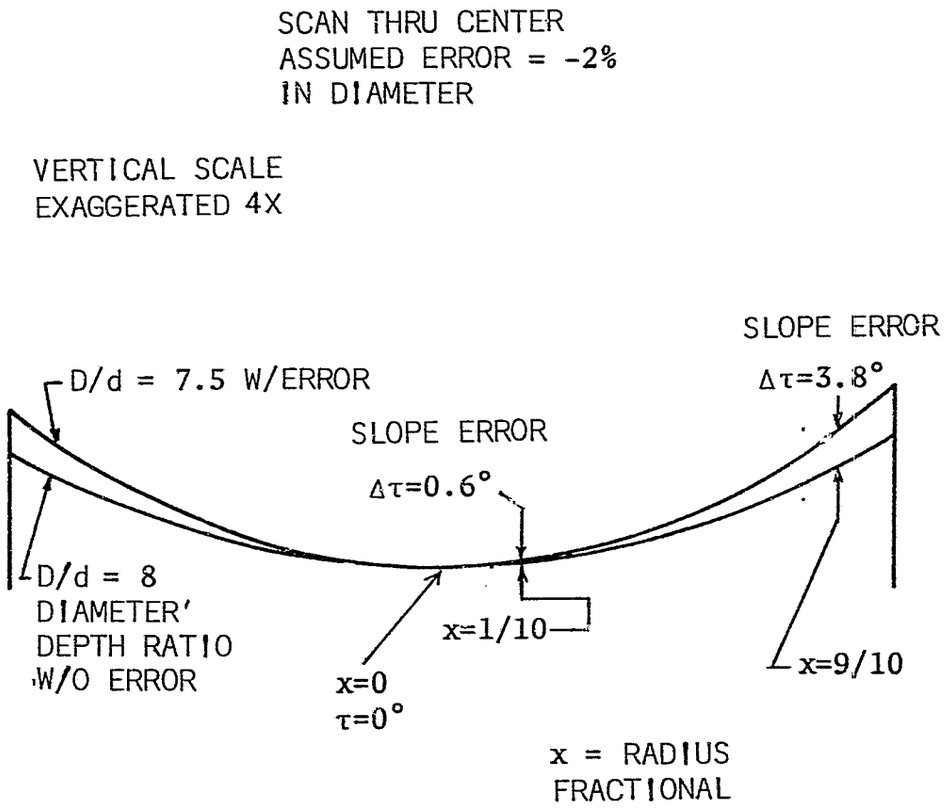

A. PROFILES OF CRATER 1 WITH AND WITHOUT ASSUMED ERROR

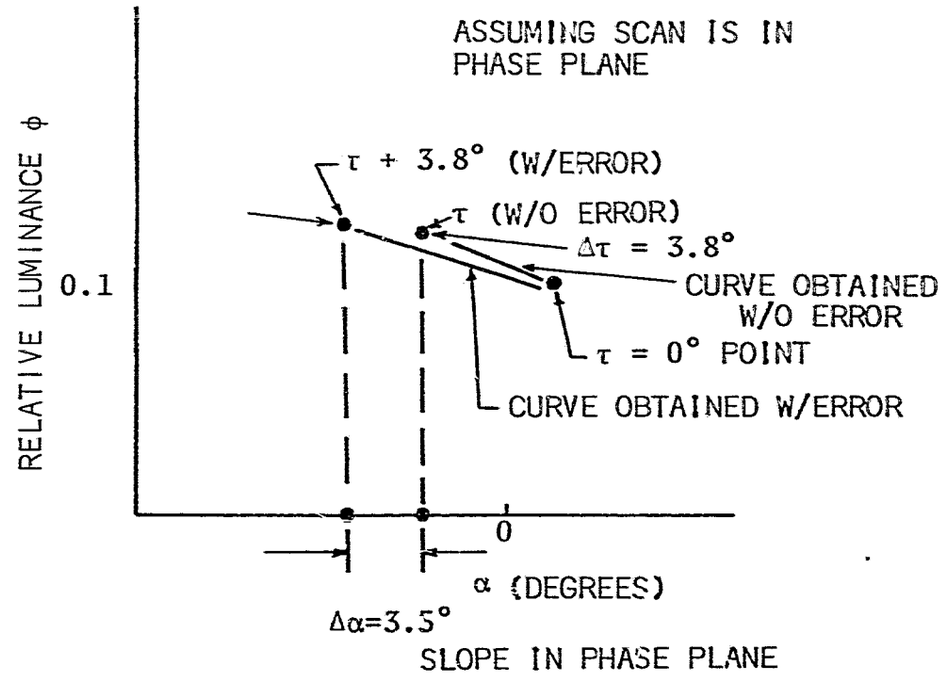

B. EFFECTS ON INTENSITY FUNCTION (ϕ VS α) DUE TO ERRORS IN MEASUREMENT OF CRATER PROFILE

FIGURE 33. EFFECTS OF D/d BEING 7.5 INSTEAD OF 8.0 IN MEASUREMENT OF THE SPHERICAL CRATER MODEL

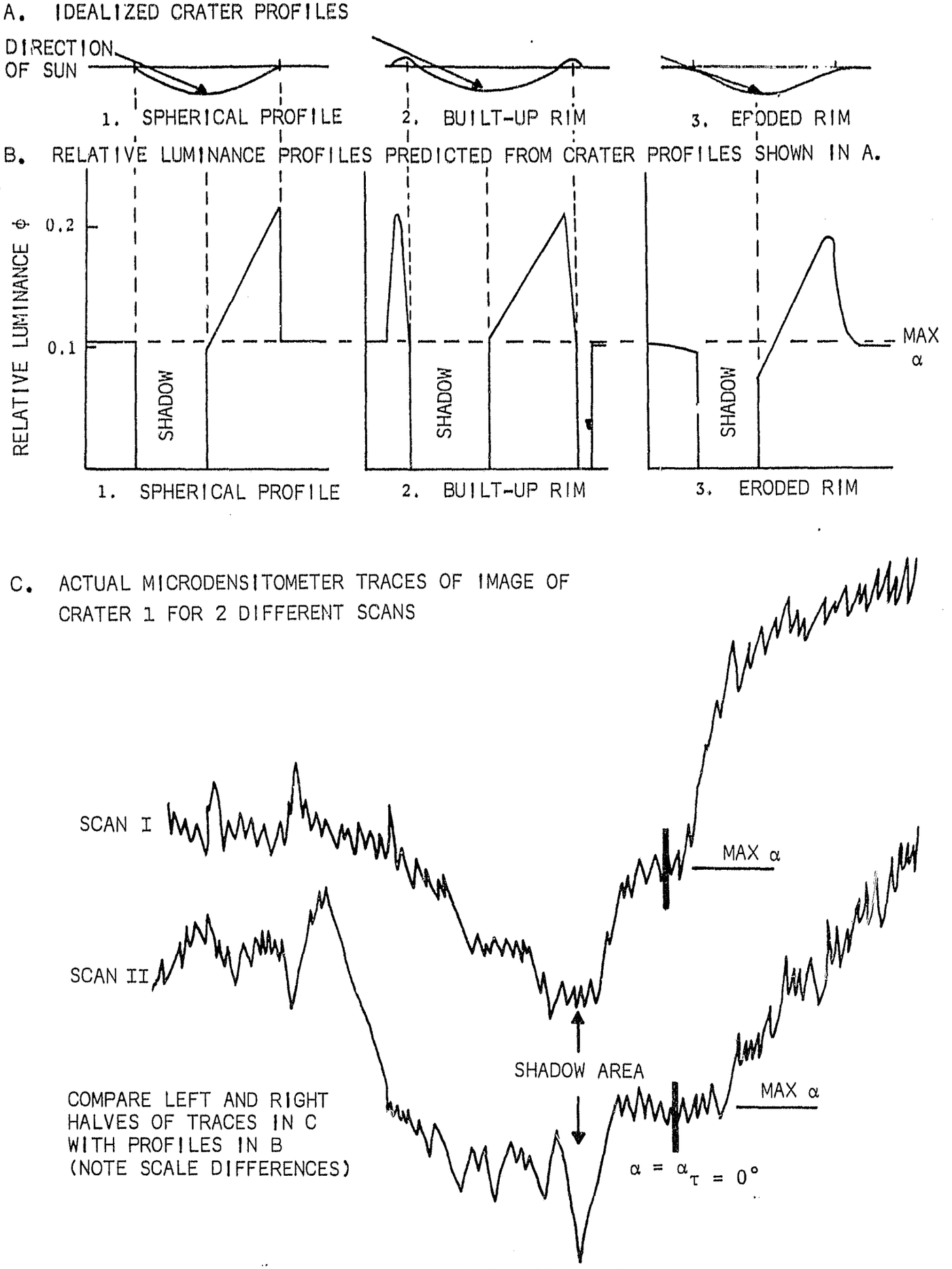

FIGURE 34. CRATER INTENSITY PROFILES

intensity function. For example, two additional craters (Craters 2 and 3) chosen for application of the spherical model technique, although well defined, do not present a shadow area, thus indicating a maximum slope of less than the sun elevation of 20°. In spite of the lack of shadow, the maximum may be found from the intensity profile (related to the central point of a scan, $\tau = 0°$ in scan plane, by the cosine of the angle between the scan and phase planes), and hence the intensity function may be compared with the lunar photometric function for the proper range of α. Changing D/d changes the slope and width of the intensity function curve because of the increased range in τ as shown in Figure 35. The intensity functions are shown for a given intensity profile for three different crater geometries. One crater profile has a diameter/depth ratio (D/d) of 7(shown in Figure 35A); this diameter/depth ratio combined with the known intensity profile gives an intensity function shown in Figure 35B, for albedo (ρ) of 0.07. Similarly, profiles are illustrated in Figure 35A for a crater of D/d=10 and for D/d= 7 with eccentricity of 0.3 (an elliptical model); their corresponding intensity functions are shown in Figure 35B and 35C for ρ of 0.07. Figure 35D shows that the intensity function for the crater with a profile having D/d of 7 can be force-fitted to the Hapke photometric function curve when ρ of 0.065 is assumed. However, the uncertainty in the photometric function and the fact that data are taken out of the phase plane prohibit an attempt to determine D/d by forcing a crater profile to fit the theoretical curve.

It is estimated that the total error in α in the measurement of Crater 1 (a possible variance in curvature of $7.5<D/d<8.5$) was less than 4°. In shallow Craters 2 and 3 the error was less. However, for an elliptical crater of the same diameter as Crater 1 but 20% deeper, a maximum difference in slope of 7° between elliptical and spherical craters occurs near the rim of the crater. In both cases the minimum error is found at $\tau = 0°$; hence, comparison with the flat area intensities and the photometric function at this point is subject to the least

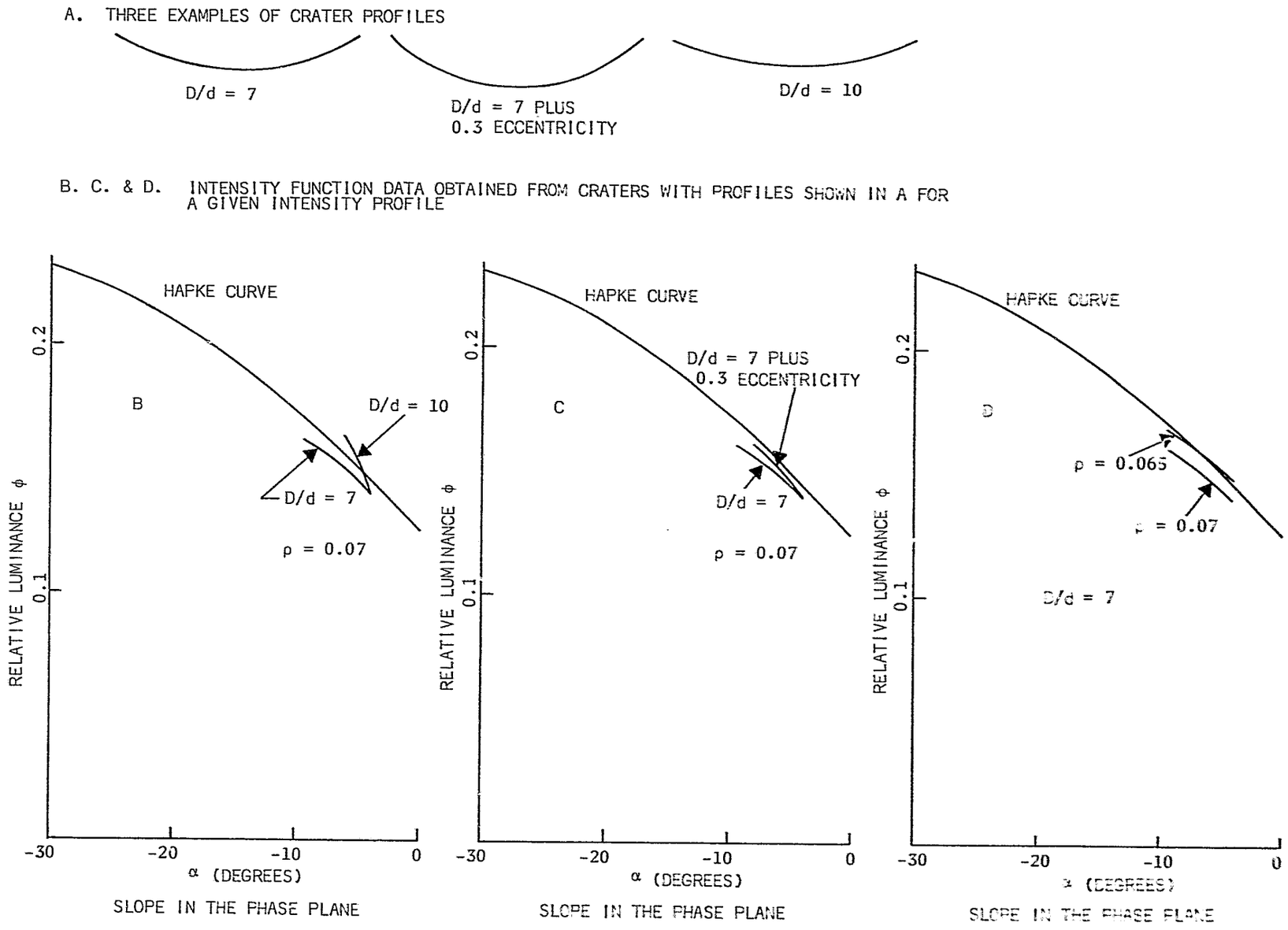

EFFECTS OF CHANGES IN CRATER SHAPE ON THE INTENSITY FUNCTION

FIGURE 35. EFFECTS OF CHANGES IN CRATER SHAPE ON THE INTENSITY FUNCTION

discrepancy. The total error in slope computation is 12° calculated from the rms sum of the maximum measurement errors (4°), a possible ellipticity ($\leq 7°$), and the estimated error in surface elevation (8°).

The photometric properties of craters are discussed in subsection 15.

The corresponding ϕ error values are derived from an rms noise of 6% (from paragraph 3, part 12 of this subsection) which together with the calibration (9%) (from paragraph 3, part 12 of this subsection) and albedo (10%) (from part 8 of this subsection) error analysis produces an error of ±14.7% in ϕ.

14. Computer Program

A computer program, LODAP, was developed for converting densities on the GRE film to exposure at the spacecraft. These values of E were converted to reflected intensities ϕ by Equation 1:

$$\phi = \frac{E\ 4N^2}{10.76\ I\ Tt\ \rho}$$

where N = f-number

T = lens transmittance

t = shutter speed, sec.

ρ = average normal albedo taken from Surveyor data and adjusted from 80mm LOP photographs

I = incident illuminance, ft. candles.

The computer program converts output voltage from the microdensitometer to relative luminosity using an estimate of normal albedo. This luminosity is compared with intensities predicted by Hapke's theoretical model. The methods for determining appropriate luminance longitude, α, and phase angle, g, for both flat areas and craters fitted to spherical models were described in parts 10 and 11 of this Subsection D.

For areas having uniform, gentle slope, LODAP uses the microdensitometer voltages from the tracing on the 24-inch photographs. For each scan, an average voltage V is calculated and the data are all truncated to values within ±5% of the average value for the scan. Each V is converted to exposure E using a third order polynominal describing the calibration of the densitometer (a combination of the voltage-density calibration of the instrument and the density-exposure relation obtained from tracing the edge print for the specific framelet). Each E is converted to relative luminosity factor ϕ:

$$\phi = k\ E/\rho \qquad \text{Equation 23}$$

where k is a constant (0.0328) derived from the camera characteristics and illumance information and ρ is the local albedo. The value of ρ is calculated for LODAP I from a combination of Surveyor information and observations on the accompanying 80mm photograph. For LODAP II the value of ρ is obtained directly from Surveyor. The program then computes an average ϕ for all the data.

A value of g is computed by Equation 21 for the midpoint of the scan and a value of α is computed by Equation 20 from the elevation data for the endpoints. Inputs for these calculations include γ_s from post-mission data and ΔX, ΔY from end-point elevation differences. The value of γ_c is calculated by:

$$\gamma_c = \tan^{-1}[d_N/(R_s - H)] + \tan^{-1}(d_N/H) \qquad \text{Equation 24}$$

where d_N is the length of the straight line between the elevation points, R_s is the distance of Lunar Orbiter from the center of the moon, and H is the height of Lunar Orbiter above the lunar surface. $\phi_c = 180 - \tan^{-1} \Delta Y/\Delta X$.

Values are calculated for the direction cosines $(\lambda, \mu, \nu) = f(\phi_c, \gamma_c, \gamma_s, g)$ used in Equation 20.

For comparison with the results obtained for ϕ by measurements, relative luminosity factors are calculated by Hapke's modified theoretical function:

$$\phi(g,\alpha) = \angle(\alpha, g)\ \Sigma\ (g)\ B(g) \qquad \text{Equation 25}$$

where $\angle(\alpha,g)$ is the Lommel Seeliger Function, Σ (g) is the average angular scattering function of a single particle of lunar soil and B(g) is the retrodirective function. ϕ is calculated for a range of g (50° to 80°) for the appropriate α and plotted as the photometric function.

LODAP performs additional operations for density measurements on craters. An input to the program is the spherical radius of the crater obtained by measurement of the diameter of the crater and the length of the shadow in the incidence plane after allowance for the penumbra. New x, y coordinates are established with the origin at the center of the crater. The location of the crater center and the point at which the scan crosses the crater rim are given in these coordinates. Values of ϕ are obtained for each point along the scan at 1 meter intervals; value for α and τ are also calculated.

LODAP is a program having limited capability. It requires that constants derived from the geometry of the photograph be provided as inputs. The program must analyze three craters and three slopes simultaneously (or these data must be represented by dummy information).

15. Results

Table XI and Figures 36 and 37 show the values of the relative luminosity factor measured from Lunar Orbiter photographs. The value of ϕ in Table XI for each crater is for a point within the crater along the wall where the projection of the slope in the phase plane is zero - this point is not the center of the crater (the traces were not made through

TABLE XI

PHOTOMETRIC FUNCTION FROM LUNAR ORBITER III PHOTOGRAPHS FOR FLAT AREAS

Frame	Framelet	Average Relative Luminance ϕ	RMS	$\Delta\phi$ From Hapke's Values	g	α	τ (scan plane)	Error in Slope $\Delta\tau$	$\Delta\alpha$
187	351	0.089	0.004	+0.01	66.9°	+5.0°	0.1°	±8.2°	5.1°
187	359	0.097	0.007	+0.015	67.1°	4.6°	0.1°	9.2°	6.4°
188	480 Cr 1	*0.110	0.012	+0.02	68.3°	2.8°	0.0°	7.3°	5.1°
187	362	0.098	0.007	+0.025	65.7	5.7°	0.4°	7.4°	5.1°
188	503	0.091	0.006	+0.001	69.0°	2.3°	0.0°	8.3°	5.7°
188	479	0.115	0.015	+0.025	69.5°	2.1°	0.3°	8.8°	6.1°
188	479 Cr 2	*0.105	0.009	+0.015	68.9°	2.0°	0.0°	7.4°	5.1°
188	479	0.088	0.0007	-0.002	67.7°	3.1°	1.2°	9.5°	6.6°
188	479 Cr 3	*0.12	0.006	+0.03	68.9°	2.0°	0.0°	7.4°	5.1°
188	479 Cr 1	*0.11	0.012	+0.02	68.3°	2.8°	0.0°	7.7°	5.3°

*The value for the point on the crater wall where the projection of the slope in the phase plane is zero.

Average value for ϕ for craters = .111

Average value for ϕ for flat areas =.096

Difference .015

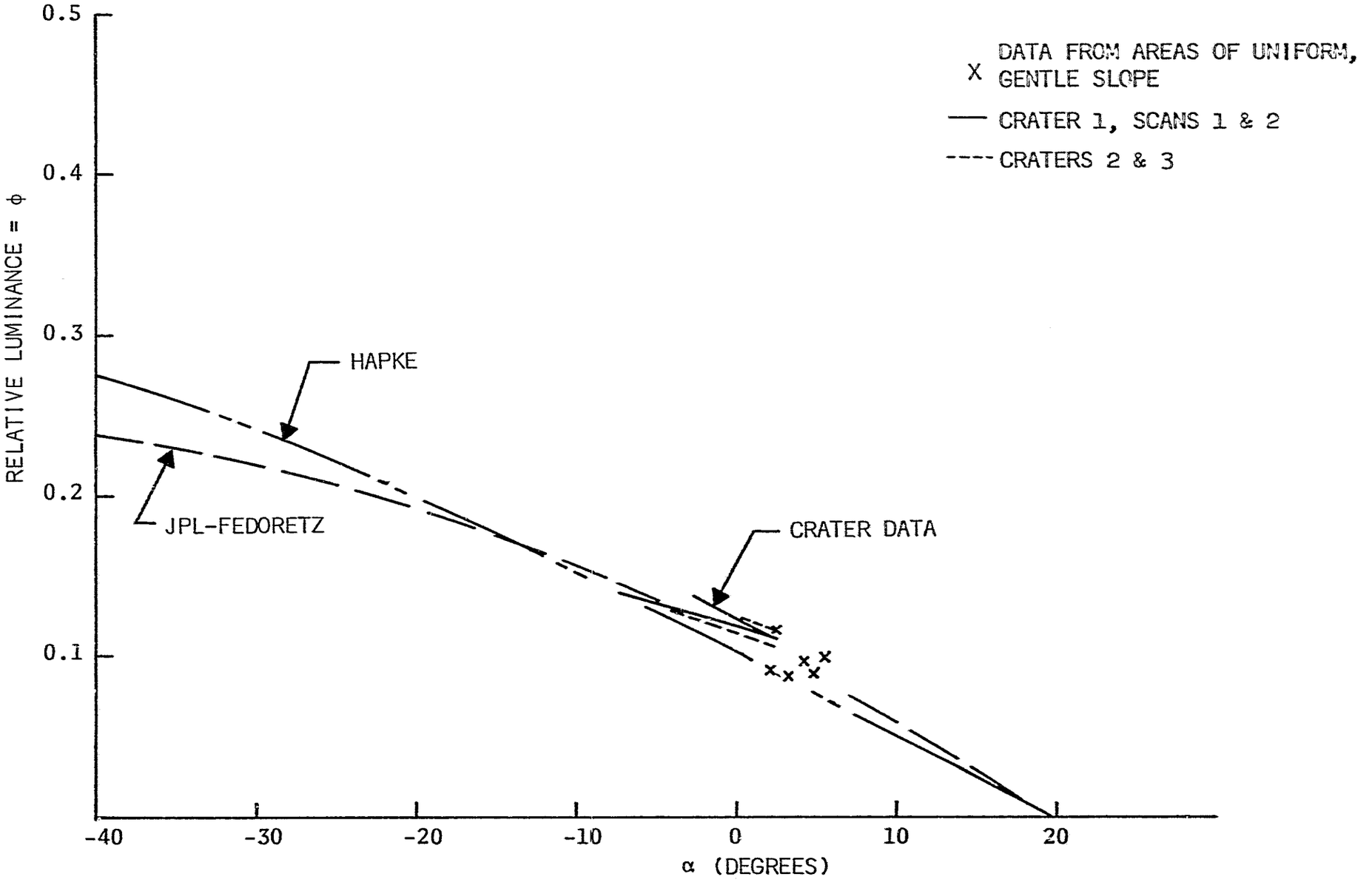

001

FIGURE 36. RELATIVE LUMINANCE VS SLOPE ANGLE
COMPARISON OF ALL DATA FROM LOP WITH HAPKE AND JPL DATA

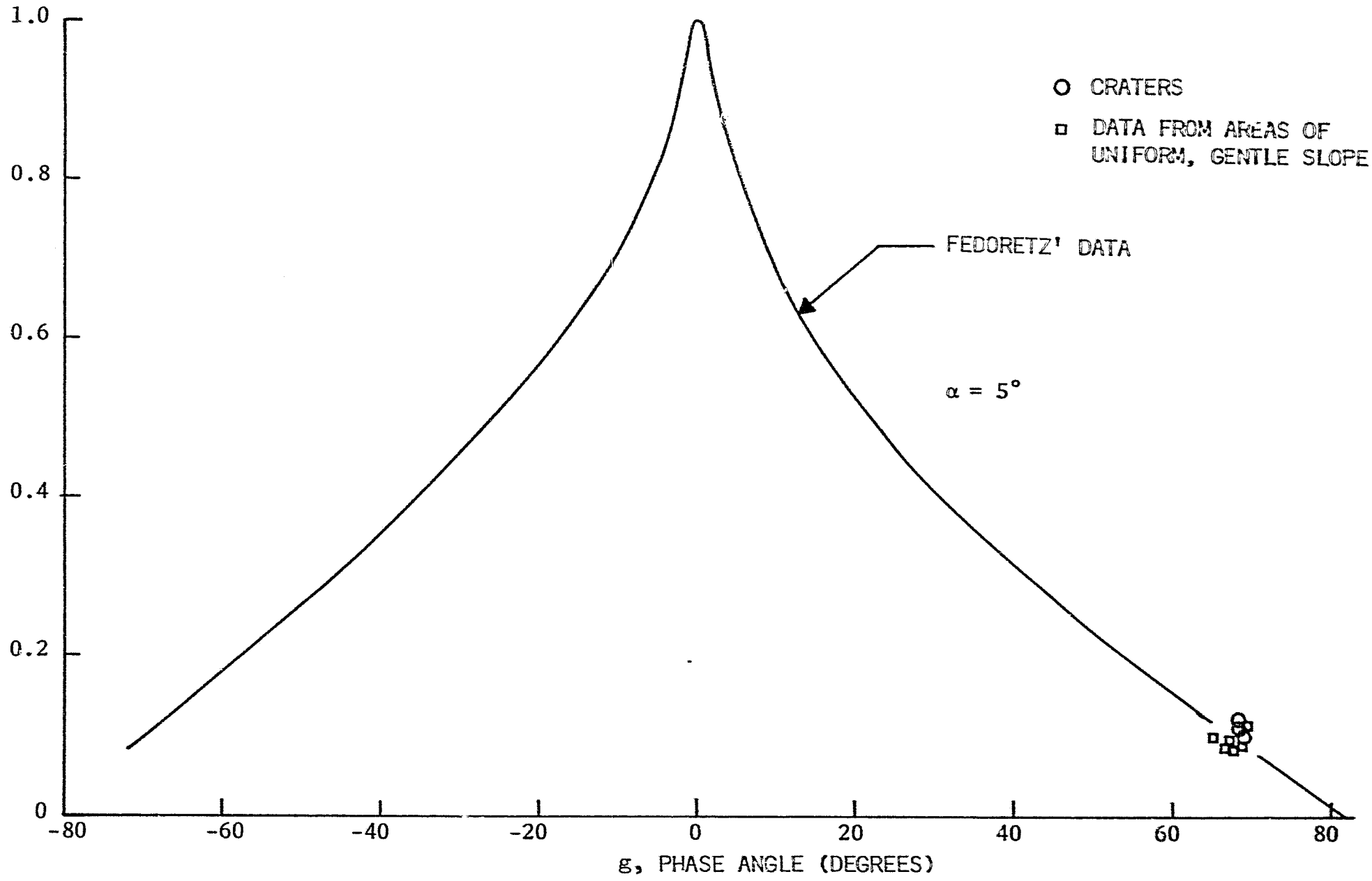

FIGURE 37. ϕ CALCULATED FROM LOP DATA VS FEDORETZ' DATA

the center). These values of ϕ provide an opportunity to check the difference between the albedo within a crater and the albedo outside of craters. The difference of 0.015 in ϕ's confirms the widely held observation that the albedo of craters is higher than for flat areas. From Equation 23 and knowledge of the average E's (0.20 for areas of uniform, gentle slope and 0.35 for craters), the albedo for craters found in the maria is calculated to be about 30% higher than the albedo for the maria.

The difference between the newly measured ϕ's and ϕ's calculated by Hapke's modified theoretical function are shown in column 5 of Table XI. The new ϕ's average about 15% higher than Hapke's ϕ's.

The ϕ's obtained by scanning craters and areas of uniform, gentle slope are shown in Figures 36 and 37. Figure 36 shows the Hapke function and JPL fit to Fedoretz data for reference; Figure 37 shows the Fedoretz data only for reference and illustrates the limited amount of information gained by analysis of Lunar Orbiter photography of a specific area under only one set of conditions.

16. Error Analysis of Results

The error estimates developed in parts 12 and 13 of this subsection are shown as error bounds on the new data in Figure 38. For clarity only the data for Crater #1 are shown. The data agree remarkably well with that from JPL and Hapke in view of the scatter in the data used to derive the JPL curve-fit to Fedoretz' data and the applicability of the Hapke theoretical model requiring 45° sloped craters covering 90% of the moon. Both Hapke's work and the JPL curves, however, are based on Fedoretz' observations. Hapke, while deriving a photometric function for a surface of specific physical structure, nevertheless, includes sufficient parameters (compaction, slopes) to enable a fit to Fedoretz data. As the curve shape (ϕ vs g) is not affected, this is equivalent to assuming a similar normal albedo, i.e., maria. Surveyor

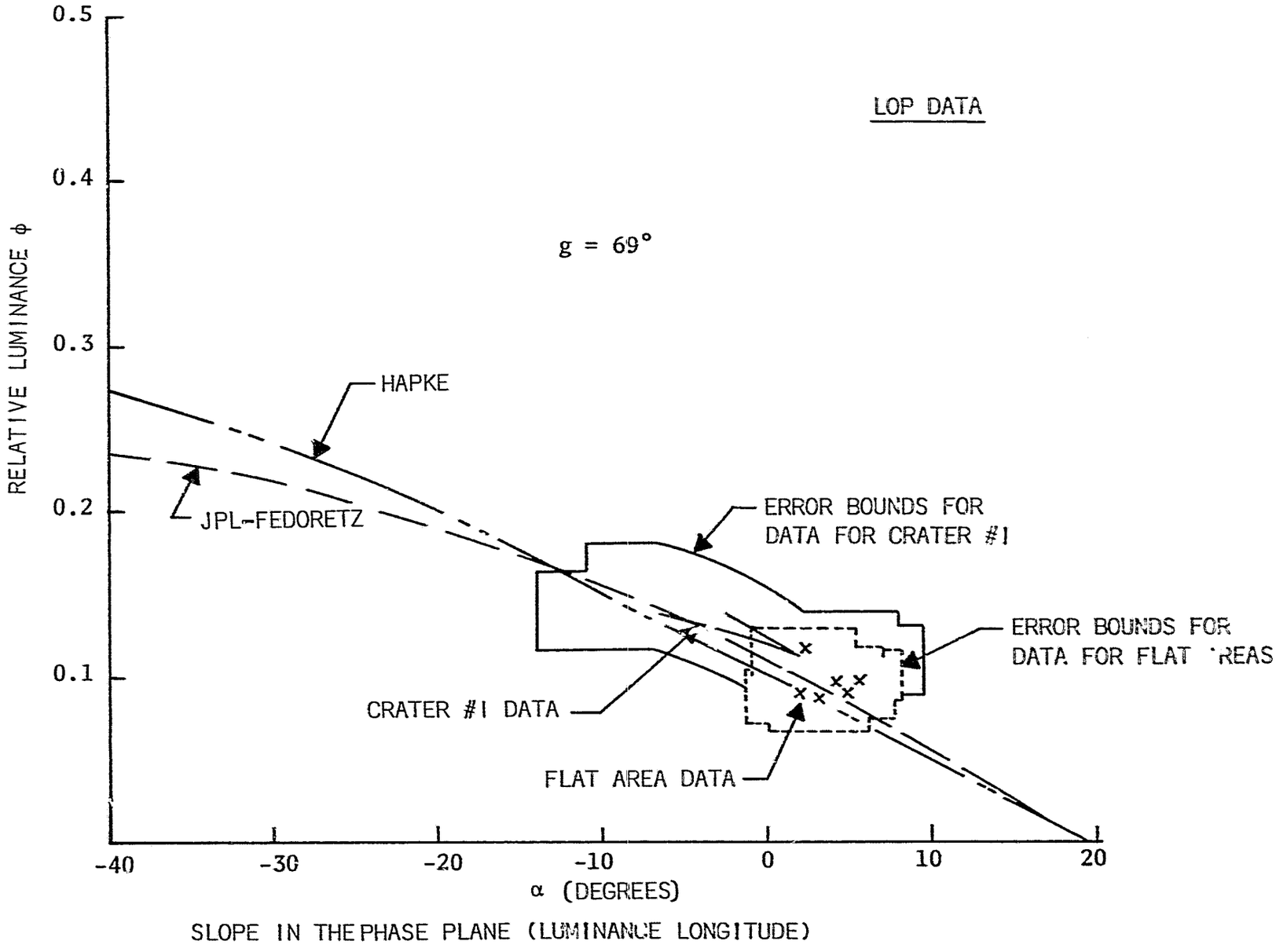

FIGURE 38. ERROR BOUNDS ON PHOTOMETRIC DATA FROM LOP PICTURES

data as presented in published literature, presents luminance values which must be extrapolated along some photometric curve to zero phase to obtain a normal albedo. Thus the uncertainty in estimating a normal albedo is still subject to the errors of terrestrial observation. It is therefore appropriate to choose a consistent normal albedo for comparison of relative intensities and their changes with phase angle with a predicted curve.

The significance of this evaluation lies primarily in the reduction of uncertainties evidenced in earlier work and in determining the shape of the photometric function. Variations found at this g and α have produced as much as 15 and 20 percent error respectively, in previous attempts to fit curves to relative and absolute earth-based lunar photometry.

The apparent consistency of results (small data scatter) is due in part to improved precision caused by the proximity of the observational instrument, the large phase angle, and the low sun elevation. The close agreement with previous work also shows the advantageous illumination geometry of earlier terrestrial observations. The major achievement of this analysis was to gain ϕ values with higher confidence in the range of Orbiter's limited phase data.

17. Conclusions and Recommendations

Lunar Orbiter photographs offer a unique opportunity to refine the measurements of the photometric function, to produce values with increased confidence for a wide variety of topographic features and to examine the effects of scale.

More work is needed to unify the results obtained from the four points of observation - Earth, Surveyor, Ranger and Orbiter.

Measurements should be made on Lunar Orbiter photographs to extend knowledge of the distribution of crater sizes and shapes and to relate this information to scene luminosity.

E. Parametric Study of Lunar Photography

1. Summary

A graphical chart was developed as a guide to making estimates of exposure requirements in lunar orbital photography after realistic limitations were set on the range of sun elevation, lunar topography and viewing geometry. The chart shows the parameters for optimum photography for several color and black and white films. Dynamic resolving power can be estimated from the chart.

2. Introduction

The requirements for exposure and latitude can be extreme for photographic films used in lunar photography if all possible combinations of conditions are taken into account. The albedo of the moon ranges from 6% to 18%, and the photometric function shows that the relative luminance for a given subject can vary over an infinite range of values from 0 to 1, depending on the geometry of viewing and illumination. For a scene with a large range of surface slopes and with no restrictions on position of photography, the range of brightness exceeds the exposure latitude of photographic films, and the requirements for exposure are set by the individual parts of the scene.

However, if realistic limitations are placed on the geometry of illumination and viewing, estimates of the required exposure and latitude of photographic films are readily made. These restrictions can be based on the need to achieve optimum photography of lunar scenes of interest. Although these calculations were made for orbital photography,

the method of analysis is valid for estimating proper exposure for pictures taken from the lunar surface.

3. Choice of Lunar Scenes

Slopes of about ±15 degrees are to be expected over most of the surface of the moon.[19] This range does not include the slopes of crater walls, but only the general lunar terrain.

The elevation of the sun is restricted to the range between 20° and 30° for optimum visibility of details. Long shadows are cast at lower sun elevations causing obscuration of details, while at higher sun elevations, the difference in brightness becomes subtle for areas having small differences in slope, and the scene acquires a "washed out" appearance. From Figure 18, the range in scene luminance is from 2 to 4 for these limits of sun elevation and slope in vertical photographs.

4. Choice of Lenses and Shutters

The range in focal lengths of lenses used for lunar photography must include realistic possibilities for hand-held cameras carried by astronauts and spacecraft-mounted units. A range from 50mm to 50 inches should be adequate to cover most potential cases. F-numbers for such lenses could vary from 2 to 8, and will most likely be about 5.6.

Shutter speeds will range from 0.1 second to 0.001 second. In most cases, the shortest possible shutter speed will be used to reduce degradation from image motion.

5. Exposure Criterion for Lunar Scenes

Because the moon has no atmosphere to scatter light and provide fill-in illumination, lunar shadows are very dark. In terrestrial aerial photography, exposure is usually set to place the shadows, which have some finite brightness, at the toe of the sensitometric curve.

For lunar photography, a realistic criterion for exposure is that which places the mid-scene luminance at the mid-point of the linear portion of the sensitometric curve.

6. Graphical Chart for Prediction of Lunar Exposure

Certain parameters involved in lunar photography can be regarded as constant. If the others vary over established ranges, a graphical chart can be constructed for use in estimating exposure and latitude requirements.

Using Equation 1, the exposure E is calculated from knowledge of the photometric function $[\phi(g,\alpha)]$, characteristics of the photographic system (N, T, t), the normal surface albedo (ρ) and the illuminance (I).

$$E = \frac{10.76\ I\rho\ Tt\phi}{4N^2}$$

N = lens f-number

t = exposure time, secs.

The illuminance is about 12,000 foot-candles. A value of 0.07 is realistic for the albedo; the range of 0.06 to 0.18 covers the extremes whereas the value of 0.07 is representative of lunar maria. A value of 0.9 is typical for the transmittance (T) of a photographic lens.

The chart shown in Figure 39 is constructed by examining the variation in exposure available to the film from changes in the remaining variables (t, ϕ and N) and relating it to the exposure required by specific films.

The films used in Figure 39 are candidates for lunar photography because of their speed, resolving power and latitude. Color films have been included.

The chart is read by starting from the log exposure scale in the upper right hand quadrant I of Figure 39 which shows the log E's corresponding to the midpoints of the linear portions of the respective characteristic curves.

Quadrant I is constructed by plotting the ϕt product required to give a specific E for various lens f-numbers. The ϕt product is an artifice with little physical significance.

Quadrant II in the upper left hand part of the chart is constructed by plotting the ϕt product versus t for various phase angles (g) for zero surface slope. This part of the chart assumes nadir photography of a horizontal (zero slope) plane on the lunar surface. This procedure can be justified by the fact that the films proposed have more than sufficient latitude to cover the 2 stop (0.6 log E) range in exposure expected from slopes of $\pm 15^{\circ}$ from horizontal. No allowances have been made for reciprocity law failure, which is low for each of these films over the expected range of exposure time.

Quadrant III in the lower left hand part of the chart relates lens focal length and smear for orbital photography at several altitudes. For a circular orbit around the moon the velocity of the spacecraft varies little with altitude at typical mission altitudes (a velocity change of 2% occurs in going from 80 n. mi. to 40 n. mi.) and is rounded

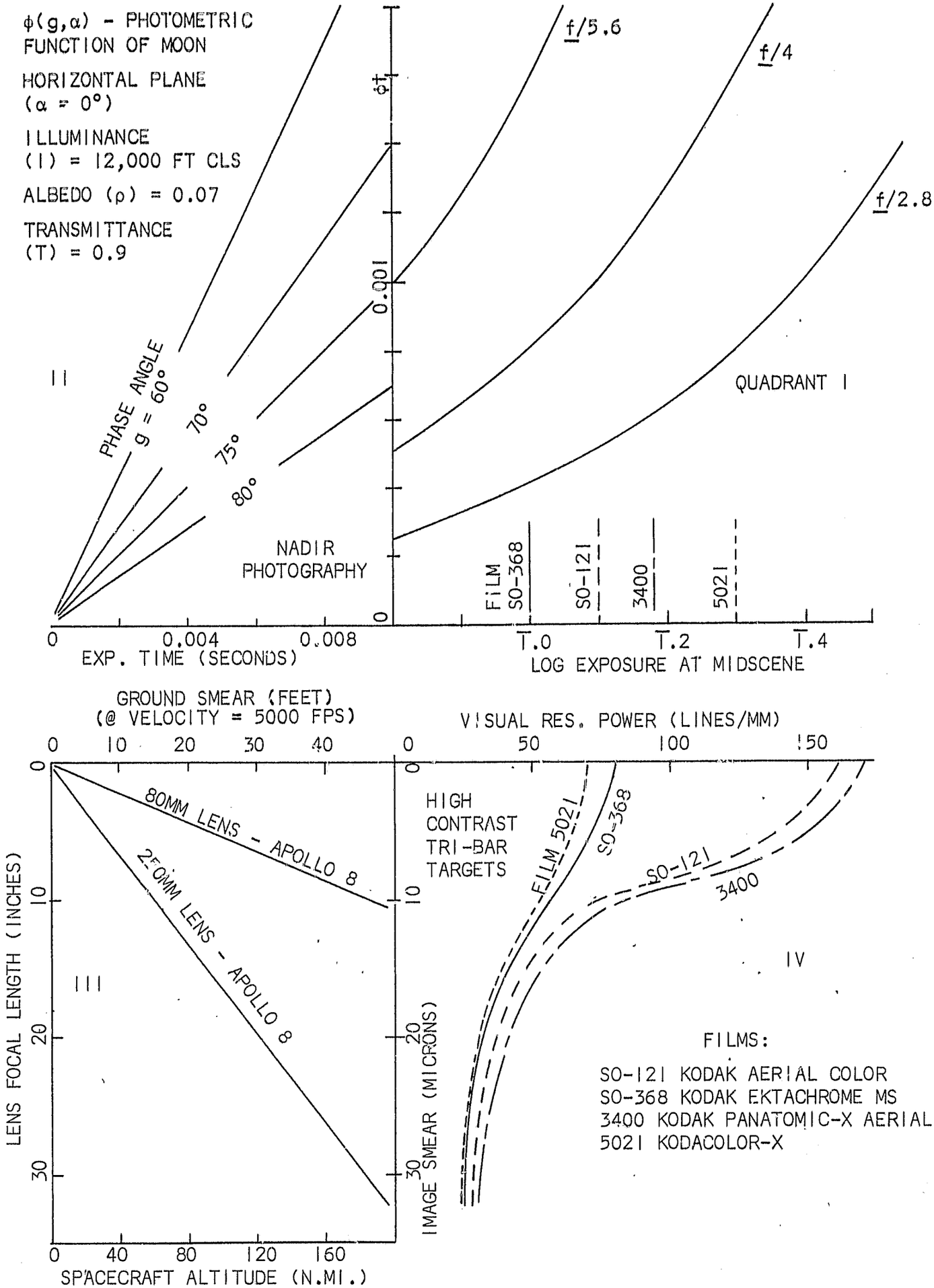

FIGURE 39. GRAPHICAL CHART FOR ESTIMATING LUNAR EXPOSURE REQUIREMENTS AND PERFORMANCE

off to 5000 feet/second for simplicity of calculation. This smear rate is assumed constant for all altitudes of interest (less than 120 n. mi.) and may be multiplied by the exposure time to get the image smear projected onto the lunar surface. The corresponding smear in the image depends on the photographic scale, the ratio of the lens focal length to the spacecraft altitude. The scales for focal length and altitude are also shown on the axes of quadrant III, for convenience in preparing a line of constant photographic scale. Two specific examples are shown, for lenses with 80mm and 250mm focal length on the Apollo 8 flight. Note that the scale of image smear is derived for a camera without IMC. The line of constant photographic scale for the 250mm lens at 60 nautical miles is the same for a lens of twice the focal length at twice the altitude.

Quadrant IV relates the image smear to the dynamic resolving power. This estimate of the visual resolving power for a tri-bar target is based on the static resolving power for a high contrast (1000:1) target. The prediction uses the relationship between static and dynamic resolving power given by D. Paris.[20] The ultimate film resolution is shown by the values of static resolving power in quadrant IV for zero image smear.

(The detection and identification of lunar subjects has been related to resolving power in Phase I work and was re-examined in Subsection III D of this report.)

7. Application

The chart in Figure 39 was developed to make estimates of exposure requirements and performance of photo-optical systems using specific films under limited, specific conditions.

Since the calculated performance is assumed to be mainly limited only by the resolution of the film, lenses of high relative aperture (low f-number) are shown on the chart. The lens transmittance is assumed to be 0.9.

The spacecraft is assumed to be in a circular orbit at an altitude between 40 and 120 nautical miles traveling over the lunar surface at 5000 fps. The predictions are for nadir photography, on axis. Changes in exposure are not shown for subjects recorded off-axis by wide-angle systems or for oblique photography.

The lunar surface is assumed to be a horizontal plane with an albedo of 0.07. The chart is designed for sun elevations of about 10° to 30°. The general slope of the lunar surface is not expected to exceed 15°, excluding crater walls. These conditions are assumed to establish the luminance in the mid-range of scene luminances.

The criterion used to set exposure matches mid-scene exposure to the exposure at the middle of the sensitometric curve. The latitude of each film is sufficient to cover the range in luminance experienced from changes in lunar slope and changes in sun elevation within the specified range. This criterion gives a starting point for setting exposure; this criterion should be refined for photography of specific subjects or areas of interest. In addition, the log exposure for the mid-point of the sensitometric curve should be established for the specific emulsion and process to be used.

The chart was prepared for representative film and processing information and is intended as a guide to further calculations. When any of these films is considered for lunar photographic applications, the user must establish the availability of the film, the availability of a specific process and the compatibility of the film with the equipment for processing and printing the film.

III. INFORMATION CONTENT OF LUNAR PHOTOGRAPHS

A. Introduction

This portion of the work examined four major areas of interest in lunar photography:

1. prediction of the ability to recognize detail in lunar photographs,
2. evaluation of performance of lunar photographic systems,
3. correlation between recognition of detail and system quality, and
4. optimum presentation and enhancement of lunar photographs.

Much of this work was an extension of the initial efforts of Phases I and II. The new effort used photographs from Lunar Orbiter rather than only laboratory simulations.

Two new techniques included in the study on maximizing detail recognition were rapid presentation of photographic sequences and ring smear enhancement.

B. Performance Prediction

1. Summary

A lunar modulation (LM) curve for predicting the threshold identification of lunar details was established from subjective data collected in Phase I. An attempt to demonstrate the validity of the LM curve using photographs of Lunar Model KLM 6-65 showed that the curve was not independent of phase angle. The influence of phase angle makes the LM curve unreliable for predicting threshold identification of lunar detail.

It was shown that a more reliable method of predicting threshold identification of lunar detail uses the tri-bar threshold modulation (TM) curve with MTF curves for optical systems to make a prediction unrelated to phase angle, followed by the application of Phase I data to modify the prediction for phase angle effects.

Although this study was carried out using only vertical photographs with small fields of view, the results of Phase I work indicate the technique is equally applicable to oblique photographs.[21]

2. Background

The threshold modulation (TM) curve of a photographic material describes the minimum modulation that the aerial image of a tri-bar at a particular frequency must have to be recorded successfully. Successful recording is achieved if the tri-bar pattern can be identified in the developed image.

A TM curve is obtained empirically by evaluation of photography in which the modulation of the aerial image is varied over a range of spatial frequencies presented to the film/process combination under test. Variations in modulation are obtained by changes in target contrast and f-numbers for a lens of known MTF's. The photographic images are evaluated subjectively for limiting resolving power at each condition.

Much is known, both theoretically and experimentally, about the transfer of the intensity distribution of a tri-bar through an optical system. From this theory one is able to predict with a reasonable degree of confidence the limiting tri-bar resolution of a photooptical system from the TM curve for the film-process combination and the modulation transfer function of an optical system.

Extending the TM concept to other targets can be done only on an empirical basis. The manner in which an optical system transfers an intensity distribution of a complex object is not known and therefore the manner in which the object will be recorded cannot be predicted. However, experience with aerial photographs has shown that some correlation exists between information in the picture and the pitch of 2:1 contrast tri-bars at limiting resolution.

Since we have less experience with lunar photography than terrestrial photography, no correlation has been found between tri-bar resolution and the photographic recording of lunar objects of various shapes. On the Lunar Orbiter Program some correlation was found between tri-bar resolution and the resolution of right circular cones. The final report[22] of Lunar Photo Study Contract NAS 9-3826 Phase I provides the best source of information relating tri-bar resolution and the diameter of the smallest lunar detail identifiable under various lighting conditions. These results are shown in Figure 40.

These data have been used in an attempt to extend the TM concept to the identification of lunar detail, calling the resulting curve a lunar modulation (LM) curve to distinguish between the application of TM to tri-bar subjects and LM to lunar-like subjects.

3. Development of the LM Curve

The objective of developing an LM curve is to establish a technique for predicting the identification of lunar details for any optical system. The results presented in Figure 40 are a function of three variables, phase angle, film MTF and lens MTF. To create a general curve, the effect of the lens and phase angle must be removed from the data.

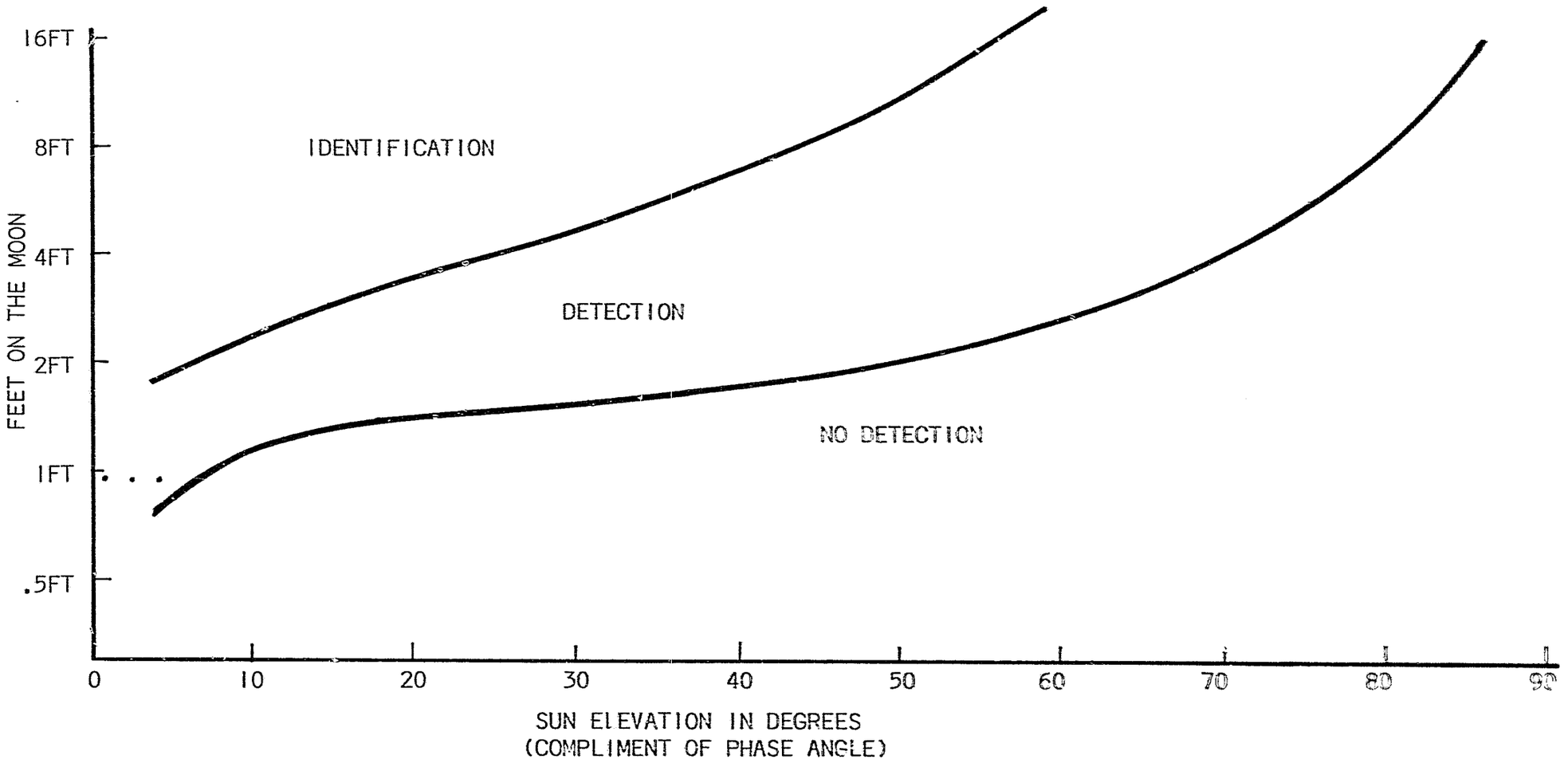

.... INDICATES PITCH OF LIMITING TRIBAR FOR A 220 LINE PER MILLIMETER PHOTO SYSTEM

SO-243 FILM D-19 PROCESS LIMITING RESOLUTION = 220 LINES/MM

FIGURE 40. READER RESPONSE FOR VERTICAL MONOSCOPIC PHOTOGRAPHY OF GEOMETRIC SHAPES

With this goal in mind an LM curve was generated by expressing the identification curve of Figure 40 in terms of new variables, frequency and modulation. This change was carried out point by point by first converting the diameters of object-space details identified to pitch of image-space tri-bar patterns using the relationship:

$$\text{Image Pitch} = \frac{\text{Object Diameter}}{\text{Scale Factor}} \qquad \text{Equation 26}$$

and converting this pitch to frequency for the new abscissa:

$$\text{Frequency} = \frac{1}{\text{Pitch}} \qquad \text{Equation 27}$$

Then, the lens effect was removed by dividing the corresponding phase angle by the modulation transfer function of the lens for the specific frequency to get values along the new ordinate. This operation leaves the LM curve in Figure 41 a function of film and phase angle, where the quotient (phase angle divided by lens MTF) was plotted against frequency. The values were arbitrarily multiplied by 1000 to get familiar-looking values. The ordinate units (degrees/modulation) are meaningless. The LM curve still has the phase angle effect, to be removed when the curve is applied to a specific set of conditions.

4. Experimental Test of the LM Curve

Because this work has no theoretical basis, its validity could be established only empirically.

The experimental test of the LM curve was carried out by analyzing photographs of Lunar Model KLM 6-65. Two different optical systems, one capable of a resolving power of 30 lines/mm and the other of 120 lines/mm, were used to take photographs at a scale of 1:30,000, using SO-243 film processed in D-19. Phase angles of 80°, 60°, and 45°

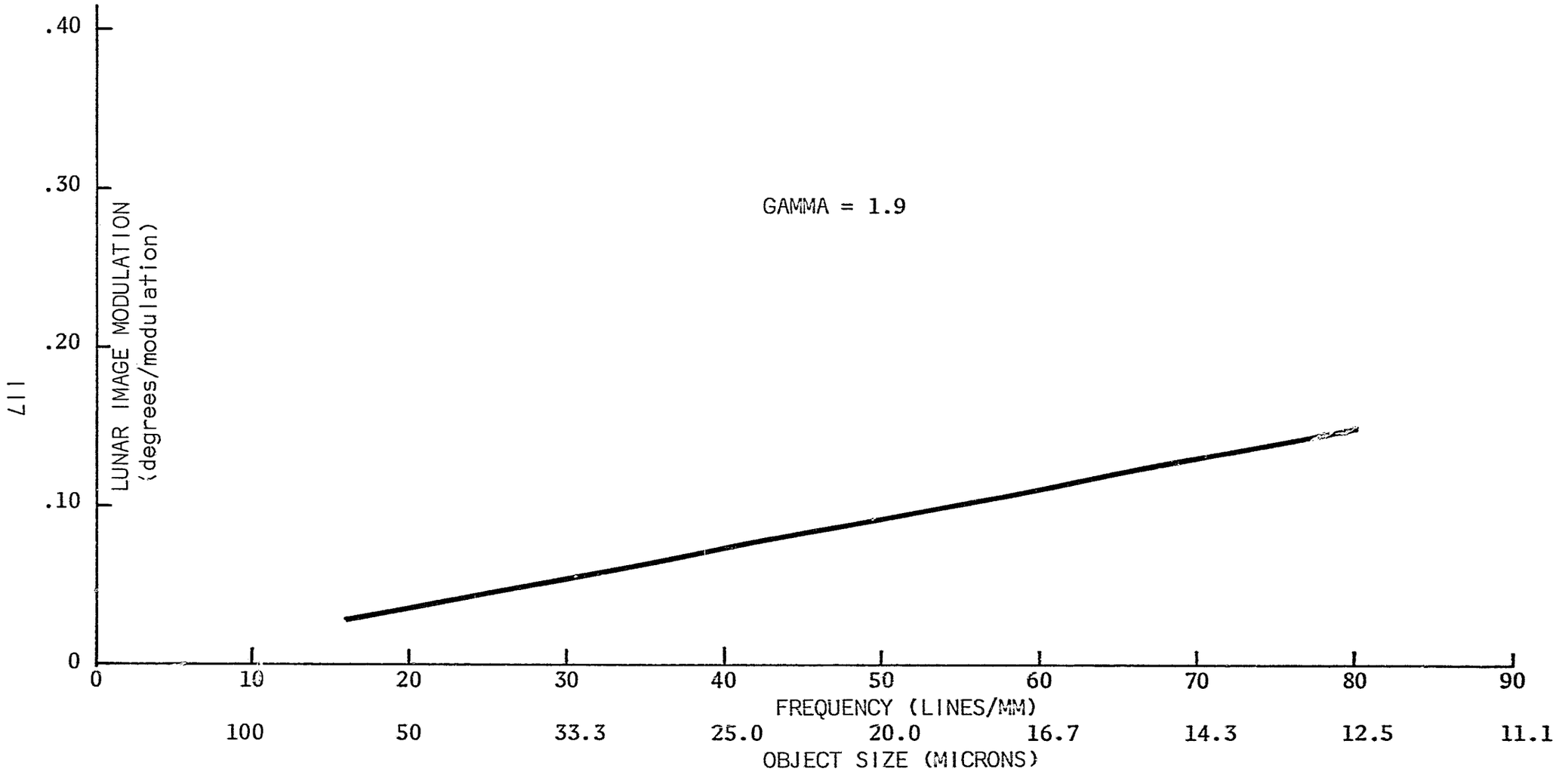

FIGURE 41. LUNAR MODULATION CURVE FOR SO-243 FILM PROCESSED IN D-19

wc e used. Figure 42 shows the transfer functions of the two optical systems. To eliminate the phase angle effect in the LM curve, the lens MTF curve was multiplied by the phase angle. This procedure corresponds to the technique used to scale the MTF curve when predicting limiting tri-bar resolution for several target contrasts using the TM curve. The modified curves are shown in Figure 43 for both optical systems at the three different phase angles. This scaling technique is intended to allow the LM curve to be used for predicting results at any phase angle.

Table XII lists the smallest identifiable crater predicted by crossing the scaled MTF curves with the LM curve.

Three observers examined each of the six photographs under magnification ranging from 40 to 100X. The observers were free to choose any magnification they desired.

The observers were asked to locate in each photograph the smallest object they could confidently say was a crater. Crater size was determined by measuring the objects on a high resolution photograph of KLM 6-65. Table XIII lists the average size craters identified in each case. The ratios of actual to predicted size for both systems are plotted against phase angle in Figure 44.

The differences between predicted and actual results increase as phase angle decreases. The increasing differences indicates that linearly scaling the lens MTF by the phase angle does not eliminate the phase angle dependency. Also there is a slight difference between the phase angle dependence for the two different optical systems indicating that a constant correction factor cannot be applied.

These differences between predicted and actual results and the lack of any theoretical background limit the value of the Lunar Modulation concept.

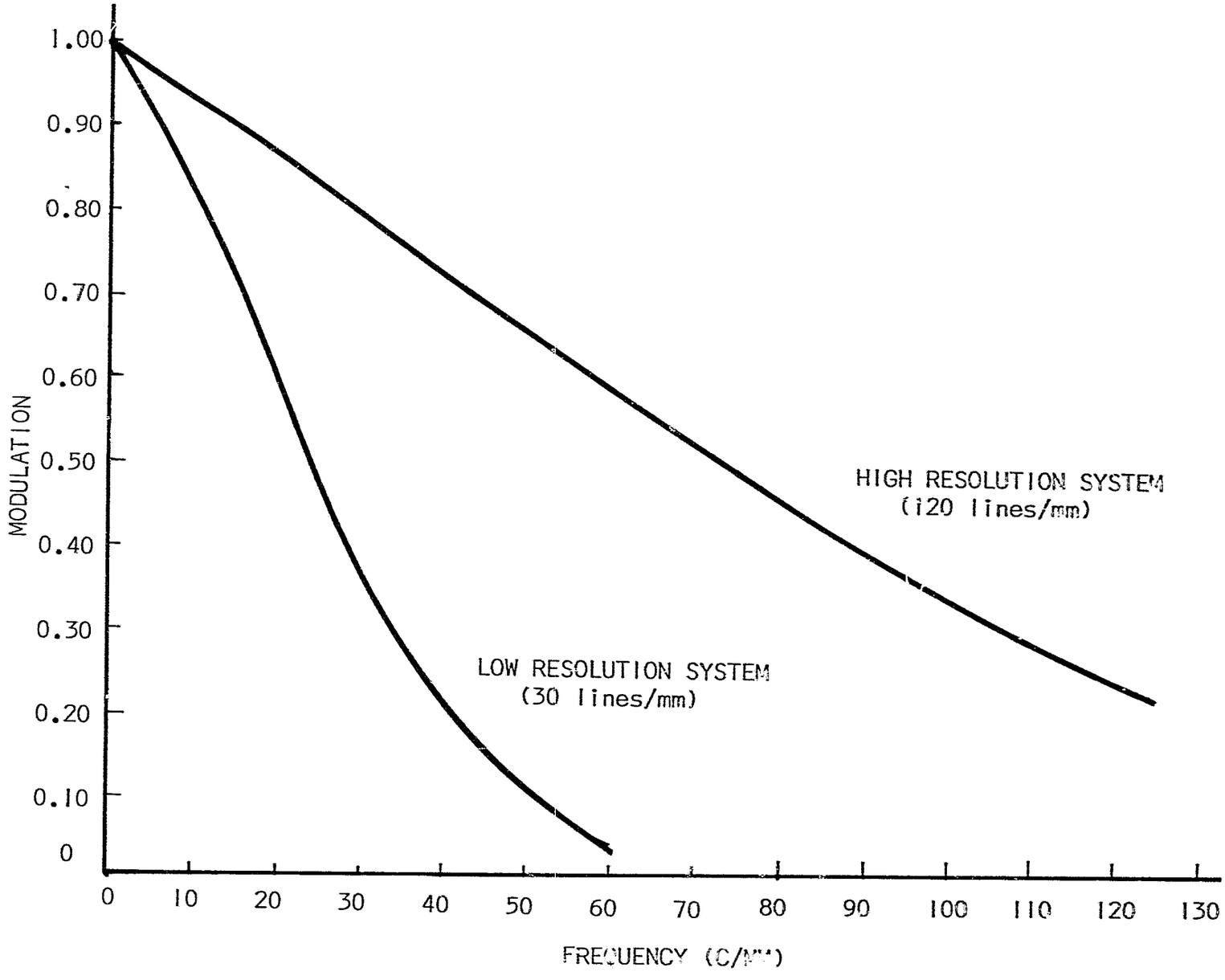

FIGURE 42. MODULATION TRANSFER FUNCTIONS OF THE TWO OPTICAL SYSTEMS USED IN VERIFYING THE LM CURVE

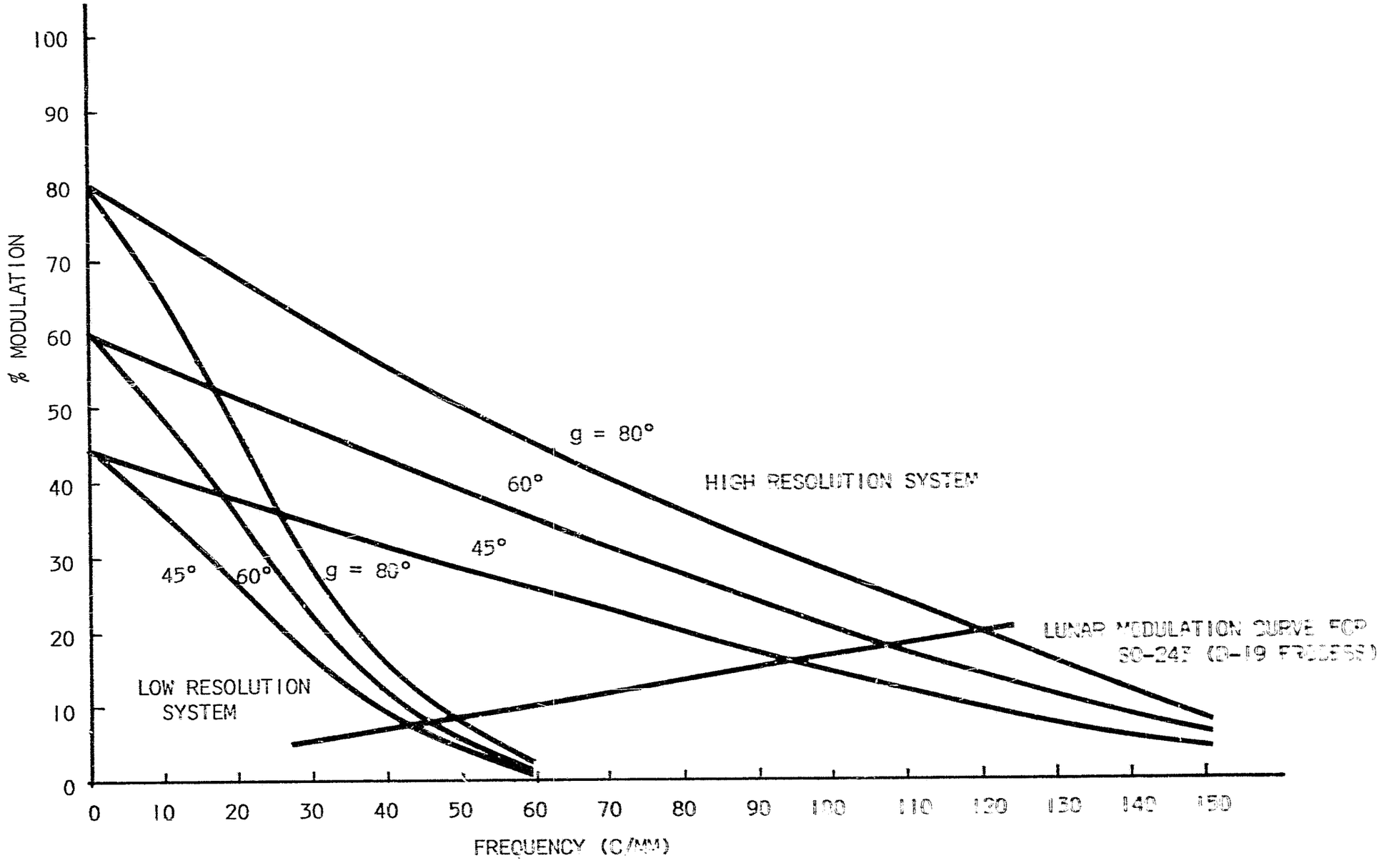

FIGURE 43. MTF CURVES SCALED FOR PHASE ANGLES (g) OF 80°, 60°, AND 45° (CROSSED WITH LUNAR MODULATION CURVE FOR SO-243 FILM)

TABLE XII

PREDICTED CRATER SIZES FOR THRESHOLD OF IDENTIFICATION USING THE LUNAR MODULATION CURVE

Phase Angle, degrees	Crater Diameter (meters) High Resolution System	Crater Diameter (meters) Low Resolution System
45	.31	.70
60	.28	.65
80	.25	.61

TABLE XIII

AVERAGE DIAMETER OF CRATERS IDENTIFIED (meters)

Phase Angle degrees	High Resolution System	Low Resolution System
45	1.8	4.8
60	.68	1.7
80	.59	1.4

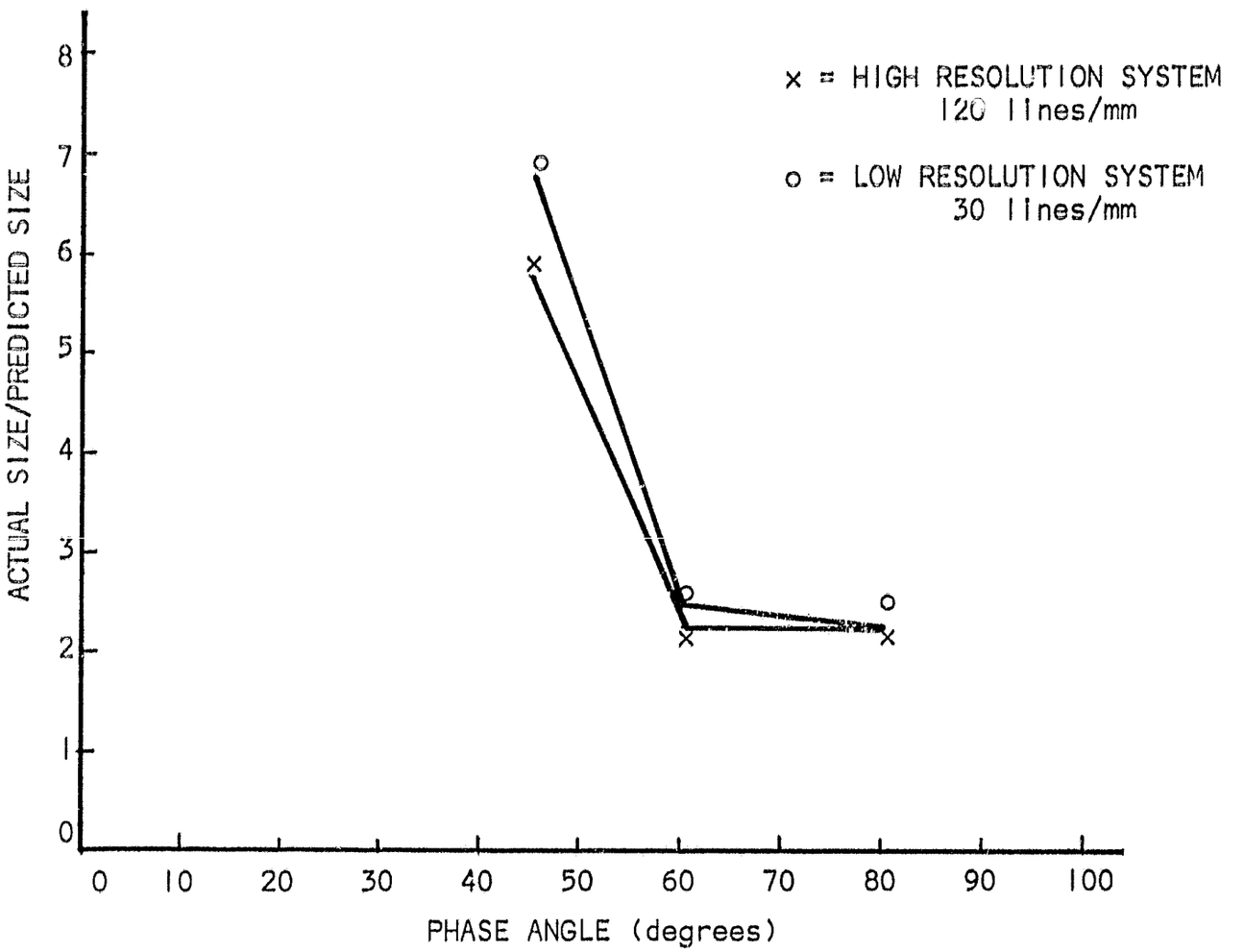

FIGURE 44. COMPARISON OF ACTUAL SIZE WITH THAT PREDICTED BY LUNAR MODULATION CURVE (SO-243, D-19 PROCESS)

It is felt that a better way for predicting resolvable lunar detail would be to use the conventional tri-bar threshold modulation curve to predict limiting 10:1 tri-bar resolution, then scaling the resolution values by using the relationships established in the Phase I work for diameter/pitch ratio versus phase angle. A target contrast of 10:1 was chosen to simulate the contrast of craters with shadowed interiors, because a crater shadow is not infinitely black as the photometric function indicates but is slightly lighted by reflection and scattering from the lighted part of the crater. The slope is about 28° at the edge of a crater with diameter/depth ratio of 8. At a sun elevation of about 35° the ratio of luminances is about 10:1 at the edges for the opposite walls of the crater for an observer looking along the vertical. The contrast increases for lower sun elevations. In practice, however, performance for systems at contrasts higher than 10:1 differs very little from the performance at 10:1 contrast.

This approach was tested in Figure 45 by crossing the TM curve for SO-243 film (D-19 process) with the MTF's of the two optical systems scaled to 10:1 contrast. The intersection of the MTF and the TM curve predicts limiting tri-bar resolution for 10:1 contrast. These limiting resolutions of 120 and 30 lines/mm were converted to pitch, and the pitch values scaled for various phase angles using the graphical relationship established during the Phase I work. This relationship is shown in Figure 46 and, Table XIV lists the predicted diameters of the smallest identifiable craters.

The predictions were tested by calculating the ratio of actual to predicted size detected. Since these ratios for the two systems were almost identical, only the results from the high resolution system are plotted against phase angle in Figure 47.

Figure 47 shows that the TM method of predicting lunar detail is superior to the LM technique. All of the ratios are near 1.0, indicating excellent correlation. Within the accuracy of this study no

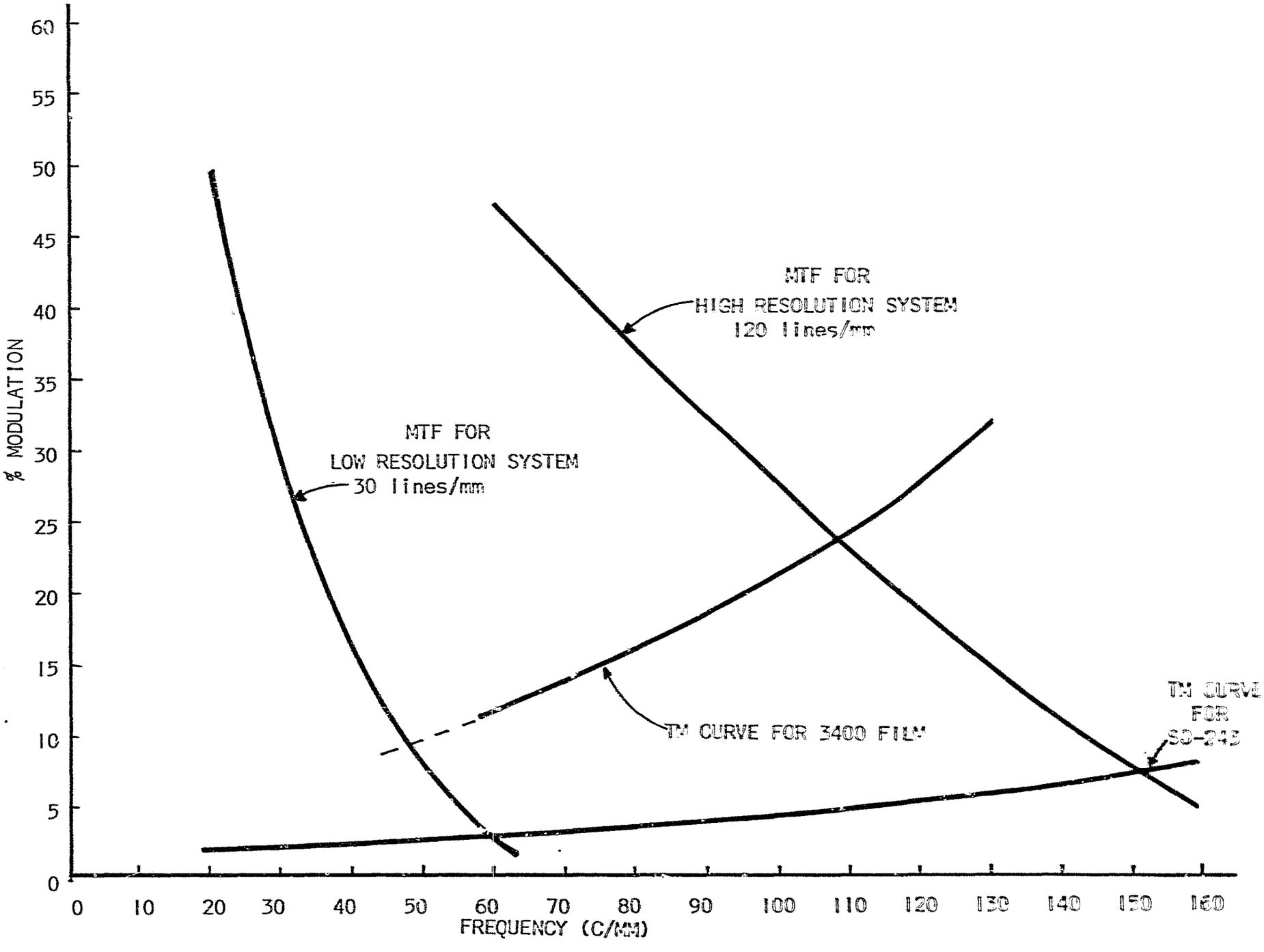

FIGURE 45. MTF OF TWO OPTICAL SYSTEMS SCALED TO 10:1 CONTRAST AND CROSSED WITH THE THRESHOLD MODULATION CURVES FOR SO-243 AND 3400 FILMS

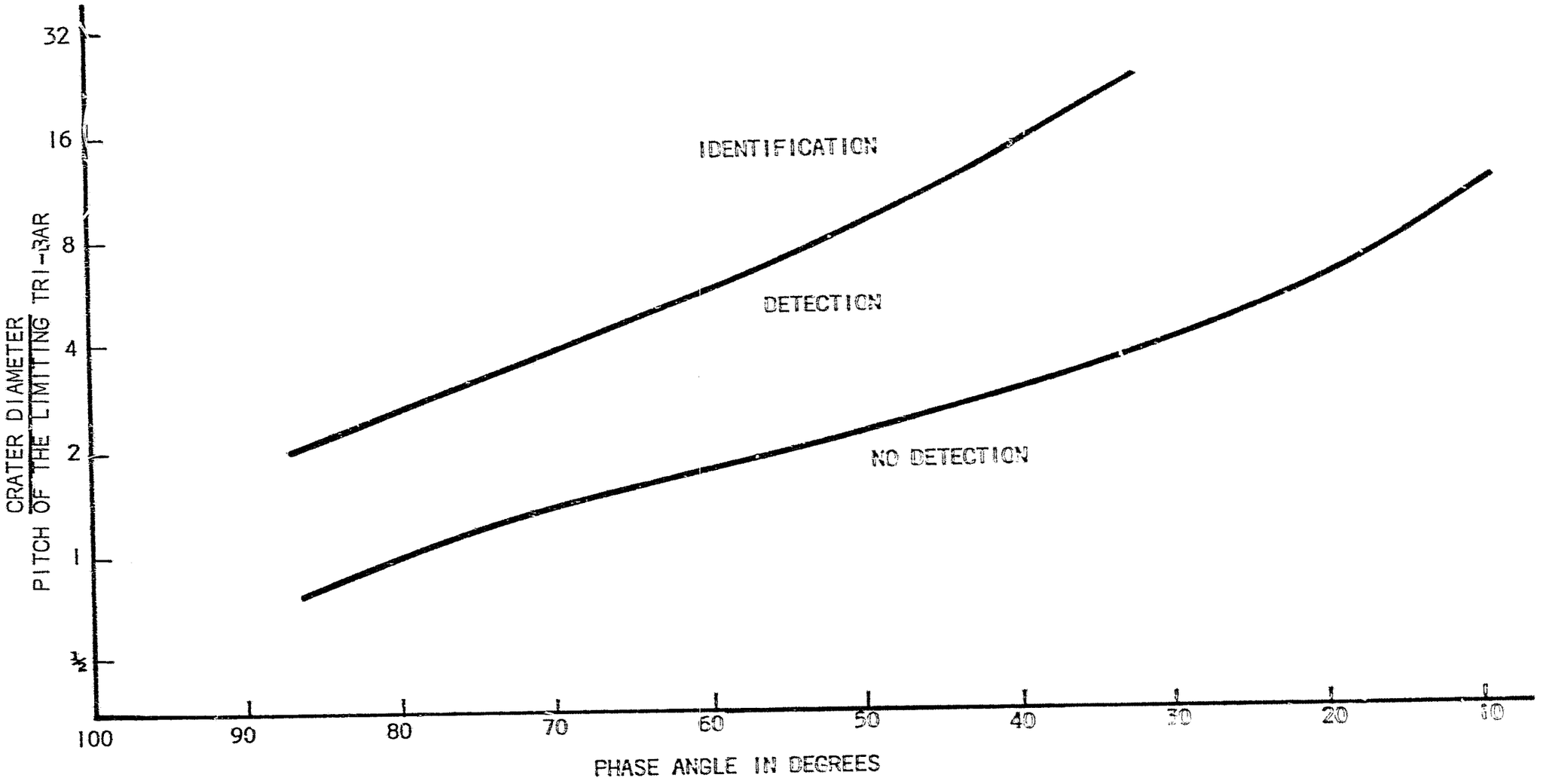

FIGURE 46. ESTIMATED SMALLEST CRATER IDENTIFIED BY READERS OBSERVING PHOTOGRAPHY OF "L" 5-65

TABLE XIV

PREDICTED CRATER FOR THRESHOLD OF IDENTIFICATION USING THE THRESHOLD MODULATION CURVE

Crater Diameter (meter)

Phase Angle, degrees	High Resolution System	Low Resolution System
45	2.28m	5.7m
60	0.64	1.6
80	0.54	1.4

AVERAGE DIAMETER OF CRATERS IDENTIFIED (meters)

FROM TABLE XIII

Phase Angle degrees	High Resolution System	Low Resolution System
45	1.8	4.8
60	.68	1.7
80	.59	1.4

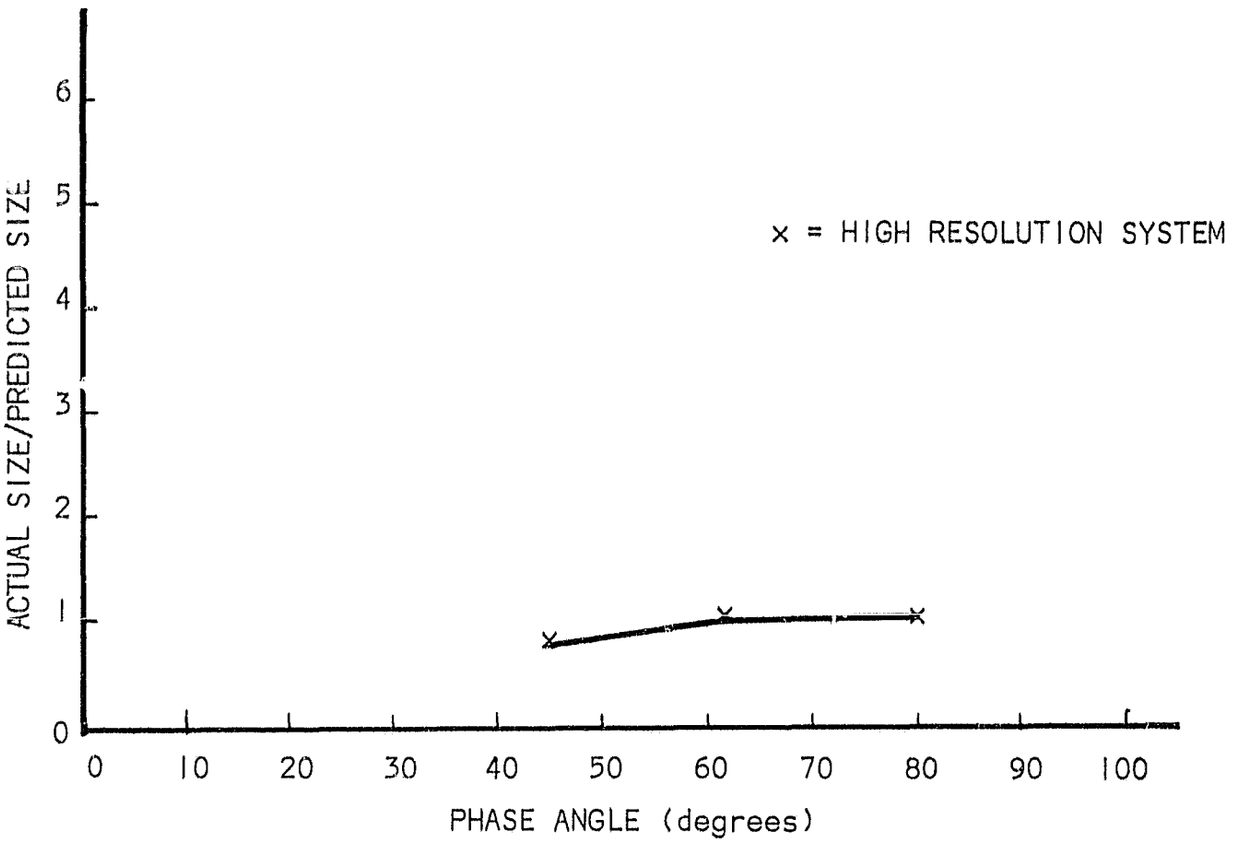

FIGURE 47. COMPARISON OF ACTUAL SIZE WITH THAT PREDICTED BY THRESHOLD MODULATION CURVE (SO-243, D-19 PROCESS)

dependency on phase angle is present. The TM theory is well developed and the diameter-to-pitch factors established during Phase I have been verified, at least at 70° phase angle, by analysis of LOP photographs in another part of the current work.

The good agreement between predicted and actual results plus the presence of well established theory makes use of the TM curve the preferred method for predicting the resolution of threshold lunar detail.

Figure 45 includes the TM curve for a faster film, Type 3400 for which lower resolution values are predicted. These predictions for the two films are for static conditions. In orbital photography, the effects of smear must be considered by modifying the MTF curves for the optical systems to include smear. Since the two films have different speeds, the amount of smear is different for the two films in a system without IMC because the slower film requires a longer exposure time.

C. Performance Evaluation by Edge Gradient Analysis

1. Summary

The sun-lit to shadow edge of craters in photographs of Lunar Model KLM 6-65 and LOP photographs have been used as test objects for measuring modulation transfer functions. These edges make suitable test objects providing the crater chosen is small enough, relative to the resolution of the system, so that the penumbra is not resolved. Results of this work showed that the crater diameter should be no greater than 20 to 40 times the pitch of a tri-bar at limiting resolution, or about 7-14 times the diameter of the smallest crater identified in the image.

BIMAT-processed SO-243 exhibits large adjacency effects. These adjacency effects produce non-linearities which prohibit cascading of the modulation transfer functions. Instead, a non-linear synthesis must be used.

2. Theory

The modulation transfer function (MTF) is a representation of the transfer characteristic of an optical system or photographic film for spatial frequencies. When the components of a system including the photographic film are linear and independent, the MTF's may be combined with one another to produce the MTF of the complete system.

Crossing the MTF of a lens with the threshold modulation (TM) curve of a photographic film allows one to predict the limiting tri-bar resolution of that lens-film system.

The MTF of a component or a system can be measured in many ways, but most techniques require the use of special targets. Variable transmission or variable area sine wave targets are the most common test objects used in laboratory measurements.

Since special targets usually are not available in a scene, other targets occurring naturally must be used if the MTF of the operating system is to be measured.

The edges of shadows cast by objects can be used in measuring MTF. The photographic image of an edge is scanned with a microdensitometer using a long, narrow slit. Care must be used to select a slit which is short enough to cover only the edge which must be straight and free from anomalies.

The output of the microdensitometer in density is converted to exposure, which is linear with optical characteristics. After conversion to exposure, either the edge data is differentiated to produce the line spread function and Fourier-transformed or the edge data is Fourier-transformed directly and the transform differentiated. The choice between these techniques depends on the way in which the data are handled in the computer; both techniques produce the same MTF curve.

3. Edge Gradient Analysis Using Lunar Scenes

The sunlit-to-shadow edge of a lunar crater represents a good test object for edge gradient analysis. Care must be taken to choose a crater with diameter and depth small enough so that the penumbra is not resolved by the system. If the penumbra is resolved, the calculated MTF curve will be much lower than the true curve for the system. The intensity distribution of the edge is assumed to be a step function and any significant deviation from this perfect edge will result in a lower MTF curve. If the penumbra is resolved, the resultant MTF curve is one representing the MTF of the system plus the test object. Figure 48 shows the relative luminance profile[23] of the edge of a crater (spherical) shadow with a penumbra. Superimposed on it is an ideal step function.

Care also must be used in selecting the length of the microdensitometer slit. Since the shadow of a crater is not straight, if too long a slit is used this deviation from straightness will produce a lower MTF curve. A slit length 1/20 the diameter of the crater has been shown to be satisfactory.[24]

a. Edge Gradient Analysis Using Lunar Models

Lunar Model KLM 6-65 dusted with cupric oxide was used to study the effect of the crater penumbra and the applicability of edge gradient analysis techniques to systems using BIMAT-processing. BIMAT

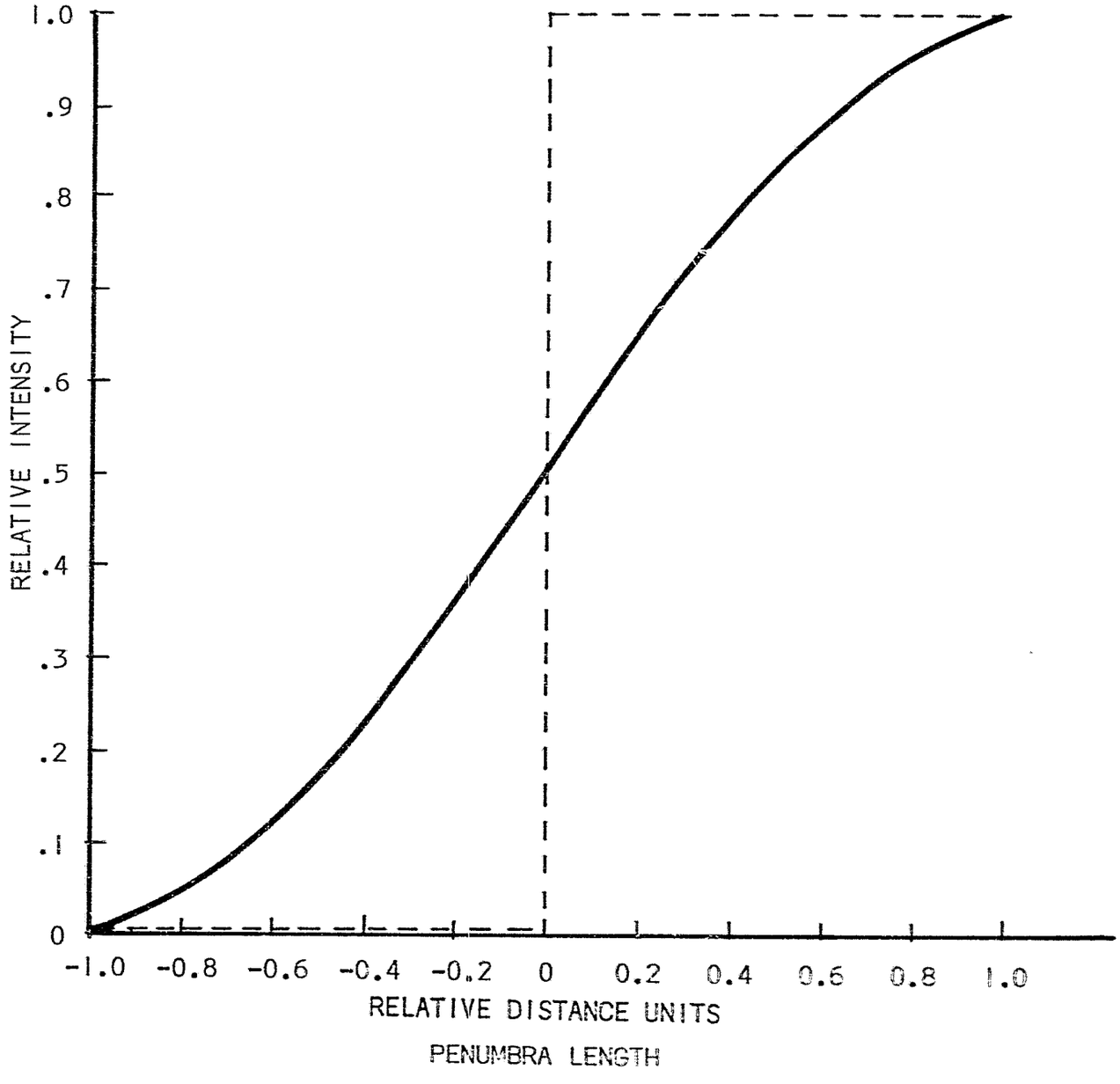

FIGURE 48. RELATIVE LUMINANCE PROFILE OF THE EDGE OF A CRATER (SPHERICAL) SHADOW WITH A PENUMBRA COMPARED TO A PERFECT EDGE

processing introduces non-linearities which make difficult the interpretation of results from edge gradient analysis.

The lunar model was illuminated by a source subtending 1/2° at the model simulating the sun at an elevation of 30°. Type SO-243 film processed in a one-to-one mixture of D-19/D-76 was used. Two photographs were taken at a scale of 1:30,000 (1:48 model scale and 1:625 photographic scale) using for one an optical system capable of resolving 30 lines/mm and for the other a system capable of 120 lines/mm.

The photographs showed no edges suitable for edge gradient analysis. Therefore the sun elevation was reduced to 20° and the photography repeated twice with the sun subtending 1/2° and 1°. From the second and third sets of photographs a crater equivalent to 12 meters in diameter on the lunar surface was traced with a microdensitometer using a 1 x 25 micron slit (length 1/16 the diameter of the crater). In a visual comparison, the edge traces showed no significant differences between the photos taken with the source subtending 1/2° and those taken with the source subtending 1°. Later work indicated that a difference would likely have shown up if the analysis had been carried out.

It was decided to abandon the use of the model for study of the penumbra and to defer this study to the analysis of Lunar Orbiter III photographs. This decision was based on two reasons. The first was that there were no craters on the model larger than the 12 meter crater used and that this evidently was not large enough to make the effect of the penumbra significant. Secondly, the LOP photographs provided an opportunity to analyze real lunar scenes where a variety of crater sizes are available.

To study the effects of processing on edge gradient analysis new photographs of KLM 6-65 were taken. The sun elevation was lowered to 10° with an angular subtense of 1/2° and two sets of photographs were

taken using the 30 and 120 lines/mm systems. The lower sun elevation increased the number of crater edges suitable for edge gradient analysis. One set of photographs was processed in a one-to-one mixture of D-19/D-76. The other set was BIMAT-processed. Figure 49 shows the characteristic curves of the two films.

A control edge was included in the model photographs. This control edge consisted of a long straight edge of black thin paper mounted on a white cardboard. The contrast was approximately 12:1. The image of the edge was small compared to the field of view, keeping the effect of flare to a minimum. The exposure was adjusted to make the minimum and maximum densities of the crater the same as those of the control edge. The control edge and the shadow edge of a crater approximately 200 microns in diameter on the film (6 meters on lunar surface) were scanned with a microdensitometer using a 1 x 25 micron slit. Both images were scanned six times. Each time the microdensitometer slit was realigned to the edge and the focus checked.

The traces were hand-smoothed to eliminate grain noise and the data converted to digital form for computer analysis. Eighty samples were taken at 6-micron increments on the 30 lines/mm edges. According to the sampling theorem this procedure corresponds to a maximum frequency of approximately 80 lines/mm and a frequency increment of 2 lines/mm. The sampling rate for the 120 lines/mm edges was every 2 microns to a total of 80 samples. This corresponds to a maximum frequency of 200 lines/mm and a frequency increment of 5 lines/mm. The digital edge data and data relating microdensitometer output to exposure were used as inputs to the computer program EGADS used to compute MTF curves from edge trace data. In this program the digitized microdensitometer data of voltage versus distance is converted to exposure versus distance, and the Fourier transform taken using the Cooley-Tukey fast-Fourier Technique. The transformed data is differentiated to produce the MTF curve.

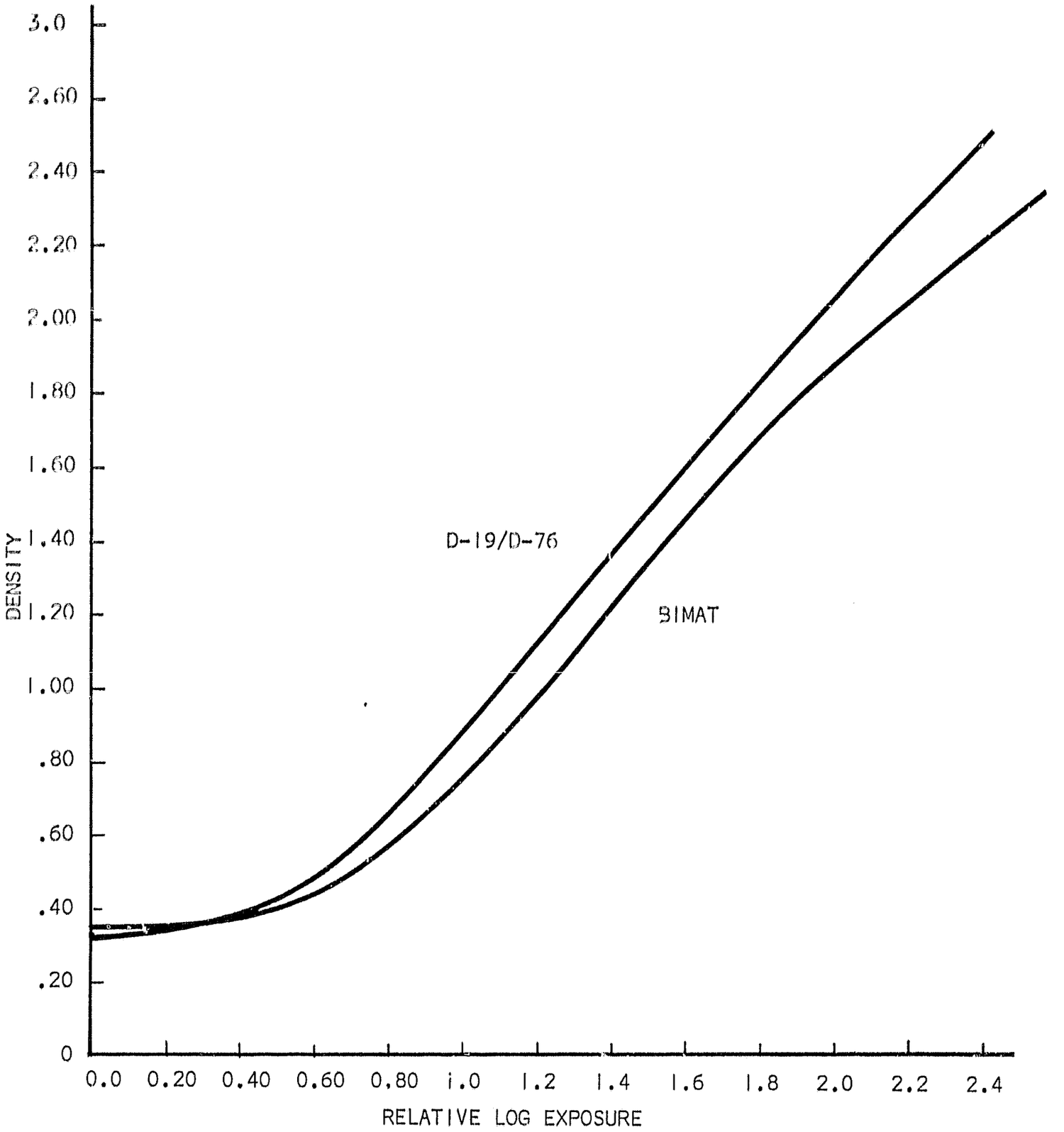

FIGURE 49. SENSITOMETRIC CHARACTERISTIC CURVES FOR SO-243 FILM PROCESSED IN BIMAT AND D-19/D-76

An average MTF curve is computed based on an average of the edge traces. The averaging is done in the exposure domain by taking the first two edges and sliding them, relative to each other, to achieve a minimum in the sum of the squared deviation in exposure values throughout the central, sloping part of the trace. At the point of best fit, a new curve is formed from the average of the exposure values of the two curves for each increment of distance. A third curve is slid into the averaged curve and the process repeated. The average of the first two is given the weight of two while the third curve is weighted by one to prevent the last curve from dominating earlier curves. This continues until an average curve based on all the individual edges is formed. This average edge is transformed to get the average MTF curve.

Figure 50 shows the averaged MTF curves for the control edge and the crater on the 30 and 120 lines/mm photographs processed in D-19/D-76. Note the close agreement between the control edge and crater for the 30 lines/mm system and the extreme difference between the two for the 120 lines/mm system.

The effect of the crater penumbra explains the wide difference between the two high resolution curves although it was felt that the crater diameter chosen would be small enough to have a penumbra which would not be resolved. The earlier visual examination of edge traces of a 12 meter crater gave the impression that the penumbra was unresolved. The intensity distribution of the penumbra reduces the steepness of the shadow edge and yields a poorer transfer function for the system. The penumbra was apparently just below detection by the 30 lines/mm system and therefore did not affect the MTF curve.

It is a little surprising that the 120 lines/mm system was able to detect the penumbra as well as it did. The Cornell study[25] indicates that on the film the penumbra is only 3.6 microns for a 6-meter crater of 8:1 diameter-to-depth ratio at a sun elevation of 10°.

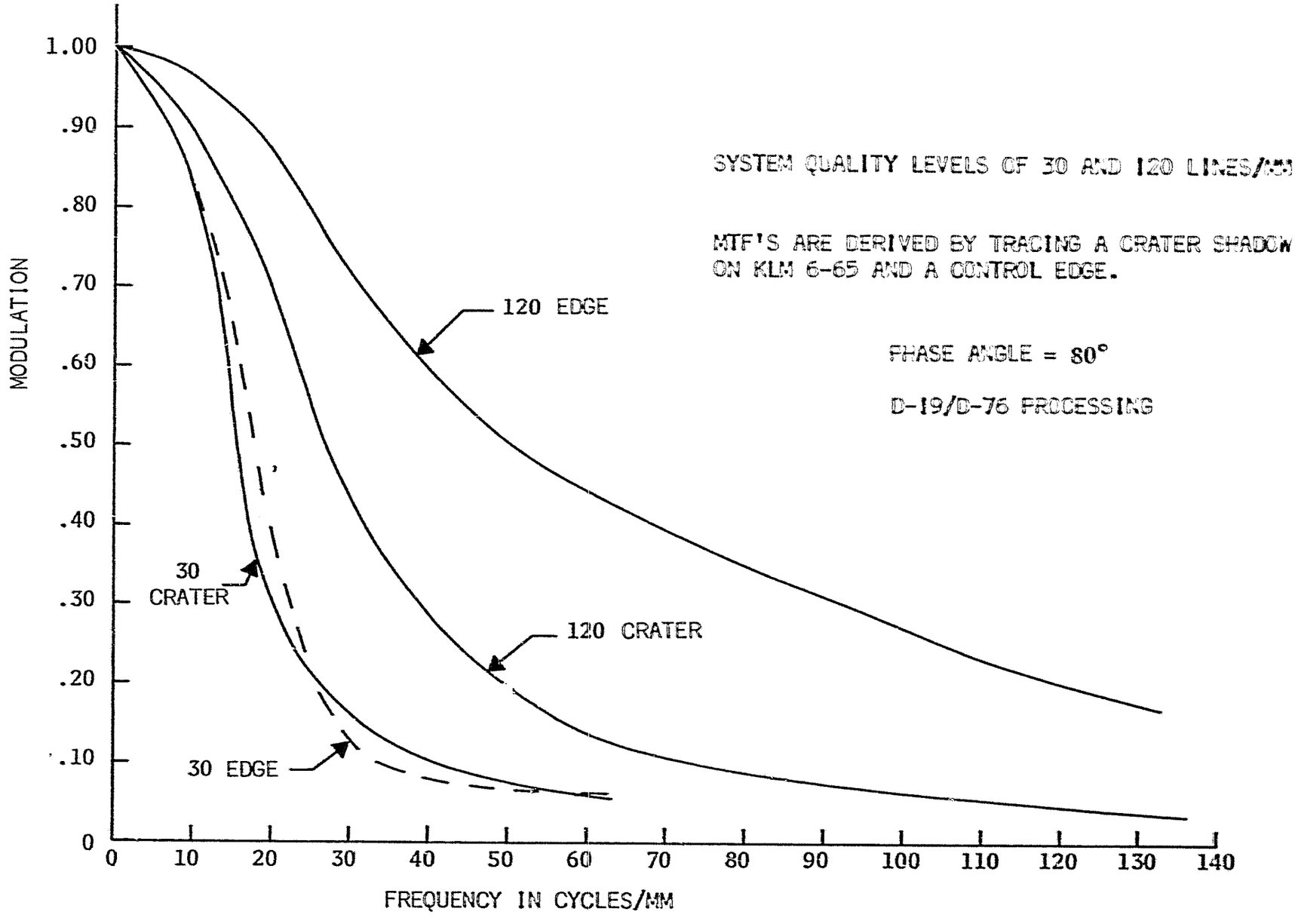

FIGURE 50. SYSTEM MTF DERIVED BY EDGE TRACE ANALYSIS FOR D-19/D-76 PROCESSING OF SO-243 FILM

The pitch of a tri-bar pattern at a limiting resolution of 120 lines/mm is 8.4 microns. The penumbra still influences the MTF curve when it is 2.5 times smaller than the pitch of the limiting tri-bar.

To further substantiate the penumbra effect, the MTF curve from the 120 lines/mm crater edge was divided by the MTF curve from the control edge to produce effectively an MTF curve of the penumbra. EGADS was used to compute the MTF from the penumbra intensity distribution shown in Figure 48.

Assuming that the difference between the control-edge MTF and crater-edge MTF was caused by the penumbra and assuming that the photo-optical system used to produce the photographs can be treated as a linear system, the MTF derived from the penumbra intensity distribution should agree with the MTF of the difference between the crater and control-edge curves.

Figure 51 shows the comparison of the two MTF curves. While the agreement between the two is not exact, it is close enough to indicate that the penumbra played a significant role in creating the difference between crater and control edge MTF. The residual discrepancy in Figure 51 is within the experimental error in this study.

Figure 52 shows the effect of adjacency effects on the average MTF curve derived from the edge and the crater on the 30 lines/mm and 120 lines/mm photographs for BIMAT processing. Accurate determination of the optical response of a system is difficult because the adjacency effects introduce non-linearities that prevent accurate photographic photometry.

Adjacency effects are caused by the diffusion of developer across an area which has received a large amount of exposure relative to an adjacent area which has received less exposure. The developer

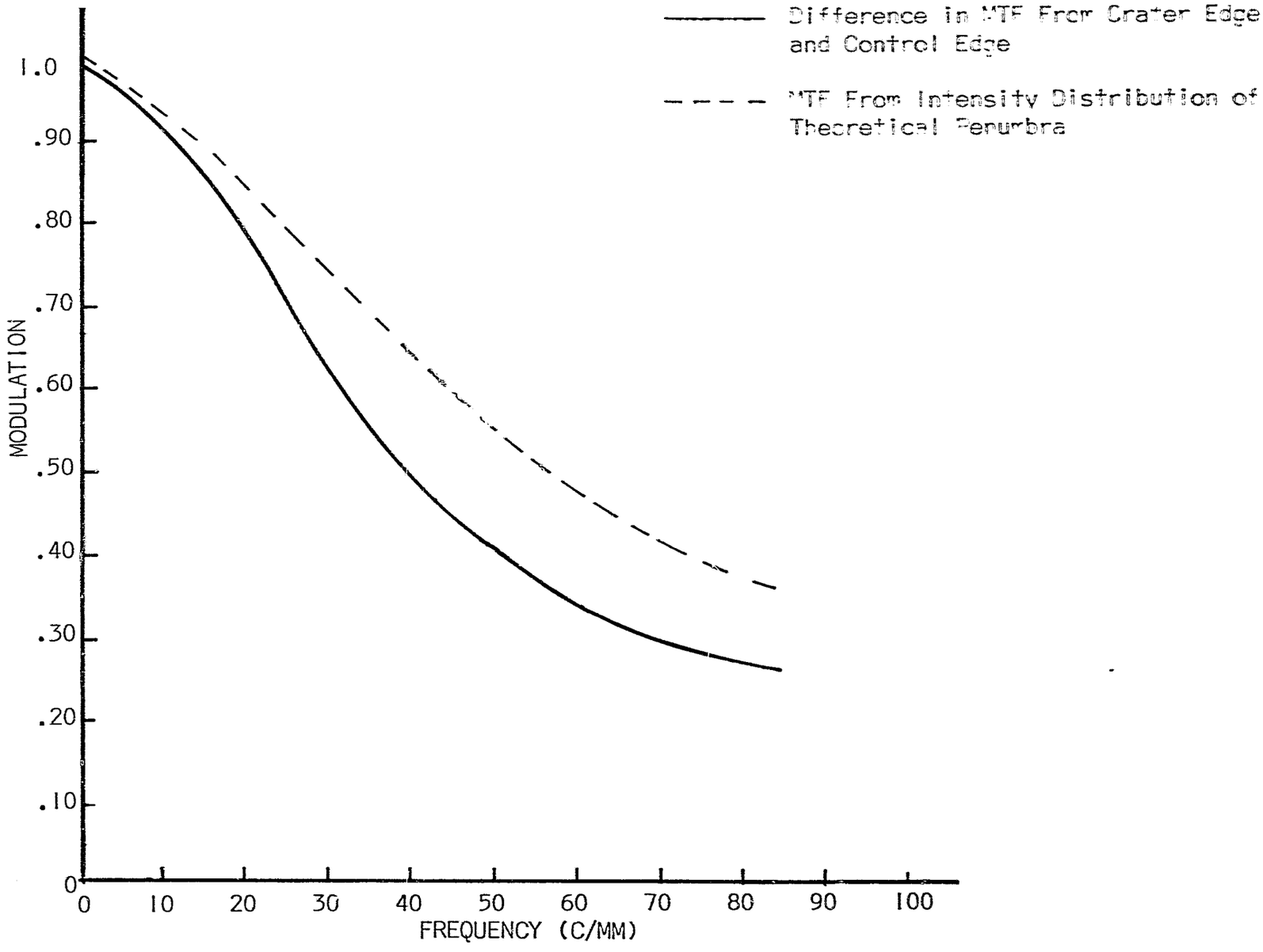

FIGURE 51. MTF CURVES FOR PENUMBRA EFFECT

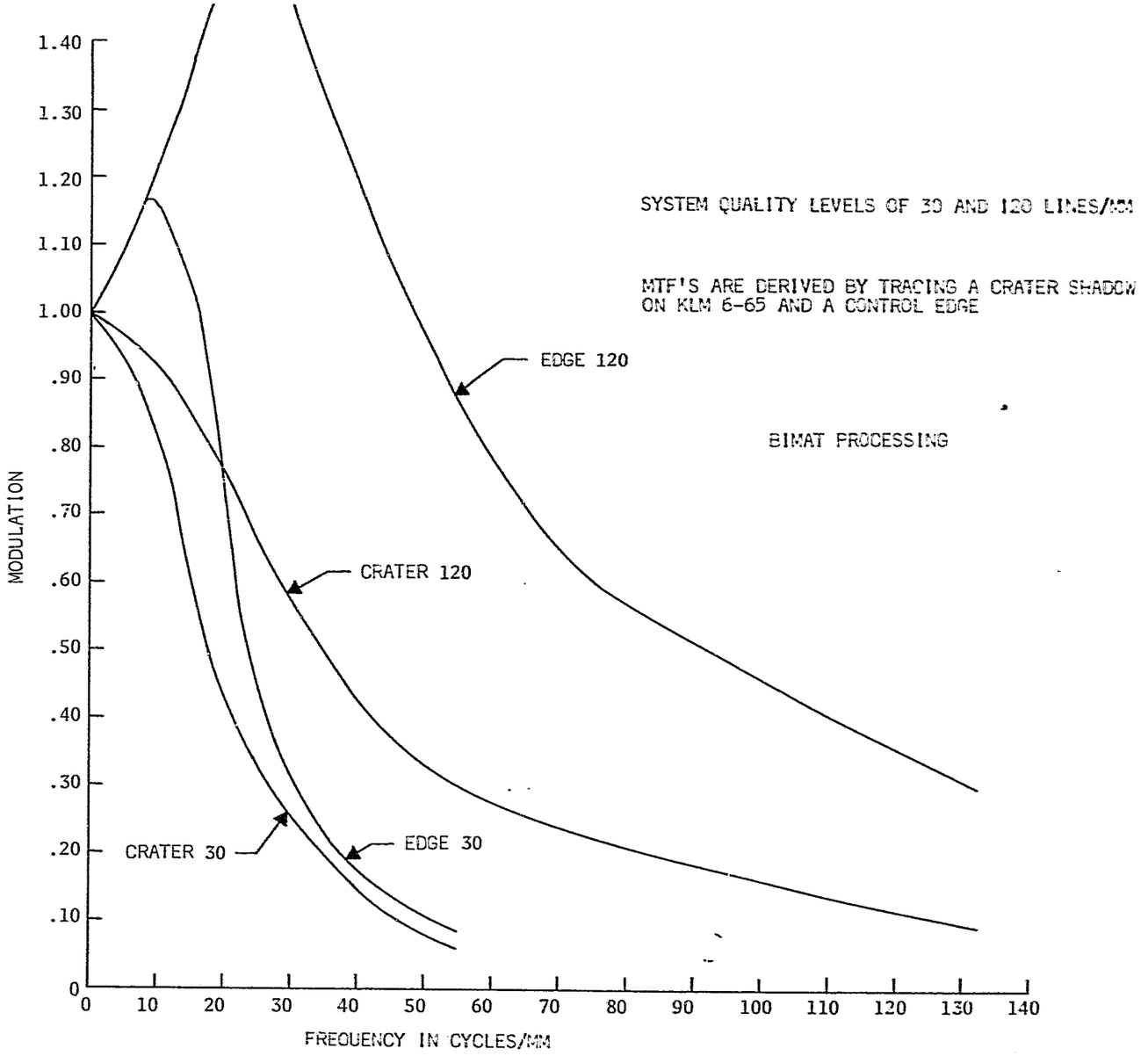

FIGURE 52. SYSTEM MTF DERIVED BY EDGE TRACE ANALYSIS FOR BIMAT PROCESSING OF SO-243 FILM

diffusing from the high exposure area is badly oxidized by the reduction of many exposed silver halide crystals. The oxidized developer retards development while fresh developer accelerates development near the edge. This retardation and acceleration produce an area of lower density on the edge of the low exposure side (fringe effect) and an area of higher density on the edge of the higher exposure side (border effect).

Figure 52 shows the MTF curves from crater and edge for the BIMAT-processed material. The transfer functions derived from control edges imaged at both quality levels exceeds a value of one at low frequencies. This anomaly is characteristic of an MTF curve for a film that has strong adjacency effects present. The 120 lines/mm crater edge MTF curve does not exhibit the overshoot because of the penumbra which reduces the steepness of the edge intensity distribution which reduces or eliminates the adjacency effects. The 30 lines/mm crater MTF curve does not exhibit adjacency effects while the 30 lines/mm control MTF does. Why the MTF from the control edge at 30 lines/mm shows some adjacency effects and the one from the crater edge does not is not completely understood. One possible cause could be the penumbra effect but if the penumbra were affecting the transfer function in any way the agreement between the 30 lines/mm control and crater edge MTF for the D-19/D-76 processed photographs would not have been as close.

If the components of an optical system are linear, the MTF's of the components may be combined to produce a system MTF by multiplying their modulation values frequency by frequency. The inverse procedure is also possible for a linear system; that is, if an MTF curve for the system is available, its components may be separated by division.

The MTF of the system (lens, target and film) shown in Figures 50 and 52 was divided by the film MTF leaving the lens-target transfer function. Assuming a linear system and no influence by the target, this resulting MTF should be the MTF of the lens used to take the photographs.

In Figure 53 the agreement between the measured lens MTF and the MTF derived from the control edge is quite good for the film processed in D-19/D-76 at a quality level of 30 lines/mm. The agreement between the MTF from the control edge and the lens MTF for the 120 lines/mm system is also quite close. The agreement between the MTF from the crater edge and the lens MTF for the 120 lines/mm system is very poor because of the effect of the penumbra (target).

In Figure 54 the transfer function derived from the BIMAT-processed photographs does not agree as well with the lens MTF as did the data from photographs processed in D-19/D-76.

The adjacency effects introduce non-linearities which make it incorrect to simply divide by the film MTF. Another reason for the poorer agreement is that the MTF of the film-developer combination is difficult to measure. C. N. Nelson and F. C. Eisen of the Kodak Research Labs[26] have found that there is no unique MTF curve for a film-developer combination exhibiting adjacency effects. There is, instead, a whole family of curves whose shape depends on the modulation of the input signal and the density level; the greater the signal modulation and density level, the greater are the adjacency effects.

The MTF curves for the film used in this study were measured using sine wave targets of 5:1 contrast. The crater edge and control edge were photographed to produce densities corresponding to a contrast slightly greater than 10:1. The MTF curve derived from the 5:1 targets would exhibit smaller adjacency effects than the curve determined from the crater or control edges. When the lens-film MTF curve was divided by the film data some residual film effect was left. This residual plus the fact we were dealing with a non-linear system explains the poor agreement shown in Figure 54.

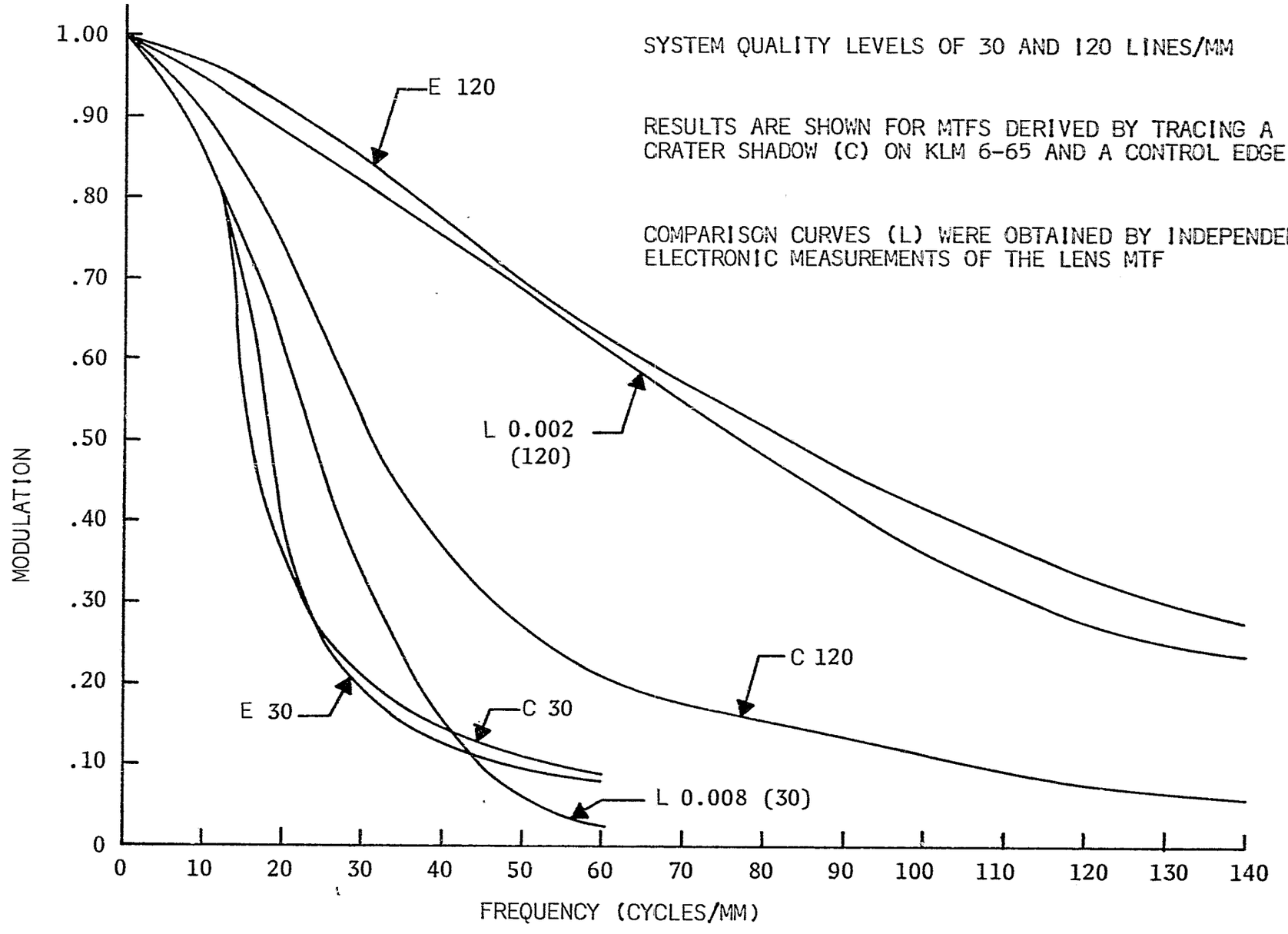

FIGURE 53. MTF CURVES FOR LENS DERIVED BY EDGE TRACE ANALYSIS FOR D-19/D-76 PROCESSING OF SO-243 FILM

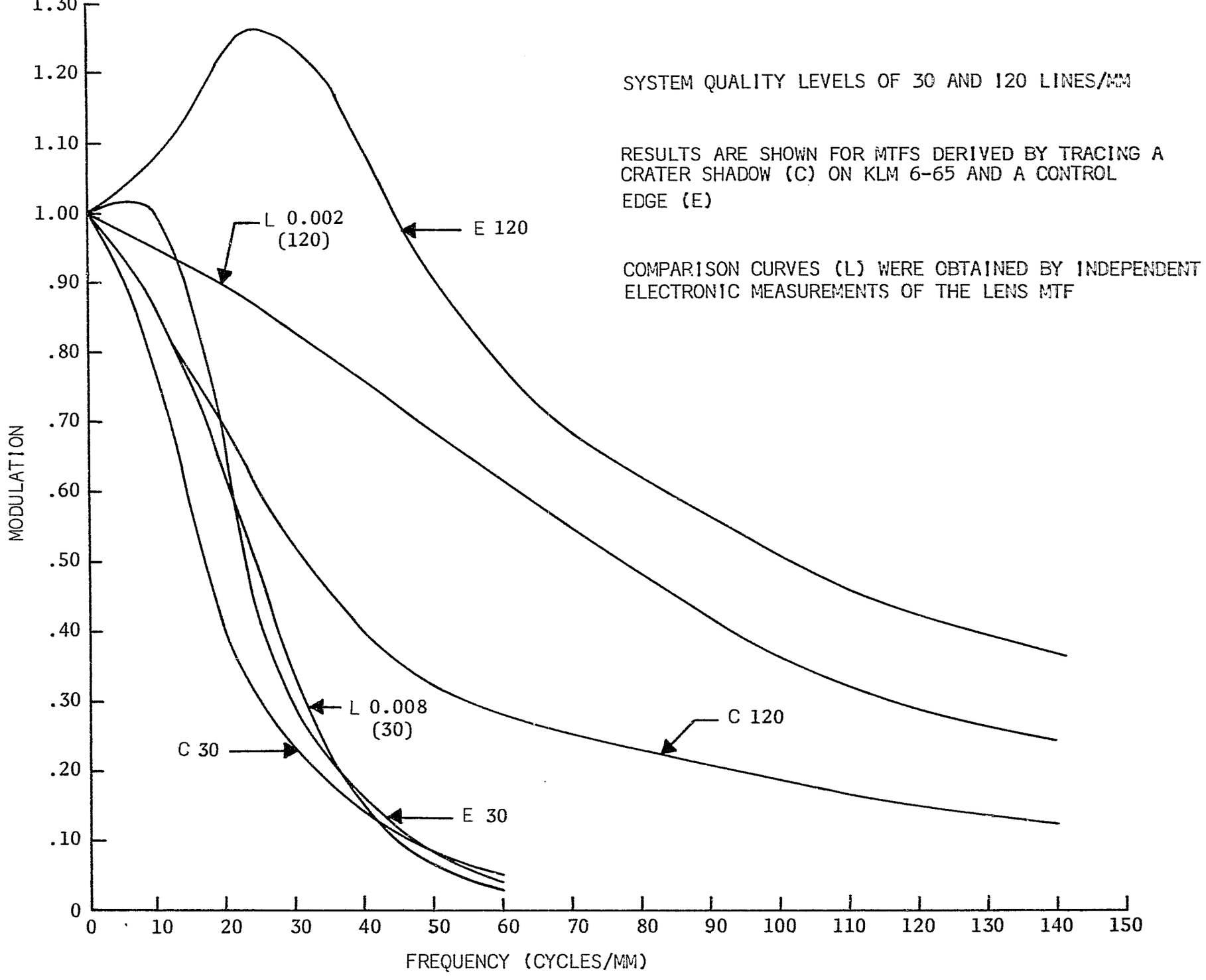

FIGURE 54. MTF CURVES FOR LENS DERIVED BY EDGE TRACE ANALYSIS FOR BIMAT PROCESSING OF SO-243 FILM

The techniques developed by C. N. Nelson were used to investigate further the adjacency effects of the BIMAT-processed SO-243.

The chemical spread function was measured for the BIMAT-processed SO-243 at a density difference of approximately 1.0 (0.38 to 1.40). The chemical spread function is determined from an edge image made by exposure to X-rays. Since X-rays suffer little or no scattering within the emulsion, the resulting edge trace should be almost a perfect step function if adjacency effects were not present. The edge is scanned with a microdensitometer and the weighted slope determined as shown in Figure 55. The exponent n in the equation for slope b is a function of the relationship between density and the mass of silver per unit area. For BIMAT-processed SO-243 n was determined to be 1.0.

Figure 56 shows the chemical spread function for BIMAT-processed SO-243 based on an average of 5 curves. Figure 57 describes the non-linear process of combining the optical spread function caused by scattering and diffusion of light within the emulsion with the chemical spread function. Because of the non-linearities it has not been possible to reverse the process, e.g., start with the D' density distribution and work back to the nominal density distribution D. If this were possible we could remove mathematically the film effect from the system MTF and determine the lens MTF.

Because the system could not be broken down into the component characteristics, we synthesized it from the system's components. The line spread function of the diffraction limited f/5.6 lens used to photograph the model was convolved with an edge. This intensity distribution was convolved with the optical spread function of the film. The film optical spread function was represented by the following equation.

$$A(x) = \frac{a}{2\sqrt{\pi}} e^{-(ax/2)^2} \qquad \text{Equation 28}$$

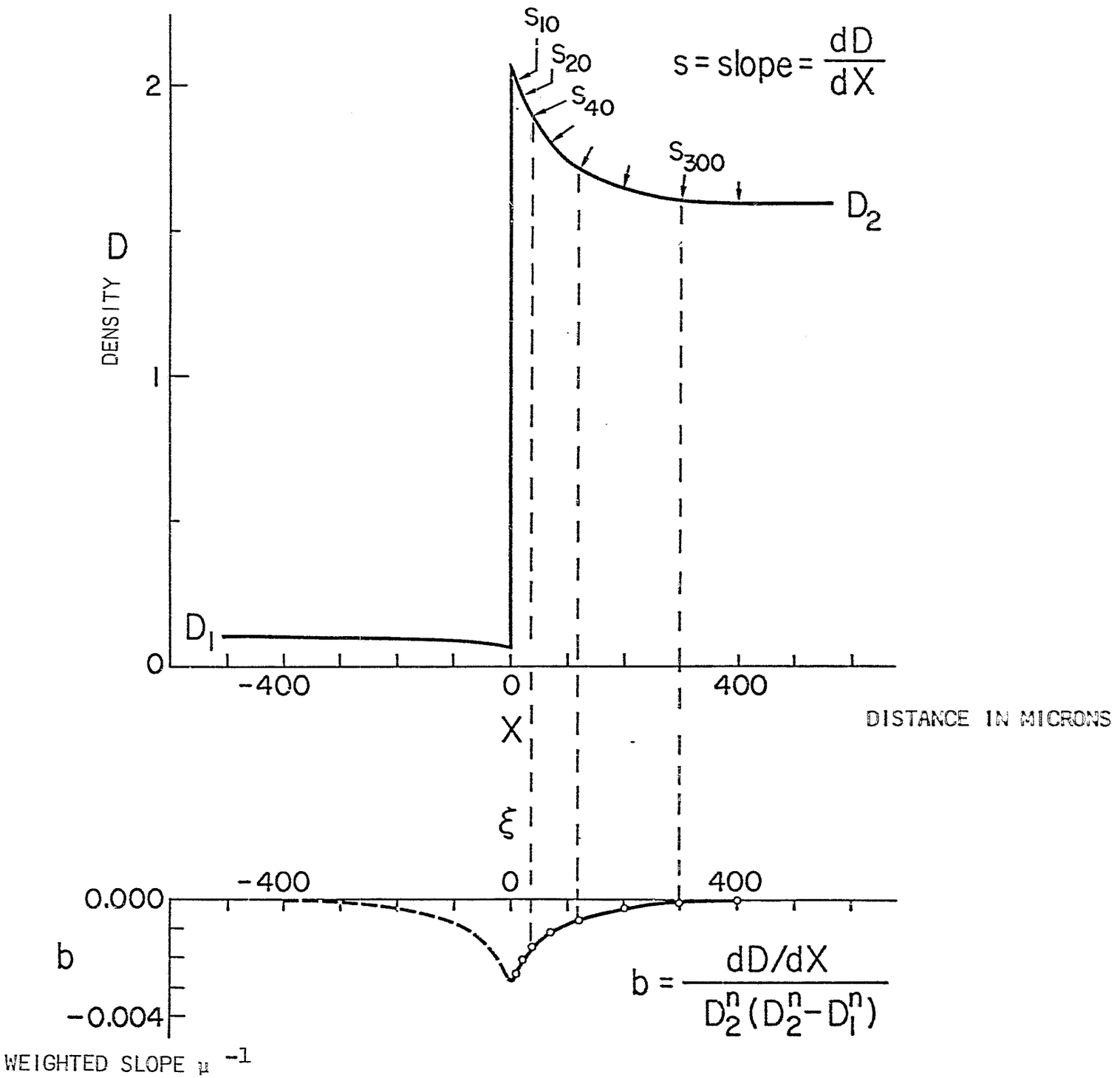

FIGURE 55. DETERMINATION OF CHEMICAL SPREAD FUNCTION FROM EDGE TRACE

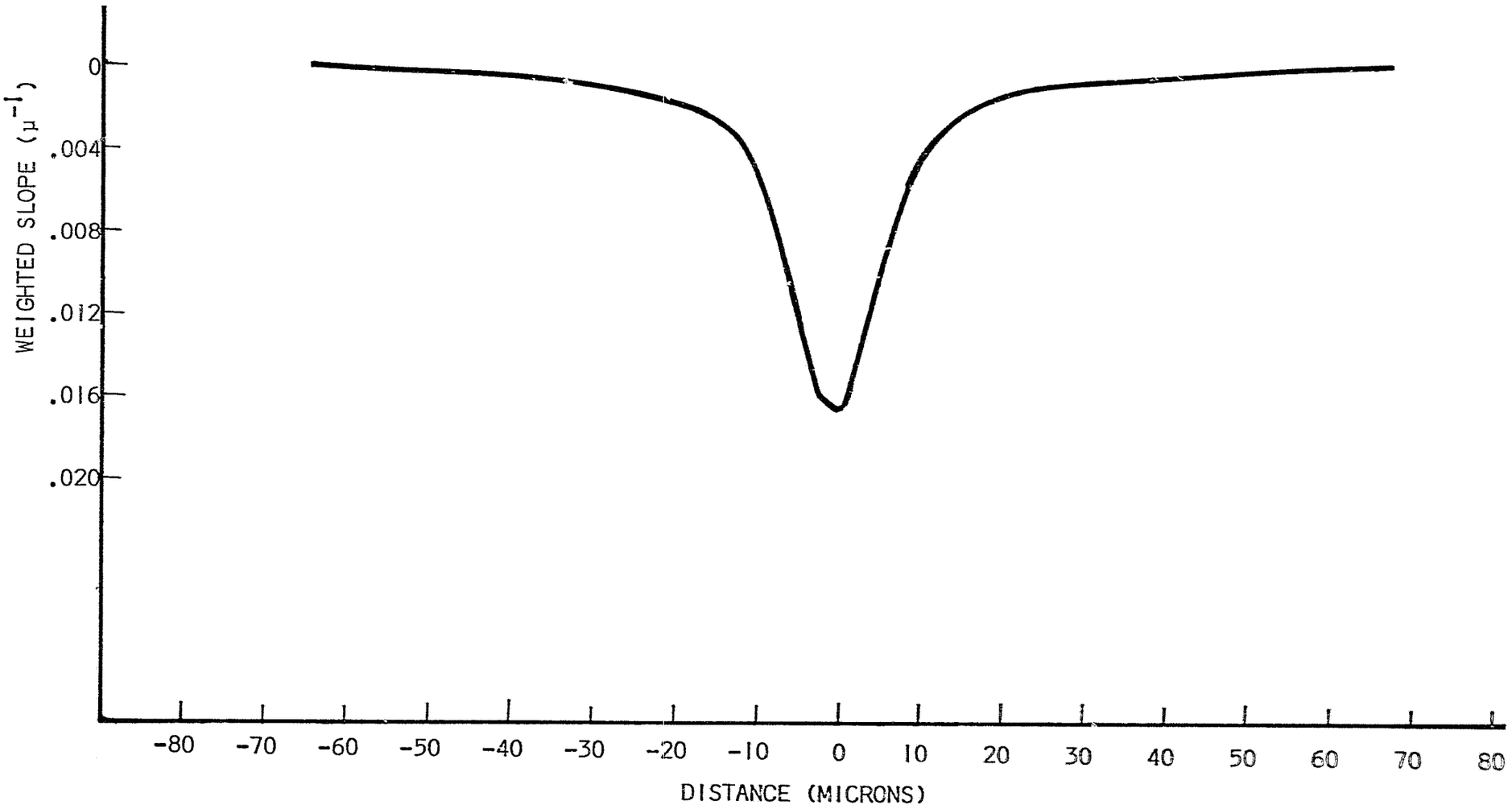

FIGURE 56. CHEMICAL SPREAD FUNCTION FOR SO-243 BIMAT PROCESSED

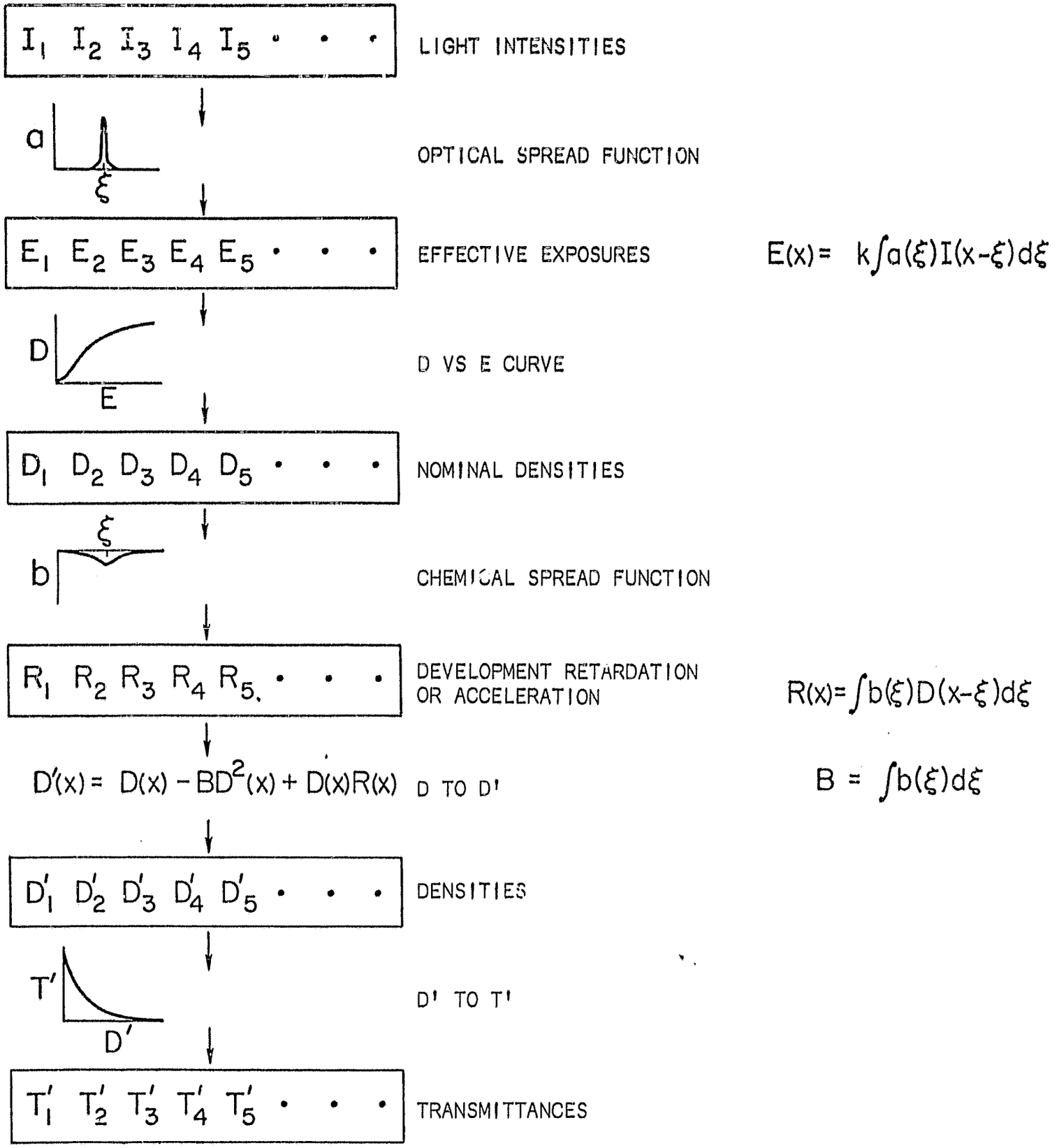

FIGURE 57. PROCEDURE FOR NON-LINEAR COMBINATION OF COMPONENTS OF A PHOTO-OPTICAL SYSTEM

A value of 4.5 was used for the variable a, based on work described in the literature.[27]

The calculated intensity distribution was converted to density using the film characteristic curve. The chemical spread function was convolved with this density distribution to form the distribution labeled R in Figure 57. A new density distribution was created using the D to D' equation shown in Figure 57. A value of 0.29 was used for B, the area under the chemical spread function. The new density distribution was converted to transmittance and the data used as input to EGADS, the edge gradient analysis computer program. Figure 58 shows the calculated MTF curve for the 120 lines/mm system compared to the MTF curve derived from the control edge.

The agreement is quite good. The difference between the two curves at higher frequencies is probably caused by errors in the shape and size assumed for the optical spread function of the film. The selected distribution was based on the best estimate available at the time. Normal procedure when working with non-linear synthesis is to repeat the combination many times using different film optical spread functions until a close fit is obtained.

b. Edge Gradient Analysis Using LOP Photographs

Edge gradient analysis was used to determine the MTF of the Lunar Orbiter III system. Ten craters were selected on medium resolution frames 187 and 188. The size of the craters ranged from approximately 40 to 440 meters in diameter. Table XV lists the diameters on the GRE film. Each crater was visually examined on the 24-inch photograph to insure that its shape was suitable, eliminating craters with boulders around the rims, large collars or other similar features which could distort the shadow edge and yield unusable edge data.

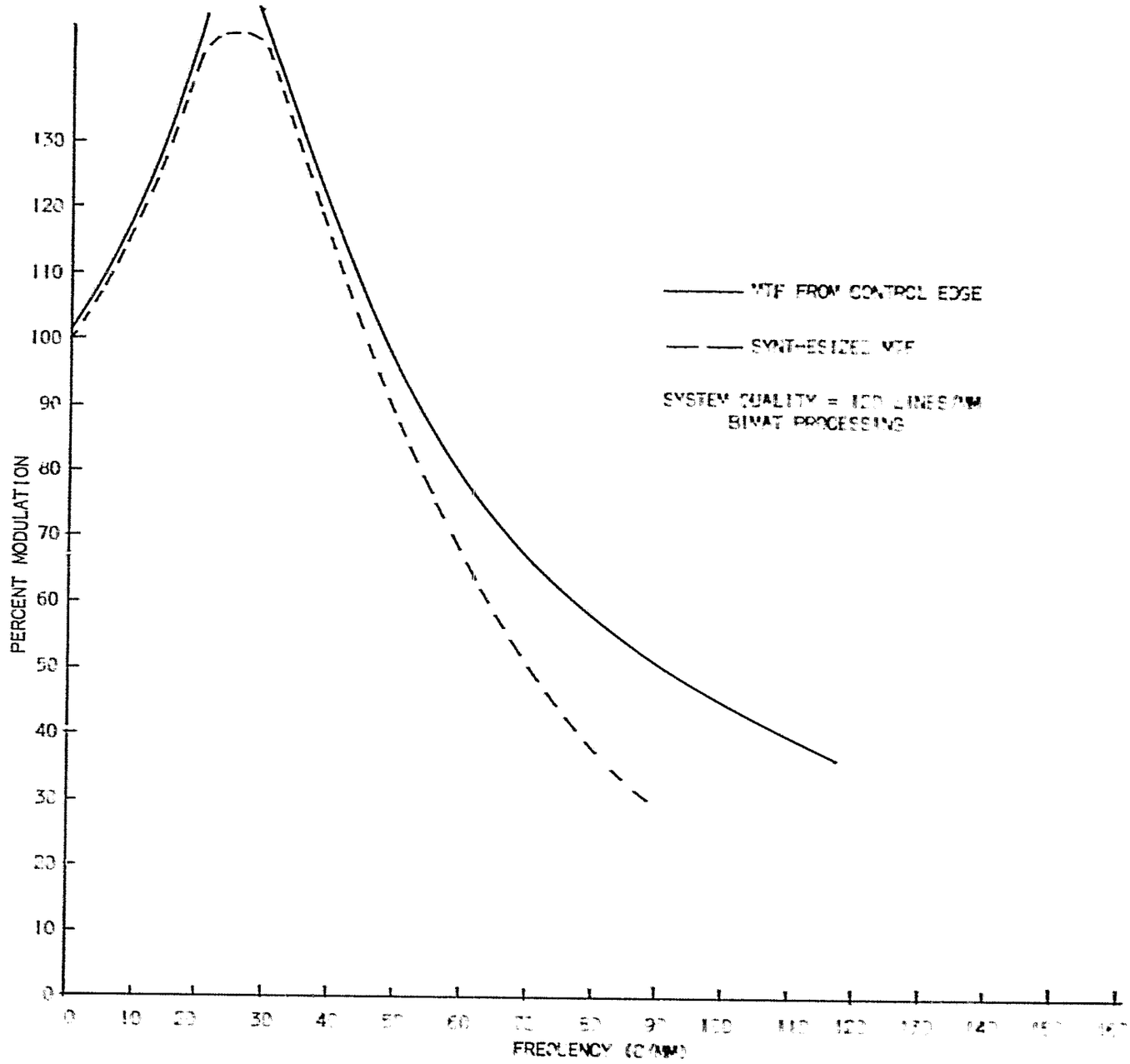

FIGURE 58. COMPARISON OF MEASURED AND SYNTHESIZED MTF CURVES

TABLE XV

LOCATION AND SIZE OF CRATERS USED IN PERFORMING EDGE GRADIENT ANALYSIS ON LUNAR ORBITER III PHOTOGRAPHS

Crater ID Number	Size	Frame Number
1	438 meters	187
2	255	187
3	390	187
4	130	187
5	75	187
6	390	188
7	40	188
8	150	188
9	175	188
10	340	188

Each crater edge was scanned five times using a microdensitometer with a slit of 1 x 50 microns. The data were digitized taking 1000 points per scan at intervals of 2 microns. The scan line signature, superimposed on the edge data, was removed by the filter shown in Figure 59. The digitized edge data was Fourier-transformed into the spatial frequency domain, multiplied by the filter and then back transformed into the distance domain. Figure 60 shows an edge before and after filtering. The filtered edge was hand-smoothed to eliminate low frequency noise passed by the filter and again digitized for analysis by computer program EGADS. The step tablet in the edge data was used to convert the densities to exposures.

Originally filter characteristics were set up so that information at frequencies of 15 to 30 cycles/mm would be attenuated by the cosine function. The higher frequencies passed by this filter caused considerable noise in the trace. Reducing the bandwidth to 15 to 20 cycles/mm decreased this noise considerably. Additional filtering reduced the slope of the edge trace. This slope reduction signifies the removal of important GRE film information instead of just unwanted scan lines and noise.

The photographic film characteristics in the Lunar Orbiter system have non-linear transfer characteristics.[28] The system must therefore be divided into at least two transfer functions. Consideration of the non-linearities introduced by the adjacency effects of the BIMAT-processed SO-243 might require more than two transfer functions for the system.

Two transfer functions, one for the scanner and GRE and one for lens and film were used in previous LOP analyses.[29] Edges in the calibration images at the border of the film were used as test objects to obtain the scanner and GRE transfer functions, and crater edges were used to obtain the lens-film transfer function. Calibration data were

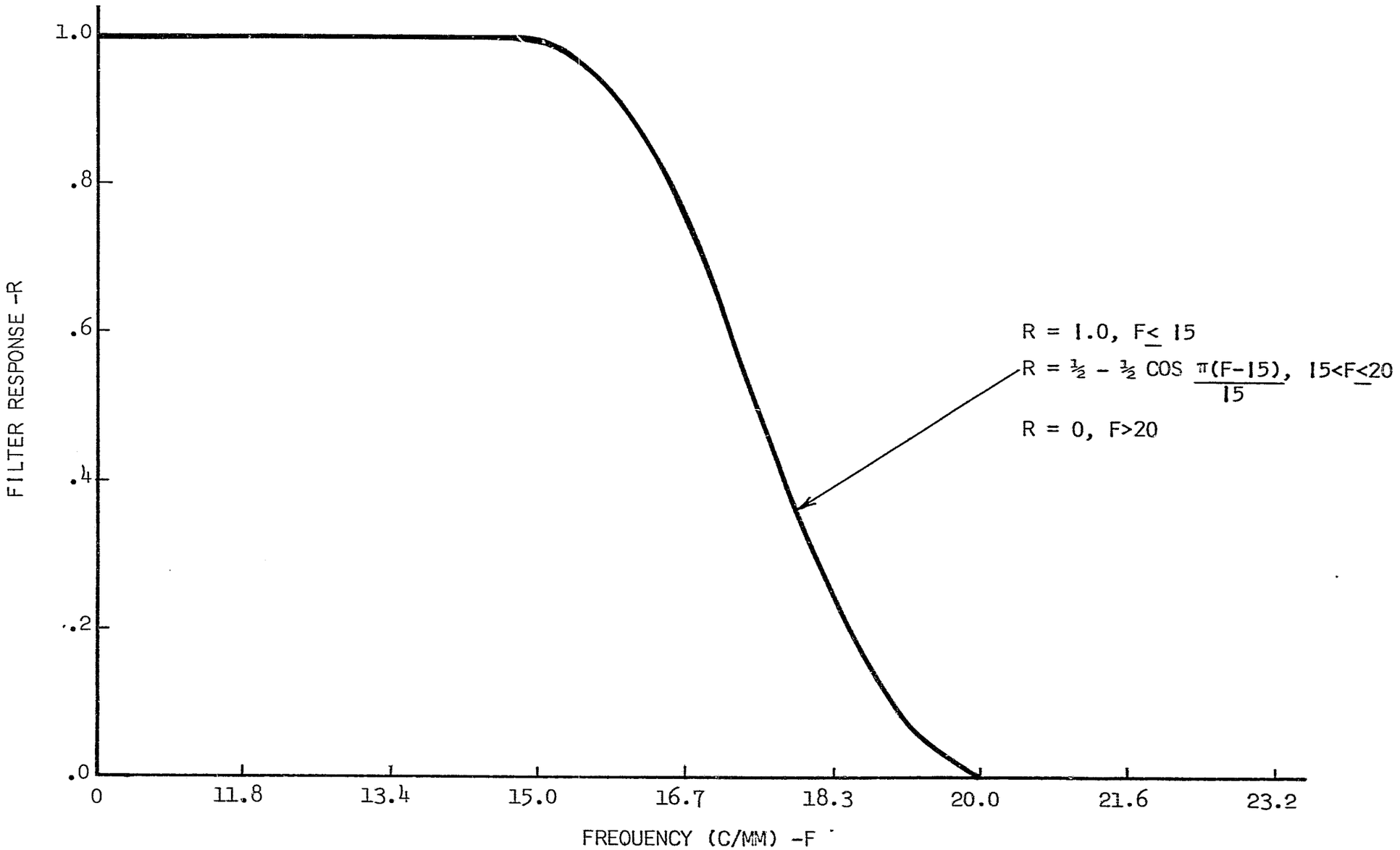

FIGURE 59. SCAN LINE FILTER FOR EDGE GRADIENT ANALYSIS ON LOP FILMS

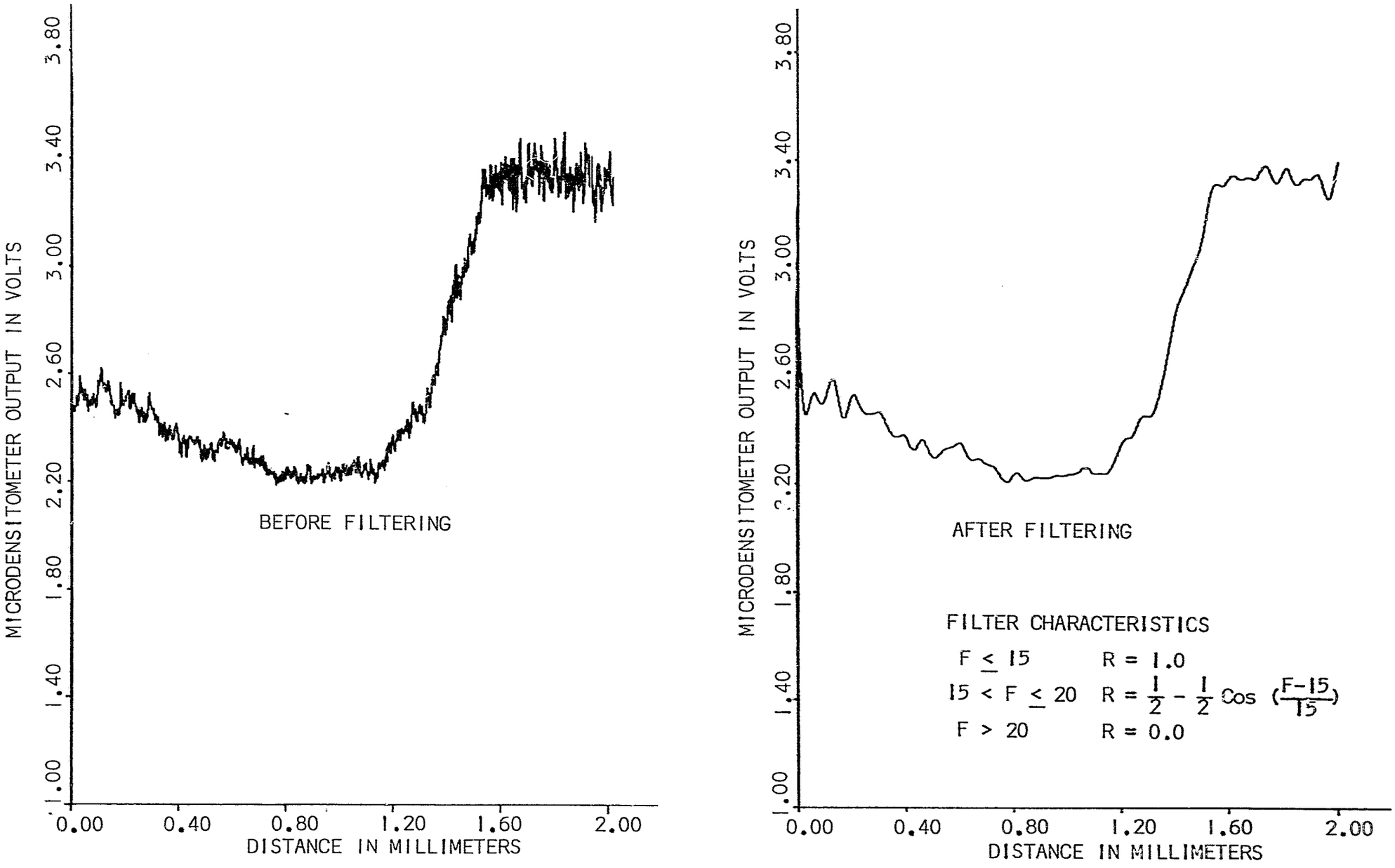

FIGURE 60. COMPARISON OF EDGE TRACES OF A LUNAR ORBITER PHOTOGRAPH WITH AND WITHOUT SCAN LINE FILTERING

used for the SO-243 film processed in the spacecraft before launch to correct for the fact that the edge data did not provide an ideal edge. The prelaunch processed film is no longer available for Orbiter III; therefore, the density profile of the edge test object is not available to this investigation.

The objective of this part of the study was to determine the size of the crater whose penumbra produced a significant difference in the measured MTF. The Lunar Orbiter was assumed to be a linear system. The necessary data were not available to do otherwise. This assumption would not affect the results of the penumbra study because the data were obtained from a single system permitting a relative comparison of results.

Figure 61 shows the MTF curves generated from the largest (440 meter) and smallest (40 meter) craters. The MTF curve from the large crater is influenced by the penumbra, as shown by the lower MTF curve.

The size of the crater whose penumbra significantly affected the MTF data was determined by statistically comparing in the Student t test for comparing means the mean MTF values at 10, 20, and 40 lines/mm of the transfer functions derived from the various size craters to the mean MTF values of the 40 meter crater at the same frequencies. The crater size at which at least 2 of the 3 MTF values were significantly different at the 95% confidence level was said to have a penumbra length significantly large enough to be resolved by the system. The three craters 438, 390, and 340 meters in diameter produced MTF curves significantly lower than the 40 meter crater.

The MTF curves from craters 4, 5, 7, 8 and 9 in Table XV were combined to get an average MTF curve for the medium resolution system of Lunar Orbiter III. This curve and 2-sigma limits are shown in Figure 62.

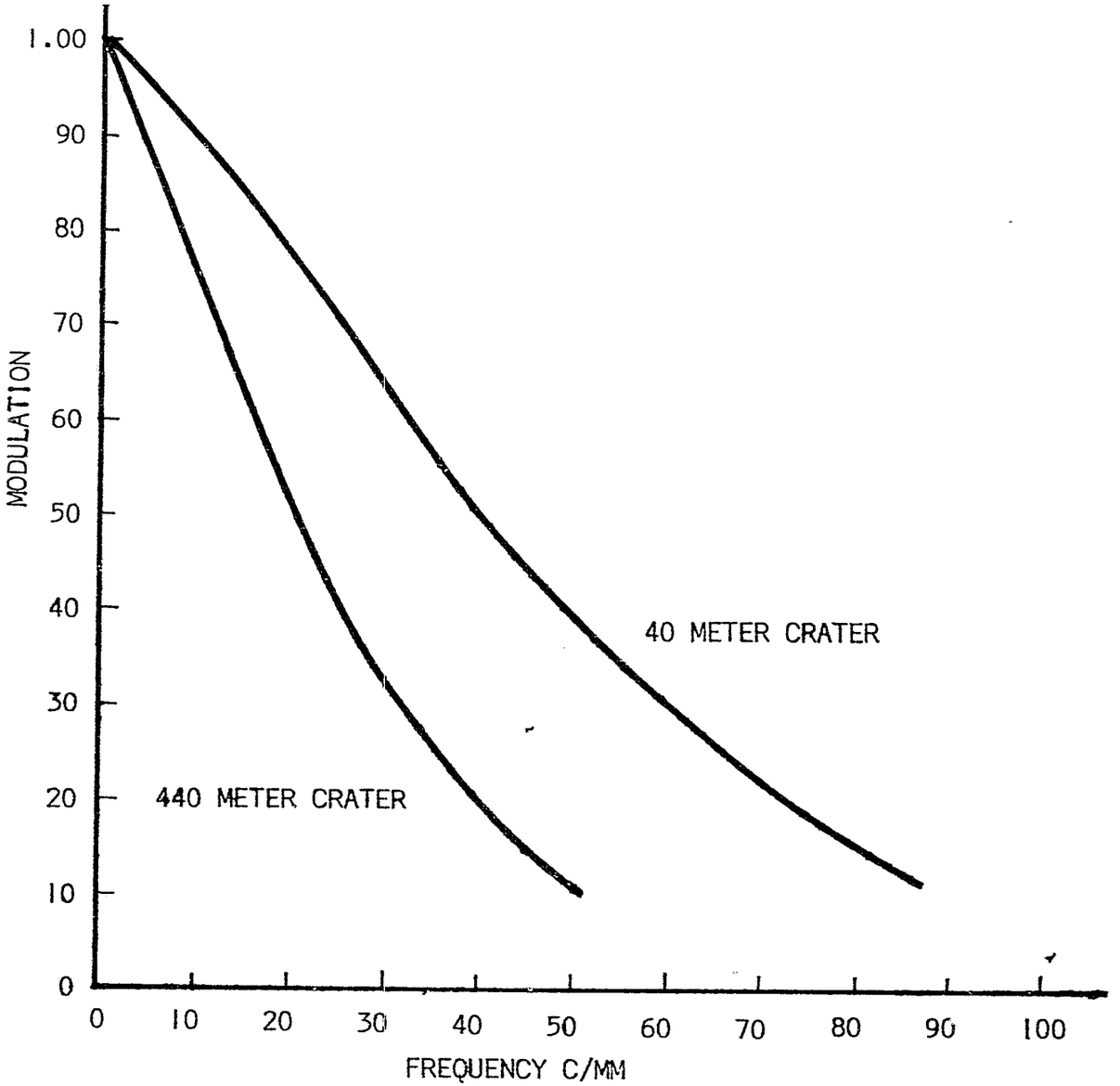

FIGURE 61. MTF MEASURED FOR THE LOP III MEDIUM RESOLUTION SYSTEM FRAMES 187 AND 188. TWO DIFFERENT CRATER SIZES USED TO MEASURE MTF; EACH CURVE AVERAGE OF 5 TRACES

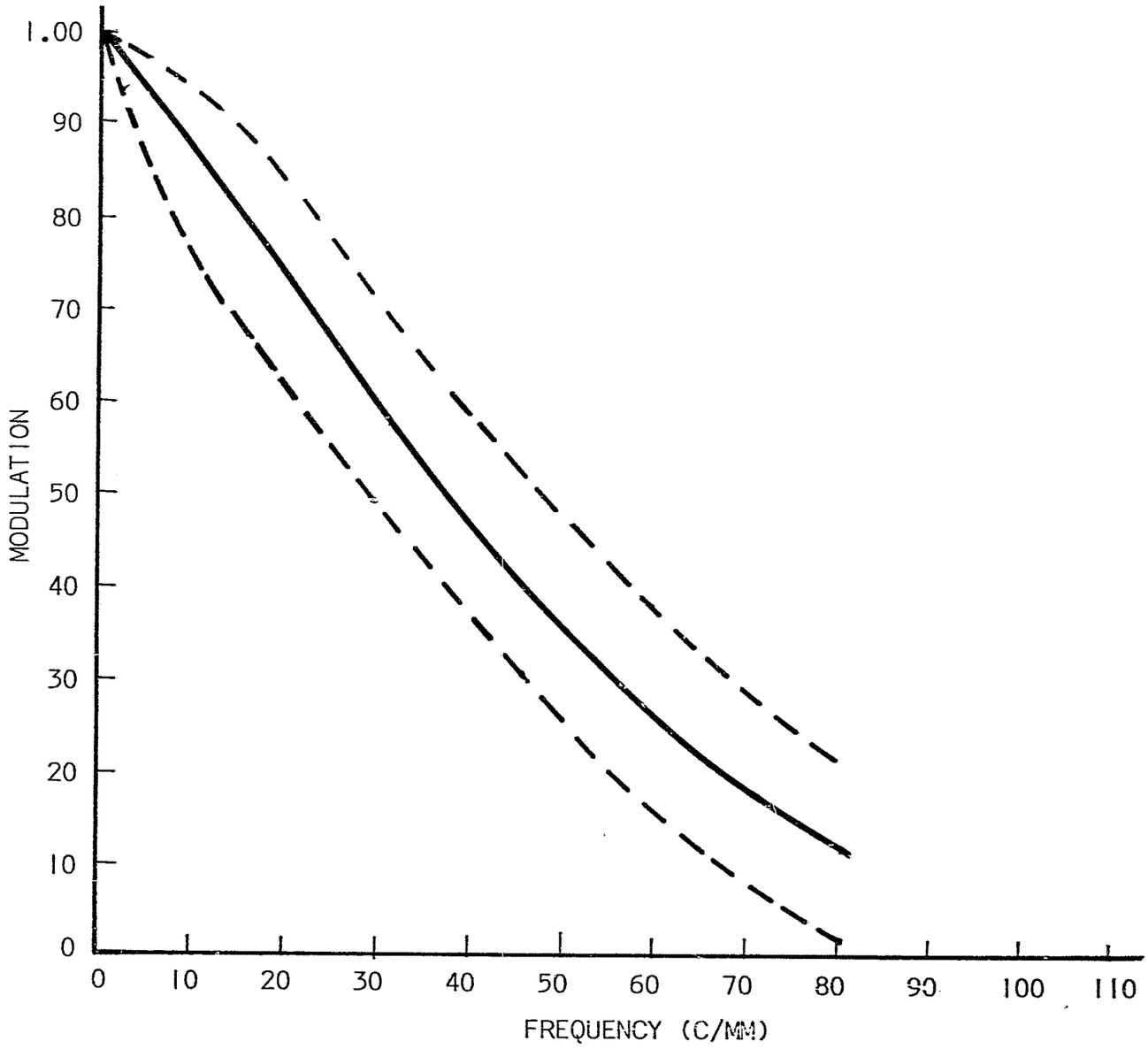

FIGURE 62. LOP. III MEDIUM RESOLUTION SYSTEM AVERAGE OF RESULTS OBTAINED FROM 5 DIFFERENT CRATERS BOUNDED BY 2 SIGMA LIMITS

4. Conclusions

From images of dusted lunar models the modulation transfer function of a photo-optical system can be measured by scanning the sunlight-to-shadow edge of lunar craters whose image diameter is less than 20 times the pitch of the limiting high contrast tri-bar resolution for the system. No lower limit on crater size was established.

In LOP III photography the penumbra did not significantly affect the determination of system MTF until the crater diameter was 40 times the nominal tri-bar pitch at limiting resolution.

The difference in results between the two sets of data is attributed to uncertainties associated with the LOP analysis. Close control of all variables was possible when photographing the model, while many assumptions as to the linearity of the system had to be made in the LOP analysis. Also, in many cases the minimum values obtained from traces of crater edges were less than the minimum from tracing edge print data. This observation reduces the confidence in the calibration data and in the measured MTF values.

Systems using film-developer combinations which exhibit adjacency effects must be treated as non-linear. Components of the system cannot be combined in a linear manner and no satisfactory way has been found to remove the MTF of the component from a system transfer function.

A system can be synthesized from its components providing the chemical spread function is taken into consideration and a non-linear combination is used.

D. Detail Recognition

1. Summary

Analysis of LOP photographs by five observers showed the results of the identification/detection studies done in Phase I work using lunar models to be applicable to vertical photographs of the lunar surface. The major difference between the results of the Phase I and the current work was that the percentage of objects detected was less on the LOP photographs. This reduction is attributed to phosphor noise, scan line structure and scene complexity in the LOP pictures.

2. Previous Work

The Phase I study dealt in part with the determination of the visual detection capability for a variety of expected lunar conditions. Section C[30] of that report evaluated an observer's ability to detect and identify several geometric shapes of different sizes photographed at a number of sun elevations and exposures. In addition, viewing stereo negatives provided data on the effect of phase angle and compared stereo and monoscopic resolution. Three readers viewed the negatives under several magnifications. Their observations of ten spherical and conical convexities and concavities were numerically weighted to differentiate the levels of recognition and displayed in matrices relating detection ability to target size for a given incident illumination and film resolution. The data were also presented to show identification capability as a function of object size relative to the tri-bar resolution limit. A cursory analysis of reader consistency indicated some reliability among observers for detecting geometric targets.

Section D[31] of the Phase I study attempted to check these conclusions with a simulated lunar model. To provide direct correlation with the earlier work, four of the geometric shapes were included in a

target area simulating a LM landing site of 160 feet on a side. In addition, boulders, fault lines, a crater chain, a shallow ditch, and several albedo differences gave realism to the site. Evaluation proceeded as before, including stereo analysis and observation made outside the ecliptic plane.

Attention was given to earliest detection and identification of each feature as the phase angle was increased. Although little quantitative correlation was achieved or even deemed significant, qualitative agreement with work done in Section C for detection capability showed remarkably similar trends quite independent of type of object or film threshold resolution (i.e., diameter/pitch ratio is the same). The results indicated Model KLM 6-65 was a realistic intermediate step that provided additional predictions as to identification of minimum crater size and percentage of craters identified as a function of phase angle for a number of photographic systems. It was also concluded that ability to detect details was similar when using either positive or negative images although readers expressed a preference for the former.

3. Present Work

A logical consequence of these studies was a determination of reader ability based upon evaluation of Lunar Orbiter photography. Verification of previous work, however, is somewhat limited by the specific parameters of Lunar Orbiter missions, e.g., Mission III: monoscopic; resolution 100 lines/mm on axis; sun elevation 6-30°; phase angle = (90° minus sun elevation) ±10°.

As the Orbiter limitation of camera and sun configuration cannot be changed, we tried to find targets similar to those used in the Phase I analysis. Scale correlation suggested Orbiter Mission III should be used as the primary source from which to conduct a search for

the required features. Objects most easily correlated with the Phase I study are: craters, D/d = 8:1, domes, D/d = 8:1, and rocks, D/d = 4:1. Table XVI lists the LOP framelets requested from NASA for use in this study.

Twelve areas displaying craters, domes, and rocks were selected from the 80mm framelets. Each area was about 1/2 inch square and contained approximately twenty objects. Table XVII lists the framelets selected and the major objects in each area. Figure 63 shows a typical area used in the study.

Each of five observers was asked to examine each test area and sketch the features he saw on the 80mm photographs. If he detected something but could not identify it, he was instructed to place an "X" on the sketch. A stereo microscope with variable magnification from 10 to 40X was used. The observers were free to choose the magnification and to vary focus. Some found it easier to decide on an object's identity by viewing the framelet slightly out-of-focus or by rapidly going back and forth through focus.

The number of objects detected or identified by an individual was compared to the possible number of objects. This latter number was established by comparison of the medium and high resolution photographs of the same area by an experienced astronomical observer. Objects were considered to be detectable when they were judged to be at or above the threshold limit of resolution on an 80mm framelet and their presence could be confirmed on the corresponding photograph taken with the 24-inch lens.

Table XVIII lists the average percentage of objects detected, identified, and detected or identified. Standard deviation values are also included.

TABLE XVI

PHOTOGRAPHS REQUESTED FOR DETECTION/IDENTIFICATION STUDY

Lunar Orbiter	Frame	Lens	Framelets
III	33	80 mm	353, 354, 355
	73	80 mm	618, 619, 620
	94	80 mm	361
	96	24 inch	418, 419, 420
	162	80 mm	575, 576
IV	133	80 mm	all
		24 inch	all

TABLE XVII

FRAMELETS SELECTED FOR STUDY AND SUBJECT MATTER

Scene Number	Mission Number	Frame Number	Framelet Number	Objects
1	IV	133	46	Domes, Craters
2	III	94	360	Domes
3	III	94	361	Rocks, Craters
4	III	94	361	Rocks, Craters
5	IV	133	42	Domes, Craters
6	IV	133	42	Domes, Craters
7	IV	133	46	Shallow Craters, Domes
8	IV	133	46	Shallow Craters, Domes
9	IV	133	46	Shallow Craters
10	III	94	359	Craters, Large Shallow Crater
11	III	94	359	Craters
12	III	94	360	Craters
13	IV	133	53	Craters
14	IV	133	41	Craters
15	IV	133	53	Craters
16	IV	133	41	Craters
17	III	73	276	Craters and Domes
18	III	73	276	Craters and Domes
19	IV	133	48	Craters
20	IV	133	47	Craters

A. SKETCH OF AREA SHOWN IN 80MM PHOTOGRAPH IN B WITH DETAILS IDENTIFIED FROM 24-INCH PHOTOGRAPH

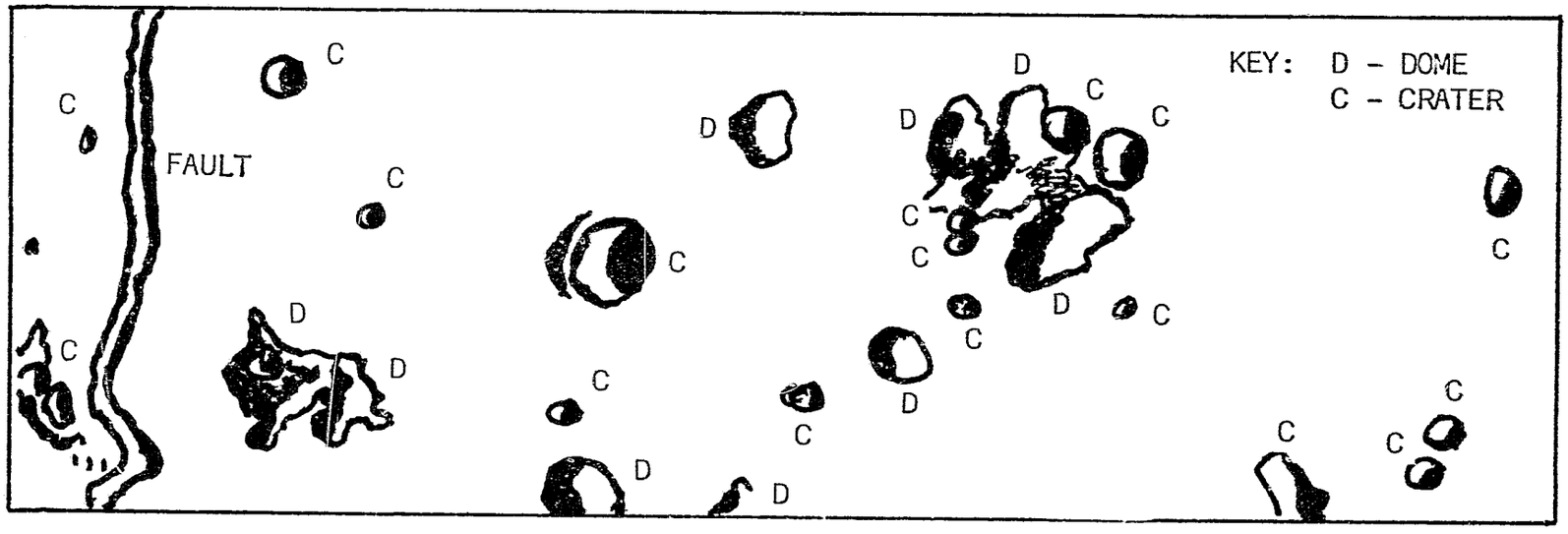

B. STUDY AREA IN 80MM PHOTOGRAPH FROM LUNAR ORBITER

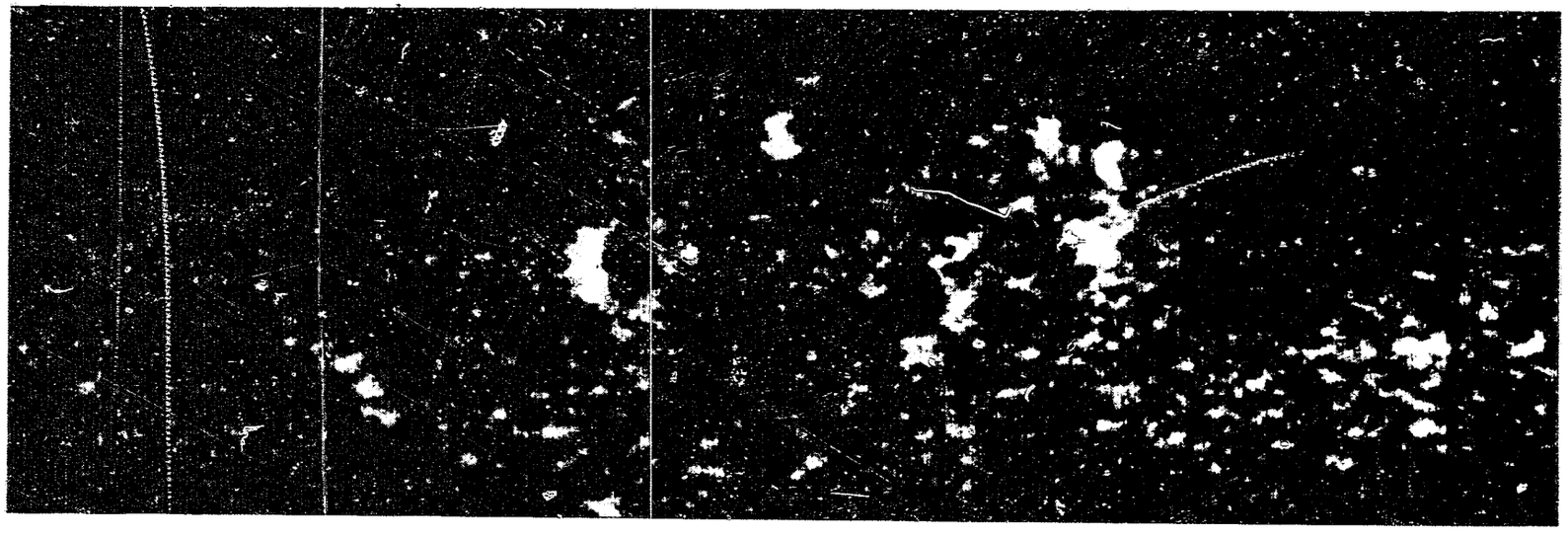

FIGURE 63. SAMPLE PHOTOGRAPH USED IN DETAIL RECOGNITION STUDY

TABLE XVIII

AVERAGE OF OBJECTS DETECTED AND/OR IDENTIFIED BY FIVE OBSERVERS IN LOP PHOTOGRAPHS WITH STANDARD DEVIATIONS

Phase Angle 70°

Object	Percent Identified	Percent Detected	Percent Detected or Identified
Crater	35±22	10±20	46±21
Domes	21±26	35±25	54±26
Rocks	40±36	36±30	76±34

The diameters of the craters selected were in the 15 to 30-meter range for Orbiter III photos and in the 150 to 220-meter range for Orbiter IV photos. Assuming a nominal high contrast resolution of 100 lines/mm for both Orbiters, the ratio of crater diameter to tri-bar pitch (D/p) ranged from 3 to 5.

The detection/identification study performed during the Phase I work at 70° phase angle showed identification of 70% of the craters for a D/p ratio of 3 to 5 compared to the 35% obtained in viewing LOP pictures. The difference between the Phase I results and these results is attributed to the presence of phosphor noise, scan line structure and the more complex scene which made it difficult for the observer to report everything he saw.

The variability between readers is represented by the values of standard deviation associated with the various percentages. This large variability is also attributed to phosphor noise and scene complexity. Furthermore, the observer's experience played some part in this variability, as those observers with more experience in looking at lunar scenes showed less variability than others.

An estimate of reader repeatability was obtained by asking two of the five readers to re-examine eight of the twelve test areas. Many weeks elapsed between the two readings, making unlikely any scene memorization by the reader.

The number and types of objects detected and/or identified in the second examination were compared to the results of the first examination. This comparison showed excellent reader repeatability. About 90% of the objects found in the first examination were also found in the second by both readers. The most common change occurred with shallow craters. Both readers identified many of the shallow craters the first time but only detected something in the second examination. No difference in detection of other objects was noted between the first and second examination.

The smallest crater identified on 80mm Orbiter III photographs was on the average 20 meters and on Orbiter IV was 180 meters. These values correspond to a diameter/pitch ratio of about 3. The Phase I work determined that a diameter-to-pitch ratio of slightly less than three was sufficient for identification at a phase angle of 70°, making the agreement between the two studies quite good.

The smallest dome identified was 1500 to 2000 meters in diameter. Orbiter IV framelets were used for this determination. These domes had a ratio of diameter to height of approximately 10.

a. Phase Angle Study

The ability of an observer to detect lunar objects varies as the phase angle changes. Two areas were selected on both Framelets 053 and 041 of Lunar Orbiter IV, Frame 133 for use in determining the effect of phase angle on identification and detection of lunar data. A cursory analysis showed that the phase angle difference between the two areas was about 10 degrees.

Sketches made by the five observers were compared to sketches made from the 24-inch photographs as before.

An exact calculation of the phase angle of each test area was made using the following relationships:[32]

$$\text{Cos } g = \text{Cos}\gamma_s \text{ Cos}\gamma_c - \text{Sin}\gamma_s \text{ Sin}\gamma_c \text{ Cos}\phi_c \qquad \text{Equation 21}$$

where g = phase angle

γ_s = angle between surface normal at camera axis intersect and sun line

$$\gamma_c = \tan^{-1} \frac{d_N}{R_S - H} + \tan^{-1} \frac{d_N}{H} \qquad \text{Equation 29}$$

H = Spacecraft Altitude

R_S = Distance from Spacecraft to center of moon

$d_N = \sqrt{x^2 + y^2}$

x = Distance on lunar surface between camera axis intersect and object. Measured perpendicular to edge of frame. Negative when point is between sun and camera axis intersect; positive when camera axis intersect lies between sun and object.

y = Distance on lunar surface between object and camera axis intersect. Measured parallel to edge of frame.

$$\phi_c = 180 - \tan^{-1} \frac{y}{x} \quad .$$

The maximum phase angle difference between any of the four scenes was found to be less than five degrees. The average phase angle for the four scenes was 69°.

There were no differences in the number of objects identified or detected in the four scenes. The small phase angle differences explain why this is true. A phase angle difference of at least 10 degrees, about a nominal value of 70° would be required before a subjective evaluation should reveal a significant difference in the size and quantity of objects detected.

The results of this study were the same as obtained with the twelve scenes examined at a phase angle of 70° in the first part of this experiment.

b. Obliquity Study

Two areas containing craters and domes were chosen on Framelet 276 of Moderate Resolution Frame 73, Lunar Orbiter III, photographed at an oblique angle of 52 degrees.

Sketches made by the five observers were compared to sketches drawn from 24-inch vertical views of the same areas.

The readers' results agreed very well with those obtained from vertical photos at the same phase angle (70°). Thus an oblique view of 52° does not reduce the size or amount of detail detectable in a lunar scene. These results are consistent with those found in the Phase I work.

c. Scene Complexity

One of the major causes of reduction in the quantity of lunar objects detected in the LOP photographs was felt to be the scene complexity. Though care was taken to choose scenes which did not contain a complex background nor a tremendous quantity of different objects, the Lunar Orbiter samples were more complex than the photographs of Lunar Model KLM 6-65 used in the Phase I work.

To get some idea of the importance of scene complexity, two rugged and complex areas were chosen in Framelets 47 and 48 of Orbiter IV, Frame 133.

The five observers were asked to find the smallest item they could confidently say was a crater. They indicated their choice by superimposing on the crater the center of a pair of crosshairs located in the eyepiece of the microscope. The size of this crater was measured on the corresponding 24-inch photograph.

The average size of the craters and the standard deviation was 210 ± 35 meters. This value was statistically compared by the Student t test to the average size (180 meters) of the smallest crater detected in Orbiter IV photographs during the first part of this study and found not to be significantly different.

In this test scene complexity did not affect the size of the smallest object detectable.

E. Optimum Presentation and Enhancement

1. Summary

Two experiments were carried out to investigate techniques to increase the recognition of detail in lunar photographs. These experiments dealt with the use of multiple photographs, viz., the value of rapid presentation of photographs of a subject from different aspects, and the enhancement of duplicate photographs by grain integration and ring smear masking.

Recognition of details of lunar surface features is increased with multiple photographs from different aspect. The value of rapid presentation is questionable.

Grain integration and ring smear enhancement were demonstrated on laboratory photographs to improve the recognition of lunar surface detail. The techniques were found not to be so valuable when applied to GRE photographs representing repetitive reconstructions of a single readout of a Lunar Orbiter photograph. The methods are believed to be applicable to Lunar Orbiter on redundant readouts of a photograph from a single mission, stereo photographs from a single mission and multiple photographs of a single area from different missions.

2. Rapid Presentation of Multiple Photographs

a. Purpose

The objective of the study was to determine if the rapid presentation of a series of photographs of different views of the same lunar area increases an observer's ability to detect detail on or near the threshold of resolution for a single static view of that area.

b. Preparation of Test Materials

Photography was accomplished in two phases. Lunar Model KLM 6-65 was dusted with copper oxide. High and low contrast tri-bar targets were attached adjacent to the model.

A 1/2-degree light source was used at an elevation of 20 degrees. Five camera positions were selected at phase angles of 30, 50, 70, 90, and 110 degrees. The model was photographed in the phase plane with an 8 x 10 camera at a 6X reduction on Tri-X Ortho film. The exposures were balanced so as to produce the same image density in the same area in each negative. The negatives were processed to a gamma of 0.8 and contact-printed onto Type 2420 duplicating film to produce positive transparencies. This film was processed to a gamma of 1.25 producing a system gamma of 1.0.

The second phase of photography consisted of photographing each of the five transparencies with a 16mm Kodak Cine Special equipped with a 15mm Cine Ektar lens and Plus-X reversal Film. The film was processed to a gamma of 1.5 producing a total system gamma of 1.5. All transparencies were registered together before photography and then carefully registered separately on an illuminator to be photographed. This procedure was required so each image occupied the same relative position in the 16mm film format. The views from 60° on either side of vertical were discarded because of severe distortion of perspective.

When viewing the projected images of each transparency, it was apparent there was too much detail in the scene to ask an observer to evaluate with any accuracy. The transparencies were rephotographed with the camera lens defocused to reduce the resolution from 57 lines/mm to 6 lines/mm on the 16mm film. This change placed 1-inch objects on the model at the threshold of resolution and reduced the number of objects in the scene to a reasonable number.

One motion picture was made showing only the vertical view of the model continuously. This motion picture corresponded to the single static view, presented to the observers in the same manner as the rapid sequences.

It was decided that, rather than use the entire model as a test object, certain selected areas would be used with a distribution of object sizes bracketing the resolution limit. This procedure permitted more control over the observer's responses and reduced the viewing time needed for each scene. Seven areas were selected and delineated by circles drawn to the proper size on the projection screen. By proper registration and magnification of the projected image the selected areas were readily defined.

The five views were then spliced together to produce sequences for repetitive projection for various time intervals for each view, making about three minutes of projection time for each motion picture. The times chosen were 16, 8, 4, 2 seconds, 1 second, 1/2 second, and 1/4 second per view. Preliminary analysis indicated that the 16-, 8-, and 4-second viewing times were too long and, therefore, these viewing times were discontinued.

When projected, the pictures showed one fault immediately. Objects off-axis shifted position on the screen as the views changed, giving an effect of changing perspective. The severity increased with

distance off axis making it impossible to keep the content of each of the seven areas constant for all five views. Because the effect was most severe at the two most extreme camera positions, these views were eliminated. The circles were enlarged slightly and two areas were replaced by two new ones closer to the optical axis. These changes reduced the effect substantially but did not eliminate it.

The spliced films were then duplicated by a direct reversal process and spliced into loops for continuous projection.

c. Observational Procedure

A panel of observers was asked to mark objects detected or identified within each circle. Some circles contained detail above the static resolution threshold, detail just at the threshold, and some below. Some other circles contained no detail as a check on the observers.

Figure 64 is a sample sheet for data collection. Eight observers were asked to view the films. Of the eight, six were experienced tri-bar resolution readers and two were trained astronomical observers. Each was asked to view each film for as long as he wanted. In each area, the observer was to indicate everything he could see by placing a C for a crater, R for a rock, or X for an unidentifiable object in approximately the same position in the circle on the data sheet as it occupied in the corresponding circle on the screen.

The first film shown was a single view looking normal to the model. The observer was given unlimited viewing time for this film. The observer was then shown the 2-second, 1-second, 1/2-second, and 1/4-second films. Each time the observer was requested to sketch what he saw in each area. The observer was also asked to answer the questions at the bottom of the data sheet after each film. In addition

VIEW-DURATION _____

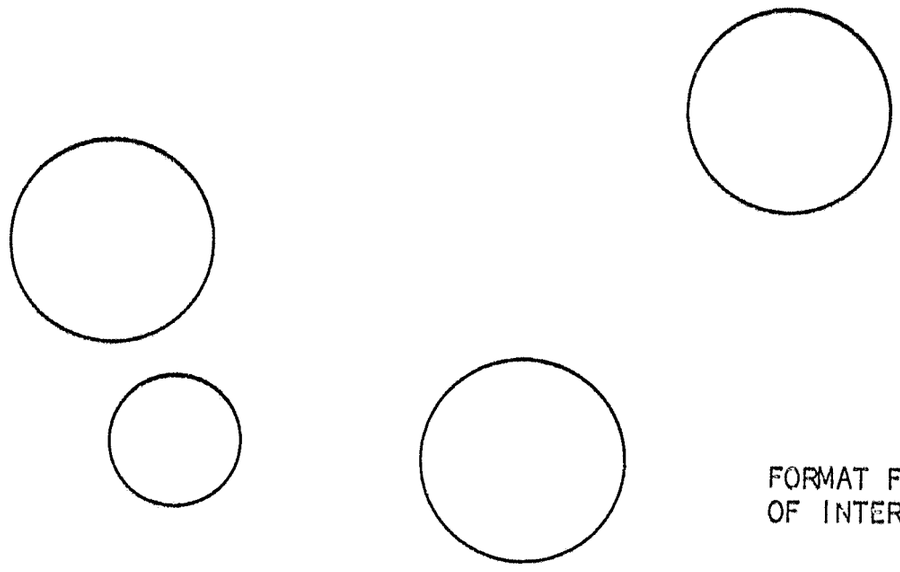

FORMAT FOR AREAS
OF INTEREST

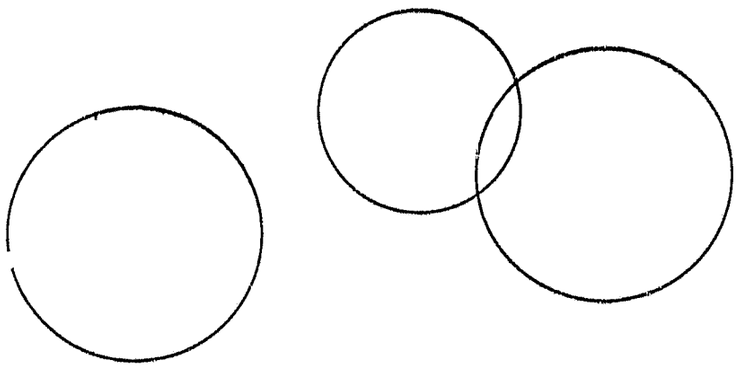

PLEASE ANSWER THE FOLLOWING QUESTIONS BY CHECKING THE APPROPRIATE RESPONSE.

	YES	NO
1. DID THE MOVEMENT OF THE PROJECTED IMAGE FROM VIEW-TO-VIEW MAKE IT DIFFICULT TO CONCENTRATE ON THE IMAGE?	____	____
2. DID THE BRIGHT FLASHES CAUSED BY THE SPLICES MAKE IT DIFFICULT TO CONCENTRATE ON THE IMAGE?	____	____
3. WOULD YOU HAVE PREFERRED A LARGER PROJECTED IMAGE?	____	____
4. WOULD YOU HAVE PREFERRED A SMALLER PROJECTED IMAGE?	____	____
5. WAS THE SCENE BRIGHTNESS LEVEL TOO HIGH?	____	____
6. WAS THE SCENE BRIGHTNESS LEVEL TOO LOW?	____	____
7. DID ALL VIEWS APPEAR TO HAVE EQUAL FOCUS QUALITY?	____	____
8. DID ALL VIEWS APPEAR TO HAVE THE SAME EXPOSURE?	____	____

9. REMARKS:

FIGURE 64. SAMPLE DATA COLLECTION SHEET FOR RAPID PRESENTATION STUDY

to answering the questions, he was asked to make any other comments relevant to the films.

d. Data Analysis

Figure 65 shows the responses of each reader to each film.

All viewers felt there was an increase in ability to detect objects with three views rather than one and reported the rapid presentation offered no gain and, in fact, cost some degree of confidence as the presentation rate became faster. Except for Observer 3, all observers show an increase in the number of objects detected with three views over a single view. The observers did not feel that the rate at which the views were presented had any effect on detection at low rates. A check of the graphs of observers' responses shows for most observers a zero or slight negative slope as rate increases, but observers 5 and 7 showed a definite positive slope from the 2-second to the 1/4-second rate. These people were two experienced astronomical observers, suggesting that the familiarity of the observer with lunar scenes has an influence on the amount of benefit derived from this method. Over half the observers felt that they had less confidence in identifying objects as the presentation rate increased to high rates.

An analysis of variance was performed to compare observers and presentation rate. The results show the observers to be the greatest source of variation, while there was no significant effect because of presentation rate. A second analysis of variances was made to compare observers and the single view and 2-second rate. Again the observers proved to be the larger source of variability. The two presentation rates were not statistically different; however, they showed a much greater difference than did the comparison between rates in the first test. The error term, however, comprises 22.4 percent of the

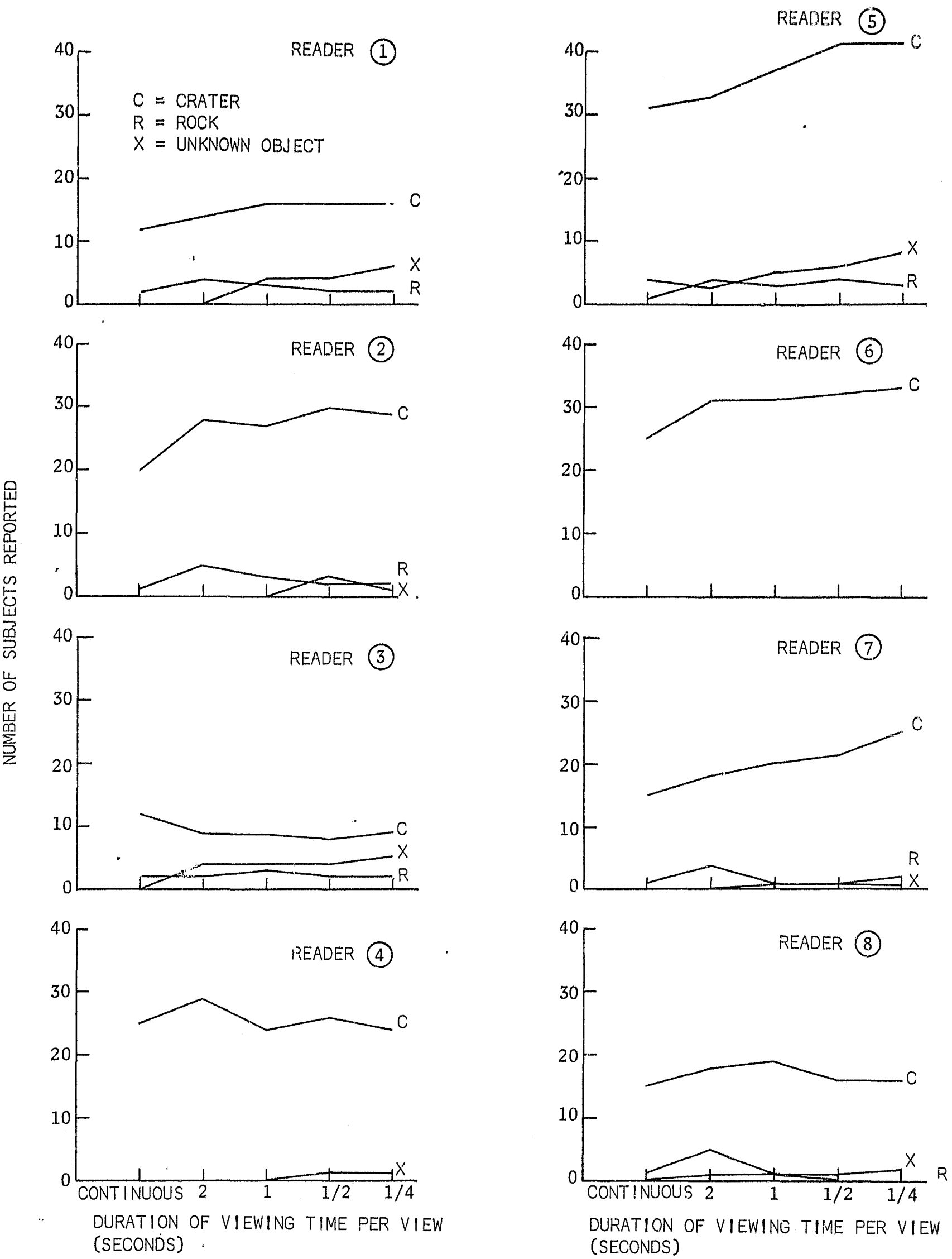

FIGURE 65. RESPONSES OF READERS TO RAPID PRESENTATION OF 3 VIEWS OF THE SAME LUNAR AREA FOR DIFFERING VIEWING TIMES

total variation indicating the need for replicate data sets to determine if any interaction exists between the two factors.

All observers complained of being distracted by the shifting of objects from view to view. Most felt the effect became more troublesome as the rate increased. Several, however, said the 1-second rate was the most difficult to view. As they viewed more films, they became used to the movement, and found it less distracting. Since the views are projected sequentially, the movement develops a rhythm or cyclic pattern which makes concentration easier for some people. A random order of presentation may be useful in reducing or eliminating this effect.

The two astronomical observers felt the single view used as a standard should have been the view with the largest phase angle which would have the highest contrast for the views used in this study.

All observers noticed that the splices produced flashes as they passed through the projector. At the 1/2-second and 1/4-second presentation rates, these interruptions became objectionable.

This technique for rapid presentation of pictures is a time-consuming method to use. It is difficult to produce scenes of equal contrast, brightness and resolution. The image shift caused by changes in perspective from view to view is a serious problem that detracts from an observer's ability to concentrate. It can only be eliminated by restricting attention to areas within a few degrees of the optical axis and restricting the angle through which the views are obtained.

e. Conclusions

The results of six untrained and two trained astronomical observers show increased detection with multiple views, and a marginal

improvement due to the rapid presentation for the trained observers and little or no improvement for the untrained observers. By far the largest source of variation in the data is caused by the individual observers.

3. Enhancement of Lunar Details by Grain Integration and Ring Smear

a. Background

Techniques have been developed by Eastman Kodak Company for the enhancement of photographic images using grain integration and ring smear. These techniques were applied to laboratory photographs of a model and to Lunar Orbiter photographs to estimate their effectiveness on improving lunar photographs.

In grain integration[33] several photographs are made of the same scene and separate, registered exposures are made from each photograph to produce a single print with reduced granularity.

Ring smear[34] is a special case of unsharp masking in which a mask having a particular modulation transfer function is generated to produce an enhancement over a controlled frequency bandwidth.

The ring smear enhancement is used to increase the modulation of the fine details while the grain integration increases the ratio of signal to grain noise. Generally, the greatest enhancement is obtained when both ring smear and grain integration are performed simultaneously on the same scene. These techniques are particularly applicable to photographs of low contrast, fine detail objects such as the lunar surface in the absence of shadows.

i. Grain Integration - A photographic image is composed of many silver grains. The number of these grains per unit area is related statistically to the number of photons per unit area incident on

the film during exposure. A measure of the number of these grains and hence of the original exposure is the optical density for a given area of developed film. Density is expressed by the following relationship:

$$D = \log_{10} (1/T) \qquad \text{Equation 30}$$

where D = density of the area

T = transmission of the area = $\frac{\text{flux transmitted}}{\text{flux incident}}$

The accuracy with which a given density (or transmission) may be attributed to a definite exposure is limited. For film, this limitation arises primarily from the variation in size and quantity of developed silver grains that are encountered per unit area for the same original exposure. The fluctuations in the original exposure because of photon statistics are generally unimportant in relation to grain statistics. The fluctuations in measured density, for a given uniform exposure, over different regions of the developed film can be described by Selwyn's Granularity Law. This law is expressed by the following relation:

$$G = (A)^{\frac{1}{2}} \cdot \sigma_D \qquad \text{Equation 31}$$

where G = a constant, known as Selwyn's Granularity

A = the image area of interest

σ_D = the RMS fluctuations in measured density for the area A over different regions of the uniformly exposed film.

Thus, it should be apparent that if one wished to attribute a measured density for an area A to some original exposure, the inaccuracy in the measurement of D, due to σ_D, limits the process.

The signal-to-noise ratio in a photographic image is given by:

$$S/N = \Delta D/\sigma_D \qquad \text{Equation 32}$$

Thus, any decrease in σ_D, the RMS granularity, will cause an increase in the signal-to-noise ratio. One technique to accomplish a reduction in RMS granularity is "grain integration." This technique involves the superposition in excellent registration of a number of first-generation photographs of the same scene. Each photograph must have the same scale and aspect angle. The resulting composite image will have an RMS granularity given by:

$$\sigma_{D'} = \sqrt{N} \cdot \sigma_D \qquad \text{Equation 33}$$

where $\sigma_{D'}$ = the RMS granularity of the composite

σ_D = the RMS granularity of each photograph. It is assumed that the value of σ_D for each of the separate photographs is, point for point, the same.

N = the number of separate, but identical photographs being superimposed.

This relationship is a direct result of the statistics associated with the measurement of density. That is, if density is measured over a number of small areas of a piece of uniformly exposed film, the recorded density values will form a Gaussian or Normal distribution. The standard deviation of this distribution is σ_D, the RMS value of the density measurements. When a number of separate negatives are superimposed, the value of σ_D, for the resulting composite will be the root-sum-square of the values of σ_D for each separate photograph. That is,

$$\sigma_{D'} = (\sigma_{D_1}^2 + \sigma_{D_2}^2 + \ldots\ldots + \sigma_{D_N}^2)^{\frac{1}{2}} \qquad \text{Equation 34}$$

but since it is assumed that $\sigma_{D_1} = \sigma_{D_2} = \ldots\ldots \sigma_{D_N}$

$$\sigma_{D'} = (N \cdot \sigma_D^2)^{\frac{1}{2}} = \sqrt{N} \cdot \sigma_D \qquad \text{Equation 35}$$

The density (the expected value) of the composite photograph will be point-for-point the sum of the individual densities in the separate photographs. In other words,

$$D' = N \times D \qquad \text{Equation 36}$$

where D' = the density of the composite
D = the density of the individual photographs
N = the number of photographs being superimposed

The signal-to-noise ratio in the composite is then given by:

$$S/N = N \cdot \Delta D/\sqrt{N} \cdot \sigma_D = \sqrt{N} \cdot \Delta D/\sigma_D \qquad \text{Equation 37}$$

That is, the signal-to-noise ratio of the composite photograph is greater than the signal-to-noise of one of the photographs by a factor equal to $\sqrt{N}$.

The effect of grain integration is observed when one views stereo pairs. The degree of this "visual grain integration" depends upon the difference in quality and aspect angle between the pair, and the relief height of the object being observed. For two-dimensional subjects such as tri-bar targets, an improvement in resolution of about one $\sqrt{6/2}$ target increment, or about 12 percent has often been observed in viewing stereo pairs.

ii. Unsharp Masking (Ring Smear) - The general nature of the photographic image resulting from lunar photography may be characterized near the limit of resolution by low contrast, fine detail. Historically, unsharp masking has been used to increase the contrast of such fine detail relative to that at lower spatial frequencies. This has been accomplished by generating a "fuzzy," negative copy of the original, which is then used with the original to generate a composite by superposition. Because the overall contrast of the composite is reduced, relative to the original picture, high contrast printing is used in recording the composite image. The resulting image will have a lower contrast at low frequencies than at high frequencies. The sketch in Figure 66 illustrates this conventional form of unsharp masking.

Armitage, Lohmann and Herrick have proposed a variation of the usual technique that produces a greater relative increase in the contrast of fine details. In this ring smear technique, a modulation transfer function is applied in making the mask that provides a phase inversion in the fine detail of the image spectrum. The sketch in Figure 66 illustrates the effect of this modified method of unsharp masking.

The results of the analysis performed by Armitage, Lohmann and Herrick show that, under certain conditions, the transfer function of the unsharp masking process is given by the following relation:

$$\tau = 1 - \gamma_m \cdot \tau_m \qquad \text{Equation 38}$$

where τ = the transfer function of the unsharp masking procedure

γ_m = the gamma of the photographic material upon which the unsharp mask is recorded

τ_m = the transfer function of the unsharp mask generation procedure

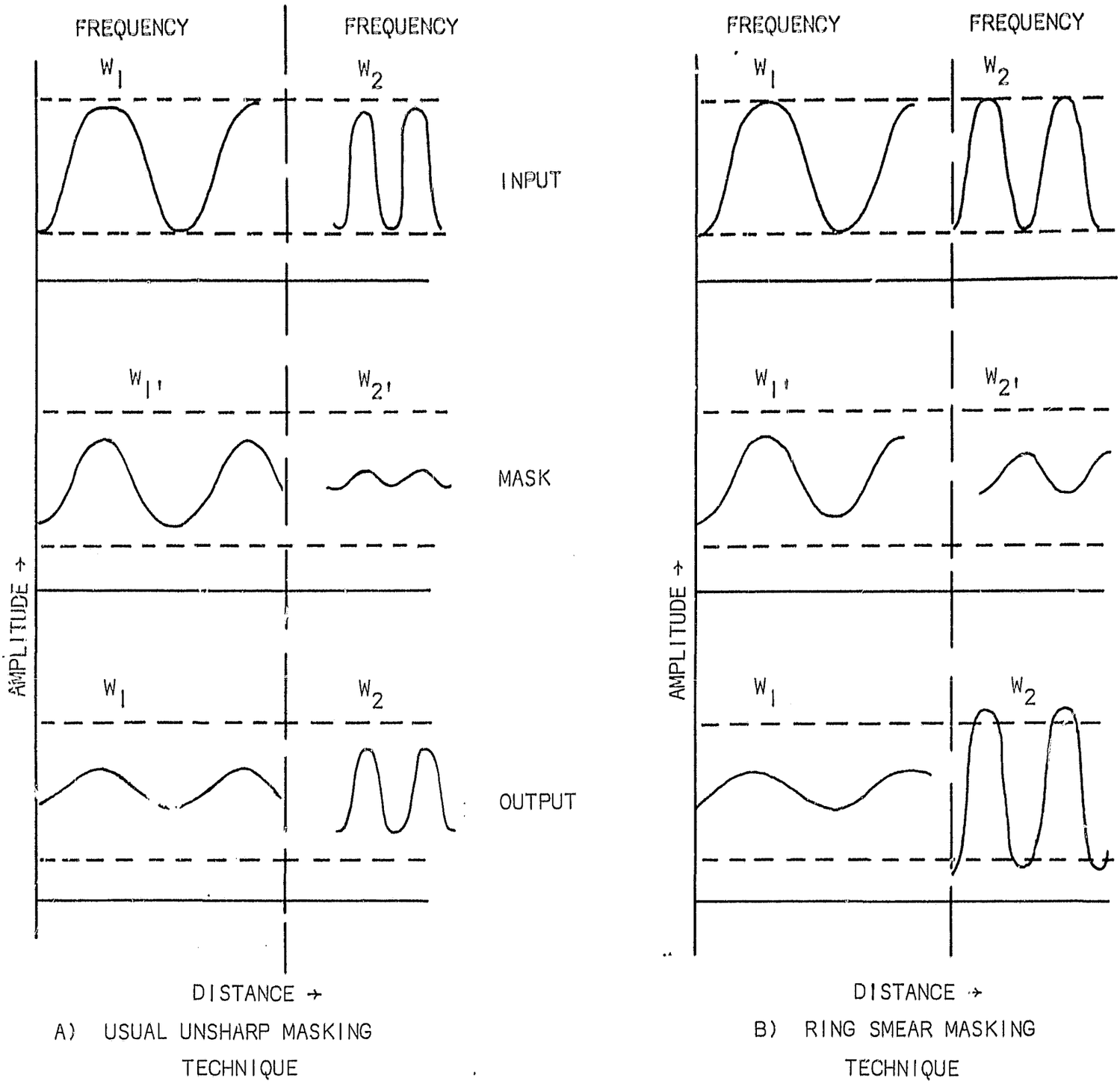

FIGURE 66. THE EFFECT OF CONVENTIONAL AND RING SMEAR MASKING ON THE AMPLITUDE OF TWO SPATIAL FREQUENCIES

The conditions required for this relationship to hold are that the modulation of the unsharp mask be less than that of the original, and that the modulation of both be less than some maximum value, approximately 0.3. Both of these conditions can be reasonably well satisfied. The quantity τ, given in the above equation, is the transfer function corresponding to the processing spread function of the unsharp masking process. Any desired form of τ may be obtained, provided the appropriate mask transfer function, τ_m, can be generated. To obtain enhancement over some band of frequencies, the value of τ must be greater than 1.0. It can be readily seen that this condition will occur for the appropriate value of γ_m, whenever τ_m becomes negative. Such transfer functions are known. A defocused lens is one example. However, Armitage, Lohmann and Herrick proposed another method of generating a very strongly negative transfer function. This method is called "ring smear." To generate an unsharp mask by this method, every point in the original photograph is smeared into a ring in the mask. The transfer function of this process is given by:

$$\tau_m = J_0 (2 \pi \rho \nu) \qquad \text{Equation 39}$$

where J_0 = a Bessel function of the first kind, of zero order
ρ = the radius of ring smear
ν = the spatial frequency

This transfer function, plotted in Figure 67, goes very strongly negative to a maximum of about -0.4. The resulting enhancement function, τ, given by Equation 38, is plotted in Figure 68 for m = 1.0. Note that τ goes above 1.0 to a maximum value of 1.4.

The ring smear technique uses a precision enlarger. The unsharp mask is generated by rotating during the exposure a tilted glass plate 3.0mm thick placed in the optical path of the enlarger system. A sketch of this experimental apparatus is shown in Figure 69 while Figure 70 outlines the procedure for making and using the mask in ring smear enhancement.

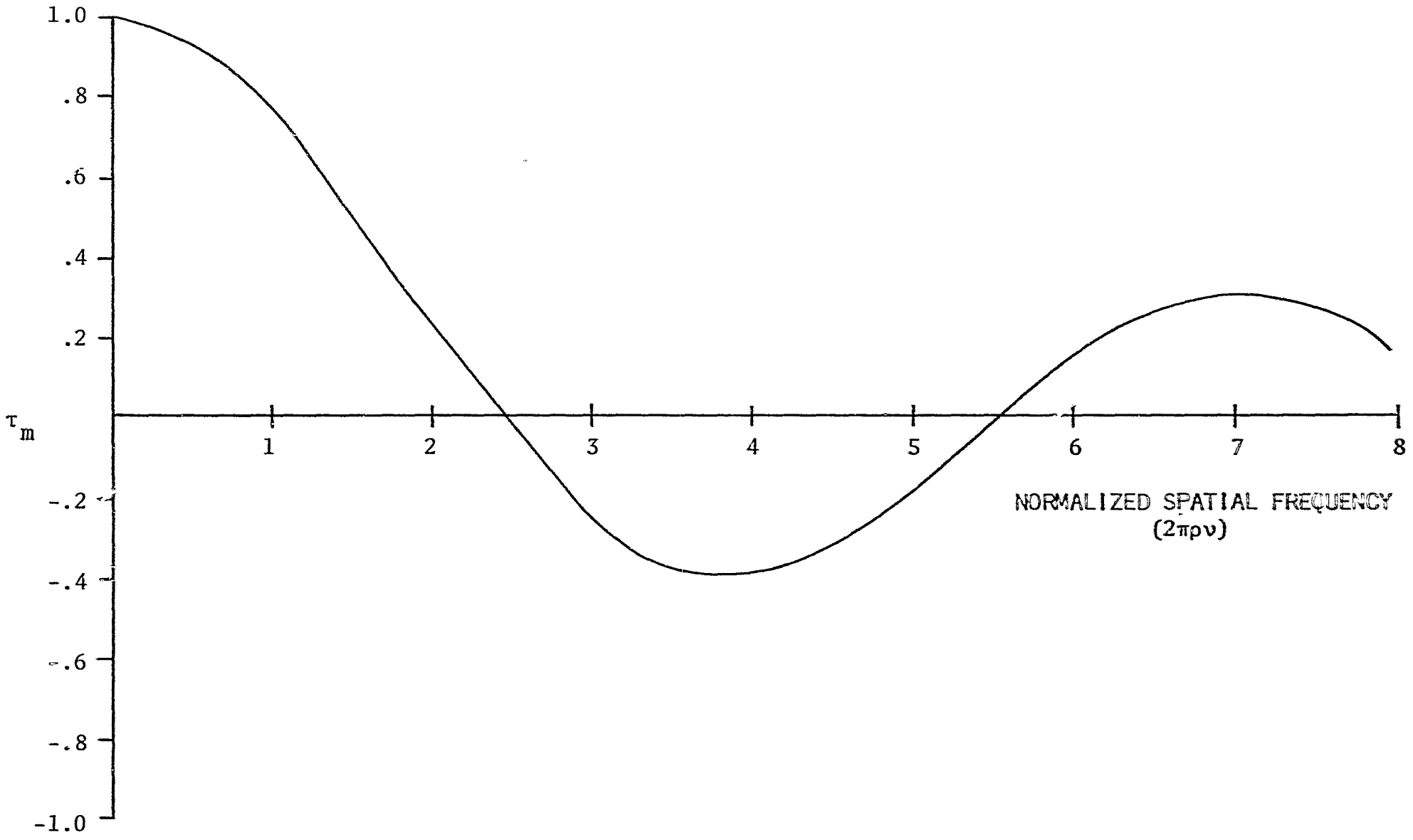

FIGURE 67. MASK TRANSFER FUNCTION τ_m RING SMEAR

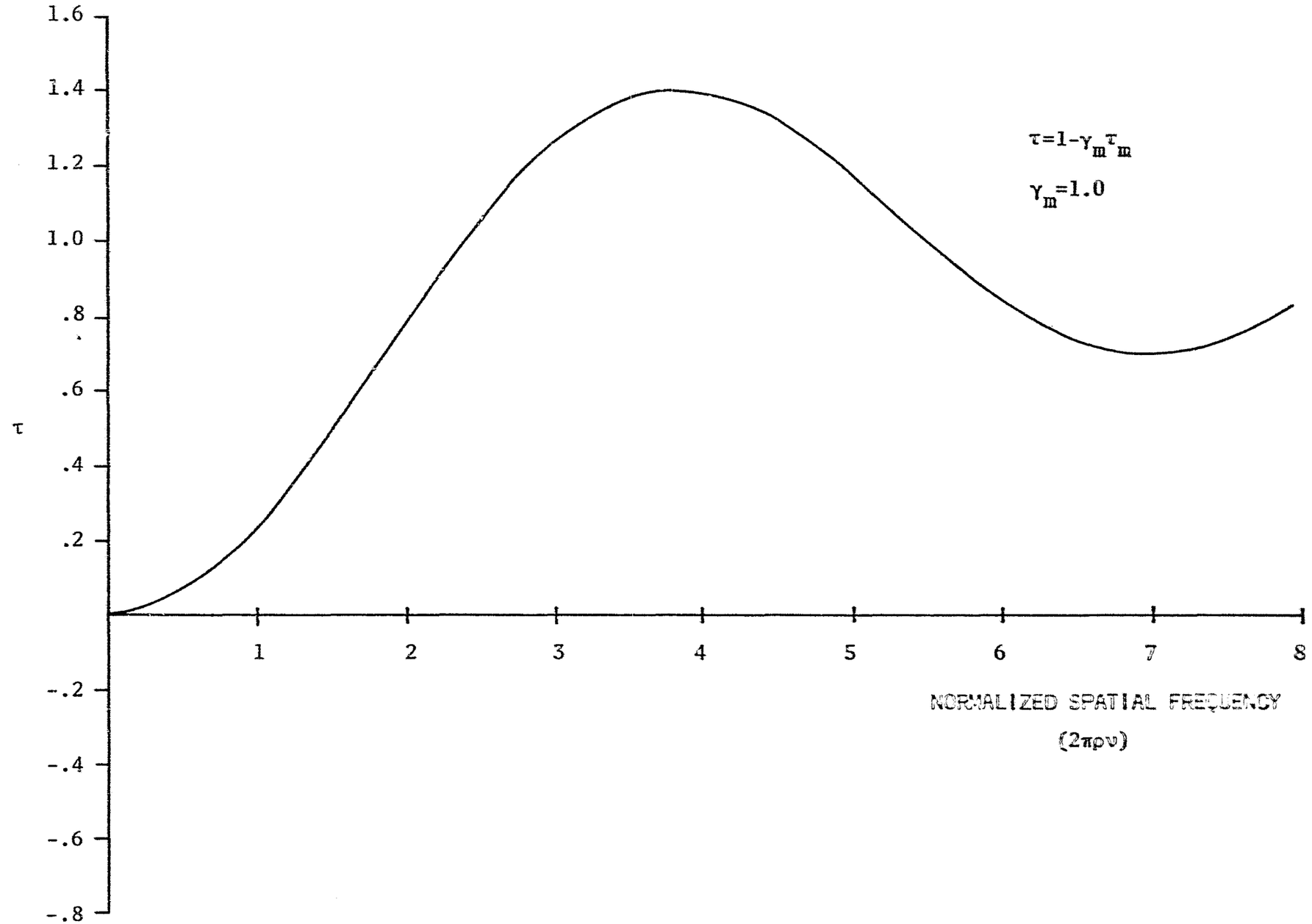

FIGURE 68. SYSTEM TRANSFER FUNCTION - FOR RING SMEAR

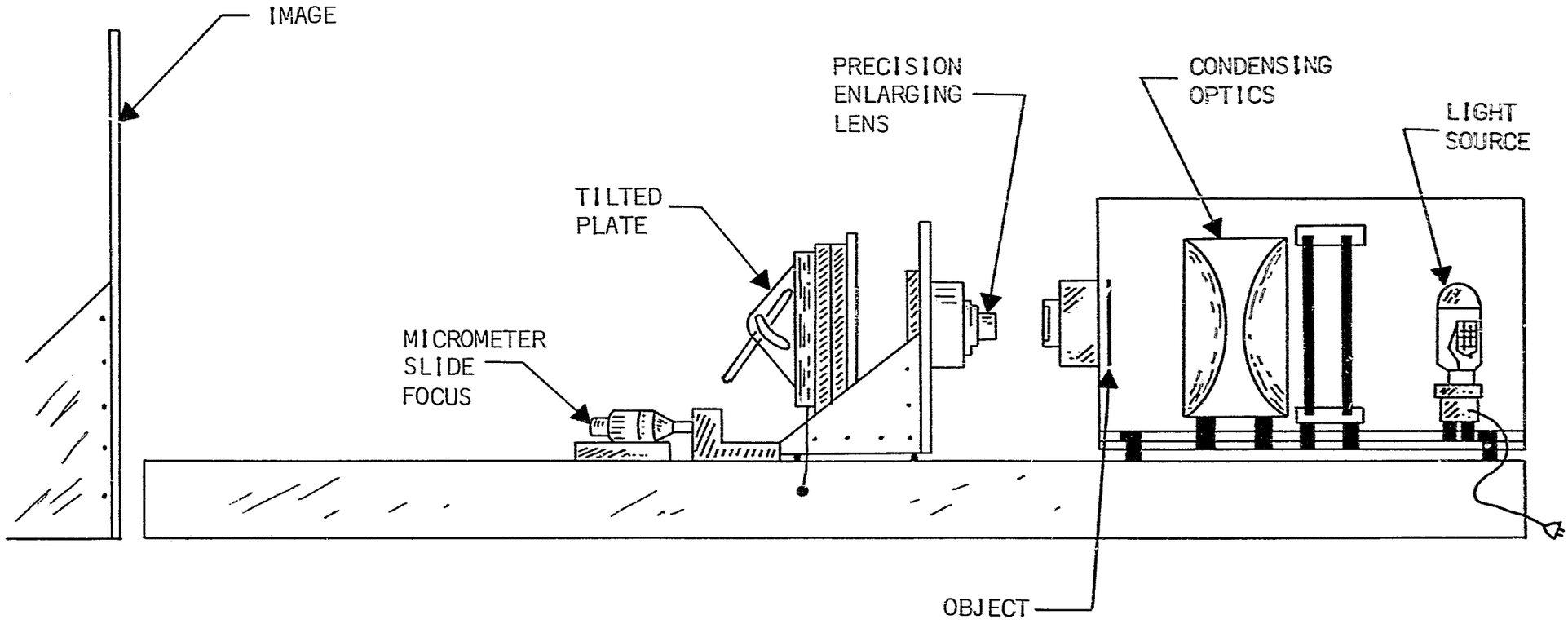

TILTED PLATE IS ROTATED DURING EXPOSURE TO PRODUCE RING SMEAR

FIGURE 69. SKETCH OF RING SMEAR APPARATUS

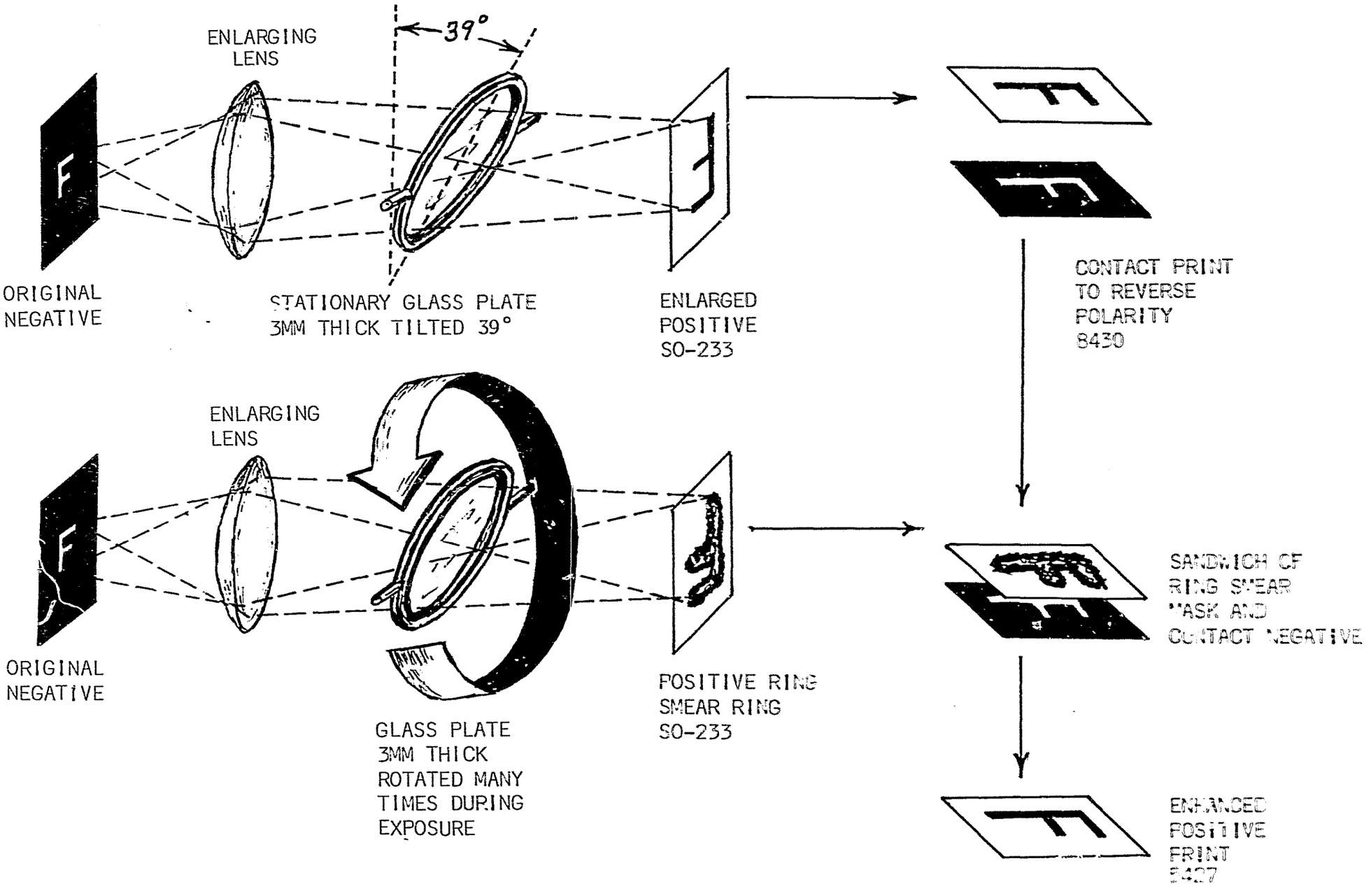

FIGURE 70. SCHEMATIC DIAGRAM OF THE PROCEDURE FOR RING SMEAR ENHANCEMENT

b. Demonstrations of Grain Integration and Ring Smear

Experiments with the technique of grain integration were performed, during the course of this study, to determine how well the technique worked with lunar photography. The methods were first applied to laboratory photographs of a lunar model and then to Lunar Orbiter photographs.

i. Laboratory Photographs - Photographs were made on SO-243 film at a scale of 1:30,000 and at a sun elevation of 30°. The image quality of the pictures was degraded by defocusing to 50 lines/mm from 120 lines/mm. This film resolution is equivalent to 23.6-inch resolution on the lunar surface.

For the grain integration experiment, three nominally identical simulations of 50 lines/mm quality were used. A print from one of these is shown in Figure 71A. The grain structure of each simulation negative should be statistically independent of the others. A print showing the results of superimposing three separate negatives is shown in Figure 71B. The granular appearance of the composite is less than that of any one individual negative, suggesting that the signal-to-noise characteristics have been improved by the grain integration process.

Ring smear enhancement with grain integration was performed on the lunar simulation with 50 lines/mm quality, degraded from 120 lines/mm by defocus. The bandwidth over which enhancement occurred was chosen so that the enhancement stopped at the observed resolution of the simulation. This cutoff was chosen because experience gained from other work has shown that enhancement applied beyond the system cutoff frequency increased the film grain noise excessively. Figure 71C shows a 40X enlargement of the original simulation negative enhanced by ring smear only. Figure 71D shows the same scene enhanced by the combined

ring smear and grain integration techniques. Enhancement occurred from 20 to 48 lines/mm; maximum enhancement occurred at a frequency of 34 lines/mm.

The maximum enhancement of details is shown by comparing Figure 71A made from the original single negative with Figure 71D, a composite print combining grain integration and ring smear masking. No new details are seen; the observer finds that all threshold information in the enhanced photo is present in the conventional reproduction. However, the observer has improved confidence in his detection and identification of subjects.

The lack of new details is not a universal result of these techniques. The gain achieved by grain integration depends on whether the initial photography is primarily limited by optical quality as in this demonstration, or by film grain.

ii. Lunar Orbiter Photographs - Multiple images from one GRE and duplicate images from another GRE were used in this attempt to enhance LOP photography. The purpose of this short study was to determine if LOP photography could be enhanced by either random noise integration or ring smear masking. GRE film from telephoto Frame 137, LOP Mission III were furnished by NASA for this work.

α. Grain Integration - It was assumed that the noise apparent in the GRE image was caused by phosphor noise in the GRE. Since the input signal from the spacecraft was an analog signal, the noise from the GRE phosphor should be random. If the noise actually were random, then superposition of multiple images should reduce the apparent noise as it has done in "grain integration" of normal photography. The effect of noise integration is most apparent when the signal is limited by random noise and not by optics or systematic noise.

A. UNENHANCED ORIGINAL

B. ENHANCED BY GRAIN INTEGRATION

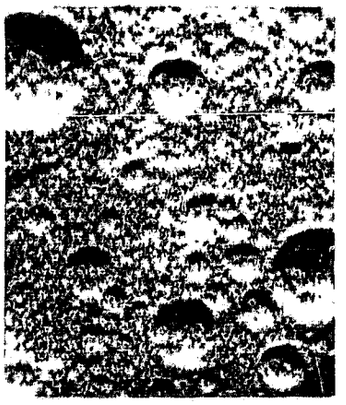

C. ENHANCEMENT BY RING SMEAR

D. ENHANCEMENT BY GRAIN INTEGRATION AND RING SMEAR

FIGURE 71. ENHANCEMENT OF LUNAR MODEL PHOTOGRAPHS BY GRAIN INTEGRATION AND RING SMEAR

Two methods of noise integration were attempted:

1. Four positives from 1 GRE
2. Two positives from each of 2 GREs

A suitable scene, which showed fine detail, coarse detail and tonal gradients, was selected for the enhancement study. This scene was cut from the GRE prints and sensitometrically and visually evaluated to ensure that each copy was essentially of the same quality and characteristics.

The linearity pattern indicated a large amount of distortion in the image. The distortion would not hurt the enhancement study since it was caused by the readout and, therefore, would be included in each GRE image.

Images were superimposed using a precision enlarger at an 8 X enlargement. The limiting resolution of the scene was estimated to be 14 lines/mm. With an 8 X enlargement the finest detail presented to the eye is 1.75 lines/mm.

Images were made at the following conditions:

1. Straight print
2. Two positive superimposition, 1 GRE
3. Three positive superimposition, 1 GRE
4. Four positive superimposition, 1 GRE
5. Four positive superimposition, 2 GREs (two positives from each)

The enlarger was set up as shown in Figure 72.

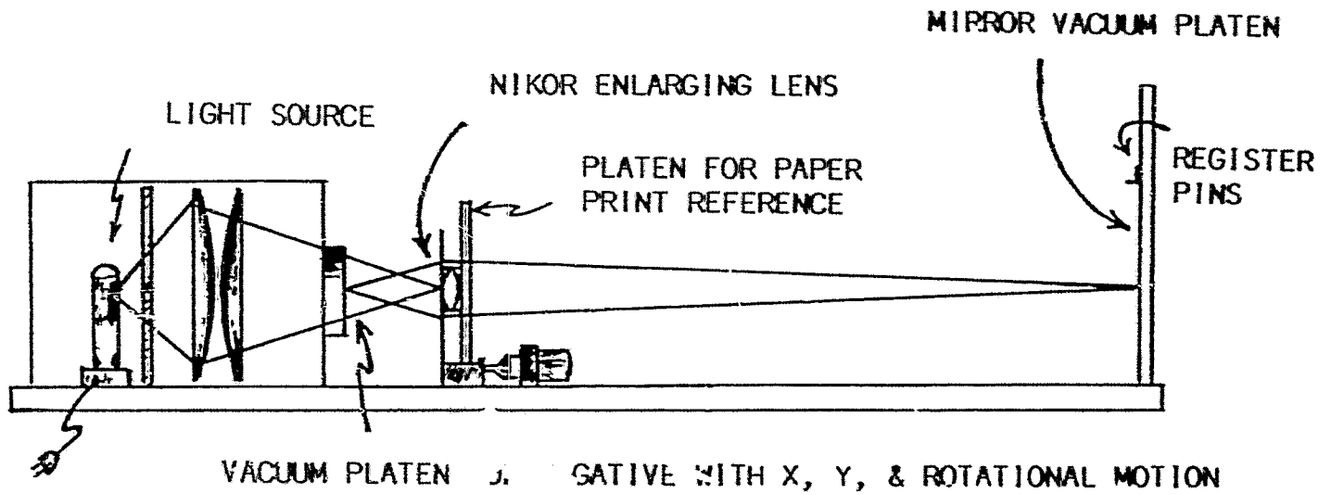

FIGURE 72. PRECISION ENLARGER SET-UP FOR GRAIN INTEGRATION

The first step in the procedure was to make a best straight print from one positive for use as a comparison print for subsequent enhancement work.

A reference paper print is made by reflecting the image from the mirror at the primary platen back toward the lens to the reference print platen. The image is made at the best focus on the reference print platen. The processed reference print is placed back on the reference platen. All subsequent photographs are aligned with this reference print. Two factors make this type of alignment very accurate. First, there is an optical lever of about 2 X magnification over the enhanced print because the working distance is approximately doubled. Also, since the reference print is a negative, and the GRE image to be aligned is a positive, the eye is extremely sensitive to minute registration errors. With perfect registration, the image suddenly goes black; any registration errors show up as white lines on a black background. In making the integrated prints, the enlarger is focused for best imagery at the primary platen.

To make a print with four superimposed images, for example, the images are aligned successively with the reference print and each of the four images is given 1/4 of the total exposure. This process was performed for combinations of 2, 3 and 4 superimposed images with appropriate adjustments in exposure for the number of superimpositions. The differences in density for the different GRE images was compensated for when calculating the exposure times so each GRE image would produce an equal effect.

It is not possible to make four separate enlarged prints and superimpose these images to make an enhanced sandwich, because adding prints on top of each other effectively is adding gammas, therefore, increasing contrast.

As shown in Figures 73A, B, C and D, no significant difference was noticed between the reference print and prints made by noise integration from 2, 3, or 4 positives. This result indicates that the limiting noise is not random and that noise integration would not be useful. To verify this finding, a pair of images from one GRE were evaluated on a comparison microscope and the noise patterns appeared to be identical as shown by the enlargements in Figure 74. It is felt that the noise was created by the phosphor in the spacecraft flying spot scanner, and therefore, would be common to each GRE reproduction.

Superimposed images made from the two GREs also verified the conclusion that the noise was created in the spacecraft. Visual comparison of these images again showed a similar noise pattern. Also, when superimposed images were made, the photographs showed a moiré pattern, indicating a slightly different scale, in one direction, between images. Figure 73E shows superimposed images from two GREs with the moiré pattern. This scale difference could be compensated for in the printing stage by tilting the platen. However, since the noise was not random, no improvement would be expected from superimposing the images and this additional adjustment was not attempted.

Three approaches might be used to apply grain integration techniques to these GRE films. One technique uses mathematical filtering of the noise before it is printed in the GRE. A cursory examination indicates that the noise spectrum is completely contained in the signal spectrum and, therefore, could not be filtered out without degrading the signal. In order for this technique to work, the noise spectrum would have to exceed the signal spectrum, a condition implying that the noise is created at a different and later stage of the image-forming process. This approach is not promising but should be examined more thoroughly before being discarded.

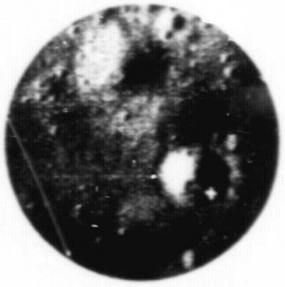

B. SUPERIMPOSITION OF 2 POSITIVES FROM GRE 12T

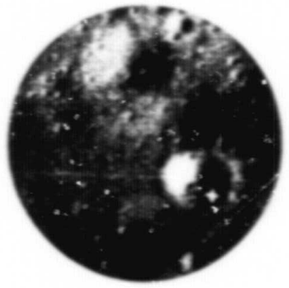

C. SUPERIMPOSITION OF 3 POSITIVES FROM GRE 12T

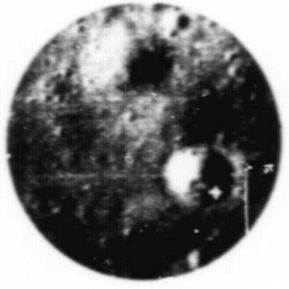

A. PRINT FROM SINGLE POSITIVE FROM GRE 12T

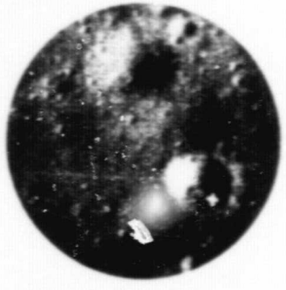

D. SUPERIMPOSITION OF 4 POSITIVES FROM GRE 12T

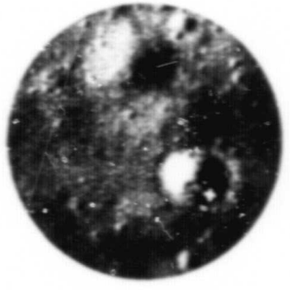

E. SUPERIMPOSITION OF 2 POSITIVES FROM GRE 12T AND FROM GRE 02T

FIGURE 73. DEMONSTRATION OF GRAIN INTEGRATION OF LOP GRE FILMS, 3X REDUCTIONS OF GRAIN INTEGRATION WORK DONE AT 8X ENLARGEMENT FROM GRE POSITIVES

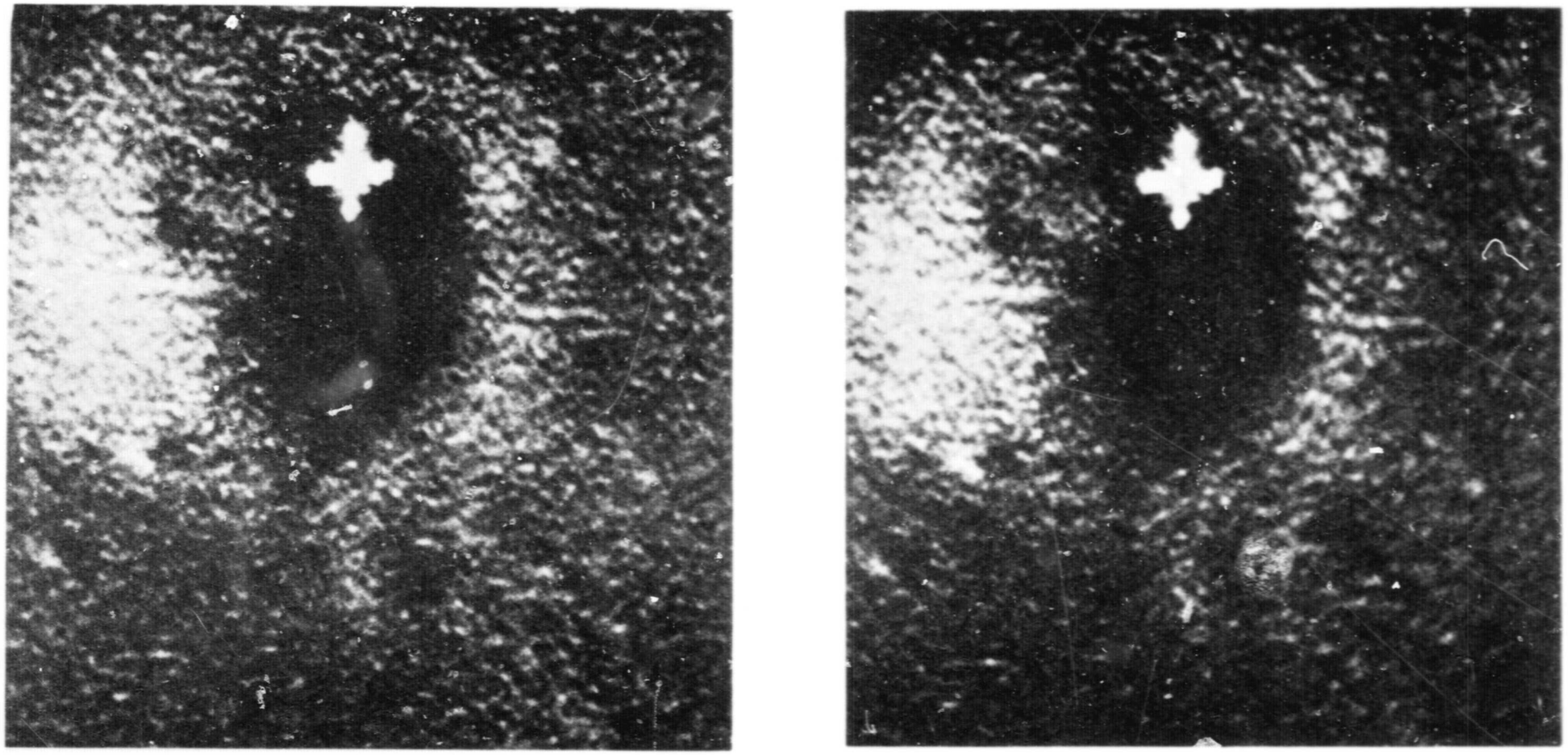

A RUN 1 B RUN 2

FIGURE 74. 20X ENLARGEMENT OF 2 READOUTS FROM A SINGLE GRE (12T) MADE FROM SEQUENTIAL READOUTS OF TAPE RECORD OF FRAME 137 HR, MISSION 111, LOP

A second approach involves working with stereo pairs from one mission or frames showing a common area from different missions. This procedure is considered to be too difficult experimentally to be useful.

The most promising prospect involves making noise-integrated photographs from scenes which received multiple readouts (priority and final). In this case, the noise should be random.

β. Ring Smear Masking - Use of the ring smear technique assumes that the signal spectrum can be enhanced in relation to the noise spectrum. This condition requires that the noise spectrum is at least partially in a region other than the bandwidth of the signal. Since it has already been shown that the major noise spectrum for LOP photographs lies completely within the signal spectrum for a single readout, we would not expect that ring smear would enhance the signal in relation to the noise. It would be possible to rearrange the relative modulation at different frequencies. However, this rearranged modulation would still include the noise modulation.

One procedural modification was made for this study which is different from the ring smear work described in Figure 70. The change was that the ring smear mask was not physically made. Instead, a straight print was made by exposing through the base of the Type 8430 print film with the original positive firmly attached to the vacuum platen. After processing, this straight print was placed back on the platen at the same position by the use of register pins. The high contrast print film (Type 5427) was placed behind the straight print. The emulsion of the straight print was held in intimate contact with the Type 5427 raw stock by a vacuum. The effect of a ring smear mask was created by rotating the glass plate during exposure. The 5427 film was processed to make an enhanced negative print.

This technique has several advantages:

1. Elimination of a printing stage; thereby reducing sharpness losses.
2. Elimination of a film base thickness, also reducing a sharpness degradation and allowing a more accurate representation of the theoretical mask transfer function.
3. Allowance for the possibility of enhancing over a wider band of frequencies by using several tilt angles of the glass plate in one enhanced image.
4. Improvement in turn-around time so as to reduce cost.

The enhanced images were made at the following conditions:

1. Plate tilt = 29°
   Maximum enhancement at 10.4 lines/mm
2. Plate tilt = 39.5°
   Maximum enhancement at 6.4 lines/mm
3. Plate tilt = 21°
   Maximum enhancement at 14 lines/mm
4. Three separate exposures each occupying 1/3 of the total exposure, with the ring smear plate set sequentially at 22°, 29°, and 39.5°

Figure 75 shows these enhanced prints compared with an unenhanced straight print. The differences are negligible between enhanced prints and the straight print. This result can again be attributed to the fact that the major noise contributor is non-random phosphor noise from the spacecraft.

B. PRINT MADE WITH RING SMEAR FOR ENHANCEMENT AT 14 LINES/MM (21° TILT ANGLE)

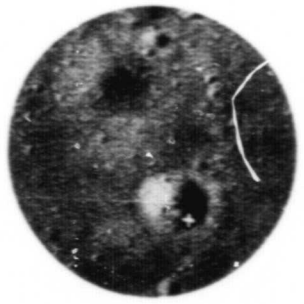

C. PRINT MADE WITH RING SMEAR FOR ENHANCEMENT AT 10.4 LINES/MM (29° TILT ANGLE)

A. PRINT MADE WITH NO RING SMEAR

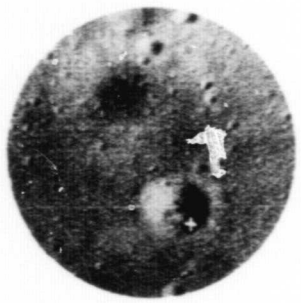

D. PRINT MADE WITH RING SMEAR FOR ENHANCEMENT AT 6.4 LINES/MM (39.5° TILT ANGLE)

E. PRINT MADE WITH RING SMEAR FOR EQUAL ENHANCEMENT AT 6.4, 10.4 AND 14 LINES/MM

FIGURE 75. DEMONSTRATION OF RING SMEAR MASKING OF LOP GRE FILMS, 3X REDUCTIONS OF ENHANCED PRINTS MADE AT 8X ENLARGEMENT FROM GRE POSITIVES

IV. RECOMMENDATIONS FOR FUTURE WORK

On the basis of the experience and progress made on this current contract, we have outlined four activities for future work. A brief summary of the justification for each activity follows the list of tasks under each activity.

A. Calibration of Hand-Held Cameras for Apollo Crewmen

1. Prepare specifications describing the characteristics to be measured and the accuracy and precision requirements for these measurements. These measurements will include, but not be restricted to, the following:

    a. Lens transmittance

        i. Spectral - 400 - 700 mμ (on axis only)
        ii. Integrated - source equivalent to sunlight over range 400 - 700 mμ and detector with pan film response (on-axis and off-axis)
            Measured
            Calculated

    b. Filter pass band - 350 - 750 mμ
    c. Flare characteristic at different f-numbers
    d. Shutter reproducibility (in atmosphere and vacuum)
        i. Reproducibility at each setting for repeated actuations
        ii. Reproducibility at each setting for changes in settings
    e. Aperture control reproducibility

2. Prepare written procedures to be followed to make measurements on the cameras with the accuracy and precision required.

The prospect of taking photographs of the moon by a man standing on the surface and/or in low orbit and having the films returned to earth offers a unique opportunity to do photographic photometry. This activity will require careful sensitometry in order to get maximum value from the photographs. Careful measurements are required on all photometric characteristics of the cameras, i.e., those characteristics of the cameras controlling the amount of light reaching the film.

Special attention is required in considering the effects of the hard vacuum environment, the presence of ultra-violet radiation and the influence of flare in photographing subjects having a wide range of brightness.

B. Preparation of Lunar Orbiter Photographs with Enhancement

1. Devise optimum techniques for enhancing prints from GRE films

   a. Grain integration

      i. Repeat runs from single GRE
      ii. Repeat runs on different GRE's
      iii. Primary and final readouts
      iv. Stereo pairs from one mission
      v. Duplicate photos from different missions

   b. Ring smear masking
   c. Combination of grain integration and ring smear

2. Prepare enhanced photographs of selected areas from Lunar Orbiter GRE films

The use of Lunar Orbiter photographs in preparing contour maps of the lunar surface requires extracting the maximum amount of density information from them. The Lunar Orbiter system produces

multiple photographic copies of each original photograph and lends itself naturally to the classic form of photographic enhancement by superimposition of duplicate negatives in printing.

The ratio of signal to noise in a composite photograph is theoretically increased by the square root of the number of duplicate negatives used to prepare the composite.

Four sources of grain noise existed in the Lunar Orbiter system: (1) the photographic grain in the original negative; (2) the phosphor grain in the readout system; (3) the phosphor grain in the Ground Reconstruction Electronics system, and (4) the photographic grain in the recording film.

Superimposition of duplicate GRE films made on the same GRE from the same original tape recording of the spacecraft signal will reduce effects of recording film grain noise. Little image enhancement is expected by this activity since recording film grain noise is not a large contributor to system noise. A limited demonstration has confirmed this prediction.

Superimposition of GRE films from different GRE's will eliminate phosphor grain noise in the Ground Reconstruction Electronics system, although this noise contribution is not very large. Differences in the optical system in the different GRE's can introduce additional problems. A limited demonstration has shown little gain in photographic quality.

The phosphor grain noise in the readout system is probably the largest contributor to the noise in the final print. Two possibilities exist for reducing the effects of this noise. On each LOP mission, readouts of certain photographs were made twice, once in priority and once in final readout. Direct superimposition of GRE films

for these readouts would reduce this large contributor to system noise. In addition, stereo photographs were made in certain areas of interest. Several problems are introduced in superimposing GRE films from those photographs. Differences in orbital position and altitude produced changes in scale and perspective. Passage of time between orbits produced changes in shadows. The latter problem could not be readily overcome but the former problem would be reduced by using rectification techniques. Finally, superimposition could be tried with multiple photographs of specific areas by the different Lunar Orbiters. Some of the same problems would exist in this work as were described for multiple photographs from the same Orbiter vehicle.

Photographic masking using the ring smear technique can be applied to any of the photographs prepared with or without grain integration. This form of enhancement provides selective relative suppression of very low spatial frequencies and the high noise frequencies, giving a crispening effect to edges. Usually, ring smear enhancement gives the reader greater confidence in detection and enhancement of details. No attempt has been made to use photoclinometric mapping techniques to prepare a contour map from a photograph enhanced by ring smear.

Spatial frequency filtering could be applied to Lunar Orbiter photographs to reduce the effects of repetitive noise caused by the raster of the readout. Such methods have not been used to date.

C. Extension of Measurement of Lunar Photometric Function

1. Apply techniques developed to measure photometric function to specific lunar areas using LOP photographs

   a. Potential landing sites
   b. Continents (highlands)

c. Crater interiors
d. Ray systems
e. Transition zones (between marias and continents)
f. Aristarchus region

2. Correlate photometry measured from earth, Surveyor, Ranger and Lunar Orbiter.
3. Extend measurements of diameter/depth ratio and population density of craters on Lunar Orbiter photographs.
4. Relate new crater shape and population data to average luminance of lunar photographs as an aid in determination of correct exposure for photographs taken from lunar orbit.

The original measurements of lunar photometric function were made using integrated light from the whole moon. Measurements from earth cannot avoid the limitation imposed by the limiting resolution of telescopes, a factor of about 1000 poorer than the resolution of Lunar Orbiter. Measurements from Surveyors are limited to very small areas.

Lunar Orbiter photographs offer a unique opportunity to refine the measurements of photometric function, to produce values with increased confidence for a wide variety of topographic features and to examine the effects of scale.

Work should be carried out to unify the results obtained from the four points of observation--Earth, Surveyor, Ranger and Orbiter.

Measurements should be made on Lunar Orbiter photographs to extend knowledge of the distribution of crater sizes and shapes and to relate this information to scene luminosity.

Our most recent attempt to extend this information followed the impact landings of Rangers VII and IX, from which limited information

could be gained because of resolution limitations in high altitude photographs and small area sampling in the final frames.

A comparison of the number of small craters in the contour map prepared by NASA for the area of Sinus Medii with the number of craters expected from Ranger VII data shows a large difference.

One generally unappreciated but important consequence of the population distribution of sizes and shapes of craters is the effect on average scene luminance. Because the density of craters (number per unit area) increases very rapidly with smaller sizes, the average scene luminance changes with altitude. For example, based on Ranger VII data, if the limiting ground resolution of a camera is a 10 ft. diameter crater at 100 nm altitude, and the field of view is one square mile, a photograph under these conditions should show 16000 craters at limiting resolution. From an altitude of 50 nm, the field of view is 1/4 square mile and the limiting ground resolution is a 5 ft. diameter crater. A photograph under these conditions should show 20000 craters at limiting resolution. The result of this difference in number of craters at limiting resolution or larger is a difference in the apparent average scene luminance for scenes that otherwise would look alike.

D. Preparation of Training Motion Pictures

1. Assemble camera components and models to enable the preparation of additional motion pictures simulating lunar landings showing the full view from LM window.

2. Prepare motion pictures using this equipment

   a. 1:50 model (EKC) of Sinus Medii (10' x 10')
   b. 1:2000 model (AMS) (14' x 22')

Motion pictures prepared on previous contracts have been improved in stages, making more realistic the simulation of the Lunar Module landing approach. The main purpose of these previous motion pictures has been to show the relative visibility of subjects under a limited variety of conditions for use by personnel studying lighting conditions for a lunar landing.

This previous work has brought about the development of techniques for producing a realistic model and making motion pictures with a minimum of distracting faults. This experience should be used to prepare motion pictures without the current limitations set by size of model and field of view.

BIBLIOGRAPHY

Reference Number	Source
1	Final Report, Lunar Photo Study, Contract NAS 9-3826, 1 October 1965
2	Final Report, Phase II Lunar Photo Study, Contract NAS 9-3826, 1 November 1966
3	The Lunar Reflectivity Model for Ranger Block III Analysis, TR 32-664 JPL, 2 November 1964
4	Reference 2, page 4
5	Reference 1, page 30
6	Reference 2, page 144
7	Reference 2, page 154
8	Reference 3, page 2
9	Manual of Photogrammetry, American Society of Photogrammetry, Third Edition, Vol. 1, page 31
10	Quality Control Test Report 1206-204, paragraphs 6.9.12-6.9.21
11	LOP Quality Control Procedure QC-B-325 Rev. F, "In Process Test Procedure for Readout Section"
12	Hansell, J.R. to A. Conderacci. "SO-243 Flight Film, (1202-234-2) Rev. B-1 for use in PS5" Eastman Kodak Letter L-024248-KU, 12 January 1967
13	Eastman Kodak Utility Technical Manual 1228-113 "Operation and Service Instructions Ground Reconstruction Electronics"
14	Rennilson, J.J., Holt, H.E. and Morris, E.C., J. Opt. Soc. Am. 58,747, 1968
15	Reference 3, page 10
16	Hapke, B. Astronomical Journal 71,333, 1966
17	A Study of Lunar Orbiter Photographic Evaluation (Project SLOPE) NASA CR-66493

Reference Number	Source
18	Reference 17, Appendix B
19	A. G. Herriman et al, "Ranger Preflight Science Analysis and the Lunar Photometric Model," JPL Technical Report No. 32-384 (Rev), 10 (1963)
20	D. Paris, Phot. Sci. and Eng., 6, 55 (1962)
21	Reference 1, page 113
22	Reference 1, page 69
23	A study of Lunar Orbiter Photographic Evaluation (Project SLOPE) NASA CR-66158, page 12
24	Reference 17, page 17
25	Reference 23, page 13
26	Nelson, C.N., Eisen, F.C. and Higgins, G.C., "Effect of Nonlinearities When Applying Modulation Transfer Techniques to Photographic Systems", Paper Presented at SPIE Seminar 22 March 1968
27	Paris, D.P., "Approximation of the Sine-Wave Response of Photographic Emulsions" J. Opt. Soc. Am. 51,988, 1961
28	Reference 23, page 8
29	Reference 23, page 19
30	Reference 1, page 62
31	Reference 1, page 94
32	Reference 17, page 151
33	Kohler, R. and Howell, H. Photo. Sci. and Eng. 7, 241, 1963
34	Armitage, J., Lohmann, A. and Herrick, R., Appl. Opt. 4, 445, 1965